

Surface electrons at dielectric plasma walls

Inauguraldissertation

zur

Erlangung des akademischen Grades eines

Doktors der Naturwissenschaften

der

Mathematisch-Naturwissenschaftlichen Fakultät

der

Ernst-Moritz-Arndt-Universität Greifswald

vorgelegt von

Rafael Leslie Heinisch

geboren am 21. Februar 1985

in Tübingen

Greifswald, 19 August 2013

Dekan:

Prof. Dr. Klaus Fesser

1. Gutachter:

PD Dr. Franz Xaver Bronold

2. Gutachter:

Prof. Dr. Karl-Heinz Spatschek

Tag der Promotion:

30. Oktober 2013

Contents

1	Summary	1
1.1	Introduction	1
1.2	Electron surface layer — Article I	3
1.3	Electron physisorption — Articles II, III, and IV	10
1.4	Mie scattering by a charged dielectric particle — Articles V and VI	17
1.5	Conclusions	23
2	Thesis Articles	27
	Article I — Electron surface layer at the interface of a plasma and a dielectric wall	29
	Article II — Phonon-mediated desorption of image-bound electrons from dielectric surfaces	43
	Article III — Phonon-mediated sticking of electrons at dielectric surfaces	63
	Article IV — Physisorption of an electron in deep surface potentials off a dielectric surface	73
	Article V — Mie scattering by a charged dielectric particle	85
	Article VI — Optical signatures of the charge of a dielectric particle in a plasma	91
	Bibliography	101
	Publications and Conferences	105
	Erklärung	109
	Curriculum Vitae	111
	Acknowledgement	113

1 Summary

1.1 Introduction

The surface of a macroscopic object exposed to an ionised gas usually accumulates electrons. The negative charge it thereby acquires stems from the higher electron flux compared to the ion flux in the bulk of the discharge which is due to the higher temperature and smaller mass of the electrons compared to the ions. After the object is brought into contact with the plasma the electron influx exceeds the ion influx. The collection of electrons then gives rise to a repulsive Coulomb potential which reduces the further influx of electrons until—in quasi-stationarity—electron and ion flux onto the surface balance each other. This charge transfer leads to the formation of a charge double layer at the plasma wall. It consists of the plasma sheath, the electron depleted region adjacent to the wall, and the electron adsorbate on the wall.

The traditional modelling of the plasma boundary has been focused on the plasma sheath which is the macroscopic manifestation of the charge transfer at the plasma wall. From the perspective of the sheath model the wall is the position where the boundary conditions for the distribution functions of the charged plasma species are enforced. The wall-bound electron adsorbate has no spatial extent and its main function is to regulate the Coulomb barrier which confines the majority of electrons to the bulk of the plasma. The time-scale of the microscopic processes responsible for the charge-up is usually assumed to be too short to be of significance for the discharge development [1]. Instead, the wall is considered a perfect absorber for the charged species of the plasma, that is, electrons and ions are assumed to recombine instantly at the wall.

While this approach may be sufficient for large discharges with small surface to volume ratios it becomes questionable for the modelling of small discharges with large surface to volume ratios. Indeed, the nature and build-up of surface charges have received increasing attention in theory [2] as well as in various novel set-ups of bounded plasmas, such as dusty plasmas, dielectric barrier discharges and micro-plasmas (illustrated in Fig. 1).

In dusty plasmas [3–5], for instance, the charge the dust particles accumulate from the plasma is a central quantity of interest. It controls the overall charge balance of the discharge [6] as well as the coupling of the particles among each other and to external electromagnetic fields. As a consequence, various methods have been devised to measure the particle charge. For instance for particles trapped in the plasma sheath [7,8], the charge can be inferred from a force balance which, however, requires the local plasma parameters. Alternatively, the charge can be obtained from wave dispersion measurements [9], normal mode analysis [10] or dust cluster rotation [11]. These methods are independent of the plasma parameters but less accurate. Thus, the precise determination of the particle charge remains a challenge.

In dielectric barrier discharges [12], where either one or both of the electrodes are covered with a dielectric material, surface charges determine the spatio-temporal structure of the discharge [13–15]. Surface charges, for instance, may pin the filaments in the filamentary mode of a dielectric barrier discharge and give the discharge a memory across several cycles.

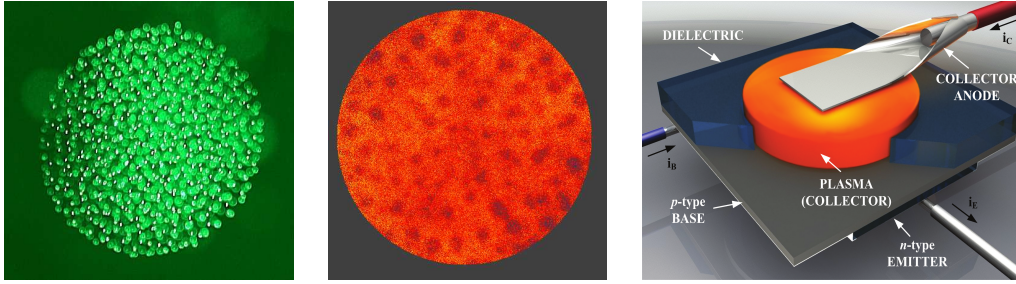


Fig. 1: Three novel bounded plasmas where surface charges matter. Left: The particle charge controls interactions between dust grains forming a spherical dust ball. Middle: Surface charges (negative charges in blue over neutral background in red) pin the location of filaments for a filamentary dielectric barrier discharge (courtesy of Robert Wild). Right: The plasma serves as a collector in a plasma transistor (reproduced from [24]).

Important questions are thus how electrons are trapped and released and how mobile they are in the lateral direction to the wall. Only recently, the experimental detection of surface charges has made significant progress. Using the opto-electronic Pockels effect time and spatially resolved studies of surface charges have become possible [16–19].

Lastly, in solid-state based microdischarges [20–23] the miniaturisation of the discharge increases the surface to volume ratio to such an extent that the (biased) plasma wall becomes an integral part of the discharge. For instance in the plasma transistor [22,24,25], the charge transfer from the plasma into the solid and vice versa may even be used to lend new functionality to electronic devices. Here, the field in the sheath can induce a bending of the energy bands in the semiconductor while the control of the carrier density in the semiconductor varies the effective secondary electron emission coefficient of the surface.

An improved modelling of the plasma boundary for discharges which are strongly influenced by surface charges exceeds the scope of traditional sheath models. Instead, it has to focus on the surface electrons, their distribution in the short-ranged surface potential and the charge-transferring processes such as electron trapping and release (illustrated in Fig. 2). A first step to a model for the surface electrons has been taken by Emeleus and Coulter [26,27] as well as Behnke and coworkers [13,28] who envisaged a surface plasma of ions and electrons coupled to the bulk plasma by phenomenological rate equations characterised by sticking coefficients, residence times, and recombination coefficients.

Here, we consider the build-up, distribution and release of surface electrons from a surface physics point of view quantum mechanically. The problem of wall charging then separates into two parts: the classical kinetics on a macroscopic lengthscale until the electron hits the effective surface of the object and the microscopic charge transfer processes which follow. Our focus lies on the microphysics of the surface electrons. For simplicity we consider a floating wall exposed to a quasistationary plasma. Complications due to the individual break-downs in a dielectric barrier discharge or due to peculiarities of the electron and ion kinetics around a dust particle (as for instance the effect of charge exchange collisions [29,30]) are not considered. In this work we study the surface electrons at the plasma wall employing microscopic models. Specifically, we consider (i) the dependence of trapping sites for surplus electrons on the type of dielectric, (ii) sticking and desorption of electrons, and (iii) the surface charge effects on the scattering of light by a dust particle.

We begin with a model for the electron surface layer (ESL) which includes the Coulomb as well as the short-range surface potential and complements the plasma sheath. In this model we calculate the potential and charge distribution of a floating plasma wall in quasi-

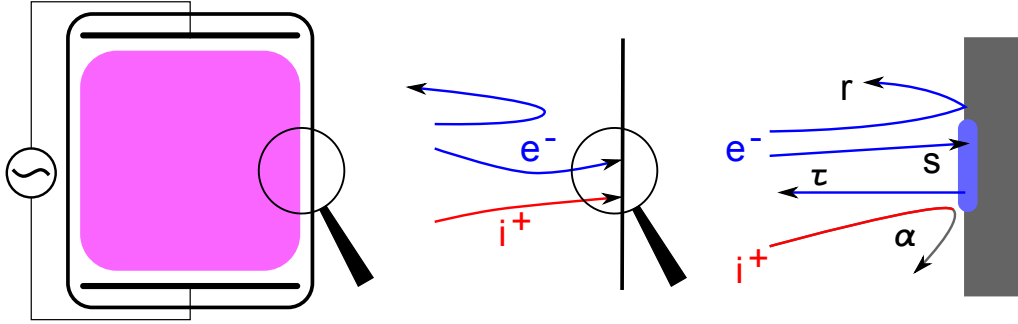


Fig. 2: Illustration of the plasma and its boundary. The bulk plasma (left) is characterised by quasi-neutrality. In the sheath (middle) ions outweigh electrons, quasi-neutrality does not hold and a potential gradient is formed. Note that the bulk as well as the sheath have macroscopic extent and can be described classically. The microscopic processes at the surface (right), for instance electron reflection, sticking or desorption as well as electron-ion recombination occur on a length scale smaller than the shortest collision length of the plasma and have to be described by quantum mechanics.

stationarity. This gives us a framework for identifying trapping sites for electrons. They depend on the potential offset between the plasma and the conduction band inside the dielectric which is characterised by the electron affinity χ of the dielectric. Guided by the ESL model we will then identify scenarios for the wall charge-up, which again depend on χ . For the case where electron trapping takes place in the image states ($\chi < 0$) we will consider electron physisorption in detail and calculate sticking coefficients and desorption times. Then we turn to an intrinsic property of the surface electrons: their effect on the scattering of light by a dust particle. Surplus charges affect the scattering signal through their electrical conductivity which, for a dielectric, is limited by the scattering with optical phonons. Analysing the different scattering regimes we look for charge signatures in the Mie signal. They could be used as a novel diagnostic for the charge of a dust particle in a plasma.

This thesis is the first detailed microscopic study of the surface electrons at a dielectric plasma wall. The starting point of our investigations was the electronic physisorption in the image states. Later our work on the ESL showed us that this scenario applies only to dielectrics with $\chi < 0$. For reasons of clarity the material and corresponding manuscripts in this thesis are not ordered chronologically but thematically starting with the ESL.

1.2 Electron surface layer — Article I

In this section we consider the surface electrons on a floating plasma wall in quasi-stationarity. To capture the spatial extent of this interface-bound electron distribution we introduce our concept of the electron surface layer (ESL). It describes the electron distribution immediately at the plasma-solid interface and complements the modelling of the sheath which gives the electron and ion density in the positive space charge region on the plasma side of the interface. Together ESL and sheath give the spatial resolution of both parts of the charge double layer at the plasma boundary.

Our model for the electron surface layer focuses on the interface-specific electron distribution which is supplied by the plasma but thermalised with the solid. Specifically, we calculate the potential as well as the distribution of wall-bound electrons under the

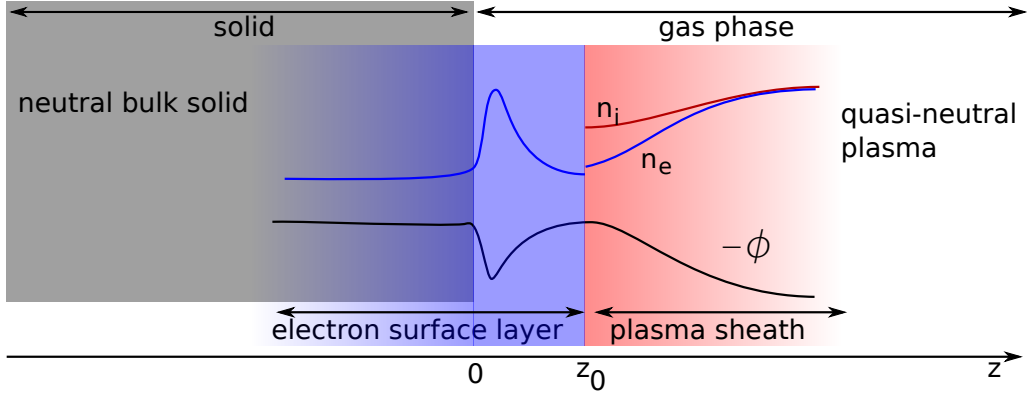


Fig. 3: Qualitative sketch of the charge double layer formed at a plasma wall. The electrons depleted from the plasma sheath are accumulated in the ESL. Note that the boundary between sheath and ESL is located in front of the crystallographic interface.

assumption that at quasi-stationarity they are thermalised with the wall. For this we use a one-dimensional model of an ideal dielectric surface (sketched in Fig. 3). The crystallographic interface is located at $z = 0$, the plasma occupies the half space $z > 0$, and the dielectric occupies the half space $z < 0$. In the following, we will identify the boundary position between the ESL and the sheath, relate the number of plasma-supplied charges to a simple sheath model, construct a surface potential from a graded interface model [31], and use concepts of density functional theory [32] to calculate the electron distribution in the ESL (for details see Article I [E]).

The ESL is the region where electrons can be temporarily bound to the surface due to the short-range surface potential. Its boundary with the sheath at z_0 is located in front of the crystallographic interface where the forces on the electron from the attractive surface potential ϕ_{surf} and the repulsive sheath potential ϕ_{sheath} compensate each other. Thus, z_0 is given by the force balance

$$\left. \frac{d\phi_{\text{surf}}}{dz} \right|_{z_0} + \left. \frac{d\phi_{\text{sheath}}}{dz} \right|_{z_0} = 0. \quad (1)$$

For $z < z_0$ an electron is attracted to the surface and thus contained in the ESL while for $z > z_0$ it is repelled back into the plasma. The position z_0 is an effective wall for plasma electrons and ions at which the flux balance between electron flux j_e and ion flux j_i has to be fulfilled. We use for simplicity the perfect absorber model $j_e = j_i$. The effective wall position also gives the distance to the surface at which the description of the plasma sheath based on the long-range potential breaks down as the short-range surface potential becomes dominant.

Within this quasi-static model for the ESL the number of plasma-supplied electrons at the wall equals the number of electrons missing in the sheath. Thus, the surface density of electrons in the ESL can be obtained from a model for the plasma sheath together with a flux balance condition at z_0 .

For simplicity, we use a collision-less sheath model [1], more realistic sheath models [1, 33, 34] make no difference in principle. In this model ions enter the sheath with a velocity v_{i0} . They satisfy a source-free continuity equation $n_i v_i = n_0 v_{i0}$ and an equation of motion

$$v_i \frac{dv_i}{dz} = -\frac{e}{M} \frac{d\phi}{dz}, \quad (2)$$

with n_0 the plasma density and n_i the ion density (M is the ion mass and e the elementary charge). Electrons are thermalised, that is their density $n_e = n_0 \exp(e\phi/k_B T_e)$, with T_e the electron temperature. The potential ϕ satisfies Poisson's equation which takes the form

$$\frac{d^2}{dz^2}\phi = -4\pi en_0 \left[\frac{v_0}{v_i} - \exp\left(\frac{e\phi}{k_B T_e}\right) \right]. \quad (3)$$

Introducing dimensionless variables $\eta = -e\phi/(k_B T_e)$, $\xi = z/\lambda_D$ and $u = v_i/c_s$, where $\lambda_D = \sqrt{k_B T_e/4\pi n_0 e^2}$ and $c_s = \sqrt{k_B T_e/M}$, Eq. (2) becomes $uu' = \eta'$. This can be integrated and gives $u = -\sqrt{2\eta + u_0^2}$, where $u_0 = v_{i0}/c_s$ is the reduced velocity of ions entering the sheath. Then Eq. (3) becomes

$$\eta'' = -\frac{u_0}{\sqrt{2\eta + u_0^2}} - \exp(-\eta). \quad (4)$$

The potential and the field vanish far inside the plasma, that is, $\eta \rightarrow 0$ and $\eta' \rightarrow 0$ for $\xi \rightarrow \infty$. Using this boundary condition Eq. (4) can be integrated once and we obtain

$$\eta' = -\sqrt{-2u_0\sqrt{2\eta + u_0^2} + 2\exp(-\eta) + 2u_0\sqrt{u_0^2} - 2}. \quad (5)$$

For ions entering the sheath with the Bohm velocity $u_0 = -1$. The field at the effective wall as a function of the wall potential $\eta_w = \eta(\xi_0)$ is then given by

$$\eta'_w = -\sqrt{2\sqrt{2\eta_w + 1} + 2\exp(-\eta_w) - 4}. \quad (6)$$

The surface density of surplus ions in the sheath can be related by Poisson's equation to the field at the wall and reads

$$N = \int_{z_0}^{\infty} dz(n_i - n_e) = -n_0 \lambda_D \eta'_w. \quad (7)$$

Combining Eqs. (7) and (6) gives the total surface density of electrons to be inserted into the ESL as a function of the wall potential.

The wall potential itself is determined by the flux balance condition, $j_e = j_i$, which, in the ESL model, is assumed to be fulfilled at $z = z_0$. Using the Bohm flux for the ions and the thermal flux for the electrons,

$$j_i = n_0 \sqrt{\frac{k_B T_e}{M}} \quad \text{and} \quad j_e = \frac{1}{4} n_0 \sqrt{\frac{8k_B T_e}{\pi m}} \exp\left(\frac{e\phi}{k_B T_e}\right), \quad (8)$$

(m is the electron mass) the wall potential is given by [1]

$$\eta_w = \frac{1}{2} \ln\left(\frac{M}{2\pi m}\right) \quad \text{and} \quad \phi_w = -\frac{k_B T_e}{2e} \ln\left(\frac{M}{2\pi m}\right). \quad (9)$$

In the collision-less sheath model the wall potential depends only on the electron temperature and the ion to electron mass ratio. The surface density of electrons in the ESL depends moreover on the plasma density.

We can now move on to the distribution of surplus electrons in the surface layer. It is primarily determined by the potential in the interface region surrounding an ideal dielectric interface. We first single out the relevant microscopic potentials at the interface (illustrated

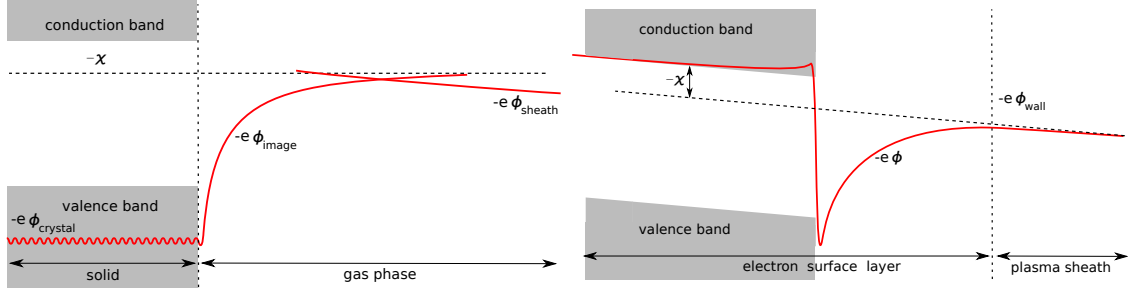


Fig. 4: Left: Microscopic potentials at the interface between a plasma and a dielectric wall. The crystal potential merges continuously with the image potential and the sheath potential. Inside the dielectric the crystal potential gives rise to a band structure. The electron affinity χ gives the offset of the conduction band minimum to the long-range potential in front of the surface which is given by the asymptote of the image potential (dashed line). Right: Effective potential for the graded interface on which the model of an ESL is based. It encompasses the image potential as well as the potential offset at the interface. The restoring force from the positive charge in the sheath leads to the overall tilt of the potential (reproduced from Article I).

on the left panel of Fig. 4) and then describe an effective model for them (sketched on the right panel of Fig. 4).

Far away from the surface the potential is given by the repulsive sheath potential. Closer to the surface an attractive surface potential, the image potential, which stems from the dielectric mismatch at the interface, becomes dominant. Classically the image potential is given by the expression [35]

$$\phi_{\text{im}}(z) = \frac{\epsilon_0 - 1}{4(\epsilon_0 + 1)} \frac{e}{z}, \quad (10)$$

where ϵ_0 is the static dielectric constant. This expression is valid far away from the wall. Closer to the wall the $1/z$ shape is modified as the potential merges continuously with the crystal potential in the bulk of the dielectric. Even more important inside the dielectric is the band structure. For a dielectric the valence band is filled while the conduction band is completely empty. Thus, surplus electrons can populate the conduction band and the conduction band minimum acts as a long-range potential for the electrons. In addition to the image potential, the surface potential comprises an offset due to a charge double layer formed immediately at the surface. It is due to electron density leaking out of the solid—a consequence of free energy minimisation—or to relaxation and polarisation of the atomic bonds at the surface—a consequence of the truncation of the lattice. This offset of the conduction band minimum at the surface to the potential in front of it is characterised by the electron affinity of the solid χ . For $\chi < 0$ the conduction band minimum lies above the potential just in front of the solid, for $\chi > 0$ it lies below it.

So far we have considered an uncharged surface. This raises the question whether the electronic structure of the surface is changed by the surplus electrons from the plasma. In comparison to the electrons responsible for the chemical binding within the dielectric the additional electrons coming from the plasma are only a few. The available electronic states and the offset of the energy bands in the bulk with respect to the potential outside the dielectric will thus not be changed significantly by the presence of the wall charge. Note however, that a chemical modification of the plasma wall can change the electronic structure. In particular the electron affinity is susceptible to surface coating and ad-atoms.

Surface termination by elements with small electronegativity, for instance hydrogen, may induce a negative electron affinity [36], while elements with larger electronegativity, for instance oxygen, can lead to a positive electron affinity [37].

From these microscopic potentials we construct an effective surface potential. For this we employ the model of a graded interface which gives a realistic image and offset potential without performing an atomistically accurate calculation. This model is parametrised by experimentally measured (or where not available theoretically calculated) values for the electron affinity χ , the dielectric constant ϵ_0 , and the conduction band effective mass m . First proposed by Stern [31] to remove the unphysical singularity of the image potential at $z = 0$ and later extended to potential offsets at semiconductor heterojunctions [38] it assumes the smooth variation of parameters that change abruptly at the interface over a length on the order of the lattice constant. For our purposes we assume a sinusoidal interpolation of the dielectric constant, the offset of the long-range potential and the effective electron mass with a grading half-width of 5×10^{-8} cm. The details of this model are found in Article I. It does not account for effects associated with intrinsic surface states (Shockley or Tamm states [39]) or additional states which may arise from the short-range surface potential. Nevertheless the graded interface model is a reasonable description of the surface, suited for dielectrics with ionic bonds which typically have no intrinsic surface states.

The total surface potential calculated with the graded interface model is continuous across the crystallographic interface at $z = 0$ and enables us thereby to also calculate a smoothly varying electron distribution in the ESL. The surface potential,

$$\phi_{\text{surf}}(z) = \phi_{\text{im}}(z) + \phi_{\text{offset}}(z), \quad (11)$$

includes the graded image and offset potentials. Using the force-balance condition Eq. (1) we can now determine the effective wall position z_0 . As the field in the sheath is relatively weak compared to the image force the boundary is so far away from the crystallographic interface that ϕ'_{offset} vanishes and the image potential obeys Eq. (10). Thus, the boundary between the ESL and the plasma sheath is given by

$$z_0 = \sqrt{\frac{(\epsilon_0 - 1)e}{4(\epsilon_0 + 1)\phi'_w}} \quad (12)$$

with $\phi'_w = -(k_B T_e \eta'_w)/(e\lambda_D)$ and η'_w given by Eq. (6).

We now turn to the distribution of the plasma-supplied electrons in the ESL. For our quasi-static model we assume that the wall-bound surplus electrons are in thermal equilibrium with the wall. Thus, their distribution minimises the grand canonical potential and satisfies Poisson's equation. To minimise the grand canonical potential we apply, inspired by Tkharev and Danilyuk [32], density functional theory [40, 41] to the graded interface. For simplicity we will use density functional theory in the local approximation. In our one-dimensional model the ground state electron density that minimises the grand canonical potential satisfies

$$-e\phi(z) + \mu^h(z) - \mu = 0, \quad (13)$$

where $\mu^h(z)$ is the chemical potential of the homogeneous system. The electrostatic potential $\phi(z) = \phi_{\text{surf}}(z) + \phi_C(z)$ consists of the potential of the bare surface given by Eq. (11) and the internal Coulomb potential which satisfies Poisson's equation

$$\frac{d}{dz} \left(\epsilon(z) \frac{d}{dz} \phi_C(z) \right) = 4\pi en(z) \quad (14)$$

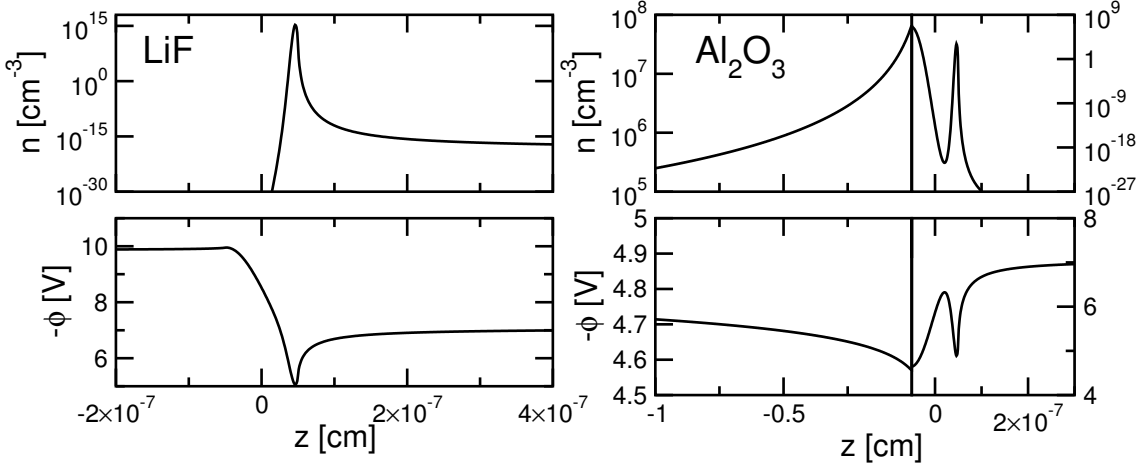


Fig. 5: Plasma-supplied excess electron density n (upper panel) and the potential $-\phi$ (lower panel) it gives rise to for a LiF (left) and an Al₂O₃ (right) surface in contact with a helium discharge with $n_0 = 10^7 \text{ cm}^{-3}$ and $k_B T_e = 2 \text{ eV}$. Note the different scales of the axes for the left and right panels. On the scale where variations in the space charge for Al₂O₃ are noticeable the electron distribution for LiF is basically a vertical line.

with the graded dielectric constant $\epsilon(z)$. The boundary conditions $\phi_C(z_0) = \phi_w$ and $\phi'_C(z_0) = \phi'_w$ guarantee continuity of the potential at z_0 and include the restoring force from the positive charge in the sheath. As the electron density of the surplus electrons is relatively small and the temperature of the surface is rather high, typically a few hundred Kelvins, we can use for the chemical potential of the homogeneous electron system $\mu^h(z) \equiv \mu^h(n(z), T)$ the expression adequate for a homogeneous, non-interacting, non-degenerate electron gas

$$n(z) = \frac{1}{\sqrt{2}} \left(\frac{m(z) k_B T}{\pi \hbar^2} \right)^{\frac{3}{2}} e^{\frac{\mu^h(z)}{k_B T}}, \quad (15)$$

where $m(z)$ is the graded effective electron mass and T the surface temperature.

For the calculation of the quasi-stationary distribution of surplus electrons Eqs. (13) and (14) have to be solved iteratively (until μ is stationary) subject to the additional constraint $\int_{z_s}^{z_0} dz n(z) = N$ which guarantees charge neutrality between the ESL and the plasma sheath. The position $z_s < 0$ is a cut-off which has to be chosen large enough in order not to affect the numerical results. In a more refined model for the ESL the crossover of the wall charge to the neutral bulk of the dielectric can be taken into account by splitting the ESL into an interface specific region and a space charge region. This approach which turns z_s from an ad-hoc cut-off into the boundary between two regions is described in Article I. For the charge distribution at the interface the simple model is however sufficient.

We now apply the ESL model to a helium discharge in contact with a LiF and Al₂O₃ surface and calculate the electron density and potential at the interface. Depending on the electron affinity χ of the dielectric one of two scenarios for the distribution of surplus electrons in the ESL may be realised.

For $\chi < 0$ the conduction band lies above the potential in front of the surface. It is energetically unfavourable for electrons to populate the conduction band. Instead, they are bound in the image potential in front of the surface (see left panel of Fig. 5 for LiF). As the image potential is very deep the plasma-supplied electrons form a quasi two-

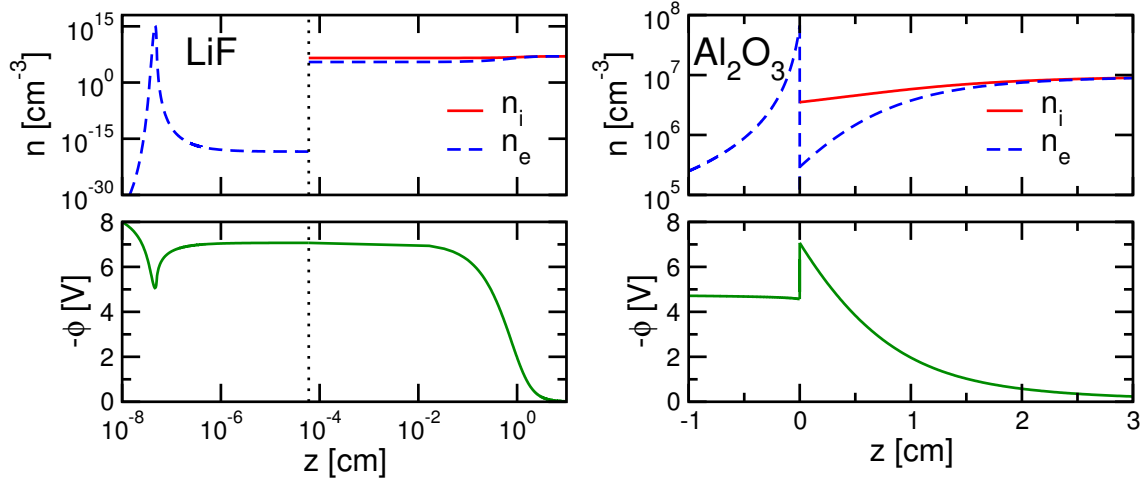


Fig. 6: Density of plasma-supplied surplus electrons trapped in the ESL, electron and ion density in the plasma sheath, and electric potential for a LiF (left) and an Al_2O_3 surface (right) in contact with a helium discharge with plasma parameters $n_0 = 10^7 \text{ cm}^{-3}$ and $k_B T_e = 2 \text{ eV}$ (reproduced from [F]). The crystallographic interface is at $z = 0$. Note the different scales of the two panels. The deep penetration of the Al_2O_3 wall charge is due to the neglect of defect states and other collision centres.

dimensional electron gas in front of the crystallographic interface, similar to the surface plasma anticipated by Emeleus and Coulter [26, 27].

For $\chi > 0$ the conduction band minimum is below the potential in front of the surface. This changes the situation dramatically. Electrons now accumulate at the bottom of the conduction band inside the dielectric where they form an extended space charge region (see right panel of Fig. 5 for Al_2O_3). The deep electron penetration into the solid leads to a bending of the energy bands close to the surface. Inside the dielectric the electrons are confined close to the interface by the restoring force from the sheath. This force increases when more electrons are removed from the sheath and accumulated in the ESL. Hence, a higher surface density of electrons, due to a higher plasma density or electron temperature, leads to an electron distribution which is more peaked at the interface (see Article I).

To conclude this exposition of the ESL we will compare the charge distribution in the ESL with the ones in the sheath. The electrons in the ESL are the quasi-stationary electron distribution in thermal equilibrium with the wall which balances the influx of electrons and ions at the sheath-ESL boundary. On top of this wall-thermalised electron distribution, the plasma sheath injects steady currents of electrons and ions into the ESL. They emanate at z_0 and persist up to the position where electron trapping or electron-ion recombination takes place. These currents are relevant for the charge carrier concentration between z_0 and the crystallographic interface. As they are not encompassed by our ESL model the electron and ion densities shown in Fig. 6 are discontinuous at z_0 . The neglect of the charge densities associated with the electron and ion fluxes for $0 < z < z_0$ does, however, not affect the potential because the densities are too small to cause a significant potential variation over the short distance between z_0 and the crystallographic interface.

Figure 6 compares the ESL and the plasma sheath for LiF ($\chi < 0$, left) and Al_2O_3 ($\chi > 0$, right). Far away from the surface the potential approaches the bulk plasma value chosen to be zero. Closer to the surface it develops a Coulomb barrier and immediately at the surface it follows the attractive image potential. For LiF the negative χ then leads to a

barrier at the crystallographic interface while for Al_2O_3 the positive χ induces a potential well inside the dielectric. For LiF the electrons are bound in the image potential, where they form a two-dimensional electron gas, while for Al_2O_3 they form a space charge in the conduction band. The sheath is in both cases a space charge region.

Our model for the ESL captures the plasma-supplied but wall-thermalised electrons at the plasma boundary. They are separated from the bulk plasma by the plasma sheath but coupled to the discharge by a flux balance condition. Thus, the ESL should be considered as the ultimate part of the plasma boundary.

1.3 Electron physisorption — Articles II, III, and IV

We can now turn to the electron kinetics in the ESL. Depending on the electron affinity χ two distinct scenarios for electron trapping emerge which are schematically shown in Figs. 7 and 8. For $\chi < 0$ (see Fig. 7) electrons that overcome the sheath potential do not penetrate into the solid as their energy falls in the band gap where no internal states are available. Instead, they are trapped in the image potential in front of the surface. Transitions between unbound and bound electronic states are due to surface vibrations associated with a bulk longitudinal acoustic phonon. Due to the large depth of the image potential compared to the energy of this phonon mode and as the wave-functions of the unbound states are suppressed close to the surface the probability for sticking is small. The calculation of sticking coefficients and desorption times for this scenario, which we have investigated in detail, will be outlined below.

For $\chi > 0$ (see Fig. 8) electrons that overcome the sheath potential penetrate into the solid. There they initially occupy high-lying states of the conduction band. Subsequent electron energy relaxation is due to scattering with bulk phonons of the dielectric and the plasma-supplied electrons are eventually trapped at the bottom of the conduction band in the potential well created by the restoring force from the plasma. Due to the high-density of states in the conduction band and an efficient scattering mechanism we expect the sticking coefficient to be much larger in this case. However, a detailed analysis of this scenario still remains to be done.

We now turn to the physisorption of an electron in the image potential in front of a dielectric with $\chi < 0$. This scenario is studied in Articles II, III, and IV [A-C]. (There we applied it to several dielectrics also with $\chi > 0$. With hindsight of the ESL model this approach should be only applied to dielectrics with $\chi < 0$.) The image potential supports a series of bound states. Electrons that are thermalised with the solid predominantly occupy the lowest bound state. Electron trapping is due to a transition from an unbound continuum state to any of the bound states. This is followed by a series of transitions within the image states until the electron reaches the lowest state or makes its way back into the continuum. This sequence of transitions within a manifold of surface states points to a similarity to neutral particle physisorption. In this case the series of transitions in the surface potential, modelled for instance by a Morse potential, can be described with a rate equation with quantum mechanically calculated transition rates [42, 43]. Such a rate equation captures all three characteristic stages of physisorption: initial trapping, subsequent relaxation and desorption [44, 45].

Following Gortel and Kreuzer [42, 43], the time-evolution of the bound state occupation

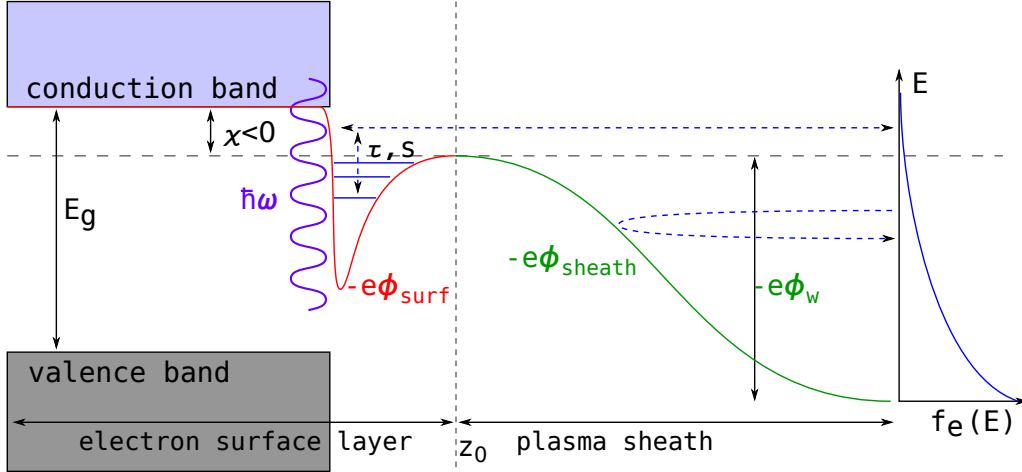


Fig. 7: Electron trapping in the ESL in front of a dielectric with $\chi < 0$.

is described by the rate equation,

$$\frac{d}{dt}n_n(t) = \sum_{n'} [W_{nn'}n_{n'}(t) - W_{n'n}n_n(t)] - \sum_k W_{kn}n_n(t) + \sum_k \tau_t W_{nk}j_k(t), \quad (16)$$

where $W_{n'n}$ is the transition rate from a bound state n to another bound state n' . W_{kn} and W_{nk} are the transition rates from the bound state n to the continuum state k and vice versa, and $\tau_t = 2L/v_z$ is the transit time through the surface potential of width L , which, in the limit $L \rightarrow \infty$, can be absorbed into the transition probability. We rewrite the rate equation as

$$\frac{d}{dt}n_n(t) = \sum_{n'} T_{nn'}n_{n'}(t) + \sum_k \tau_t W_{nk}j_k(t), \quad (17)$$

where the matrix $T_{nn'}$, defined implicitly by the above equation, subsumes all transitions originating from a bound state. The last term in Eqs. (16) and (17), respectively, represents transitions of incoming electrons into bound states.

The initial trapping is characterised by the prompt energy-resolved sticking coefficient

$$s_{e,k}^{\text{prompt}} = \tau_t \sum_n W_{nk}, \quad (18)$$

which gives the probability for an approaching electron in state k to make a transition to any of the bound states.

To describe relaxation following the initial trapping as well as desorption we follow Brenig [45] and solve Eq. (16) treating the incident electron flux as an externally specified parameter. Then,

$$n_n(t) = \sum_{\kappa} e^{-\lambda_{\kappa}t} \int_{-\infty}^t dt' e^{\lambda_{\kappa}t'} e_n^{(\kappa)} \sum_{kl} \tilde{e}_l^{(\kappa)} \tau_t W_{lk} j_k(t'), \quad (19)$$

where $e_n^{(\kappa)}$ and $\tilde{e}_n^{(\kappa)}$ are the right and left eigenvectors to the eigenvalue $-\lambda_{\kappa}$ of the matrix $T_{nn'}$. If the modulus of one eigenvalue, λ_0 , is considerably smaller than the moduli of the other eigenvalues λ_{κ} we can distinguish between a slow and a fast component of the

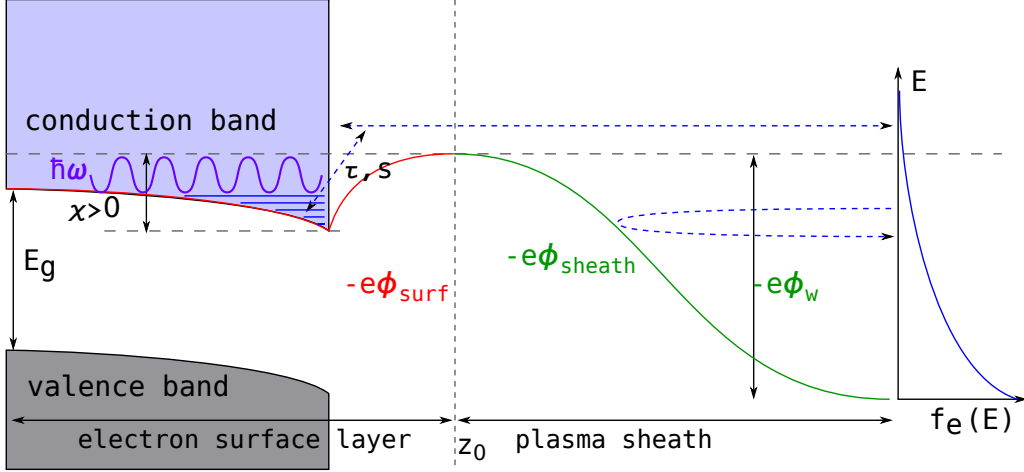


Fig. 8: Electron trapping in the ESL in a dielectric with $\chi > 0$.

electron kinetics in the image states. In this case λ_0 governs the long-time behaviour of the equilibrium occupation of the bound states, $n_n^{\text{eq}} \sim e^{-E_n/k_B T_s}$, and its inverse can be identified with the desorption time, $\lambda_0^{-1} = \tau_e$. The bound state occupancy $n_n(t)$ splits into a slowly varying part $n_n^0(t)$ given by the $\kappa = 0$ summand in Eq. (19) and a quickly varying part $n_n^f(t)$ given by the sum over $\kappa \neq 0$ in Eq. (19).

The electron adsorbate is given by the slowly varying part $n^0(t) = \sum_n n_n^0(t)$. It remains in the surface states for about as long as the desorption time. Differentiating $n^0(t)$ with respect to the time,

$$\frac{d}{dt}n^0(t) = \sum_k s_{e,k}^{\text{kinetic}} j_k(t) - \lambda_0 n^0(t), \quad (20)$$

we can identify the kinetic energy-resolved sticking coefficient

$$s_{e,k}^{\text{kinetic}} = \tau_t \sum_{n,n'} e_{n'}^{(0)} \tilde{e}_n^{(0)} W_{nk} \quad (21)$$

which captures the probability for both, initial trapping and subsequent relaxation [45].

If the incident unit electron flux corresponds to an electron with Boltzmann distributed kinetic energy, the prompt or kinetic energy-averaged sticking coefficient is given by

$$s_e^{\text{kinetic}} = \sum_k s_{e,k}^{\text{kinetic}} k e^{-\beta_e E_k} / \sum_k k e^{-\beta_e E_k}, \quad (22)$$

where $\beta_e^{-1} = k_B T_e$ is the mean electron energy.

The transition rates required for the kinetic equations have to be calculated from a microscopic model for the electron surface interaction. Transitions between image states are due to dynamic perturbations of the surface potential. The image potential is very steep near the surface. A particularly strong perturbation arises therefore from the surface vibrations induced by the longitudinal acoustic (LA) bulk phonon perpendicular to the surface. We describe this phonon using a Debye model: the maximum phonon energy is the Debye energy $\hbar\omega_D$.

The depth of the image potential can be classified with respect to the Debye energy. For this we measure energies in units of $\hbar\omega_D$ and introduce the parameters $\epsilon_n = E_n/\hbar\omega_D$ and $\Delta_{nn'} = (E_n - E_{n'})/\hbar\omega_D$, where $E_n < 0$ is the energy of the n th bound state. If

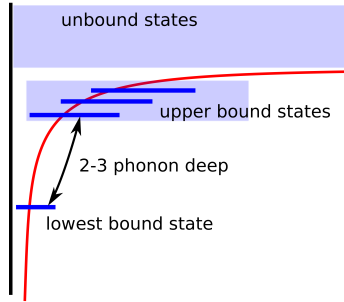


Fig. 9: Schematic representation of the series of image states in the image potential. For typical dielectrics the lowest bound state lies very deep and is connected to a group of upper bound states only by two- or three-phonon processes. The upper bound states are connected by one-phonon processes to the unbound states.

$\epsilon_1 > -1$ we call it shallow. For a shallow potential the lowest bound state is coupled by a one-phonon transition to the continuum. If $-n + 1 > \Delta_{12} > -n$, we call the potential n -phonon deep. If the potential is n -phonon deep a n -phonon process links the lowest bound state to the second bound state, which is linked by one-phonon transitions either directly or via intermediates to the continuum. For the dielectrics we consider, the potential is two-phonon (MgO) or three-phonon deep (LiF). A schematic representation of the image states is given in Fig. 9.

To calculate the transition probabilities for the rate equation, we need a microscopic model for the image potential and the electron-surface vibration interaction. From a macroscopic point of view the image potential ensues from the dielectric mismatch at the interface. On a microscopic level it arises from the coupling of the electron to a polarisable surface mode of the solid. For a dielectric this is a surface phonon. For LiF and MgO the low-frequency dielectric function is dominated by a transverse optical (TO) phonon with frequency ω_{TO} . It can be approximated by

$$\epsilon(\omega) = 1 + (\epsilon_0 - 1) \frac{\omega_{TO}^2}{\omega_{TO}^2 - \omega^2}, \quad (23)$$

where ϵ_0 is the static dielectric constant [46]. The bulk TO-phonon gives rise to a surface phonon. Its frequency $\omega_s = \omega_{TO} \sqrt{(1 + \epsilon_0)/2}$ is determined by the condition $\epsilon(\omega_s) = -1$. The electron couples to this surface phonon according to

$$H_{\text{int}} = -\frac{\hbar^2}{2m} \Delta + \sum_{\mathbf{Q}_{\parallel}} \hbar \omega_s a_{\mathbf{Q}_{\parallel}}^{\dagger} a_{\mathbf{Q}_{\parallel}} + \sum_{\mathbf{Q}_{\parallel}} \left(\phi_{\mathbf{Q}_{\parallel}}(\mathbf{x}_{\parallel}) a_{\mathbf{Q}_{\parallel}} + \phi_{\mathbf{Q}_{\parallel}}^*(\mathbf{x}_{\parallel}) a_{\mathbf{Q}_{\parallel}}^{\dagger} \right) \quad (24)$$

with $\phi_{\mathbf{Q}_{\parallel}}(\mathbf{x}_{\parallel}) = 2\sqrt{\pi\omega_s\Lambda_0\hbar e} e^{-Q_{\parallel}|z|} e^{i\mathbf{Q}_{\parallel}\mathbf{x}_{\parallel}} / \sqrt{Q_{\parallel}A}$ where $\Lambda_0 = (\epsilon_0 - 1)/(4(\epsilon_0 + 1))$ [46, 47]. The subscript \parallel denotes vectors parallel to the surface, and $a_{\mathbf{Q}_{\parallel}}^{(\dagger)}$ are annihilation (creation) operators for surface phonons.

The simplest way to extract the image potential from this coupling is by means of a unitary transformation [47]. It separates the coupling into a static part which takes the classical form of the image potential $\sim 1/z$ and a dynamic part of the electron-surface phonon coupling, which encodes recoil effects and encompasses momentum relaxation parallel to the surface. While the classical image potential allows a simple description of the image states which captures their properties fairly well it is not sufficient for the calculation of probabilities for transitions induced by surface vibrations, as they perturb the electronic states most strongly close to the surface where the image potential is steepest. Unfortunately, in this region the classical image potential has an unphysical divergence. To obtain a potential without this divergence we use a variational procedure to extract the static image potential [46]. Thereby, we keep some recoil effects which make the

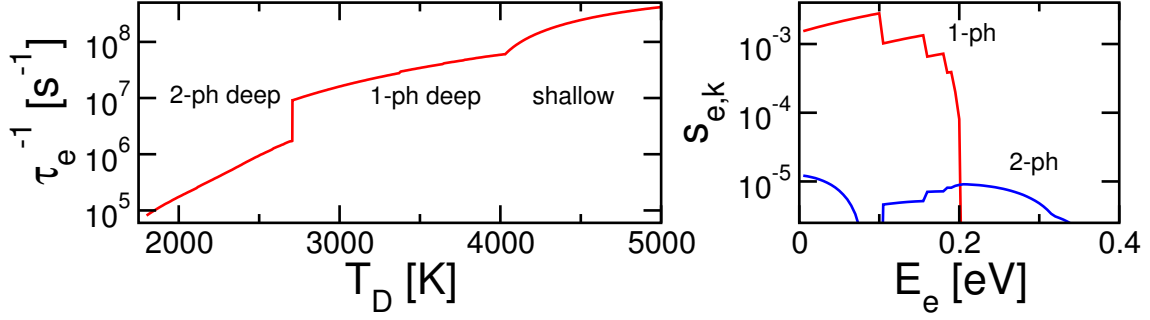


Fig. 10: Left: Inverse desorption time τ_e^{-1} in the two-phonon approximation for $T_D/T = 5$ as a function of the Debye temperature T_D . Data for $T_D = 2500$ K apply to graphite. Right: Prompt energy-resolved sticking coefficient as a function of the electron energy for a two-phonon deep potential ($T_D = 2500$ K and $T_s = 357$ K). The contribution of one-phonon processes (red) far outweighs the contribution from two phonon processes (blue).

recoil-corrected image potential $\sim 1/(z + z_c)$ with a cut-off parameter $z_c = \sqrt{\hbar/2m\omega_s\pi^2}$ divergence free (see Article II).

Transitions between the eigenstates of the recoil-corrected image potential are due to the LA bulk phonon perpendicular to the surface which is responsible for surface vibrations. This coupling is given by the Hamiltonian $H = H_e^0 + H_{ph}^0 + H_{e-ph}^{\text{dyn}}$ where $H_e^0 = \sum_q E_q c_q^\dagger c_q$ describes the electron in the recoil-corrected image potential, $H_{ph}^0 = \sum_Q \hbar\omega_Q b_Q^\dagger b_Q$ the free dynamics of the LA phonon, and $H_{e-ph}^{\text{dyn}} = \sum_{q,q'} \langle q' | V_p(u, z) | q \rangle c_{q'}^\dagger c_q$ the dynamic coupling of the electron to the LA phonon. The perturbation $V_p(u, z)$ can be identified as the difference between the displaced surface potential and the static surface potential. It reads, after the transformation $z \rightarrow z - z_c$,

$$V_p(u, z) = -\frac{e^2\Lambda_0}{z+u} + \frac{e^2\Lambda_0}{z}, \quad (25)$$

where u is the displacement due to the LA phonon.

In general, multi-phonon processes can arise both from the nonlinearity of the electron-phonon coupling H_{e-ph}^{dyn} as well as from the successive actions of H_{e-ph}^{dyn} encoded in the T-matrix equation,

$$T = H_{e-ph}^{\text{dyn}} + H_{e-ph}^{\text{dyn}} G_0 T, \quad (26)$$

where $G_0 = (E - H_e^0 - H_{ph}^0 + i0^+)^{-1}$. The transition rate from an electronic state q to an electronic state q' encompassing both types of processes is given by

$$W_{q'q} = \frac{2\pi}{\hbar} \sum_{s,s'} \frac{e^{-\beta_s E_s}}{\sum_{s''} e^{-\beta_s E_{s''}}} |\langle s', q' | T | s, q \rangle|^2 \delta(E_s - E_{s'} + E_q - E_{q'}), \quad (27)$$

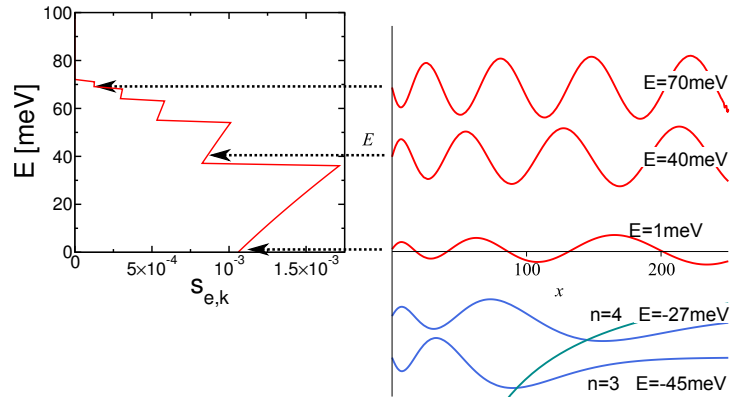
where $\beta_s = (k_B T_s)^{-1}$, with T_s the surface temperature, and where we have averaged over initial and final phonon states [48].

In principle, multi-phonon transition rates can be obtained by iterating the T-matrix and evaluating Eq. (27). Up to $\mathcal{O}(u^3)$, for instance, the T-matrix reads

$$T = V_1 + V_2 + V_3 + V_1 G_0 V_1 + V_2 G_0 V_1 + V_1 G_0 V_2 + V_1 G_0 V_1 G_0 V_1, \quad (28)$$

where the $V_i \sim u^i$ originate from expanding Eq. (25) in the displacement u . The T-matrix enters as $\langle T \rangle \langle T^* \rangle$ into the transition probability. The term $\langle V_1 \rangle \langle V_1^* \rangle$ can be identified as

Fig. 11: Energy-resolved prompt sticking coefficient for MgO (left) and schematic representation of the bound and continuum wavefunctions (right). The suppression of the amplitude of the continuum wave-function close to the surface for small electron energies leads to the small sticking coefficient.



the Golden Rule transition probability. Proportional to u^2 it is a one-phonon process. Two-phonon processes, proportional to u^4 , are represented by the terms

$$\begin{aligned} & \langle V_1 \rangle \langle V_3^* \rangle, \langle V_3 \rangle \langle V_1^* \rangle, \langle V_1 \rangle \langle V_2^* G_0^* V_1^* \rangle, \langle V_1 G_0 V_2 \rangle \langle V_1^* \rangle, \langle V_1 \rangle \langle V_1^* G_0^* V_2^* \rangle, \\ & \langle V_2 G_0 V_1 \rangle \langle V_1^* \rangle, \langle V_1 \rangle \langle V_1^* G_0^* V_1^* G_0^* V_1^* \rangle, \langle V_1 G_0 V_1 G_0 V_1 \rangle \langle V_1^* \rangle, \end{aligned} \quad (29)$$

and

$$\langle V_2 \rangle \langle V_2^* \rangle, \langle V_1 G_0 V_1 \rangle \langle V_1^* G_0^* V_1^* \rangle, \langle V_2 \rangle \langle V_1^* G_0^* V_1^* \rangle, \langle V_1 G_0 V_1 \rangle \langle V_2^* \rangle. \quad (30)$$

A complete two-phonon calculation would take all these processes into account as they stand. This is however not always necessary. A closer analysis (see Article II) of the first group of terms reveals that they are two-phonon corrections to transitions already enabled by a one-phonon process. We assume that these corrections are small and evaluate only the second group for transitions where they enable two-phonon transitions which are not merely corrections to one-phonon transitions. The details of the evaluation of the transition probabilities, including a regularisation of divergences by taking a finite phonon lifetime into account, can be found in Article II and III.

The expansion of the T-matrix allows the calculation of transition probabilities for the two-phonon deep potentials of graphite and MgO. However, for a three-phonon deep potential, for instance for LiF and CaO, this approach is no longer feasible. In the Articles II and III we qualitatively assess the relevance of different types of multi-phonon processes. For continuum to bound state transitions, for instance, one-phonon processes are sufficient at low electron energies. We will therefore compute the transition probabilities between bound and continuum states in the one-phonon approximation. For transitions between bound states, we found that multi-phonon processes due to the nonlinearity of the electron-phonon coupling tend to be more important than the multi-phonon processes due to the iteration of the T-matrix. Hence, we expect that an approximation which takes only the nonlinearity of the electron-phonon interaction nonperturbatively into account to be sufficient for the identification of the generic behaviour of multi-phonon-mediated adsorption and desorption. This approach is described in Article IV.

We now turn to results for the desorption time and the sticking coefficient for physisorption in image states. Before showing results for MgO and LiF, we consider the dependence of the electron kinetics on the potential depth and the relevance of one or two-phonon processes. For this, we show in the left panel of Fig. 10 the inverse of the desorption time as a function of the Debye temperature $T_D = \hbar\omega_D/k_B$ which sets the energy scale of the acoustic phonons. While the absolute depth of the potential remains constant, varying the phonon energy tunes the effective potential depth. Figure 10 reveals that for a shallow

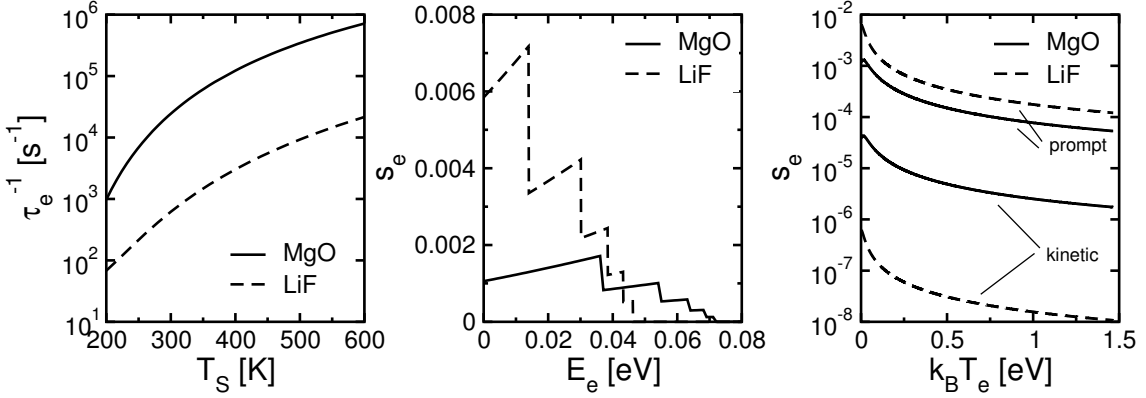


Fig. 12: Inverse desorption time τ_e^{-1} (left), prompt energy-resolved sticking coefficient (middle) and prompt as well as kinetic energy-averaged sticking coefficient (right) for MgO and LiF.

potential desorption is most efficient while for a one-phonon deep potential it gradually becomes less efficient. When the potential becomes two-phonon deep desorption suddenly becomes even slower which reflects the small magnitude of two-phonon transitions compared to one-phonon transitions. This justifies our approximation of neglecting two-phonon corrections to transitions already enabled by a one-phonon process. For a Debye temperature $T_D = 2500K$ the results apply to graphite.

The energy-resolved prompt sticking coefficient, plotted in the right panel of Fig. 10 for graphite, shows that also for bound state-continuum transitions one-phonon processes far outweigh two-phonon processes. Thus, sticking is mainly due to one-phonon processes. Moreover, we find that the sticking coefficient drops sharply at specific energies (see also Fig. 11). These accessibility thresholds occur whenever one bound state becomes no longer accessible from the continuum because the energy difference exceeds one Debye energy.

The sticking coefficient takes relatively small values—on the order of 10^{-3} . This is due to the small matrix elements between bound and continuum states. Fig. 11 shows the wave functions of representative bound and continuum states for MgO. For large energies the continuum wave functions have a sinusoidal shape whereas for small energies their amplitude is significantly suppressed close to the surface. These two behaviours correspond to two limits for the wave function. For simplicity we discuss this for a $1/x$ potential without cut-off. The continuum wave functions read $\phi_k(x) \sim M_{\frac{-i}{k}, \frac{1}{2}}(2ik\Lambda_0 x) / \sqrt{k}$ where $x = z/a_B$ ($M_{k,m}(z)$ is the confluent hypergeometric function [49]). For $x \rightarrow \infty$ we obtain $\phi_k(x) \sim \sin(\Lambda_0 k x)$ which also holds for large k while for $k \rightarrow 0$ we obtain $\phi_k(x) \sim \sqrt{k} \sqrt{2\Lambda_0 x} J_1(\sqrt{8\Lambda_0 x})$ ($J_n(z)$ is the Bessel function). The proportionality to \sqrt{k} entails a strong suppression of the wave function for low energy.

Electron physisorption at a dielectric surface with negative electron affinity is an intriguing phenomenon due to the interplay of potential depth, magnitude of matrix elements and surface temperature. Initial trapping of an electron, characterised by the prompt sticking coefficient, occurs in the upper bound states by one-phonon transitions. Relaxation after initial trapping depends on the strength of transitions from the upper bound states to the lowest bound states. If the lowest bound state was linked to the second bound state by a one-phonon process the electron would relax for all surface temperatures. If these two states are linked by a multi-phonon process relaxation takes place only for low temperature. At room temperature a relaxation bottleneck ensues as the electron desorbs from the

upper bound states before it drops to the lowest bound state. This leads to a severe reduction of the kinetic sticking coefficient compared to the prompt sticking coefficient. The dominant desorption channel depends also on the depth of the potential. For a shallow potential desorption occurs directly from the lowest bound state to the continuum. For deeper potentials desorption proceeds via the upper bound states. Desorption occurs then via a cascade in systems without and as a one-way process in systems with a relaxation bottleneck.

An overview of results for the desorption time as well as prompt and kinetic sticking coefficients for MgO and LiF is given by Fig. 12. Most important for the plasma context is that $s_e \ll 1$ and $\tau_e^{-1} \neq 0$, implying that a dielectric surface with a negative electron affinity is not a perfect absorber for electrons.

1.4 Mie scattering by a charged dielectric particle — Articles V and VI

Light scattering by small particles is both a fundamental problem of electromagnetic theory as well as an important diagnostic for dust particles in space, the atmosphere or the laboratory [50]. For spherical particles Mie's theory [51] gives an exact solution which encompasses a wealth of phenomena. The scattering behaviour of an uncharged particle is determined by the size of the particle and the frequency-dependent dielectric constant $\epsilon(\omega)$ of the particle material. For a dielectric particle $\epsilon(\omega)$ depends on the phonon modes of the solid. In this section we turn to the influence of plasma-supplied surplus electrons on the scattering of light by small particles. Our aim is to identify the charge signatures in the Mie signal and to assess whether they could be used as an optical measurement of the charge on a dust particle in a plasma.

Surplus electrons can influence the scattering behaviour of the particle through their electrical conductivity which either modifies the boundary conditions for the electromagnetic fields at the surface of the sphere or gives rise to an additional polarisability of the particle [52–54]. However, at which frequencies surplus charges affect the Mie signal and how strong their effect is has remained an open question. To answer it, we calculate the electrical conductivity from a microscopic model and analyse its effect on the different scattering regimes of the particle (details in Articles V and VI [G,I]).

Dust particles immersed in a plasma can be considered as internal plasma walls. Hence, to set up a model for the calculation of the electrical conductivity of the surplus electrons, we turn to the ESL model. For $\chi < 0$ surplus electrons are bound in the image potential in front of the surface, where they form a spherical two-dimensional electron gas around the particle. This electron film on the particle may sustain a surface current $\mathbf{K} = \sigma_s \mathbf{E}_{\parallel}$ which is proportional to the surface conductivity in the image states σ_s and is induced by the in-plane electric field. This changes the boundary condition for the magnetic field to $\hat{\mathbf{e}}_r \times (\mathbf{H}_i + \mathbf{H}_r - \mathbf{H}_t) = 4\pi \mathbf{K}/c = \tau \mathbf{E}_{\parallel}$ (i denotes the incident, r the reflected, and t the transmitted field), where

$$\tau(\omega) = 4\pi\sigma_s(\omega)/c, \quad (31)$$

is the dimensionless surface conductivity (c is the velocity of light).

For $\chi > 0$ surplus electrons are trapped inside the particle. The space charge they form in the conduction band is relatively wide. Hence, for micron-sized particles we can assume a homogeneous distribution in the bulk. The bulk conductivity σ_b of electrons in

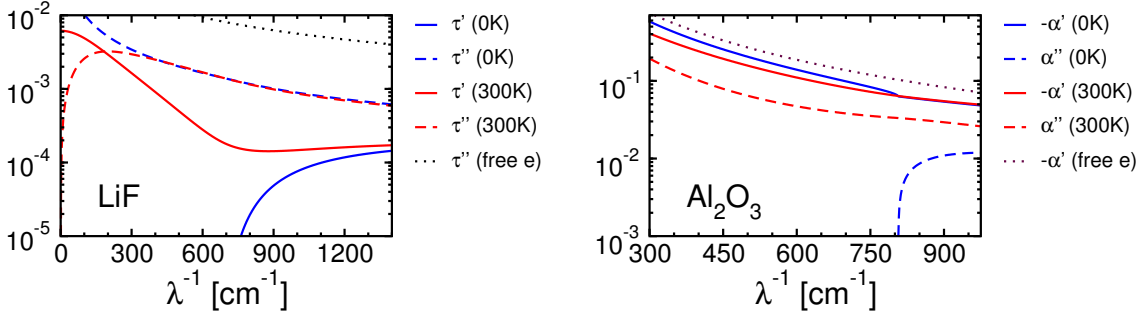


Fig. 13: Dimensionless surface conductivity $\tau = \tau' + i\tau''$ for LiF (left) for $n_s = 10^{13} \text{ cm}^{-2}$ and polarisability of excess electrons $\alpha = \alpha' + i\alpha''$ for Al_2O_3 (right) for $n_b = 3 \times 10^{17} \text{ cm}^{-3}$, which corresponds to $n_s = 10^{13} \text{ cm}^{-2}$ for a micron-sized particle, as a function of the inverse wavelength λ^{-1} (adapted from Article V). At $T = 0\text{K}$ light absorption is only possible above the surface or LO phonon frequency which leads to $\tau' = 0$ for $\lambda^{-1} < \lambda_s^{-1} = 675 \text{ cm}^{-1}$ and $\alpha'' = 0$ for $\lambda^{-1} < \lambda_{LO}^{-1} = 807 \text{ cm}^{-1}$.

the conduction band gives rise to an additional polarisability

$$\alpha = 4\pi i\sigma_b/\omega, \quad (32)$$

which modifies the refractive index $N = \sqrt{\epsilon + \alpha}$ of the particle.

The dominant mechanism at room temperature which limits the electrical conductivity of the surplus electrons is electron-phonon scattering. To calculate the surface conductivity in the image states for $\chi < 0$ we use a planar model. The interaction of the electron with the surface phonon comprises a static part, which gives rise to the image potential, and a dynamic part, which is responsible for momentum relaxation parallel to the surface and thereby limits the surface conductivity. The calculation of transition rates between image states was very sensitive to the potential close to the surface so that we could not use the classical image potential. For the calculation of the surface conductivity the divergence of the classical image potential is less problematic. Thus, to separate static and dynamic part of the electron-surface phonon coupling we apply the unitary transformation $H \rightarrow UHU^{-1}$ with $U = e^{iS}$, $S = (i/\hbar\omega_s) \sum_{\mathbf{Q}_{\parallel}} [a_{\mathbf{Q}_{\parallel}} \phi_{\mathbf{Q}_{\parallel}} - a_{\mathbf{Q}_{\parallel}}^{\dagger} \phi_{\mathbf{Q}_{\parallel}}^*]$ [47]. The static image potential, $V = -\Lambda_0 e^2/z$ with $\Lambda_0 = (\epsilon_0 - 1)/(4(\epsilon_0 + 1))$ supports a series of bound states whose wave functions read

$$\phi_{n\mathbf{k}}(\mathbf{x}, z) = \frac{1}{\sqrt{A}} e^{i\mathbf{k}\mathbf{x}} \sqrt{\frac{\Lambda_0}{a_B n n!^2}} W_{n,1/2} \left(\frac{2\Lambda_0 z}{na_B} \right) \quad (33)$$

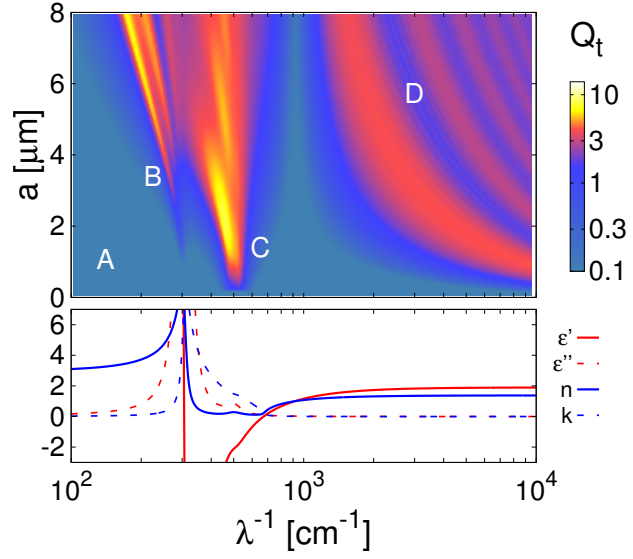
with a_B the Bohr radius, $\mathbf{k} = (k_x, k_y)$, $\mathbf{x} = (x, y)$, A the surface area and $W_{n,m}$ Whittaker's function [49]. Electrons that are thermalised with the surface occupy the lowest image band $n = 1$. For a surface electron with energy $E_{\text{kin}}/k_B = 300 \text{ K}$ the de Broglie wavelength $\lambda_{dB} \approx 8 \times 10^{-7} \text{ cm}$. Thus, for particle radii $a > 10 \text{ nm}$ the plane-surface approximation is justified. The dynamic coupling in the lowest image band which limits σ_s is given by

$$H_{\text{int}} = \frac{1}{\sqrt{A}} \sum_{\mathbf{k}, \mathbf{Q}} M_{\mathbf{k}, \mathbf{Q}} c_{\mathbf{k}+\mathbf{Q}}^{\dagger} (a_{\mathbf{Q}} - a_{-\mathbf{Q}}^{\dagger}) c_{\mathbf{k}}, \quad (34)$$

where the matrix element, calculated with the wave function given by Eq. (33), is

$$M_{\mathbf{k}\mathbf{Q}} = \frac{2e\sqrt{\pi\Lambda_0\hbar^3}}{m\sqrt{\omega_s Q}} \left(\frac{2\Lambda_0}{Qa_B + 2\Lambda_0} \right)^3 \left[\mathbf{Q} \cdot \mathbf{k} + \frac{Q^2}{2} \right] \quad (35)$$

Fig. 14: Top: Extinction efficiency for a LiF particle as a function of the inverse wavelength λ^{-1} and the particle radius a . The labels indicate the four characteristic scattering regimes: low frequencies (A), ordinary resonances (B), anomalous resonances (C), and interference and ripple structure (D). Bottom: Dielectric constant $\epsilon = \epsilon' + i\epsilon''$ and refractive index $N = n + ik$ for LiF as a function of λ^{-1} . Note that ϵ' is large and positive below the TO phonon resonance at $\lambda_{TO}^{-1} = 306 \text{ cm}^{-1}$ (not shown).



(m is the electron mass). Within the memory function approach [55] the surface conductivity can be written as

$$\sigma_s(\omega) = \frac{e^2 n_s}{m} \frac{i}{\omega + M(\omega)} \quad (36)$$

with n_s the surface electron density. The memory function is then evaluated up to second order in the electron-phonon coupling. As $M(\omega)$ does not depend on n_s the surface conductivity is proportional to the surface density of electrons n_s (see Article V for details).

For $\chi > 0$ the interaction of the electron with a longitudinal optical (LO) bulk phonon limits the bulk conductivity. The coupling of the electron to this mode with frequency ω_{LO} is given by $H_{\text{int}} = \sum_{\mathbf{k}, \mathbf{q}} M c_{\mathbf{k}+\mathbf{q}}^\dagger c_{\mathbf{k}} (a_{\mathbf{q}} + a_{-\mathbf{q}}^\dagger) / \sqrt{V} q$, where $M = \sqrt{2\pi e^2 \hbar \omega_{LO} (\epsilon_\infty^{-1} - \epsilon_0^{-1})}$ [56]. For the calculation of σ_b we employ again the memory function approach. The bulk conductivity is proportional to the bulk electron density n_b .

The scattering behaviour of the particle is controlled by the scattering coefficients a_n^r and b_n^r . To determine them, we expand the incident plane wave, $\mathbf{E}_i = E_0 e^{ikz - i\omega t} \hat{\mathbf{e}}_x$, in spherical vector harmonics—the solutions of the vector wave equation in spherical coordinates—and match reflected and transmitted partial waves. Following Bohren and Hunt [52] this gives the scattering coefficients

$$a_n^r = - \frac{j_n(N\rho) [\rho j_n(\rho)]' - [N\rho j_n(N\rho)]' j_n(\rho) + i\tau \rho j_n(N\rho) j_n(\rho)}{j_n(N\rho) [\rho h_n^{(1)}(\rho)]' - [N\rho j_n(N\rho)]' h_n^{(1)}(\rho) + i\tau \rho j_n(N\rho) h_n^{(1)}(\rho)} \quad (37)$$

and

$$b_n^r = - \frac{j_n(\rho) [N\rho j_n(N\rho)]' - N^2 j_n(N\rho) [\rho j_n(\rho)]' - i\tau [N\rho j_n(N\rho)]' [\rho j_n(\rho)]' / \rho}{h_n^{(1)}(\rho) [N\rho j_n(N\rho)]' - N^2 j_n(N\rho) [\rho h_n^{(1)}(\rho)]' - i\tau [N\rho j_n(N\rho)]' [\rho h_n^{(1)}(\rho)]' / \rho} \quad (38)$$

where $\rho = 2\pi a/\lambda$ is the size parameter and a the radius. For $\chi < 0$ surplus charges enter through the dimensionless surface conductivity τ and the refractive index $N = \sqrt{\epsilon}$. For $\chi > 0$ charges enter through $N = \sqrt{\epsilon + \alpha}$ and $\tau = 0$. In Eqs. (37) and (38) j_n and $h_n^{(1)}$

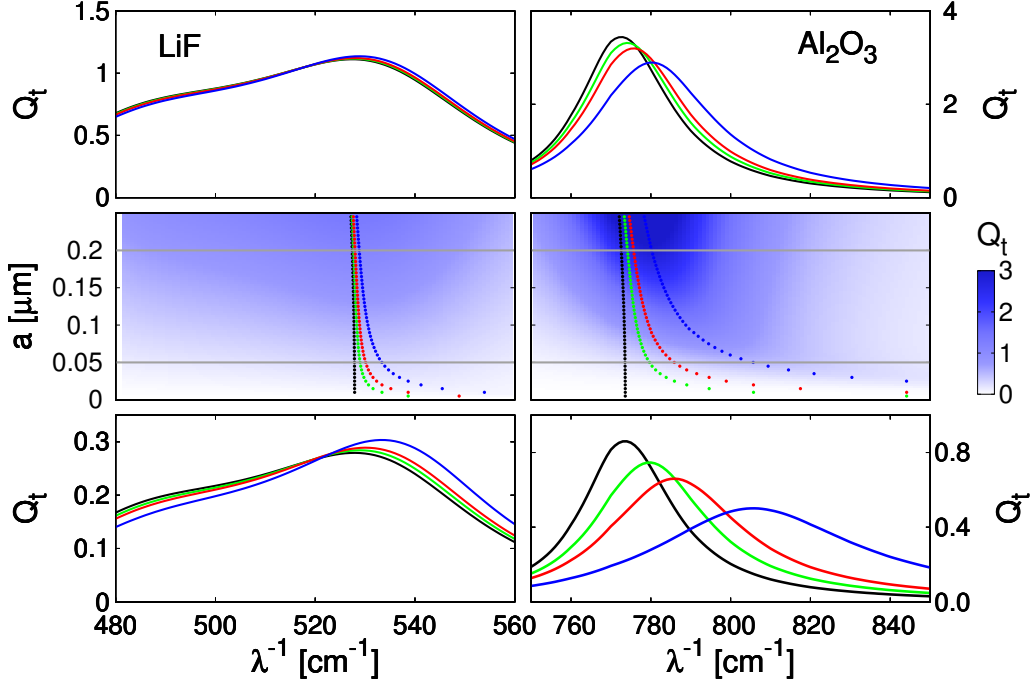


Fig. 15: Middle panel: Extinction efficiency Q_t as a function of the inverse wavelength λ^{-1} and the radius a for a LiF particle with $n_s = 5 \times 10^{12} \text{ cm}^{-2}$ (left) and an Al_2O_3 particle with $n_b = 3n_s/a$ (right) for $T = 300 \text{ K}$ (adapted from Article VI). The dotted lines indicate the extinction maximum for $n_s = 0$ (black), 10^{12} (green), 2×10^{12} (red), and $5 \times 10^{12} \text{ cm}^{-2}$ (blue). Top and bottom panel: Extinction efficiency Q_t for different electron densities as a function of λ^{-1} and two radii $a = 0.2 \mu\text{m}$ (top) and $a = 0.05 \mu\text{m}$ (bottom). For LiF a secondary phonon mode at 503 cm^{-1} distorts the Lorentzian line-shape.

are the spherical Bessel and Hankel function of the first kind. As for uncharged particles the scattering (s) and extinction (t) efficiencies are

$$Q_s = \frac{2}{\rho^2} \sum_{n=1}^{\infty} (2n+1) (|a_n^r|^2 + |b_n^r|^2) , \quad Q_t = -\frac{2}{\rho^2} \sum_{n=1}^{\infty} (2n+1) \text{Re}(a_n^r + b_n^r) . \quad (39)$$

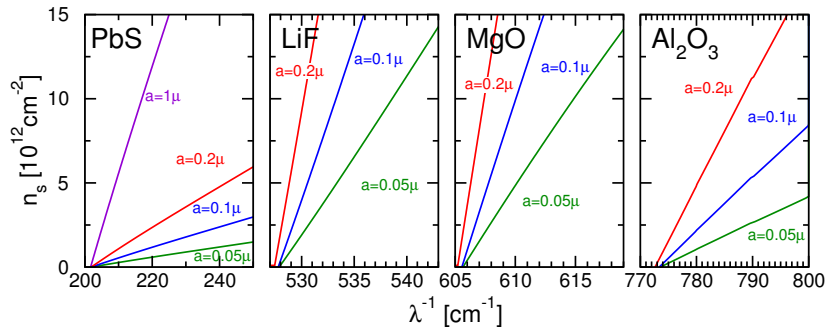
The absorption efficiency is given by $Q_a = Q_t - Q_s$. For small particles compared to the wavelength $\rho \ll 1$. Expanding the scattering coefficients in ρ the leading coefficient is $b_1 \sim \mathcal{O}(\rho^3)$, which corresponds to the electrical dipole oscillation. The extinction efficiency in this limit is given by

$$Q_t = \frac{12\rho(\epsilon'' + \alpha'' + 2\tau'/\rho)}{(\epsilon' + \alpha' + 2 - 2\tau''/\rho)^2 + (\epsilon'' + \alpha'' + 2\tau'/\rho)^2} . \quad (40)$$

The effect of surplus charges is encoded in the dimensionless surface conductivity $\tau = \tau' + i\tau''$ or the polarisability $\alpha = \alpha' + i\alpha''$. They are shown in Fig. 13 for MgO and Al_2O_3 as a function of the inverse wavelength λ^{-1} . Both are small even for a highly charged particle and, at room temperature, decrease slowly with increasing frequency. For $\lambda^{-1} \rightarrow 0$ the bulk and surface conductivities tend to a small real static value which implies $\tau' > \tau''$ and $\alpha'' > -\alpha'$ for small λ^{-1} . For larger λ^{-1} we find $\tau'' > \tau'$ and $-\alpha' > \alpha''$.

We now turn to the scattering behaviour of an uncharged particle (for details see Article VI). The particles we consider have a strong TO phonon resonance in the infra-red which

Fig. 16: Position of the extinction resonance depending on the surface charge n_s (or equivalent bulk charge $n_b = 3n_s/a$) for PbS, LiF, MgO, and Al_2O_3 particles with different radii a (adapted from Article VI).



controls the dielectric constant $\epsilon = \epsilon' + i\epsilon''$. Such particles have four characteristic scattering regimes (see Fig. 14 for LiF). For low frequencies extinction is small as $\epsilon'' \ll 1$. Below the TO phonon mode ϵ' is large which gives rise to ordinary optical resonances. Above it $\epsilon' < 0$ which leads to a series of anomalous optical resonances. Far above the TO phonon mode the scattering behaviour is dominated by an interference and ripple structure. It turns out, that surplus electrons affect only the low-frequency regime and the anomalous optical resonances significantly.

In the low-frequency regime extinction is for micron-sized particles mainly due to absorption. As $\rho \ll 1$ the extinction efficiency is approximately given by Eq. (40). In the static limit the dielectric constant is real. As a consequence, its imaginary part ϵ'' is small at low frequencies. This implies that absorption, which is proportional to ϵ'' , is small for uncharged particles. For charged particles, the real part of the electrical conductivity of the surplus electrons offers an additional channel for energy relaxation on the particle. This leads for charged particles to an increase in absorption which is proportional to the particle charge (for details see Article VI).

The most prominent effect of surplus electrons on light scattering is found at the anomalous optical resonances which appear where $\epsilon' < 0$ and $\epsilon'' \ll 1$. They correspond to the resonant excitation of transverse surface modes of the sphere [57] and their location is very sensitive to small changes of ϵ' . For metallic particles the anomalous resonances have recently been identified by Tribelsky et al. [58,59]. In this case they are tied to a plasmon mode and lie in the ultra-violet. For a dielectric they are induced by the TO phonon and lie above the TO phonon frequency in the infra-red.

The location of the anomalous resonances is sensitive to small changes in τ or α and thus to surface or bulk surplus electrons (for details see Article V and VI). Surplus charges lead to a blue-shift of the resonances. This effect is most significant for particles with radii $a < 1 \mu\text{m}$. Figure 15 shows this blue-shift for the small-particle tail of the lowest resonance for submicron-sized LiF and Al_2O_3 particles. For small particles $\rho \ll 1$ so that the extinction efficiency is well approximated by Eq. (40). The extinction resonance is located where $\epsilon' + 2 - 2\tau''/\rho = 0$ for $\chi < 0$ or $\epsilon' + \alpha' + 2 = 0$ for $\chi > 0$. For an uncharged particle the resonance condition is $\epsilon' = -2$. Provided ϵ' can be approximated linearly and ϵ'' does not vary strongly close to $\epsilon' = -2$ the resonance has a Lorentzian line shape which follows from Eq. (40). Figure 15 confirms this for Al_2O_3 though not for LiF, where a secondary TO phonon leads to a distortion of the line-shape.

In Fig. 16 we compare the resonance shift for LiF, MgO, PbS and Al_2O_3 particles. Qualitatively both bulk and surface electrons lead to a similar resonance shift. In the resonance condition surface electrons enter by τ/ρ and bulk electrons by α . As they enter

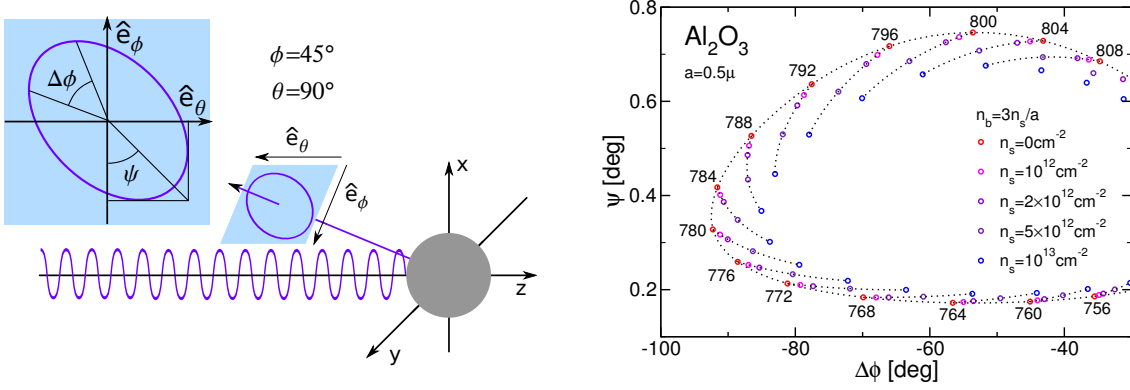


Fig. 17: Left: Schematic representation of the scattering geometry and polarisation ellipsis of the reflected wave in the direction $\theta = \pi/2$, $\phi = \pi/4$. This direction is perpendicular to the z axis along which the incident wave propagates and at 45° to the x direction in which the incident light is polarised. Right: Ellipsometric angles ψ and $\Delta\phi$ for scattering by an Al_2O_3 particle with $a = 0.5 \mu\text{m}$ in the direction $\theta = \pi/2$ and $\phi = \pi/4$ for different bulk electron densities $n_b = 3n_s/a$ (adapted from Article VI). The annotated values at the base point give the wave-number. From there the electron density increases counter-clockwise along the branches.

on the same footing we conclude that the resonance shift is primarily an electron density effect on the polarisability of the particle. The shift is larger for Al_2O_3 and PbS ($\chi > 0$) than for MgO and LiF ($\chi < 0$). This is due to the small conduction band effective mass for Al_2O_3 and PbS which benefits the electrons' mobility in the bulk. Moreover for PbS the resonance is located at a low frequency where the conductivity is particularly large.

Finally, we turn to the polarisation of scattered light. While the extinction efficiency only contains information about the amplitude of the scattering coefficients, the polarisation of scattered light includes the phase information of the scattering coefficients. Whenever one of the scattering coefficients becomes resonant the phase of this coefficient varies rapidly by π . Hence, the phase information should be particularly useful at optical resonances. Writing the reflected electric field in one particular scattering direction as

$$\mathbf{E}_r \sim E_0 \frac{e^{-i\omega t + ikr}}{ikr} \left(A_2 e^{i\phi_2} \hat{\mathbf{e}}_\theta + A_3 e^{i\phi_3} \hat{\mathbf{e}}_\phi \right) \quad (41)$$

with the amplitudes A_2 , A_3 and the phases ϕ_2 , ϕ_3 we can introduce the ellipsometric angles $\Delta\phi = \phi_2 - \phi_3$ and $\tan \psi = A_2/A_3$. The ratio of the amplitudes is given by the angle ψ . The phase difference $\Delta\phi$ determines the opening of the polarisation ellipsis. For $\Delta\phi = 0, \pm\pi$ the reflected light is linearly polarised while for $\Delta\phi = \pm\pi/2$ the opening of the polarisation ellipsis is maximal.

In the following, we will consider light that is scattered in a direction characterised by the angles $\theta = \pi/2$ and $\phi = \pi/4$. This configuration (illustrated in Fig. 17) is already used for the determination of the size of nanodust from the Mie signal [60]. We focus on the scattering at the anomalous resonances for $\epsilon' < 0$. For small particles we take only the scattering coefficients a_1^r , b_1^r and b_2^r up to order $\mathcal{O}(\rho^3)$ into account. Then the reflected electric field is given by

$$\mathbf{E}_r \sim E_0 \frac{e^{ikr - i\omega t}}{ikr} \left[\left(\frac{3}{2\sqrt{2}} a_1^r - \frac{5}{2\sqrt{2}} b_2^r \right) \hat{\mathbf{e}}_\theta - \frac{3}{2\sqrt{2}} b_1^r \hat{\mathbf{e}}_\phi \right]. \quad (42)$$

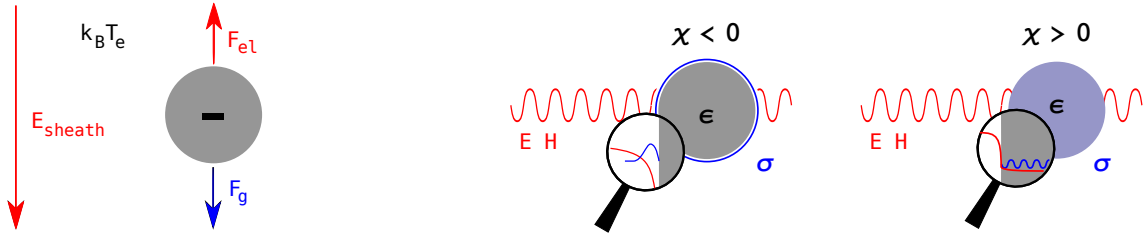


Fig. 18: Conventional charge measurement in the sheath (left) and proposed optical charge measurement by Mie scattering (right). The conventional charge measurement relies on trapping the particle in the sheath and exploiting a force balance between gravity and the electric force on the particle. The knowledge of the plasma parameters is required to infer the particle charge. The optical measurement does not require the knowledge of plasma parameters.

The anomalous resonances are linked to resonances in the coefficients b_n^r . At the resonance of b_1^r , located at $\epsilon' = -2$ for $\rho \ll 1$, the phase ϕ_2 varies by π and at the resonance of b_2^r at $\epsilon' = -3/2$ the phase ϕ_3 varies by π . Due to the proximity of these resonances the phase variations of ϕ_2 and ϕ_3 overlap and $\Delta\phi$ decreases and increases by about $\pi/2$ over the anomalous resonances (see right panel of Fig. 17 for Al_2O_3).

Surplus electrons shift the resonances in the scattering coefficients to higher frequencies. As a consequence, the increase and decrease of $\Delta\phi$ by about $\pi/2$ also takes place at higher frequencies. This can also be seen Fig. 17. For a fixed wavelength on the descending or ascending branch of the loop in $\Delta\phi$ this results in a linear shift of $\Delta\phi$ with the density of surplus electrons.

Our study of light scattering by a charged particle has revealed three charge-dependent features in the Mie signal: Surplus charges lead to (i) increased extinction at low frequencies, (ii) a blue-shift of an extinction resonance in the infra-red, and (iii) an opening and closing of the polarisation ellipsis which is shifted to higher frequencies. We suggest to try these effects experimentally as a charge diagnostic for dust particles in a plasma. The resonance shift would require a frequency-dependent extinction measurement while the low-frequency extinction measurement and the polarisation measurement of the reflected light could be performed at fixed wavelength.

An optical charge measurement would, unlike many traditional methods (see Fig. 18), not require the knowledge of the plasma parameters and it could be used for nanodust where conventional techniques are not applicable at all. Eventually the optical measurement could be combined with a traditional force balance method using suitable test particles as minimally invasive probes. The Mie signal would give the particle charge while the force measurement could be used to obtain the local electron temperature or density.

1.5 Conclusions

The concept of the electron surface layer introduced in this thesis provides a framework for the description of the microphysics of the surplus electrons immediately at the wall and thereby complements the modelling of the plasma sheath. In this work we have considered from a surface physics perspective the distribution and build-up of an electron adsorbate on the wall as well as the effect of the negative charge on the scattering of light by a spherical particle immersed in a plasma.

In our ESL model we treat the wall-bound electrons as a wall-thermalised electron distribution minimising the grand canonical potential and satisfying Poisson's equation.

The boundary between the ESL and the plasma sheath is determined by a force balance between the attractive image potential and the repulsive sheath potential and lies in front of the crystallographic interface. Depending on the electron affinity χ , that is the offset of the conduction band minimum to the potential in front of the surface, two scenarios for the wall-bound electrons are realised. For $\chi < 0$ (e.g. MgO, LiF) electrons do not penetrate into the solid but are trapped in the image states in front of the surface where they form a quasi two-dimensional electron gas. For $\chi > 0$ (e.g. SiO₂, Al₂O₃) electrons penetrate into the conduction band where they form an extended space charge.

These different scenarios are also reflected in the electron kinetics at the wall which control the sticking coefficient and the desorption time. If $\chi < 0$ electrons from the plasma cannot penetrate into the solid. They are trapped in the image states in front of the surface. The transitions between unbound and bound states are due to surface vibrations. Trapping of electrons is mediated by one-phonon transitions and takes place in the upper bound states. Owing to the large binding energy of the lowest bound state transitions from the upper bound states to the lowest bound state are due to multi-phonon processes. For low surface temperatures relaxation to the lowest bound state takes place while for higher temperature a relaxation bottleneck emerges. Desorption occurs in cascades for systems without relaxation bottleneck and as a one-way process in systems with a relaxation bottleneck. From the perspective of plasma physics the most important result is that the sticking coefficient for electrons is relatively small, typically on the order of 10^{-3} . For $\chi > 0$ electron physisorption takes place in the conduction band. For this case sticking coefficients and desorption times have not been calculated yet but in view of the more efficient scattering with bulk phonons, responsible for electron energy relaxation in this case, we expect them to be larger than for the case of $\chi < 0$.

Finally, we have studied the effects of surplus electrons on the scattering of light by a spherical particle. For $\chi < 0$ the electrons form a spherical electron gas around the particle and their electrical conductivity modifies the boundary condition for the magnetic field. For $\chi > 0$ the electrons in the bulk of the particle modify the refractive index through their bulk electrical conductivity. In both cases the conductivity is limited by scattering with surface or bulk phonons. Surplus electrons lead to an increase of absorption at low frequencies and, most notably, to a blue-shift of an extinction resonance in the infrared. This shift is proportional to the charge and is strongest for submicron-sized particles. The particle charge is also revealed in a blue-shift of the rapid variation of one of the two polarisation angles of the reflected light.

This thesis gives the first detailed microscopic model for the surface electrons at a dielectric plasma wall. The results we have presented on the charge distribution, the sticking coefficient and the desorption time or the charge effects on Mie scattering exemplify how the microphysics of the surface electrons can be modelled. In the ESL model we outline how the microscopic potentials can be cast into an effective model, which we applied to an ideal dielectric surface without intrinsic band bending or surface states. Nevertheless, following the same strategy our model can be extended to encompass intrinsic band bending or impurities and doping. Furthermore, our ESL model could provide the potential landscape for modelling the electron kinetics at biased or driven plasma walls. Another continuation of this work would be the calculation of sticking coefficients for dielectrics with positive χ , where electron trapping takes place in the conduction band.

From our work we conclude that the electron affinity is an important parameter of the surface which should affect the charge distribution as well as the charge-up. Therefore, we encourage experimentalists to study the charging of surfaces or dust particles as a

function of χ . Interesting in this respect is also if or under what conditions the electron affinity of a surface exposed to a plasma remains stable. Moreover, we suggest to use the charge signatures in Mie scattering to measure the particle charge optically. This would allow a charge measurement independent of the plasma parameters and could be applied to nano-dust where conventional methods cannot be applied.

2 Thesis Articles

Author Contribution

Article I:

“Electron surface layer at the interface of a plasma and a dielectric wall”

R. L. Heinisch, F. X. Bronold, and H. Fehske, *Phys. Rev. B* **85**, 075323 (2012)

R. L. Heinisch, F. X. Bronold and H. Fehske outlined the scope and strategy of the calculation. The calculation was performed by R. L. Heinisch. R. L. Heinisch wrote the manuscript which was edited by all authors.

Article II:

“Phonon-mediated desorption of image-bound electrons from dielectric surfaces”

R. L. Heinisch, F. X. Bronold, and H. Fehske, *Phys. Rev. B* **81**, 155420 (2010)

F. X. Bronold and H. Fehske outlined the scope and strategy of the calculation. The calculation was performed by R. L. Heinisch. R. L. Heinisch wrote the manuscript which was edited by all authors.

Article III:

“Phonon-mediated sticking of electrons at dielectric surfaces”

R. L. Heinisch, F. X. Bronold, and H. Fehske, *Phys. Rev. B* **82**, 125408 (2010)

F. X. Bronold and H. Fehske outlined the scope and strategy of the calculation. The calculation was performed by R. L. Heinisch. R. L. Heinisch wrote the manuscript which was edited by all authors.

Article IV:

“Physisorption of an electron in deep surface potentials off a dielectric surface”

R. L. Heinisch, F. X. Bronold, and H. Fehske, *Phys. Rev. B* **83**, 195407 (2011)

R. L. Heinisch, F. X. Bronold and H. Fehske outlined the scope and strategy of the calculation. The calculation was performed by R. L. Heinisch. R. L. Heinisch wrote the manuscript which was edited by all authors.

Article V:

“Mie scattering by a charged dielectric particle”

R. L. Heinisch, F. X. Bronold, and H. Fehske, *Phys. Rev. Lett.* **109**, 243903 (2012)

R. L. Heinisch, F. X. Bronold and H. Fehske outlined the scope and strategy of the calculation. The calculation was performed by R. L. Heinisch. R. L. Heinisch wrote the manuscript which was edited by all authors.

Article VI:

“Optical signatures of the charge of a dielectric particle in a plasma”

R. L. Heinisch, F. X. Bronold, and H. Fehske, accepted for publication in *Phys. Rev. E*

R. L. Heinisch, F. X. Bronold and H. Fehske outlined the scope and strategy of the calculation. The calculation was performed by R. L. Heinisch. R. L. Heinisch wrote the manuscript which was edited by all authors.

Confirmed:

(PD Dr. Franz Xaver Bronold)

Greifswald, 19 August 2013

Electron surface layer at the interface of a plasma and a dielectric wall

R. L. Heinisch, F. X. Bronold, and H. Fehske

Institut für Physik, Ernst-Moritz-Arndt-Universität Greifswald, 17489 Greifswald, Germany

(Received 7 October 2011; revised manuscript received 1 February 2012; published 29 February 2012)

We study the plasma-induced modifications of the potential and charge distribution across the interface of a plasma and a dielectric wall. For this purpose, the wall-bound surplus charge arising from the plasma is modeled as a quasistationary electron surface layer in thermal equilibrium with the wall. It satisfies Poisson's equation and minimizes the grand canonical potential of wall-thermalized excess electrons. Based on an effective model for a graded interface taking into account the image potential and the offset of the conduction band to the potential just outside the dielectric, we specifically calculate the modification of the potential and the distribution of the surplus electrons for MgO, SiO₂, and Al₂O₃ surfaces in contact with a helium discharge. Depending on the electron affinity of the surface, we find two vastly different behaviors. For negative electron affinity, electrons do not penetrate into the wall and a quasi-two-dimensional electron gas is formed in the image potential, while, for positive electron affinity, electrons penetrate into the wall and a negative space-charge layer develops in the interior of the dielectric. We also investigate how the non-neutral electron surface layer—which can be understood as the ultimate boundary of a bounded gas discharge—merges with the neutral bulk of the dielectric.

DOI: [10.1103/PhysRevB.85.075323](https://doi.org/10.1103/PhysRevB.85.075323)

PACS number(s): 52.40.Hf, 73.30.+y, 52.80.Tn

I. INTRODUCTION

Macroscopic objects in contact with an ionized gas acquire a negative charge because the influx of electrons from the plasma outruns the influx of ions. The collection of electrons at the wall (the boundary of the object) gives rise to a repulsive Coulomb potential which reduces the electron influx until the wall charge reaches a quasistationary value. As a consequence of the electron accumulation at the wall, an electron depleted region, the plasma sheath, is formed adjacent to the wall.

Most of the voltage driving the discharge drops across the sheath. Wall charges may however affect not only the spatial structure of the plasma but also surface-supported elementary processes such as electron-ion recombination and secondary electron emission, which are particularly important in dusty plasmas,¹⁻³ dielectric barrier discharges,⁴⁻⁶ and solid-state-based microdischarges.⁷⁻¹¹ A macroscopic description of the plasma-induced wall charge, sufficient for the modeling of the plasma sheath,¹² is clearly insufficient for quantifying the effect wall charges might have on these processes. A microscopic description of the plasma-induced wall charge and the potential across the plasma-wall interface it leads to is required.

Traditionally, plasma walls are treated as perfect absorbers.¹²⁻¹⁴ Irrespective of the microscopic interaction, all electrons and ions impinging on the wall are assumed to recombine instantly. From this model, only the wall potential just outside the wall can be obtained. This is the potential that balances the electron and ion influx at the wall. A first, qualitative step going beyond this model was taken by Emeleus and Coulter,^{15,16} who envisaged the wall charge as a two-dimensional surface plasma coupled to the bulk plasma via electron-ion wall recombination. No attempt was however made to put this appealing idea onto a formal basis. Later the notion of a two-dimensional surface charge was developed further by Behnke and coworkers¹⁷⁻¹⁹ utilizing phenomenological rate equations for the electron and ion surface densities. In these equations, the microphysics at the

wall is encapsulated in surface parameters, such as electron and ion sticking coefficients, electron and ion desorption times, and an electron-ion wall recombination coefficient. In principle these parameters can be calculated. Assuming, for instance, plasma electrons to adsorb and desorb in the long-range image potential of the wall, we calculated in our previous work electron sticking coefficients and electron desorption times for uncharged metallic²⁰ and dielectric surfaces.²¹⁻²³ We also made a first attempt to estimate these two quantities for charged dielectric plasma walls²⁴ and proposed a physisorption-inspired microscopic charging model for dust particles in a gas discharge.²⁵

In this work, we shift gears and focus on the potential and charge distribution across the plasma-wall interface after the quasistationary wall charge (the electron adsorbate in the notation of our previous work²⁰⁻²⁵) has been established. In other words, we extend the modeling of the plasma sheath¹²⁻¹⁴ to the region inside the solid and calculate the plasma-induced modifications of the potential and charge distribution of the surface. Although knowing the potential and charge distribution across the interface may not be of particular importance for present day technological plasmas, it is of fundamental interest from an interface physics point of view. In addition, considering the plasma wall as an integral part of the plasma sheath may become critical when the miniaturization of solid-state-based plasma devices⁷⁻¹¹ continues.

In the model outlined below we specifically consider a dielectric wall and treat the plasma-induced quasistationary wall charge, that is, the surplus charge on top of the charge distribution of the bare, free-standing surface, as an electron surface layer (ESL) of a certain extent, which is trapped by and in thermal equilibrium with the wall. In order to determine the chemical potential, width, and spatial position (relative to the crystallographic interface) of the electron surface layer, which depend on surface as well as plasma parameters, we employ a one-dimensional model for a graded interface between a collisionless plasma sheath and a dielectric surface which is assumed to be a perfect absorber; that is,

the wall potential balances at a certain distance from the crystallographic interface the electron and the ion influx from the plasma.

The model of a graded interface encompasses two important ingredients: the surface dipole of the bare surface responsible for the offset of the conduction-band minimum to the potential just outside the dielectric and the long-range image potential. The former accounts for the charge redistribution of the free-standing, uncharged surface arising from the truncation of the crystal, and the latter supports polarization-induced external surface states (image states), first predicted for liquid helium²⁶ and later studied for metallic and dielectric surfaces with negative electron affinity,^{27–32} which may trap the electron surface layer in front of the crystallographic interface.

Originally proposed by Stern for the interface between two dielectrics,³³ and later used by others for semiconductor heterojunctions³⁴ and electron trapping in nanopores,³⁵ the graded interface model also guarantees continuity of the electrostatic potential across the plasma-wall interface. The model thus allows us to study the spatial distribution of the plasma-induced wall charge across the interface. To insert the surplus charge into the interface we follow Tkharev and Danilyuk³⁶ and minimize, in the spirit of density-functional theory,^{37–39} the grand canonical potential of wall-thermalized excess electrons. We also investigate how the electron surface layer merges with the neutral bulk of the dielectric which we describe with the model of an intrinsic semiconductor.

Various improvements of the model are conceivable but the increased mathematical complexity would mask the general ideas we would like to convey. For instance, the model of a collisionless sheath could be replaced by more realistic models.^{12–14} Going beyond the perfect absorber model, on the other hand, is an unsolved problem. It would require the inclusion of electron desorption, electron sticking, and electron-ion recombination, with the respective coefficients to be self-consistently calculated for the quasistationary electron adsorbate at the wall. Replacing the graded interface by an *ab initio* theory for the surface, for instance, along the lines given in Refs. 27,28,40 and 41, possibly taking adlayers of the host gas's atoms or molecules as well as impurities and imperfections into account, is desirable but at the present stage of the investigation impractical. It would require an expensive atomistic characterization of the plasma-wall interface, either experimentally via various surface diagnostics or theoretically via *ab initio* simulations. As long as the atomistic details affect however only the offsets of the dielectric constant, the electron affinity, and the effective mass, the graded interface model already incorporates these details by a suitable parametrization. What is not well described is the nonuniversal region a few atomic units below and above the crystallographic interface. In particular, intrinsic surface states (Shockley and Tamm states⁴²) and additional surface states which may arise from the short-range surface potential due to impurities, imperfections, and adlayers are not included. If unoccupied these states could trap the electron surface layer in the vicinity of the interface, even for surfaces with positive electron affinity where image states are absent and cannot trap the surplus charge in front of the surface.

The remaining paper is structured as follows. In Sec. II we first construct a crude model for the plasma-induced electron

surface layer at the interface between a plasma and a dielectric wall. It does not account for the merging of the electron surface layer with the bulk of the dielectric. As long as the primary interest is in the region close to the crystallographic interface and the band gap of the dielectric is large enough, the crude model is sufficient. Section III describes a refinement of the model which enables one to also investigate the crossover of the electron surface layer to the bulk of the dielectric. This is particularly important for dielectrics with small energy gaps. Numerical results for the potential and the electron distribution are given in Sec. IV, and a short summary is formulated in Sec. V.

II. CRUDE ELECTRON SURFACE LAYER

As depicted in Fig. 1, we consider an ideal, planar interface at $z = 0$ with the dielectric occupying the half space $z < 0$ and the discharge occupying the half space $z > 0$. Chemical contamination and structural damage due to the burning gas discharge are discarded. At the moment we focus on the physical principles controlling the electronic properties of the plasma-wall interface. In the model we propose the plasma-induced wall charge to be treated as an ESL, which is an interface-specific electron distribution on top of the charge redistribution due to the truncation of the solid. The ESL is assumed to be thermalized with the solid and to stretch from the plasma sheath over the crystallographic interface to the bulk of the dielectric.

The boundary between the ESL and the plasma sheath is located in front of the surface at $z = z_0$. It is the position where the attractive force due to the surface potential ϕ_{surf} and the

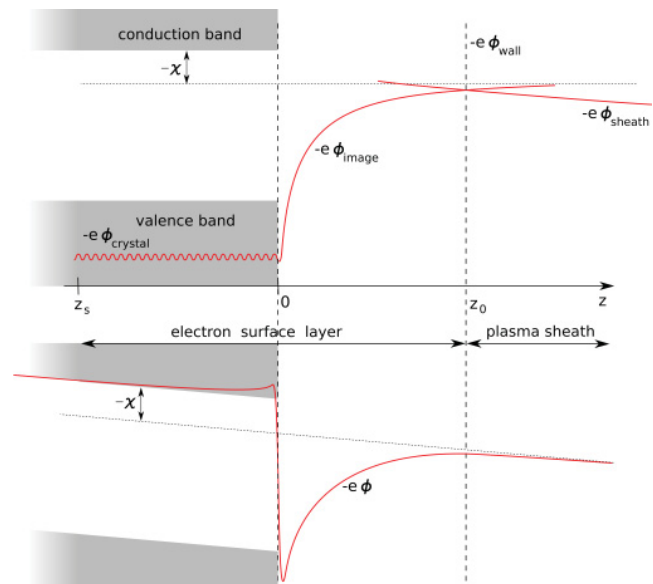


FIG. 1. (Color online) Qualitative sketch of an interface between a plasma and a dielectric wall. Upper panel: band structure, microscopic crystal potential merging with the image potential, and sheath potential. Lower panel: effective potential for the graded interface on which the model of an electron surface layer is based.

repulsive force due to the sheath potential ϕ_{sheath} balance each other. Thus, z_0 is given by

$$\phi'_{\text{surf}}(z_0) + \phi'_{\text{sheath}}(z_0) = 0. \quad (1)$$

It gives the position of an effective wall for plasma electrons and ions at which, for instance, the flux balance condition of the perfect absorber model, $j_e = j_i$, with j_e and j_i , respectively, being the electron and ion flux toward the dielectric surface, has to be fulfilled. For $z < z_0$ an electron is attracted to the surface and thus contained in the ESL, while for $z > z_0$ it is repelled back into the plasma. On the solid side, for $z < 0$, the ESL is bounded because of the shallow potential well formed by the restoring force from the positive charge in the plasma sheath.

In this section we will outline the essential building blocks of the ESL model. Putting together concepts from plasma as well as surface physics, a detailed, self-contained account seems to be helpful.

A. Plasma sheath

In the traditional view, electrons missing in the positive space-charge region (SCR) in front of the plasma wall accumulate on the wall and give rise to a wall potential. For the construction of our one-dimensional interface model we need the total number per unit area of missing sheath electrons (that is, the total surface density of missing sheath electrons) as a function of the wall potential because it is this number of electrons which can be distributed across the ESL. Hence, we require a model for the plasma sheath.

For simplicity, we use a collisionless sheath,¹² more realistic sheath models^{12–14} make no difference in principle. In the collisionless sheath, electrons are thermalized, that is, the electron density $n_e = n_0 \exp(e\phi/k_B T_e)$, with ϕ being the potential, n_0 being the plasma density, and T_e being the electron temperature. The ions enter the sheath with a directed velocity v_{i0} and satisfy a source-free continuity equation, $d(n_i v_i)/dz = 0$, implying $n_i v_i = n_0 v_{i0}$, and an equation of motion $M(v_i \frac{d}{dz} v_i) = -e \frac{d}{dz} \phi$, with n_i being the ion density and M being the ion mass. The potential ϕ satisfies Poisson's equation $d^2 \phi/dz^2 = -4\pi e(n_i - n_e)$. Thus, the governing equations for the collisionless plasma sheath are¹²

$$v_i \frac{dv_i}{dz} = -\frac{e}{M} \frac{d\phi}{dz} \quad \text{and} \quad (2)$$

$$\frac{d^2 \phi}{dz^2} = -4\pi e n_0 \left[\frac{v_0}{v_i} - \exp\left(\frac{e\phi}{k_B T_e}\right) \right]. \quad (3)$$

Using dimensionless variables

$$\eta = -\frac{e\phi}{k_B T_e}, \quad \xi = \frac{z}{\lambda_D}, \quad \text{and} \quad u = \frac{v_i}{c_s}, \quad (4)$$

where

$$\lambda_D = \sqrt{\frac{k_B T_e}{4\pi n_0 e^2}} \quad \text{and} \quad c_s = \sqrt{\frac{k_B T_e}{M}}, \quad (5)$$

Eqs. (2) and (3) become

$$uu' = \eta' \quad \text{and} \quad (6)$$

$$\eta'' = \frac{u_0}{u} - \exp(-\eta). \quad (7)$$

In the ESL model the plasma occupies not the whole half space $z > 0$ but only the portion $z > z_0$ (see Fig. 1). The integration of the first equation gives $u = -\sqrt{2\eta + u_0^2}$, where $u_0 = v_{i0}/c_s$ is the reduced velocity of ions entering the sheath, so that the second equation becomes

$$\eta'' = -\frac{u_0}{\sqrt{2\eta + u_0^2}} - \exp(-\eta). \quad (8)$$

Using the boundary condition that the potential and the field vanish far inside the plasma, that is, $\eta \rightarrow 0$ and $\eta' \rightarrow 0$ for $\xi \rightarrow \infty$, Eq. (8) can be integrated once and we obtain

$$\eta' = -\sqrt{-2u_0 \sqrt{2\eta + u_0^2} + 2 \exp(-\eta) + 2u_0 \sqrt{u_0^2} - 2}. \quad (9)$$

For ions entering the sheath with the Bohm velocity, $u_0 = -1$. The field at the wall as a function of the wall potential $\eta_w = \eta(\xi_0)$ is then given by

$$\eta'_w = -\sqrt{2\sqrt{2\eta_w + 1} + 2 \exp(-\eta_w) - 4}. \quad (10)$$

The total surface density of electrons in the ESL equals the total surface density of missing sheath electrons, in other words, the total surplus surface density of positive ions in the sheath N which can be calculated from the electric field at the wall. Integrating Poisson's equation yields

$$\begin{aligned} N &= \int_{z_0}^{\infty} dz(n_i - n_e) = -\frac{1}{4\pi e} \int_{z_0}^{\infty} dz \frac{d^2 \phi}{dz^2} \\ &= \frac{1}{4\pi e} \frac{d\phi}{dz}(z_0) = -n_0 \lambda_D \eta'_w. \end{aligned} \quad (11)$$

Combing Eqs. (11) and (10) gives the total surface density of electrons to be inserted into the ESL as a function of the wall potential.

The wall potential itself is determined by the flux balance condition, $j_e = j_i$, which, in the ESL model, is assumed to be fulfilled at $z = z_0$. Using the Bohm flux for the ions and the thermal flux for the electrons,

$$j_i = n_0 \sqrt{\frac{k_B T_e}{M}} \quad \text{and} \quad j_e = \frac{1}{4} n_0 \sqrt{\frac{8k_B T}{\pi m_e}} e^{\frac{e\phi}{k_B T_e}}, \quad (12)$$

the wall potential is given by¹²

$$\eta_w = \frac{1}{2} \ln\left(\frac{M}{2\pi m_e}\right), \quad (13)$$

that is,

$$\phi_w = -\frac{k_B T_e}{2e} \ln\left(\frac{M}{2\pi m_e}\right). \quad (14)$$

In the collisionless sheath model the wall potential depends only on the electron temperature and the ion to electron mass ratio.

B. Surface dipole

We now turn to the interface region in which the missing sheath electrons will be inserted. This region is absent in the traditional modeling of plasma walls. In our model it is an extended region surrounding an ideal dielectric surface.

In comparison to the electrons responsible for the chemical binding within the dielectric the additional electrons coming from the plasma are only a few. The electronic structure of the surface, in particular, the charge redistribution due to truncation of the solid and the offset of the energy bands in the bulk with respect to the potential outside the dielectric, will not be changed significantly by the presence of the surplus electrons comprising the wall charge.

In order to quantify the above statement let us first consider the electrostatic potential and the electronic structure of a free-standing, uncharged dielectric surface. According to Tung,⁴³ it has to minimize the thermodynamical potential and satisfy Poisson's equation, implying that the potential is continuous across the surface. Strictly speaking, the continuity of the potential only applies to the microscopic crystal potential which has to merge continuously with the surface potential outside the crystal. The averaged long-range potential, in contrast, can be discontinuous at the interface. It is this offset which is encoded in the surface dipole.

The energy of an electronic state in the bulk of the dielectric can be referenced to the vacuum level $V(\infty) = 0$, that is, the potential far outside the crystal, in the following way:⁴³

$$E_{ik}(\vec{r}) = \epsilon_{ik} - e\bar{V}_{\text{cell}} - eV_s(\vec{r}), \quad (15)$$

where ϵ_{ik} is the quantum-mechanical contribution to the energy, \bar{V}_{cell} is the averaged potential of a cell due to the charge distribution within the same cell, and $V_s(\vec{r})$ is the long-range potential due to the surface dipole, space charges, and external fields. In the simple two-band model depicted in Fig. 1, $i = v, c$. $V_s(\vec{r})$ contains the surface dipole arising from the truncation of the solid and responsible for the potential offset at the surface and a slowly varying component due to external fields and internal and plasma-induced space charges. External fields and internal space charges will be neglected in the following, and plasma-induced space charges will be accounted for by Poisson's equation (see below).

In order to judge whether the surplus charge arising from the plasma affects the surface dipole it is useful to consider first the typical strength of the surface dipole of a free-standing, uncharged dielectric surface. It results from a charge double layer in immediate proximity to the surface. Depending on the material it can have various origins. For an ionic crystal, for example, it is the lattice relaxation at the surface which makes anions or cations protrude and the other species retract (e.g., protruding oxygen and retracted cations for magnesium oxide²⁷), while for semiconductors it is the regrouping of covalent bonds which leads to charge redistribution at the surface. Even in the absence of these effects the minimization of the thermodynamic potential of the surface's electrons leads already to an electron density leaking out into the vacuum. This is particularly important for metals. As a result a charge double layer is formed over a length on the order of a lattice constant.

The dipole layer is usually characterized by a dipole strength:

$$eD = eV_s(\vec{r}_s^-) - eV(\vec{r}_s^+), \quad (16)$$

where $V_s(\vec{r}_s^-)$ is the limit of the long-range potential just inside the crystal at the surface position \vec{r}_s and $V(\vec{r}_s^+)$ is the limit of

the potential at that position just outside the surface. Usually these two potentials, which characterize the discontinuity of the long-range potential at the surface, are termed the potential just inside and the potential just outside, respectively.^{43,44} Here, just outside denotes a distance that is small compared to variations of the long-range potential due to external fields or space charges but large compared with the width of the charge double layer. Note also that, in the definition of the potential just outside the image potential is assumed to have already decreased to zero.⁴⁴ This point will be important later.

The strength of the dipole layer is a microscopic property of the surface which is relatively insensitive against the additional charges from the plasma. The reason for this lies in the small number of additional electrons from the plasma compared to the number of displaced electrons involved in the formation of the dipole layer. To prove this statement we give a simple estimate. Typical surface dipoles eD are on the order of electron volts. For a double layer of 1 Å to each side of the crystallographic interface a potential difference of 1 V requires a surface charge density of $5.5 \times 10^{13} \text{cm}^{-2}$. The surface charge density at the wall of a helium discharge with plasma density $n_0 = 10^7 \text{cm}^{-3}$ and electron temperature $k_B T_e = 2 \text{eV}$ amounts, however, only to $4.4 \times 10^6 \text{cm}^{-2}$. For typical plasma densities, the number of additional electrons is thus far too small to lead to a change of the surface dipole. Even for semiconductor-based microdischarges,^{8,10} which can have much higher plasma densities, we expect the surface dipole of the plasma wall not to be modified by the plasma.

In view of the preceding estimate, we have to revise an assumption in our previous work,²³ where we assumed the surface charge accumulating on the wall would increase the dipole energy eD by $e\phi_w$, leading to the image states being pushed from the band gap into the energy region of the conduction band. The numbers given in the previous paragraph indicate, however, that the band lineup of the conduction band and the potential just outside the solid will not be affected much by the wall charge. Hence, if a negative electron affinity supports image states in front of the uncharged surface, these states remain in the band gap for the charged surface. Electron trapping as investigated in Refs. 21 and 22 is thus possible even for charged plasma walls.

Instead of the dipole strength eD which cannot be measured directly, it is more convenient to characterize the dipole layer by the electron affinity χ which is a measurable quantity for a dielectric surface.⁴⁴ The electron affinity is the energy released when an electron is moved from just outside the surface to the bottom of the conduction band. It accounts for charge redistribution in the vicinity of the surface due to the truncation of the crystal. While many surfaces have positive electron affinity such as Al_2O_3 or SiO_2 , there are also materials with negative electron affinity, for instance, diamond,⁴⁵ boron nitride,⁴⁶ or the alkaline earth oxides.^{27,28} The electron affinity depends also on adatoms. In some cases this is even used to control the electron affinity of a surface. Terminating, for instance, a surface with weakly electronegative elements such as hydrogen induces a negative electron affinity,⁴⁷ while termination with strongly electronegative elements can lead to a positive electron affinity.⁴⁸

From Eq. (15) it is clear that χ equals eD plus a bulk contribution:

$$\chi = -eV_s(\vec{r}_s^+) - E_{ck}(\vec{r}_s^-) = eD - E_C + e\bar{V}_{\text{cell}}, \quad (17)$$

where $E_C = \epsilon_{\text{cm}}$ denotes the minimum of the conduction band. We can thus use χ to characterize the potential offset at the surface. There is however a caveat. The long-range potential inside the solid is only specified up to a constant.⁴³ Typical choices are the cell-averaged potential or the intersphere potential of the muffin-tin approximation. For our purpose it will be however more convenient to take the conduction-band minimum as the long-range potential inside the solid. This choice is motivated as follows. We are considering a dielectric with a large energy gap. The valence band is thus fully occupied and the conduction band is essentially empty. Hence, only the conduction band can be populated by additional electrons coming from the plasma, and referencing the electrostatic potential inside the solid to the conduction-band minimum allows us to relate the total surplus electron density in the interface region to the potential in the interface region, in analogy to what we have done for the plasma sheath in the previous subsection.

Adopting the above discussion to the one-dimensional model shown in Fig. 1 and assuming a quadratic dispersion for the conduction band, the energy of an electron in the conduction band is given by

$$E_k(z) = \frac{\hbar^2 k^2}{2m_c^*} - e\phi_{\text{surf}}(z), \quad (18)$$

where $\phi_{\text{surf}}(z)$ is the total surface potential to be determined in the next subsection, and the offset of the electrostatic potential at the surface,

$$e\phi_{\text{surf}}(0^-) - e\phi_{\text{surf}}(0^+) = \chi, \quad (19)$$

encompasses the surface dipole as well as the unspecified bulk contribution.

C. Image potential

The surface potential of the bare, uncharged surface comprises at least the surface dipole and a long-range contribution, the image potential, resulting from the mismatch of the dielectric constants at the surface. Far away from the surface the image potential is given by⁴⁹

$$\phi_{\text{im}}(z) = \frac{\epsilon - 1}{4(\epsilon + 1)} \frac{e}{z}. \quad (20)$$

But this expression cannot be employed for our purpose because the singularity at $z = 0$ prohibits a smooth electron distribution across the interface. In reality the image potential has to continuously merge with the crystal potential. Equation (20) is thus also unphysical.

To obtain a realistic image potential without performing an atomistically accurate calculation we employ the model of a graded interface. It also has the virtue of being parameterizable with experimentally measured values for the electron affinity,

the dielectric mismatch, and the mismatch between effective electron masses. The model incorporates therefore important properties of a surface; most importantly, it accounts for the charge redistribution due to the truncation of the solid.

Initially proposed by Stern³³ to remove the unphysical singularity of the image potential at the interface of two dielectrics, the graded interface model assumes the dielectric constant ϵ to vary over a distance on the order of a lattice constant. Later the model was extended to variations of other physical quantities and applied to semiconductor heterostructures and nanopores.^{34,35} Clearly, because of the interpolation the model cannot account for effects associated with intrinsic surface states (Shockley and Tamm states⁴²) and additional surface states which may arise from the short-range surface potential. Nevertheless, the graded interface model is a reasonable description of a surface.

In the spirit of a graded interface, we assume the dielectric constant ϵ , the electron mass m , and the potential offset at the surface to vary smoothly according to the grading function

$$g_{c^-,c^+}(z) = \begin{cases} c^- & z < -a \\ \frac{c^- + c^+}{2} - \frac{c^- - c^+}{2} \sin\left(\frac{\pi x}{2a}\right) & -a < z < a, \\ c^+ & z > a \end{cases} \quad (21)$$

where a is the half width of the graded interface and c^\mp stands for the quantity that varies across the interface. We use the value $a = 5 \text{ \AA}$, which is an estimate used in previous applications of the graded interface.³³⁻³⁵ While the grading parameter a is not based on definite experimental or theoretical results it is motivated by the assumption that the bonding and the electron density at the surface change over one to two lattice constants, implying a transition layer for the effective potential and the dielectric constant that is somewhat larger. Hence, across the interface the electron mass, the dielectric constant, and the offset potential are given by

$$m(z) = g_{m_c^*,m_c}(z), \quad \epsilon(z) = g_{\epsilon,1}(z), \quad (22)$$

and

$$\phi_{\text{offset}}(z) = \frac{1}{e} g_{\chi,0}(z), \quad (23)$$

respectively, with m_c^* being the effective mass of the conduction band.

Within the model of the graded interface, the image potential is the change in the self-energy of an electron due to the proximity of the dielectric mismatch. Positioning the electron at \vec{r}_0 it is given by³³

$$\phi_{\text{im}}(\vec{r}_0) = \frac{1}{2} [\phi^m(\vec{r}_0) - \phi^0(\vec{r}_0)], \quad (24)$$

where $\phi^m(\vec{r})$ is the potential in the medium with dielectric mismatch arising from the electron at \vec{r}_0 and $\phi^0(\vec{r})$ is the same quantity in a homogeneous medium with dielectric constant $\epsilon(z_0)$. Hence, $\phi^m(\vec{r})$ is the solution of

$$\nabla[\epsilon(z)\nabla\phi^m(\vec{r})] = 4\pi e\delta(\vec{r} - \vec{r}_0), \quad (25)$$

while $\phi^0(\vec{r})$ is the solution of

$$\nabla^2\phi^0(\vec{r}) = \frac{4\pi e}{\epsilon(z_0)}\delta(\vec{r} - \vec{r}_0). \quad (26)$$

To solve Eqs. (25) and (26) we follow Stern³³ and make the ansatz

$$\begin{aligned} \phi^{m,0}(z, \rho, \phi) &= \frac{1}{2\pi} \sum_{l=-\infty}^{\infty} \int_0^{\infty} dq q J_l(\rho q) J_l(\rho_0 q) \\ &\times e^{il(\phi - \phi_0)} A_q^{m,0}(z). \end{aligned} \quad (27)$$

Placing the electron on the z axis, $\rho_0 = 0$, which implies $J_0(\rho_0 q) = 1$ and $J_l(\rho_0 q) = 0$ for $l > 0$. Hence, we need to keep only the $l = 0$ term, so that

$$\phi^{m,0}(z, \rho, \phi) = \frac{1}{2\pi} \int_0^{\infty} dq q J_0(\rho q) A_q^{m,0}(z), \quad (28)$$

where $A_q^0(z)$ is given by

$$A_q^0(z) = \frac{-2\pi e}{\epsilon(z_0)q} e^{-q|z-z_0|} \quad (29)$$

and $A_q^m(z)$ is the solution of

$$A_q^{m''}(z) + \frac{\epsilon'(z)}{\epsilon(z)} A_q^{m'}(z) - q^2 A_q^m(z) = \frac{4\pi e}{\epsilon(z)} \delta(z - z_0), \quad (30)$$

which has to be obtained numerically. The image potential is then given by

$$\phi_{\text{im}}(z_0) = \frac{1}{4\pi} \int_0^{\infty} dq q [A_q^m(z_0) - A_q^0(z_0)]. \quad (31)$$

In contrast to Eq. (20) it is now smoothly varying across the interface with a deep well on the low- ϵ side and a small bump on the high- ϵ side.

The total surface potential comprises the graded offset potential Eq. (23) and the graded image potential. Hence,

$$\phi_{\text{surf}}(z) = \phi_{\text{im}}(z) + \phi_{\text{offset}}(z). \quad (32)$$

It is continuous across the crystallographic interface at $z = 0$ and enables us thereby to also calculate a smoothly varying electron distribution in the ESL. The band structure and the total surface potential at the graded interface are visualized in the lower panel of Fig. 1.

Using Eq. (1) we can now determine the position z_0 of the effective wall, that is, the maximum extent of the ESL on the plasma side. The derivative of the bare surface potential is $\phi'_{\text{surf}} = \phi'_{\text{offset}} + \phi'_{\text{im}}$. Due to the relatively weak field in the sheath compared to the image force, the boundary z_0 will be so far away from the interface that ϕ'_{offset} vanishes and the image potential obeys Eq. (20). Thus, the boundary between the ESL and the plasma sheath is given by

$$z_0 = \sqrt{\frac{(\epsilon - 1)e}{4(\epsilon + 1)\phi'_w}}, \quad (33)$$

with $\phi'_w = -(k_B T_e \eta'_w)/(e\lambda_D)$ and η'_w given by Eq. (10).

D. Electron distribution

The plasma-induced wall charge is assumed to be in thermal equilibrium with the wall. Hence, the distribution of the excess electrons in the ESL has to minimize the excess electron's grand canonical potential in the external potential due to the surface. The coupling to the sheath is maintained by the constraint that only as many electrons can be filled into the

ESL as are missing in the sheath and the boundary conditions to the Poisson equation, which links the electron distribution in the ESL to the (internal) electrostatic potential.

To minimize the grand canonical potential of the surplus electrons we follow Tkharev and Danilyuk³⁶ and apply density-functional theory^{37,38} to the graded interface. While more refined schemes of density-functional theory³⁹ could, in principle, be employed, we will use for the purpose of this exploratory calculation density-functional theory in the local approximation. Quite generally, the grand canonical potential of an electron system in an external potential $V(\vec{r})$ is given in the local approximation by

$$\begin{aligned} \Omega &= \int V(\vec{r})n(\vec{r})d\vec{r} - \frac{e}{2} \int \phi_C(\vec{r})n(\vec{r})d\vec{r} \\ &+ G[n] - \mu \int n(\vec{r})d\vec{r}, \end{aligned} \quad (34)$$

where $G[n]$ is the grand canonical potential of the homogeneous system with density $n(\vec{r})$ and the Coulomb potential is determined by

$$\nabla[\epsilon(\vec{r})\nabla\phi_C(\vec{r})] = 4\pi en(\vec{r}). \quad (35)$$

The ground-state electron density minimizes Ω ; that is, it satisfies

$$V(\vec{r}) - e\phi_C(\vec{r}) + \mu^h(n) - \mu = 0, \quad (36)$$

where $\mu^h(n) = \delta G[n]/\delta n$ is the chemical potential for the homogeneous system.

Specifically for the excess electrons in the one-dimensional graded interface Eq. (36) reduces to

$$-e\phi(z) + \mu^h(z) - \mu = 0, \quad (37)$$

where $\mu^h(z) \equiv \mu^h[n(z), T]$ and the electrostatic potential,

$$\phi(z) = \phi_{\text{surf}}(z) + \phi_C(z), \quad (38)$$

consists of the potential of the bare surface given by Eq. (32) and the internal Coulomb potential which satisfies Poisson's equation:

$$\frac{d}{dz} \left[\epsilon(z) \frac{d}{dz} \phi_C(z) \right] = 4\pi en(z), \quad (39)$$

with the graded dielectric constant $\epsilon(z)$ given by Eq. (22) and the boundary conditions $\phi_C(z_0) = \phi_w$ and $\phi'_C(z_0) = \phi'_w$ to guarantee continuity of the potential at z_0 and to include the restoring force from the positive charge in the sheath. Note that the Coulomb potential derived from this equation includes the attraction of an electron to the image of the charge distribution.

For the functional relation $\mu^h(z) \equiv \mu^h[n(z), T]$ we take the expression adequate for a homogeneous, noninteracting, nondegenerate electron gas:

$$n(z) = \frac{1}{\sqrt{2}} \left[\frac{m(z)kT}{\pi\hbar^2} \right]^{\frac{3}{2}} e^{\frac{\mu^h(z)}{k_B T}}. \quad (40)$$

This is justified because the density of the excess electrons is rather low and the temperature of the surface is rather high, typically a few hundred Kelvins.

In order to calculate the quasistationary distribution of the surplus electrons, Eqs. (37) and (39) have to be solved self-consistently with the additional constraint that the total

electron surface density in the ESL equals the total surface density of electrons missing in the sheath, that is,

$$\int_{z_s}^{z_0} dz n(z) = N, \quad (41)$$

with N given by Eq. (11). In the above equation we introduced a cutoff $z_s < 0$ at which the ESL terminates inside the dielectric. As long as $|z_s|$ is chosen large enough it does not affect the numerical results close to the surface. An improved treatment of the ESL, avoiding the *ad hoc* cutoff, is given in the next section.

Within the crude ESL model developed in this section the computation is performed iteratively in the interval $z_s < z < z_0$ according to the following scheme:

(i) We start with the potential of the empty surface given by Eq. (38) with $\phi_C(z)$ obtained from Eq. (39) with $n(z) = 0$ but with the boundary conditions at z_0 as specified.

(ii) We integrate both sides of Eq. (40) over z with $\mu^h(z)$ given by Eq. (37). Enforcing the constraint (41) determines μ .

(iii) Using μ we calculate from Eq. (37) a new $\mu^h(z)$ which gives with Eq. (40) a new electron density $n(z)$.

(iv) Lastly, we determine from Eq. (39) the electrostatic potential associated with the updated $n(z)$.

Steps (ii)–(iv) are iterated until μ , which is far below the conduction-band edge because of the nondegeneracy of the excess electrons, converges.

III. REFINED ELECTRON SURFACE LAYER

In the previous section we have taken into account only the electron concentration in the conduction band of the dielectric due to the electrons coming from the plasma. For wide band-gap materials this is justified, especially near the surface, as their concentration is much larger than the intrinsic carrier concentration. Deep inside the dielectric, however, charge neutrality is not enabled by a vanishing electron density but by the electron density decreasing to its intrinsic value, which is then balanced by the intrinsic hole concentration in the valence band.

To take this effect into account, which is particularly important when the additional electrons accumulate deep inside the bulk of the dielectric, we divide the ESL into two regions: a very narrow interface-specific region (ISR) and a wide space-charge region (SCR) in the bulk of the dielectric. The parameter z_s denotes now no longer an *ad hoc* cutoff but the boundary between the two regions. It has to be chosen so that the ISR includes the major effect of the image potential in the dielectric implying $z_s < -z_0$. The electron distribution and the potential in the ISR are calculated using the density-functional approach outlined in the previous section. In the SCR we use for simplicity the model of an intrinsic semiconductor to describe electron and hole densities as well as the long-range potential. As the energy bands in the dielectric follow the long-range potential the refined ESL also captures the band bending which might be induced by the presence of the wall charge. It is however only significant when most of the excess electrons are trapped in the SCR and not in the ISR.

Figure 2 schematically shows the electron and hole densities for the refined ESL model. The boundary between the plasma

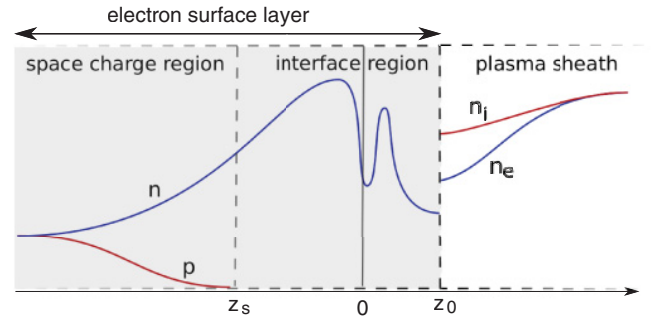


FIG. 2. (Color online) Sketch of the refined model of the interface between a plasma and a dielectric wall. In the plasma, equal densities of electrons and ions ensure quasineutrality. The positive space charge in front of the effective wall defines the plasma sheath. The ESL contains a very narrow interface-specific region (ISR), where the model of the graded interface is used, and a wide space-charge region (SCR), which allows a continuous merging with the neutral bulk of the dielectric, where intrinsic electrons and holes balance each other to guarantee charge neutrality. Note that the widths of the various regions are not to scale.

sheath and the ESL is still located at z_0 . As our model does not encompass the electron and ion flux from the plasma for $z < z_0$, the densities n_e and n_i are discontinuous at z_0 . This is obvious for the ions which are not allowed to enter the solid. The discontinuity of the electron density, in contrast, arises because we ensure only the total number of missing sheath electrons per unit area to be conserved. This global constraint cannot guarantee continuity of the electron density at z_0 . At the boundary between the ISR ($z_s < z < z_0$) and the SCR ($z < z_s$) the electron density and the potential are continuous. In principle, also the hole density p should be continuous. As $p(z_s) \ll n(z_s)$ for the materials we are considering, we can however neglect holes in the ISR.

For the modeling of the SCR it is convenient to use $\psi(z) = \phi(z) - \phi_{\text{bulk}}$ for the long-range potential, which vanishes for charge neutrality in the bulk. Here, $\phi_{\text{bulk}} = \phi(-\infty)$ (see below for an explicit relation for ϕ_{bulk}). Then, Poisson's equation is given by

$$\frac{d^2\psi(z)}{dz^2} = -\frac{4\pi}{\epsilon} [-en(z) + ep(z)], \quad (42)$$

where the electron and hole densities for an intrinsic semiconductor with parabolic bands whose extremal points are, respectively, E_C and E_V are given by⁵⁰

$$n(z) = \frac{1}{\sqrt{2}} \left(\frac{m_C^* k_B T}{\pi \hbar^2} \right)^{\frac{3}{2}} e^{\frac{1}{k_B T} [v - E_C + e\psi(z)]}, \quad (43)$$

$$p(z) = \frac{1}{\sqrt{2}} \left(\frac{m_V^* k_B T}{\pi \hbar^2} \right)^{\frac{3}{2}} e^{-\frac{1}{k_B T} [v - E_V + e\psi(z)]}. \quad (44)$$

From a comparison of the exponents in Eqs. (43) and (40), where μ_h is given by Eq. (37), we find

$$v = \mu + E_C + e\phi_{\text{bulk}}. \quad (45)$$

Far from the surface, $\psi = 0$ and $n = p = n_b$. This gives the chemical potential

$$v = \frac{E_V + E_C}{2} + \frac{3}{4}k_B T \ln\left(\frac{m_V^*}{m_C^*}\right) \quad (46)$$

and the bulk carrier concentration

$$n_b = \frac{1}{\sqrt{2}} \left(\frac{k_B T}{\pi \hbar^2}\right)^{\frac{3}{2}} (m_C^* m_V^*)^{\frac{3}{4}} \exp\left(-\frac{E_g}{2k_B T}\right), \quad (47)$$

where $E_g = E_C - E_V$. Hence, Poisson's equation becomes

$$\frac{d^2\psi(z)}{dz^2} = \frac{4\pi e}{\epsilon} n_b \left[e^{\frac{e\psi(z)}{k_B T}} - e^{-\frac{e\psi(z)}{k_B T}} \right], \quad (48)$$

and using dimensionless variables

$$\eta = \frac{e\psi}{k_B T} \quad \text{and} \quad \xi = \frac{z - z_s}{L_D} \quad (49)$$

with $L_D = \sqrt{\epsilon k_B T / 4\pi e^2 n_b}$ we obtain

$$\eta'' = e^\eta - e^{-\eta}. \quad (50)$$

This equation can be integrated once, which gives

$$(\eta')^2 = 4 \cosh(\eta) + C. \quad (51)$$

The boundary conditions in the bulk $\eta = 0$ and $\eta' = 0$ for $\xi \rightarrow -\infty$ imply $C = -4$ so that Eq. (51) becomes

$$\eta' = \sqrt{8} \sinh\left(\frac{\eta}{2}\right). \quad (52)$$

Integration with the boundary condition at z_s , that is, at $\xi = 0$, $\eta(0) = \eta_s$ and requiring $\eta \rightarrow 0$ for $\xi \rightarrow -\infty$ gives

$$\eta^\pm(\xi) = \mp 2 \ln \left[\pm \tanh\left(\frac{\mp \xi}{\sqrt{2}} + \frac{c^\pm}{2}\right) \right], \quad (53)$$

with

$$c^\pm = \pm 2 \operatorname{artanh} \left[\exp\left(\frac{\mp \eta_s}{2}\right) \right], \quad (54)$$

where the upper sign is for $\eta_s > 0$ and the lower sign is for $\eta_s < 0$.

In analogy to what we have done at the boundary of the ESL with the plasma sheath at $z = z_0$ we relate the potential η_s to the total electron surface density in the space-charge region. From Poisson's equation we obtain for the total electron surface density in the SCR

$$\begin{aligned} N^{\text{SCR}} &= \int_{-\infty}^{z_s} dz(n - p) = L_D^2 n_b \left. \frac{d\eta}{dz} \right|_{-\infty}^{z_s} \\ &= L_D n_b \eta'(0), \end{aligned} \quad (55)$$

where η' is given by Eq. (52), so that

$$N^{\text{SCR}} = \sqrt{8} L_D n_b \sinh\left(\frac{\eta_s}{2}\right) \quad (56)$$

or

$$\eta_s = 2 \operatorname{arsinh} \left(\frac{N^{\text{SCR}}}{\sqrt{8} L_D n_b} \right). \quad (57)$$

For a negative space charge $\eta_s > 0$, so that the potential is given by $\psi(z) = (k_B T/e)\eta^+[(z - z_s)/L_D]$ and the electron and hole densities are given by $n(z) = n_b e^{\eta^+[(z - z_s)/L_D]}$ and $p(z) = n_b e^{-\eta^+[(z - z_s)/L_D]}$, respectively. The relation between

ψ and ϕ is given by $\phi_{\text{bulk}} = \phi(z) - \psi(z)$. Since $\psi(z_s) = (k_B T/e)\eta_s$ we obtain $\phi_{\text{bulk}} = \phi(z_s) - (k_B T/e)\eta_s$.

Now, quite generally, the excess electrons in the ESL are distributed over the ISR and SCR according to

$$N = N^{\text{ISR}}(\mu) + N^{\text{SCR}}(\mu), \quad (58)$$

where N^{ISR} is the surface density of electrons in the ISR, μ is the chemical potential in both regions, and N is the total surface density of missing sheath electrons given by Eq. (11). The total surface density in the ISR is given by $N^{\text{ISR}} = \int_{z_s}^{z_0} dz n(z)$, where $n(z)$ is calculated with the density-functional approach for the graded interface. Requiring continuity of the electron density at z_s ,

$$\frac{1}{\sqrt{2}} \left(\frac{m_C^* k_B T}{\pi \hbar^2}\right)^{\frac{3}{2}} e^{\frac{1}{k_B T}[\mu + e\phi(z_s)]} = n_b e^{\eta_s} \quad (59)$$

gives η_s as a function of μ . From η_s we finally obtain, using Eq. (56), $N^{\text{SCR}}(\mu)$.

For the calculation of the electron distribution and the potential in the refined ESL we use the iteration cycle described in the last section with one modification. In step (ii) we solve Eq. (58) instead of Eq. (41) to fix μ . From μ we obtain, using Eq. (59), η_s , which in turn determines the electron distribution and the potential in the SCR. This gives for each iteration step a continuous potential and electron distribution at z_s . As before, the steps (ii)–(iv) are iterated until μ converges.

At the end of this section let us finally mention two simplifications of the refined ESL model, which could be used, respectively, for large band-gap dielectrics irrespective of the electron affinity and dielectrics with small band-gap and positive electron affinity. In the former case the intrinsic carrier concentration n_b is very low and the merger with the bulk occurs very deep in the dielectric. Almost all surplus electrons are however much closer to the surface where the holes can be neglected. This can be seen from the differential equation for η . For small n_b Eq. (57) gives a large η_s . As η satisfies a highly nonlinear differential equation (50), a large η_s implies a steeper gradient of η near the surface so that almost all electrons are concentrated close to the surface where neglecting the holes has little effect. Hence, for large band-gap dielectrics surplus electrons can be filled into a sufficiently large ISR for which the crude ESL model of the previous section will be sufficient provided the cutoff z_s is large enough. The merger with the bulk is of course not correctly captured by such an approach.

For dielectrics or semiconductors with small energy gaps and positive electron affinity, on the other hand, almost all surplus electrons are deep inside the material. It is thus a good approximation to neglect the ISR and to fill all electrons in a SCR. Neglecting the surface potential has little effect in this case and using the SCR already for $z \leq 0$ gives a good description of the electron distribution inside the ESL. The electron density and potential at the surface and in front of it can of course not be captured by such an approach. As before $\psi(z) = \phi(z) - \phi_{\text{bulk}}$ with $\phi_{\text{bulk}} = \phi(z_s) - (k_B T/e)\eta_s$ where $\phi(z_s)$ is now the limit of the long-range potential just inside the dielectric given by $\phi(z_s) = \phi_w + \chi/e$.

IV. RESULTS

We now use the ESL model to calculate for a helium discharge in contact with a MgO, Al₂O₃, and SiO₂ surface the potential and the density of excess electrons across the plasma wall. Our main focus lies in the identification of generic types of electron distributions in the ESL depending on plasma and surface parameters. Unless otherwise stated, we use for the plasma density $n_0 = 10^7 \text{ cm}^{-3}$ and for the electron temperature $k_B T_e = 2 \text{ eV}$. The parameters of the dielectric surfaces are given in Table I. Preferentially we used experimental data for the various quantities; only if not available, we employed theoretical values.^{28,51–60}

First we give typical values for z_0 , the position where the ESL merges with the plasma sheath. It is calculated from Eq. (1) and should thus depend not only on plasma but also on surface parameters. Our results for MgO ($z_0 = 6.08 \times 10^{-5} \text{ cm}$), Al₂O₃ ($z_0 = 6.09 \times 10^{-5} \text{ cm}$), and SiO₂ ($z_0 = 5.14 \times 10^{-5} \text{ cm}$) indicate however that z_0 is relatively insensitive to ϵ , which is the only surface parameter affecting z_0 when the sheath is assumed to be collisionless. Even the significantly smaller ϵ of SiO₂ does not alter z_0 considerably. For the helium discharge considered z_0 is irrespective of the dielectric always on the order of a micron.

Of particular importance for the distribution of the excess electrons in the ESL is the electron affinity χ , characterizing the offset of the conduction band to the potential just outside. For $\chi < 0$ (MgO) the conduction-band minimum lies above the potential just outside. It is thus energetically favorable for electrons to be located in the image potential in front of the surface. Figure 3, showing the electron density and the potential in the ESL of MgO, verifies this. The energy of an electron in the image potential $-e\phi$ indeed reaches a minimum just in front of the surface at the beginning of the graded interface. For negative electron affinity, the excess electrons coming from the plasma thus form an external surface charge in the image potential in front of the crystallographic interface. The band bending associated with it is negligible. The external surface charge is very narrow; it can thus be considered as a quasi-two-dimensional electron gas, similar to the surface plasma anticipated by Emeleus and Coulter.^{15,16}

For $\chi > 0$, on the other hand, the conduction-band minimum is below the potential just outside. It is thus energetically favorable for electrons to accumulate inside the dielectric. This can be seen in Fig. 4, which shows the electron density and the potential in the refined ESL (red line) and simplified ESL (open green circles and blue triangles) for an Al₂O₃ surface. The surface potential consists of an attractive well in front of

TABLE I. Material parameters for the dielectrics considered in this work: dielectric constant ϵ_s , electron affinity χ , conduction-band effective mass m_C^* , valence-band effective mass m_V^* , and band gap E_g .

	ϵ_s	χ (eV)	m_C^* (m_e)	m_V^* (m_e)	E_g (eV)
MgO	9.8 [51]	-0.4 [28]	0.4 [52]		
Al ₂ O ₃	9.9 [53]	2.5 [54]	0.4 [55]	4.0 [55]	8.8 [56]
SiO ₂	3.78 [57]	1.3 [54]	0.5 [58]	0.58 [59]	9.2 [54]
GaAs	13.1 [60]	4.07 [60]	0.067 [60]	0.45 [60]	1.42 [60]

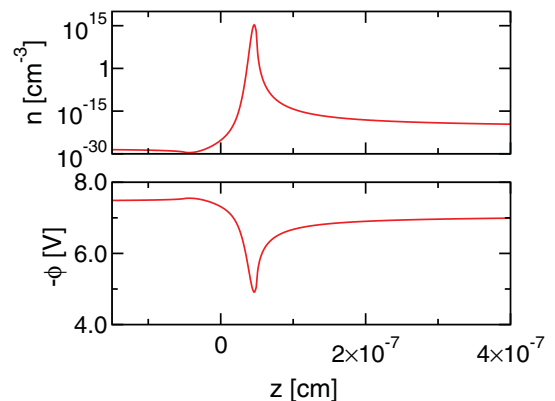


FIG. 3. (Color online) Plasma-supplied excess electron density n (upper panel) and the potential $-\phi$ (lower panel) it gives rise to, for a MgO surface in contact with a helium discharge with $n_0 = 10^7 \text{ cm}^{-3}$ and $k_B T_e = 2 \text{ eV}$ calculated without accounting for a SCR in the dielectric (crude ESL model). The cutoff of the interface region is $z_s = -z_0$. As can be seen, almost all of the plasma-induced wall charge is located in the well of the image potential in front of the surface.

the surface, but the minimum potential energy for electrons $-e\phi$ is reached inside the dielectric. Excess electrons coming from the plasma are thus mostly located inside the wall and the electron distribution extends deep into the bulk. This extended negative space charge also leads to a band bending near the surface. Note the different scales of the axes for the left and right panels of Fig. 4. On the scale where variations in the SCR are noticeable the ISR is basically a vertical line.

If one neglects the SCR and fills all excess electrons into the ISR (the crude ESL), the potential and the electron distribution

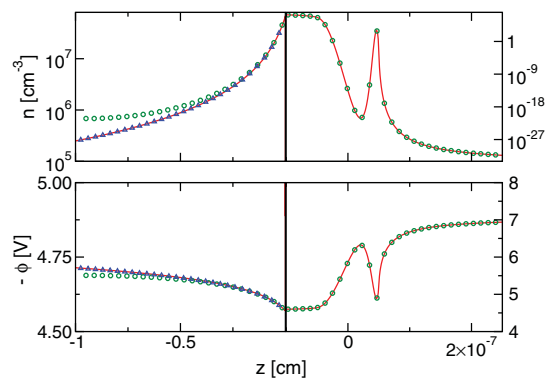


FIG. 4. (Color online) Plasma-supplied excess electron density n (upper panel) and the potential $-\phi$ (lower panel) it gives rise to, for an Al₂O₃ surface in contact with a helium discharge with $n_0 = 10^7 \text{ cm}^{-3}$ and $k_B T_e = 2 \text{ eV}$. The red lines show data obtained from the refined ESL model accounting for an ISR and a SCR, the boundary between the two was put at $z_s = -3z_0$, the green circles show data for a model which consists only of an ISR with cutoff $z_s = -0.9 \text{ cm}$ (crude ESL model), and the blue triangles show data for a model consisting only of a SCR for $z < 0$. Irrespective of the approximation, the plasma-induced wall charge extends deep into the bulk. Note the different scales of the axes for the left and right panels. On the spatial scale of the SCR shown in the left panels the ISR of the right panels becomes a vertical line.

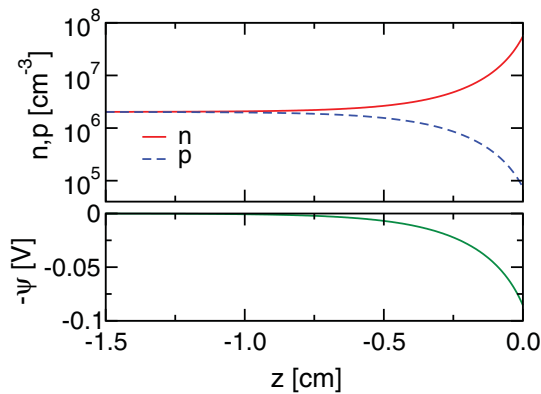


FIG. 5. (Color online) Electron density n and hole density p at a GaAs surface in contact with a helium discharge with $n_0 = 10^7 \text{cm}^{-3}$ and $k_B T_e = 2 \text{eV}$ calculated with the refined ESL model without ISR. The plasma-induced wall charge sits inside the GaAs wall. Deep inside the bulk charge neutrality is achieved by an equal density of electrons and holes.

are correctly described at and close to the surface but not far inside the dielectric (open green circles) because the *ad hoc* cutoff z_s of the crude ESL leads to an unphysical pileup of electrons near z_s . Hence, only if z_s is large enough does the crude ESL model give reliable results for the electron density and potential in the vicinity of the surface. Filling all electrons in the SCR, on the other hand, cannot describe the immediate vicinity of the surface correctly, which is however on the scale of the SCR an infinitesimally narrow region. It gives only for $z < -z_0$ a good description, that is, in the region where for $\chi > 0$ indeed most of the electrons are located (blue triangles).

While the crude ESL model containing only an ISR gives the correct electron density near the surface provided z_s is large enough, the merger of the ESL with the bulk can only be described with the refined ESL model including the SCR. This is particularly relevant for materials with smaller band gaps and larger intrinsic carrier concentrations than MgO, Al_2O_3 , and SiO_2 . To exemplify this we show in Fig. 5 the electron and hole densities (upper panel) as well as the potential $-\psi$ (lower panel) for a GaAs plasma wall, calculated for an ESL containing only a SCR. At the surface the electron density is about three orders of magnitude larger than the hole concentration. Thus, the gas phase plasma offers the possibility to manipulate the electron-hole plasmas by controlling the charge-carrier density—tantamount to doping—in the near surface region of a semiconductor. Deep inside the material, electron and hole concentrations are equal, leading to charge neutrality and a constant potential. The band bending due to the extended space charge in the ESL is about 0.09 eV.

Our results for the electron and hole densities and the potential in the dielectric depend of course on the model for the SCR. We have used for simplicity the model of an intrinsic semiconductor which is appropriate for an undoped semiconductor without impurities. Depending on doping or impurities a variety of models⁴² could be used to take material-specific aspects into account. In our exploratory calculation we obtain a rather wide SCR. Including the effect of impurities, acting as trapping sites in the band gap would probably reduce the depth of the SCR considerably.

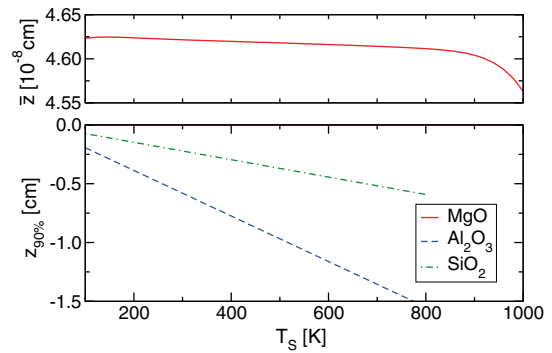


FIG. 6. (Color online) Center of gravity \bar{z} of the plasma-supplied excess electron distribution at a MgO surface (upper panel) and the $z_{90\%}$ value for the electron distribution at an Al_2O_3 and a SiO_2 surface (lower panel), all in contact with a helium discharge with $n_0 = 10^7 \text{cm}^{-3}$ and $k_B T_e = 2 \text{eV}$, as a function of the surface temperature T_s . The data shown in the upper and lower panel were obtained, respectively, from the crude ESL model and the refined ESL model without an ISR.

To summarize our results up to this point, we find that for negative electron affinity the plasma-induced electronic surface charge is located in front of the surface forming a quasi-two-dimensional electron gas, while for positive electron affinity the surplus electrons form a space-charge layer in the dielectric leading to a small bending of the energy bands.

The two distinct types of charge distributions in the ESL are also reflected in the dependence of the width of the plasma-supplied electron distribution on the surface temperature. Figure 6 shows the center of gravity \bar{z} of the electron distribution for the MgO surface ($\chi < 0$) and the $z_{90\%}$ value for the surfaces of Al_2O_3 and SiO_2 ($\chi > 0$), where $z_{90\%}$ is implicitly defined by

$$\int_{z_{90\%}}^0 dz [n(z) - p(z)] = 0.9N. \quad (60)$$

We use the $z_{90\%}$ value because it captures the depth of the SCR better than \bar{z} , which depends too strongly on the few electrons that penetrate very deep into the bulk.

For negative electron affinity (MgO, shown in the upper panel of Fig. 6) the external surface charge is strongly trapped in the deep image potential so that \bar{z} changes very little with surface temperature. The width of the internal surface charge for dielectrics with positive electron affinity (Al_2O_3 and SiO_2 , lower panel), however, increases dramatically with surface temperature. This can be understood as follows. The restoring force from the positive ions in the sheath binds internal surface charges only weakly to the surface. With increasing surface temperature, however, high-lying states in the conduction band get more and more populated. Hence, some electrons have rather high kinetic energies, are thus less confined near the surface by the weak restoring force, and penetrate therefore deeper into the bulk. As a result, the $z_{90\%}$ value decreases strongly with surface temperature.

Let us now turn to the discussion of the influence of the electron temperature $k_B T_e$ and the plasma density n_0 on the properties of the ESL. These two parameters enter through the total surface density of electrons N depleting the sheath

TABLE II. Surface density of electrons in the ESL N , wall potential ϕ_w , plasma sheath ESL boundary z_0 , and the $z_{90\%}$ value for SiO₂ in contact with a helium discharge with $k_B T_e = 2$ eV for different values of the plasma density n_0 .

n_0 (10^6cm^{-3})	N (10^6cm^{-2})	ϕ_w (V)	z_0 (10^{-5}cm)	$z_{90\%}$ (cm)
10	4.38	-7.07	5.14	-0.222
20	6.20	-7.07	4.32	-0.157
50	9.80	-7.07	3.44	-0.099
100	13.9	-7.07	2.89	-0.070

and accumulating in the ESL. How $k_B T_e$ and n_0 affect the interface depends therefore on the sheath model and the model used for the interaction between plasma particles and the surface. For simplicity we have used a collisionless sheath model and assumed the surface to be a perfect absorber for plasma electrons and ions. The results for the properties of the ESL as a function of the plasma parameters are thus to be taken as only indicative.

The effect of a variation of n_0 and $k_B T_e$ is most significant for surfaces with positive electron affinity. Table II shows the effect of the plasma density n_0 for a SiO₂ surface. If n_0 increases, the boundary z_0 between sheath and ESL moves closer to the surface. This, however, does not affect the charge distribution much as most of the electrons occupy the SCR inside the dielectric (as shown in Fig. 4 for Al₂O₃). More important is the fact that an increase in n_0 leads to an increase of the total surface electron density N . This entails a stronger restoring force from the plasma sheath so that the potential well confining the space charge inside the dielectric becomes steeper and the electrons in the SCR of the ESL are shifted toward the surface; in other words, the $z_{90\%}$ value increases with n_0 . Mathematically, the steplike shape of the electron distribution arises because a larger N leads through Eq. (57) to a larger η_s which makes the potential steeper at the surface so

TABLE III. Surface density of electrons in the ESL N , wall potential ϕ_w , plasma sheath ESL boundary z_0 , and the $z_{90\%}$ value for SiO₂ in contact with a helium discharge at $n_0 = 10^7 \text{cm}^{-3}$ for different values of the electron temperature $k_B T_e$.

$k_B T_e$ (eV)	N (10^6cm^{-2})	ϕ_w (V)	z_0 (10^{-5}cm)	$z_{90\%}$ (cm)
0.5	2.19	-1.77	7.27	-0.444
1	3.10	-3.53	6.11	-0.314
2	4.38	-7.07	5.14	-0.222
5	6.93	-17.7	4.086	-0.140

that the electron distribution is more peaked there. This trend can be seen in the lower panel for Fig. 7.

A variation of the electron temperature $k_B T_e$ has similar effects as the variation of the plasma density. If $k_B T_e$ increases, the total surface density of electrons increases also, as can be seen from Table III. As shown in the upper panel of Fig. 7, this leads again to a steplike electron distribution which is more concentrated at the surface the higher the electron temperature is.

For a surface with negative electron affinity (MgO) the surplus electrons are strongly bound in the image potential. While a variation of $k_B T_e$ or n_0 changes the total number of surplus electrons per unit area in the same way as for a surface with positive electron affinity, the distribution of the surplus electrons within the ESL is not affected significantly because of the strong image interaction.

So far we have shown the potential and the electron distribution in the ESL. Now, we will compare potential and charge distribution in the ESL with the ones in the plasma sheath. The electron distribution at the interface is the quasistationary electron gas on top of the charge redistribution due to the truncation of the solid that guarantees flux equality at the sheath-ESL boundary z_0 . As already mentioned, not included in this simple model is the flux of plasma electrons and ions in the ESL before the electrons are trapped at the surface and the ions recombine with the negative wall charge. The electron and ion densities in this model are thus discontinuous at z_0 . The potential, however, which has been obtained from the integration of Poisson's equation is continuous and differentiable everywhere. Between the well of the image potential and z_0 the electron and ion flux from the sheath would be important. The neglect of the charge densities associated with these fluxes does however not affect the potential because they are too small to have a significant effect.

Figure 8 shows the ESL and the plasma sheath in front of a MgO surface. Due to the negative electron affinity, the plasma-supplied surface electrons are bound by the image potential in front of the surface. In Fig. 8, we plot the electron and ion density (upper panel), as well as the electric potential (lower panel) over the distance from the surface z . Far from the surface, the potential approaches the bulk plasma value chosen to be zero. In the sheath the potential develops a Coulomb barrier and reaches the wall potential ϕ_w at z_0 , the distance where the sheath merges with the surface layer (vertical dotted line). The wall potential is the potential just outside to which the energies of the bulk states are referenced. Closer to the surface the potential follows the attractive image

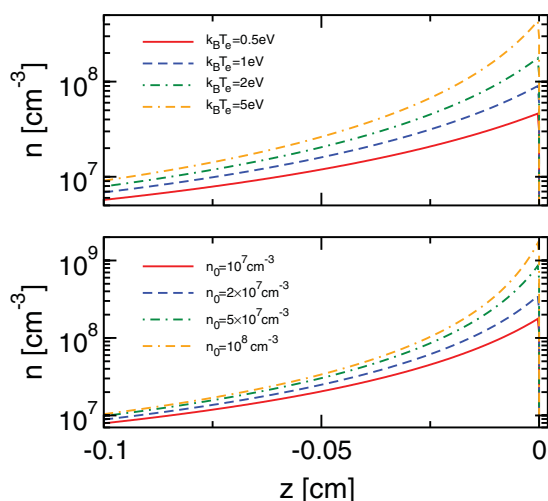


FIG. 7. (Color online) Plasma-supplied surplus electron density n at a SiO₂ surface in contact with a helium discharge as a function of the electron temperature (upper panel, $n_0 = 10^7 \text{cm}^{-3}$) and the plasma density (lower panel, $k_B T_e = 2$ eV) for $T_s = 300$ K. The refined ESL model without an ISR was employed to produce the data.

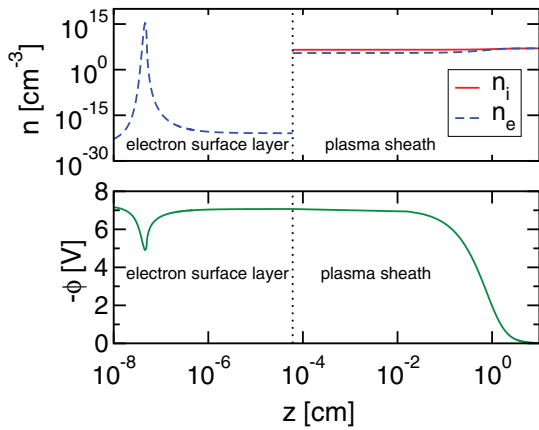


FIG. 8. (Color online) Density of plasma-supplied surplus electrons trapped in the ESL as well as electron and ion density in the plasma sheath (upper panel) and potential (lower panel) for a MgO surface in contact with a helium discharge ($n_0 = 10^7 \text{ cm}^{-3}$ and $k_B T_e = 2 \text{ eV}$). The data were obtained from the crude ESL model.

potential while at the surface the repulsive potential due to the negative electron affinity prevents the electron from entering the dielectric (only scarcely seen on the scale of the figure).

In Fig. 9 we finally plot the electron and ion densities (upper panel) as well as the electric potential (lower panel) for SiO₂. Note the linear z axis in contrast to the logarithmic z axis of Fig. 8. Due to the positive electron affinity, the excess electrons constituting the wall charge penetrate deep into the dielectric and occupy therefore the SCR of the ESL. Compared to the variation of the electric potential in the sheath the band bending in the dielectric induced by the wall charge is rather small, as indicated by the variation of ϕ inside the dielectric. This is because ϵ is large and the width of the SCR is narrow on the scale of the sheath. Only on the scale of the ISR (a vertical line at $z = 0$), the SCR of the ESL is wide.

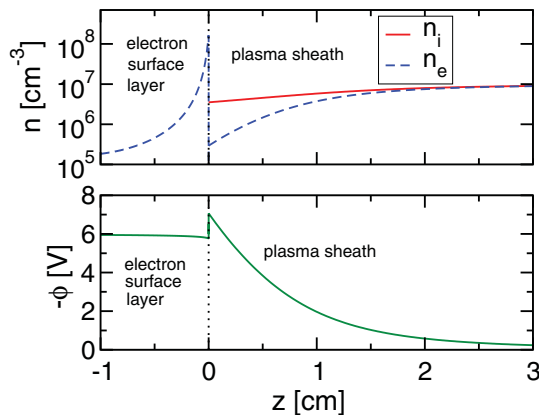


FIG. 9. (Color online) Density of plasma-supplied excess electrons in the ESL as well as electron and ion density in the plasma sheath (upper panel) and potential (lower panel) for a SiO₂ surface in contact with a helium discharge ($n_0 = 10^7 \text{ cm}^{-3}$ and $k_B T_e = 2 \text{ eV}$). The refined ESL model without an ISR was employed to produce the data.

V. CONCLUSIONS

We have studied the potential and the charge distribution across the interface of a plasma and a dielectric wall, treating the plasma-induced wall charge as a quasistationary electron gas trapped by and in thermal equilibrium with the dielectric. Our approach is based on a model for a graded surface including the offset between the potential just outside the dielectric and the conduction-band minimum arising from the redistribution of charge due to the truncation of the solid as well as the image potential due to the dielectric mismatch at the boundary. The missing electrons from the sheath populate the interface potential and thereby form an electron surface layer (ESL) which minimizes the grand canonical potential of wall-thermalized excess electrons and satisfies Poisson's equation.

Within this model the boundary between the plasma sheath and the ESL is given by the distance from the crystallographic interface where the potential for the excess electrons turns from the repulsive sheath potential into the attractive surface potential. This distance is typically on the order of a micron. It gives the position of an effective wall for plasma electrons and ions and thus of the portion of the ESL which lays in front of the surface. Most of the surplus electrons trapped in the ESL, that is, the plasma-induced wall charge, will be, however, much closer to the surface or even inside the dielectric depending on the electron affinity.

We presented numerical results for the potential and the distribution of the plasma-supplied surplus electrons at the interface between a helium discharge and the surfaces of MgO, Al₂O₃, and SiO₂, respectively. The electron distribution within the ESL strongly depends on the electron affinity. For negative electron affinity, the conduction-band minimum is above the potential just outside the dielectric. Hence, it is energetically unfavorable for electrons to penetrate into the bulk and the surface electrons are bound in the image potential in front of the surface. In this case, their spatial profiles change little over a variation of the surface temperature or the plasma parameters. For positive electron affinity the conduction-band minimum is below the potential just outside the dielectric and the surface-bound electrons accumulate inside the wall. The space charge in the bulk broadens if the surface temperature is increased and becomes more peaked if the total surface density of the electrons missing in the sheath is raised through an increase in either the plasma density or the electron temperature.

Separating the ESL into an interface-specific and a space-charge region and modeling the bulk of the dielectric as an intrinsic semiconductor, we also investigated how the ESL merges with the bulk of the dielectric. This is particularly important for dielectrics with small energy gaps and positive electron affinities, where excess electrons coming from the sheath accumulate not in the image potential in front of the surface but deep inside the wall. In this case the wall charge may also induce a significant band bending.

Whereas the crude ESL model we proposed neglects the space charge deep inside the bulk of the wall and is thus only applicable to large band-gap dielectrics with negative electron affinity, where basically the whole plasma-induced wall charge is trapped in the image potential in front of the

surface, the refined ESL model, keeping the interface-specific region as well as the space-charge region of the ESL, provides a quantitative description of the whole spatial structure of the extended charge double layer which forms at a dielectric plasma wall as a result of the electrons in the ESL and the positive space charge in the plasma sheath.

The ESL can be regarded as that part of the plasma sheath which is inside the plasma wall. It is thus the ultimate boundary of a bounded gas discharge and constitutes, depending on

the electron affinity, either a quasi-two-dimensional electron plasma in front of the wall or an electron(-hole) plasma inside the wall.

ACKNOWLEDGMENTS

This work was supported by the Deutsche Forschungsgemeinschaft through Projects No. B10 and No. A5 of the transregional collaborative research center SFB/TRR 24.

- ¹O. Ishihara, *J. Phys. D: Appl. Phys.* **40**, R121 (2007).
- ²V. E. Fortov, A. V. Ivlev, S. A. Khrapak, A. G. Khrapak, and G. E. Morfill, *Phys. Rep.* **421**, 1 (2005).
- ³D. A. Mendis, *Plasma Sources Sci. Technol.* **11**, A219 (2002).
- ⁴U. Kogelschatz, *Plasma Chem. Plasma Process.* **23**, 1 (2003).
- ⁵L. Stollenwerk, S. Amiranashvili, J.-P. Boeuf, and H.-G. Purwins, *Phys. Rev. Lett.* **96**, 255001 (2006).
- ⁶L. Stollenwerk, J. G. Laven, and H.-G. Purwins, *Phys. Rev. Lett.* **98**, 255001 (2007).
- ⁷R. Dussart *et al.*, *Eur. Phys. J. D* **60**, 601 (2010).
- ⁸C. J. Wagner, P. A. Tcherchian, and J. G. Eden, *Appl. Phys. Lett.* **97**, 134102 (2010).
- ⁹K. H. Becker, K. H. Schoenbach, and J. G. Eden, *J. Phys. D: Appl. Phys.* **39**, R55 (2006).
- ¹⁰N. P. Ostrom and J. G. Eden, *Appl. Phys. Lett.* **87**, 141101 (2005).
- ¹¹M. J. Kushner, *J. Phys. D: Appl. Phys.* **38**, 1633 (2005).
- ¹²R. N. Franklin, *Plasma Phenomena in Gas Discharges* (Clarendon, Oxford, 1976).
- ¹³M. A. Lieberman and A. J. Lichtenberg, *Principles of Plasma Discharges and Materials Processing* (Wiley-Interscience, New York, 2005).
- ¹⁴K.-U. Riemann, *J. Phys. D: Appl. Phys.* **24**, 493 (1991).
- ¹⁵K. G. Emeleus and J. R. M. Coulter, *Int. J. Electron.* **62**, 225 (1987).
- ¹⁶K. G. Emeleus and J. R. M. Coulter, *IEEE Proceedings A Science Measurement and Technology* **135**, 76 (1988).
- ¹⁷J. F. Behnke, T. Bindemann, H. Deutsch, and K. Becker, *Contrib. Plasma Phys.* **37**, 345 (1997).
- ¹⁸D. Uhrlandt, M. Schmidt, J. F. Behnke, and T. Bindemann, *J. Phys. D: Appl. Phys.* **33**, 2475 (2000).
- ¹⁹Y. B. Golubovskii, V. A. Maiorov, J. Behnke, and J. F. Behnke, *J. Phys. D: Appl. Phys.* **35**, 751 (2002).
- ²⁰F. X. Bronold, H. Deutsch, and H. Fehske, *Eur. Phys. J. D* **54**, 519 (2009).
- ²¹R. L. Heinisch, F. X. Bronold, and H. Fehske, *Phys. Rev. B* **81**, 155420 (2010).
- ²²R. L. Heinisch, F. X. Bronold, and H. Fehske, *Phys. Rev. B* **82**, 125408 (2010).
- ²³F. X. Bronold, R. L. Heinisch, J. Marbach, and H. Fehske, *IEEE Trans. Plasma Sci.* **39**, 644 (2011).
- ²⁴R. L. Heinisch, F. X. Bronold, and H. Fehske, *Phys. Rev. B* **83**, 195407 (2011).
- ²⁵F. X. Bronold, H. Fehske, H. Kersten, and H. Deutsch, *Phys. Rev. Lett.* **101**, 175002 (2008).
- ²⁶M. W. Cole and M. H. Cohen, *Phys. Rev. Lett.* **23**, 1238 (1969).
- ²⁷B. Baumeier, P. Kruger, and J. Pollmann, *Phys. Rev. B* **76**, 205404 (2007).
- ²⁸M. Rohlfing, N.-P. Wang, P. Kruger, and J. Pollmann, *Phys. Rev. Lett.* **91**, 256802 (2003).
- ²⁹V. M. Silkin, J. Zhao, F. Guinea, E. V. Chulkov, P. M. Echenique, and H. Petek, *Phys. Rev. B* **80**, 121408(R) (2009).
- ³⁰V. M. Silkin, E. V. Chulkov, and P. M. Echenique, *Phys. Rev. B* **60**, 7820 (1999).
- ³¹U. Hoefler, I. L. Shumay, C. Reuss, U. Thomann, W. Wallauer, and T. Fauster, *Science* **277**, 1480 (1997).
- ³²T. Fauster, *Appl. Phys. A* **59**, 479 (1994).
- ³³F. Stern, *Phys. Rev. B* **17**, 5009 (1978).
- ³⁴F. Stern and S. DasSarma, *Phys. Rev. B* **30**, 840 (1984).
- ³⁵J. Planelles and J. L. Movilla, *Phys. Rev. B* **73**, 235350 (2006).
- ³⁶E. E. Tkharev and A. L. Danilyuk, *Vacuum* **35**, 183 (1985).
- ³⁷N. D. Mermin, *Phys. Rev.* **137A**, 1441 (1965).
- ³⁸W. Kohn and L. J. Sham, *Phys. Rev.* **140A**, 1133 (1965).
- ³⁹R. O. Jones and O. Gunnarson, *Rev. Mod. Phys.* **61**, 689 (1989).
- ⁴⁰P. J. Jennings, R. O. Jones, and M. Weinert, *Phys. Rev. B* **37**, 6113 (1988).
- ⁴¹A. V. Gavrilenko, C. S. McKinney, and V. I. Gavrilenko, *Phys. Rev. B* **82**, 155426 (2010).
- ⁴²H. Lüth, *Solid Surfaces, Interfaces and Thin Films* (Springer-Verlag, Berlin, 1992).
- ⁴³R. T. Tung, *Mater. Sci. Eng.* **R35**, 1 (2001).
- ⁴⁴D. Cahen and A. Kahn, *Adv. Mater.* **15**, 271 (2003).
- ⁴⁵F. J. Himpsel, J. A. Knapp, J. A. VanVechten, and D. E. Eastman, *Phys. Rev. B* **20**, 624 (1979).
- ⁴⁶K. P. Loh, I. Sakaguchi, M. N. Gamo, S. Tagawa, T. Sugino, and T. Ando, *Appl. Phys. Lett.* **74**, 28 (1999).
- ⁴⁷J. B. Cui, J. Ristein, and L. Ley, *Phys. Rev. Lett.* **81**, 429 (1998).
- ⁴⁸F. Maier, J. Ristein, and L. Ley, *Phys. Rev. B* **64**, 165411 (2001).
- ⁴⁹J. D. Jackson, *Classical Electrodynamics* (Wiley, New York, 1998).
- ⁵⁰N. W. Ashcroft and N. D. Mermin, *Solid State Physics* (Saunders College Publ., Philadelphia, 1976).
- ⁵¹M. Wintersgill, J. Fontanella, C. Andeen, and D. Schuele, *J. Appl. Phys.* **50**, 8259 (1979).
- ⁵²W. H. Butler, X.-G. Zhang, T. C. Schulthess, and J. M. MacLaren, *Phys. Rev. B* **63**, 054416 (2001).
- ⁵³M. Schubert, T. E. Tiwald, and C. M. Herzinger, *Phys. Rev. B* **61**, 8187 (2000).
- ⁵⁴E. Bersch, S. Rangan, R. A. Bartynski, E. Garfunkel, and E. Vescovo, *Phys. Rev. B* **78**, 085114 (2008).

⁵⁵T. V. Perevalov, A. V. Shaposhnikov, V. A. Gritsenko, H. Wong, J. H. Han, and C. W. Kim, *JETP Lett.* **85**, 165 (2007).
⁵⁶R. H. French, *J. Am. Ceram. Soc.* **73**, 477 (1990).
⁵⁷Y. D. Glinka and M. Jaroniec, *J. Appl. Phys.* **82**, 3499 (1997).

⁵⁸R. Ludeke, H. J. Wen, and A. Schenk, *Appl. Phys. Lett.* **73**, 1221 (1998).
⁵⁹R. K. Chanana, *J. Appl. Phys.* **109**, 104508 (2011).
⁶⁰B. van Zeghbroeck, *Principles of Semiconductor Devices and Heterojunctions* (Prentice-Hall, Upper Saddle River, 2010).

Phonon-mediated desorption of image-bound electrons from dielectric surfaces

R. L. Heinisch, F. X. Bronold, and H. Fehske

Institut für Physik, Ernst-Moritz-Arndt-Universität Greifswald, 17489 Greifswald, Germany

(Received 26 January 2010; revised manuscript received 5 March 2010; published 8 April 2010)

A complete kinetic modeling of an ionized gas in contact with a surface requires the knowledge of the electron desorption time and the electron sticking coefficient. We calculate the desorption time for phonon-mediated desorption of an image-bound electron as it occurs, for instance, on dielectric surfaces where desorption channels involving internal electronic degrees of freedom are closed. Because of the large depth of the polarization-induced surface potential with respect to the Debye energy, multiphonon processes are important. To obtain the desorption time, we use a quantum-kinetic rate equation for the occupancies of the bound-electron surface states, taking two-phonon processes into account in cases where one-phonon processes yield a vanishing transition probability as it is sufficient, for instance, for graphite. For an electron desorbing from a graphite surface at 360 K, we find a desorption time of 2×10^{-5} s. We also demonstrate that depending on the potential depth and bound-state level spacing, the desorption scenario changes. In particular, we show that desorption via cascades over bound states dominates unless direct one-phonon transitions from the lowest bound state to the continuum are possible.

DOI: [10.1103/PhysRevB.81.155420](https://doi.org/10.1103/PhysRevB.81.155420)

PACS number(s): 52.40.Hf, 73.20.-r, 68.43.Nr

I. INTRODUCTION

Whenever at the surface of a solid the vacuum level falls inside an energy gap, that is, whenever the electron affinity of the surface is negative, polarization-induced external surface states (image states) exist as it is known from macroscopic electrodynamics.¹ Originally predicted² for the surfaces of liquid and solid He, Ne, H₂, and D₂, the existence of image states has by now been experimentally verified for a great number of metallic^{3–11} as well as insulating^{12–14} surfaces. In addition, there exist a variety of dielectric materials, for instance, diamond,^{15–17} boron nitride,¹⁸ and alkali-earth metal oxides,^{19–21} which have surfaces with a negative electron affinity. They should thus support image states. Interesting in this respect are also electronegative dielectric structures used in electron emitting devices such as cesium-doped silicon oxide films^{22–24} and GaAs-based heterostructures.^{25–27}

In contrast to intrinsic surface states,²⁸ originating either from the abrupt disappearance of the periodic lattice potential or unsaturated bonds at the surface, image states are not localized at the edge but typically a few Å in front of the solid. An external electron approaching the solid from the vacuum with a kinetic energy below the lowest unoccupied intrinsic electron state of the surface may thus get trapped (adsorbed) in these states provided it can get rid of its excess energy. Once it is trapped, it may detrap again (desorb) if it gains enough energy from the solid. Hence, in addition to elastic and inelastic scatterings, the interaction of low-energy electrons with surfaces may encompass physisorption—the polarization-induced temporary binding of an electron to the surface.

Unlike physisorption of neutral atoms and molecules, which has been studied in great detail ever since the seminal works of Lennard-Jones and collaborators,^{29–38} physisorption of electrons has been hardly investigated. It is only until recently that we pointed out^{39,40} that the charging of surfaces in contact with an ionized gas, as it occurs, for instance, in

the interstellar medium,^{41–43} in the upper atmosphere,⁴⁴ in dusty laboratory plasmas,^{45,46} and in dielectrically bounded low-temperature plasmas,^{47–52} could be perhaps microscopically understood as an electronic physisorption process.

Parameters characterizing physisorption of electrons at surfaces are the electron sticking coefficient s_e and the electron desorption time τ_e . Little is quantitatively known about these parameters, although they are rather important for a complete kinetic description of bounded gas discharges (as it is in fact also the case for the sticking coefficient and desorption time of neutral particles which play a central role for the kinetic modeling of bounded neutral gases^{53–55}). Very often, s_e and τ_e are simply used as adjustable parameters.

In view of the importance of s_e and τ_e for bounded plasmas, we adopted in Ref. 40 the quantum-kinetic approach originally developed for the theoretical description of physisorption of neutral particles^{37,38} to calculate s_e and τ_e for a metallic surface. Neglecting crystal-induced surface states and describing the metal within the jellium model, we obtained for an ideal surface with a classical image potential $s_e \approx 10^{-4}$ and $\tau_e \approx 10^{-2}$ s. Although s_e seems to be rather small, the product $s_e \tau_e \approx 10^{-6}$ s, which is the order of magnitude we expected from our study of charging of dust particles in low-temperature plasmas.³⁹

Physisorption of an external electron implies energy exchange between the electron and the electronic and/or vibrational elementary excitations of the surface. For a metallic surface, creation and annihilation of internal electron-hole pairs seem to be the main reason for electron energy relaxation at the surface.^{56,57} For a dielectric surface, however, the typical energy of an internal electron-hole pair is of the order of the energy gap, that is, for the dielectrics we are interested in, a few electron volts. For typical surface temperatures, this is way too large for electron-hole pairs to cause energy relaxation at the surface. At dielectric surfaces, it has to be rather the creation and annihilation of phonons which lead to electron energy relaxation.

For dielectrics with a large dielectric constant and a large energy gap, the level spacing of the two lowest states in the

TABLE I. Material parameters for graphite.

Debye temperature	T_D	2500 K
Dielectric constant	ϵ_s	13.5
TO phonon energy	$\hbar\omega_T$	170 meV
Grüneisen parameter	γ_G	1.7
Shear modulus	μ	5 GPa

(polarization-induced) surface potential turns out to exceed the maximum phonon energy, which is, within the Debye model, the Debye energy. Hence, in contrast to physisorption of neutral particles, which typically involves a few bound states with energy spacings not exceeding the Debye energy,³⁷ physisorption of electrons at (this type of) dielectric surfaces takes place in a deep potential supporting deep bound states whose energy spacings may be larger than the Debye energy. Relaxation channels involving internal electronic degrees of freedom being closed, because of the large gap, electron energy relaxation, and hence sticking and desorption of electrons have to be controlled by multiphonon processes.

Typical dielectric plasma boundaries are, in dusty plasmas,^{45,46} graphite and melamine-formaldehyde and in dielectric barrier discharges^{47–52} Duran glass, silicon dioxide, and aluminum oxide. We suspect on empirical grounds that plasma boundaries always support image states, if not intrinsically then due to chemical contamination from the discharge. Based on this hypothesis, we investigate in the following, employing a simple model for the polarization-induced interaction between an electron and a dielectric surface,^{58,59} the desorption of an image-bound electron from a dielectric surface. We are particularly interested in how multiphonon processes affect the competition between direct desorption, that is, the direct transition between bound and unbound surface states, and cascading desorption,³⁵ that is, the successive climbing up of the ladder of bound surface states until the continuum is reached.

For the plasma boundaries just mentioned, image states have been so far only observed for graphite¹³ (see Table I for the relevant material parameters). Surprisingly, the measured binding energy of the lowest image state, $E_1^{\text{exp}} \approx -0.85$ eV, is lower than the energy of the lowest bound state in the classical image potential, which should be in fact a lower bound.² Indeed, for $\epsilon_s = 13.5$, the dielectric constant of graphite, $E_1^{\text{cl}} \approx -0.63$ eV. Taking either E_1^{exp} or E_1^{cl} in conjunction with $\hbar\omega_D \approx 0.22$ eV, the Debye energy for graphite, 3.9 or 2.9 phonons would be required for a direct transition to the continuum. The probability for an electron to detrapp from the lowest image state of graphite via such a transition would be accordingly small. Cascades using higher-lying bound states as intermediaries should therefore become rather important. Indeed, for neutral particles, the enhancement of the desorption rate via cascades has been investigated by Gortel *et al.*³⁵ for phonon-mediated desorption from a physisorbed state and by Misewich *et al.*⁶⁰ for desorption from a chemisorbed state via repetitive electronic transitions.

In the case of a cascade, the largest energy difference an image-bound electron has to overcome is the one between

the two lowest bound states. Using the classical image potential for graphite, this difference would be 0.47 eV, implying that at most 2.35 phonons are required for getting a cascade running from the lowest level. Hence, for graphite, with its rather high Debye energy, the number of phonons involved in physisorption of electrons is small enough to use it as an expansion parameter for the transition probability. Taking moreover the recoil energy into account, the dipole-active elementary excitation responsible for the polarization-induced surface potential imparts onto the external electron,⁵⁹ two-phonon processes even turn out to suffice. The other dielectrics have a much smaller Debye energy. The number of phonons involved is thus much larger. Instead of a brute force expansion, other approaches seem to be more suitable in these cases.^{61–65}

The outline of the remaining paper is as follows. First, in Sec. II, we set up the quantum-kinetic rate equation for the occupancies of bound surface states and introduce a classification scheme for the depth of the surface potential. In Sec. III, we describe the microscopic model for the electron-surface interaction, including the static part which provides the surface states involved in physisorption and the dynamic part which drives the transitions between these states and is thus responsible for desorption. In Sec. IV, we calculate the transition probability up to fourth order in the displacement field, thereby taking one- and two-phonon processes into account, which we believe to be sufficient for graphite. This calculation is very lengthy⁶⁶ and cannot be totally reproduced here. Appendixes A–C provide the required mathematical details. Finally, in Sec. V, we present and discuss our results before we conclude in Sec. VI.

II. DESORPTION FROM MANY BOUND STATES

Following Gortel *et al.*,³⁵ the kinetics in a manifold of bound surface states can be described by a quantum-kinetic rate equation. Assuming that once the electron is in an unbound surface state, it is immediately pushed away from the surface, which is reasonable if we consider the electron as a test electron desorbing from a negatively charged surface (see Ref. 40 for more details). The time evolution of the occupancies of the bound surface states for the (test) electron is given by³⁵

$$\frac{d}{dt}n_q(t) = \sum_{q'} [W_{qq'}n_{q'}(t) - W_{q'q}n_q(t)] - W_{cq}n_q(t), \quad (1)$$

where $W_{qq'}$ is the probability for a transition from state q' to state q and $W_{cq} = \sum_k W_{kq}$ is the probability for a transition from the bound state q to the continuum. In compact matrix notation, Eq. (1) may be rewritten as

$$\frac{d}{dt}\mathbf{n} = \mathbf{T}\mathbf{n}, \quad (2)$$

where \mathbf{n} is the N -dimensional column vector of the occupancies of the bound surface states and \mathbf{T} is the matrix of the transition probabilities.

To determine the formal solution of this equation,

$$\mathbf{n}(t) = \exp[\mathbf{T}t]\mathbf{n}(0), \quad (3)$$

the eigenvalue equation for the matrix \mathbf{T} has to be solved. In general, \mathbf{T} is not symmetric. Thus, there are right and left eigenvectors,³⁵ \mathbf{e}^κ and $\tilde{\mathbf{e}}^\kappa$, respectively, which can be chosen to be orthogonal to each other. In terms of the right eigenvectors of \mathbf{T} ,

$$\mathbf{n}(t) = \sum_{\kappa} f^\kappa e^{-\lambda_\kappa t} \mathbf{e}^\kappa, \quad (4)$$

where the coefficients f^κ are determined by decomposing the initial distribution into eigenfunctions according to

$$\mathbf{n}(0) = \sum_{\kappa} f^\kappa \mathbf{e}^\kappa. \quad (5)$$

Due to the losses to the continuum all eigenvalues, $-\lambda_\kappa$ turn out to be negative.³⁵ Hence, for sufficiently long times, the image-bound electron escapes into the continuum and the bound-state occupation vanishes, i.e., $n_q(t \rightarrow \infty) = 0 \quad \forall q$. If the transitions leading to losses to the continuum are much slower than the transitions between bound states, i.e., $W_{cq} \ll W_{qq'}$, the bound electron evaporates slowly into the continuum. One eigenvalue, λ_0 , is then considerably smaller than all the others and its right eigenvector corresponds to the equilibrium distribution $n_q^{\text{eq}} = e_q^0$. The general solution (4) can then be split into two terms³⁵

$$n_q(t) = f^0 e_q^0 e^{-\lambda_0 t} + \sum_{\kappa > 0} f^\kappa e_q^\kappa e^{-\lambda_\kappa t}, \quad (6)$$

where the first term gives the time evolution for an equilibrium occupation of the bound states whereas the second term describes the fast equilibration of a distortion of the equilibrium occupation at the beginning of the desorption process. It is subject to much faster transitions which will be completed soon after the beginning of the desorption process. Since the fate of the electron for long times depends only on the equilibrium occupation, we identify the inverse of the desorption time with the lowest eigenvalue

$$\tau_e^{-1} = \lambda_0. \quad (7)$$

This conceptual framework of desorption requires surface states and transition probabilities between them as input. For dielectric surfaces, the transitions are driven by phonons whose energy scale, within the Debye model, is the Debye energy $\hbar\omega_D = k_B T_D$. Important parameters characterizing the potential depth are then

$$\epsilon_q = \frac{E_q}{\hbar\omega_D} \quad \text{and} \quad \Delta_{qq'} = \frac{E_q - E_{q'}}{\hbar\omega_D}, \quad (8)$$

where $E_q < 0$ denotes the energy of the q th bound state. We call the surface potential shallow if the lowest bound state is at most one Debye energy beneath the continuum, i.e., $\epsilon_1 > -1$, one-phonon deep if the energy difference between the lowest two bound states is less than one Debye energy, i.e., $\Delta_{12} > -1$, and two-phonon deep if the energy difference between the lowest two bound states is between one and two Debye energies, i.e., $-1 > \Delta_{12} > -2$.

Shallow and one-phonon-deep potentials are typical for physisorption of neutral atoms and molecules. Because of the strong polarization-induced interaction between an external electron and a surface, physisorption of electrons, however, typically takes place in at least two-phonon-deep surface potentials. Multiphonon processes should thus play an important role.

III. ELECTRON-SURFACE INTERACTION

An electron in front of a solid surface feels a polarization-induced attraction to the surface because of the coupling to dipole-active excitations of the solid. Leaving aside interband electronic excitations, which primarily affect the static dielectric constant, the relevant modes for a dielectric material are optical surface phonons.^{58,59}

If, for a dielectric solid with negative electron affinity, the kinetic energy of an external electron is less than the negative of the electron affinity, the electron cannot enter the solid, which, for the purpose of the calculation, we assume to fill the whole left half space ($z \leq 0$), being terminated at $z = 0$ with a surface whose lateral extension A is eventually made infinitely large. Evans and Mills⁵⁹ studied this situation by variational means. They found that far from the surface, the interaction potential is the classical image potential known from elementary electrostatics but close to the surface, the interaction potential is strongly modified by the recoil energy resulting from the momentum transfer parallel to the surface when the electron absorbs or emits a (dipole-active) surface phonon.

The recoil energy makes the interaction potential not only nonlocal for distances less than the bulk polaron radius $z_s = \sqrt{\hbar/2m\omega_s}$, where m is the mass of the electron, ϵ_s is the static dielectric constant, and $\omega_s = \omega_T \sqrt{(1 + \epsilon_s)/2}$ is the frequency of the surface phonon (ω_T is the TO-phonon frequency). Most importantly, it makes the interaction potential finite at the surface, in contrast to the singular behavior of the classical image potential. Denoting the lateral two-dimensional momentum transfer by \vec{K} , the simplest regular local approximation to the true interaction potential is⁵⁹

$$V(z) = -e^2 \frac{\epsilon_s - 1}{\epsilon_s + 1} \frac{\pi}{A} \sum_{\vec{K}} \frac{1}{K} \frac{e^{-2K|z|}}{1 + \frac{\hbar}{2m\omega_s} K^2}, \quad (9)$$

where K is the magnitude of the vector \vec{K} . It can be considered as a dynamically corrected classical image potential. Indeed, neglecting in the denominator the recoil energy, $\hbar K^2/2m$, the integral over \vec{K} can be easily performed and leads to

$$V_{\text{cl}}(z) = -\frac{e^2}{4} \frac{\epsilon_s - 1}{\epsilon_s + 1} \frac{1}{z}, \quad (10)$$

which is the classical image potential.

The dynamically corrected image potential (9) is attractive. The solution of the corresponding Schrödinger equation will thus yield bound and unbound surface states. To make an analytical solution feasible, we fit the dynamically corrected image potential (9) to a $1/z$ potential that is shifted

along the z axis. Forcing the two potentials to coincide at the surface, that is, at $z=0$, we obtain

$$V(z) \approx -\frac{e^2 \epsilon_s - 1}{4 \epsilon_s + 1} \frac{1}{z + z_c}, \quad (11)$$

with $z_c = z_s/\pi$. After the transformation $z \rightarrow z - z_c$, the Schrödinger equation corresponding to the shifted surface potential reads, in dimensionless variables $x = z/a_B$ and $\eta = 2\hbar^2 E/me^4$,

$$\phi''(x) + \left(\frac{2\Lambda_0}{x} + \eta \right) \phi(x) = 0, \quad (12)$$

where $a_B = \hbar^2/me^2$ is the Bohr radius and $\Lambda_0 = (\epsilon_s - 1)/4(\epsilon_s + 1)$. Assuming that electrons cannot enter the dielectric surface, we solve Eq. (12) with the boundary condition $\phi(x_c) = 0$, where $x_c = z_c/a_B$. The wave functions and energies for bound and unbound surface states, together with the additional boundary conditions we have to impose on them, are given in Appendix A.

Transitions between the eigenstates are due to dynamic perturbations of the surface potential. The surface potential is very steep near the surface. A strong perturbation arises therefore from the longitudinal-acoustic phonon perpendicular to the surface which causes the surface plane to oscillate.

Including this type of surface vibrations and using the eigenstates of Eq. (12) as a basis, the Hamiltonian for the surface electron can be split into three parts

$$H = H_e^{\text{static}} + H_{ph}^0 + H_{e-ph}^{\text{dyn}}, \quad (13)$$

where the first term is the Hamiltonian for the electron in the static surface potential,

$$H_e^{\text{static}} = \sum_q E_q c_q^\dagger c_q, \quad (14)$$

the second term is the Hamiltonian of the free acoustic phonons,

$$H_{ph}^0 = \sum_Q \hbar \omega_Q b_Q^\dagger b_Q, \quad (15)$$

where Q denotes a one-dimensional perpendicular wave vector, and the last term is the dynamic perturbation due to surface vibrations. Denoting for simplicity both bound and unbound eigenstates of the surface potential by $|q\rangle$, it is given by

$$H_{e-ph}^{\text{dyn}} = \sum_{q,q'} \langle q' | V_p(u,z) | q \rangle c_q^\dagger c_q. \quad (16)$$

The displacement of the surface u is related to the phonon creation and annihilation operators in the usual way

$$u = \sum_Q \sqrt{\frac{\hbar}{2\mu\omega_Q N_s}} (b_Q + b_{-Q}^\dagger), \quad (17)$$

with μ the mass of the unit cell of the lattice. The perturbation $V_p(u,z)$ can be identified as the difference between the displaced shifted surface potential and the static shifted surface potential. Recalling Eq. (11) and the transformation $z \rightarrow z - z_c$, it reads

$$V_p(z,u) = -\frac{e^2 \Lambda_0}{z+u} + \frac{e^2 \Lambda_0}{z}, \quad (18)$$

which, gearing toward a multiphonon calculation,³⁵ we expand in a Taylor series in u ,

$$V_p(z,u) = \frac{e^2 \Lambda_0}{z^2} u - \frac{e^2 \Lambda_0}{z^3} u^2 + \frac{e^2 \Lambda_0}{z^4} u^3 + O(u^4). \quad (19)$$

IV. TRANSITION PROBABILITIES

A. Preparatory considerations

We intend to calculate the desorption time taking one- and two-phonon processes into account. Hence, we need to evaluate the transition probabilities $W_{qq'}$ for one- and two-phonon processes. In general, multiphonon processes have two possible origins:³² (i) multiphonon terms in the perturbation of the surface potential (19) and (ii) multiple actions of the perturbation as it is encoded in the T -matrix corresponding to H_{e-ph}^{dyn} .

Using expansion (19), the dynamic perturbation H_{e-ph}^{dyn} can be classified by the order in u . Up to third order,

$$H_{e-ph}^{\text{dyn}} = V_1 + V_2 + V_3 + O(u^4), \quad (20)$$

where in second-quantized form

$$V_1 = \sum_Q \sum_{q,q'} G_{q,q'}^1(Q) (b_Q + b_{-Q}^\dagger) c_q^\dagger c_{q'}, \quad (21)$$

$$V_2 = - \sum_{Q_1, Q_2} \sum_{q,q'} G_{q,q'}^2(Q_1, Q_2) (b_{Q_1} + b_{-Q_1}^\dagger) (b_{Q_2} + b_{-Q_2}^\dagger) c_q^\dagger c_{q'}, \quad (22)$$

$$V_3 = \sum_{Q_1, Q_2, Q_3} \sum_{q,q'} G_{q,q'}^3(Q_1, Q_2, Q_3) (b_{Q_1} + b_{-Q_1}^\dagger) (b_{Q_2} + b_{-Q_2}^\dagger) \times (b_{Q_3} + b_{-Q_3}^\dagger) c_q^\dagger c_{q'}. \quad (23)$$

The matrix element of the electron-phonon interaction,

$$G_{q,q'}^n(Q_1, \dots, Q_n) = \left(\frac{\hbar}{2\mu N_s} \right)^{n/2} \frac{e^2 \Lambda_0 Z_{q,q'}^{n+1}}{\sqrt{\omega_{Q_1} \dots \omega_{Q_n}}}, \quad (24)$$

involves the electronic matrix element

$$Z_{q,q'}^n = \langle q | \frac{1}{z^n} | q' \rangle, \quad (25)$$

whose evaluation is sketched in Appendix B.

Quite generally, the transition probability from an electronic state $|q\rangle$ to an electronic state $|q'\rangle$ is given by³²

$$\mathcal{R}(q', q) = \frac{2\pi}{\hbar} \sum_{s,s'} \frac{e^{-\beta E_s}}{\sum_{s''} e^{-\beta E_{s''}}} |\langle s', q' | T | s, q \rangle|^2 \times \delta(E_s - E_{s'} + E_q - E_{q'}), \quad (26)$$

where $\beta = (k_B T_s)^{-1}$, with T_s the surface temperature and $|s\rangle$

and $|s'\rangle$ are initial and final phonon states. We are only interested in the transition between electronic states. It is thus natural to average in Eq. (26) over all phonon states. The delta function guarantees energy conservation.

The T matrix describing the interaction between the external electron and the acoustic phonons obeys the operator equation

$$T = H_{e-ph}^{\text{dyn}} + H_{e-ph}^{\text{dyn}} G H_{e-ph}^{\text{dyn}}, \quad (27)$$

where G satisfies

$$G = G_0 + G_0 H_{e-ph}^{\text{dyn}} G \quad (28)$$

and G_0 is given by

$$G_0 = (E - H_0 + i\epsilon)^{-1}, \quad (29)$$

with $H_0 = H_e^{\text{static}} + H_{ph}^0$.

For a two-phonon process we need $|\langle s', q' | T | s, q \rangle|^2$ in fourth order in u . We thus iterate T up to third order in u ,

$$T = V_1 + V_2 + V_3 + V_1 G_0 V_1 + V_1 G_0 V_2 + V_2 G_0 V_1 + V_1 G_0 V_1 G_0 V_1 + \mathcal{O}(u^4), \quad (30)$$

and write for the transition probability (26)

$$\mathcal{R}(q', q) = \sum_{n=1}^{17} \mathcal{R}^n(q', q), \quad (31)$$

where the individual transition probabilities $\mathcal{R}^n(q', q)$ can be classified by their order in u . The term of $\mathcal{O}(u^2)$,

$$\mathcal{R}^1: \langle s', q' | V_1 | s, q \rangle \langle s, q | V_1^* | s', q' \rangle, \quad (32)$$

gives rise to the standard golden rule approximation.

Transition probabilities of $\mathcal{O}(u^3)$ vanish as the expectation value of an odd number of phonon creation or annihilation operators is zero. We can thus drop from the calculation the terms

$$\mathcal{R}^2: \langle s', q' | V_1 | s, q \rangle \langle s, q | V_2^* | s', q' \rangle, \quad (33)$$

$$\mathcal{R}^4: \langle s', q' | V_1 | s, q \rangle \langle s, q | V_1^* G_0^* V_1^* | s', q' \rangle, \quad (34)$$

$$\mathcal{R}^8: \langle s', q' | V_2 | s, q \rangle \langle s, q | V_1^* | s', q' \rangle, \quad (35)$$

$$\mathcal{R}^{12}: \langle s', q' | V_1 G_0 V_1 | s, q \rangle \langle s, q | V_1^* | s', q' \rangle. \quad (36)$$

The remaining transition probabilities are of $\mathcal{O}(u^4)$ and describe two-phonon processes

$$\mathcal{R}^3: \langle s', q' | V_1 | s, q \rangle \langle s, q | V_3^* | s', q' \rangle, \quad (37)$$

$$\mathcal{R}^5: \langle s', q' | V_1 | s, q \rangle \langle s, q | V_2^* G_0^* V_1^* | s', q' \rangle, \quad (38)$$

$$\mathcal{R}^6: \langle s', q' | V_1 | s, q \rangle \langle s, q | V_1^* G_0^* V_2^* | s', q' \rangle, \quad (39)$$

$$\mathcal{R}^7: \langle s', q' | V_1 | s, q \rangle \langle s, q | V_1^* G_0^* V_1^* G_0^* V_1^* | s', q' \rangle, \quad (40)$$

$$\mathcal{R}^9: \langle s', q' | V_2 | s, q \rangle \langle s, q | V_2^* | s', q' \rangle, \quad (41)$$

$$\mathcal{R}^{10}: \langle s', q' | V_2 | s, q \rangle \langle s, q | V_1^* G_0^* V_1^* | s', q' \rangle, \quad (42)$$

$$\mathcal{R}^{11}: \langle s', q' | V_3 | s, q \rangle \langle s, q | V_1^* | s', q' \rangle, \quad (43)$$

$$\mathcal{R}^{13}: \langle s', q' | V_1 G_0 V_1 | s, q \rangle \langle s, q | V_2^* | s', q' \rangle, \quad (44)$$

$$\mathcal{R}^{14}: \langle s', q' | V_1 G_0 V_1 | s, q \rangle \langle s, q | V_1^* G_0^* V_1^* | s', q' \rangle, \quad (45)$$

$$\mathcal{R}^{15}: \langle s', q' | V_1 G_0 V_2 | s, q \rangle \langle s, q | V_1^* | s', q' \rangle, \quad (46)$$

$$\mathcal{R}^{16}: \langle s', q' | V_2 G_0 V_1 | s, q \rangle \langle s, q | V_1^* | s', q' \rangle, \quad (47)$$

$$\mathcal{R}^{17}: \langle s', q' | V_1 G_0 V_1 G_0 V_1 | s, q \rangle \langle s, q | V_1^* | s', q' \rangle. \quad (48)$$

A complete two-phonon calculation would take all these transition probabilities into account as they stand. This is however not always necessary. In the next section, we show that the two-phonon transition probabilities contain terms which are merely corrections to the one-phonon transition probability (32). Thus, for transitions already triggered by a one-phonon process, it may in some cases be reasonable to neglect, in a first approximation, these correction terms.

B. Calculation of the transition probabilities

The one-phonon transition probability $\mathcal{R}^1(q', q)$ can easily be brought into the form of the golden rule³⁵

$$\begin{aligned} \mathcal{R}^1(q', q) = \frac{2\pi}{\hbar} \sum_Q G_{q,q'}^1(Q) [G_{q,q'}^1(Q)]^* \{ n_B(\hbar\omega_Q) \delta(E_q - E_{q'} + \hbar\omega_Q) + [1 + n_B(\hbar\omega_Q)] \delta(E_q - E_{q'} - \hbar\omega_Q) \}, \end{aligned} \quad (49)$$

where the two terms in the curly brackets describe, respectively, the absorption and emission of a phonon.

To evaluate transition probabilities numerically, we assume the phonon spectrum to be adequately represented by the Debye model. Sums over phonon wave numbers can thus be transformed into integrals according to

$$\sum_Q \dots = \frac{3N_s}{\omega_D^3} \int_0^{\omega_D} d\omega \omega^2 \dots \quad (50)$$

Formula (C6) in gives the one-phonon transition probability in compact form as used in the numerical calculation.

The manipulation of the two-phonon transition probabilities is rather involved and cannot be reproduced entirely. In order to illustrate the necessary steps, we take

$$\begin{aligned} \mathcal{R}^{10}(q', q) = \frac{2\pi}{\hbar} \sum_{s,s'} \frac{e^{-\beta E_s}}{\sum_{s''} e^{-\beta E_{s''}}} \langle s', q' | V_2 | s, q \rangle \\ \times \langle s, q | V_1^* G_0^* V_1^* | s', q' \rangle \delta(E_s - E_{s'} + E_q - E_{q'}) \end{aligned} \quad (51)$$

as a representative example. It contains both types of interactions: a simultaneous two-phonon interaction V_2 and two successive one-phonon interactions V_1 linked by a virtual intermediate state arising from the iteration of the T matrix.

We begin the calculation with inserting into Eq. (51) the expressions for V_1 , V_2 , and G_0 as given by Eqs. (21), (22), and (29), respectively. Inserting, furthermore, the resolution of the identity over electron and phonon states,

$$\begin{aligned} \mathcal{R}^{10}(q', q) = & -\frac{2\pi}{\hbar} \sum_{s, s'} \frac{e^{-\beta E_s}}{\sum_{s''} e^{-\beta E_{s''}}} \sum_{q_1, q_2, s_1, s_2} \langle s' | \sum_{Q_1, Q_2} G_{q', q}^{(2)}(Q_1, Q_2) (b_{Q_1} + b_{-Q_1}^\dagger) (b_{Q_2} + b_{-Q_2}^\dagger) | s \rangle \langle s | \sum_{Q_3} [G_{q, q_1}^{(1)}(Q_3)]^* \\ & \times (b_{Q_3}^\dagger + b_{-Q_3}) | s_1 \rangle \langle s_1, q_1 | \frac{1}{E_s + E_q - H_0 - i\epsilon} | s_2, q_2 \rangle \langle s_2 | \sum_{Q_4} [G_{q_2, q'}^{(1)}(Q_4)]^* (b_{Q_4}^\dagger + b_{-Q_4}) | s' \rangle \delta(E_s - E_{s'} + E_q - E_{q'}). \end{aligned} \quad (52)$$

Using the two identities

$$\delta(x) = \frac{1}{2\pi} \int_{-\infty}^{\infty} e^{ixt} dt \quad \text{and} \quad \frac{1}{x - i\epsilon} = i \int_{-\infty}^0 e^{i(x-i\epsilon)\tau} d\tau \quad (53)$$

and the fact that the free resolvent is diagonal with respect to the electron-phonon states $|q, s\rangle$, we obtain

$$\begin{aligned} \mathcal{R}^{10}(q', q) = & -\frac{2\pi}{\hbar} \sum_{q_1} \sum_{Q_1, Q_2, Q_3, Q_4} \frac{1}{2\pi} \int_{-\infty}^{\infty} dt / \hbar e^{i(E_q - E_{q'})t/\hbar} i \int_{-\infty}^0 d\tau / \hbar e^{i(E_q - E_{q_1} - i\epsilon)\tau/\hbar} G_{q', q}^{(2)}(Q_1, Q_2) [G_{q_1, q}^{(1)}(Q_3) G_{q', q_1}^{(1)}(Q_4)]^* \\ & \sum_{s, s'} e^{-\beta E_s} \\ & \times \frac{e^{iE_s(t+\tau)/\hbar} (b_{Q_3}^\dagger + b_{-Q_3}) e^{-iE_{s_1}\tau/\hbar} | s_1 \rangle \langle s_1 | (b_{Q_4}^\dagger + b_{-Q_4}) e^{-iE_{s'}t/\hbar} | s' \rangle}{\sum_{s''} e^{-\beta E_{s''}}} \langle s' | (b_{Q_1} + b_{-Q_1}^\dagger) (b_{Q_2} + b_{-Q_2}^\dagger) | s \rangle \langle s | e^{iE_s(t+\tau)/\hbar} (b_{Q_3}^\dagger + b_{-Q_3}) e^{-iE_{s_1}\tau/\hbar} | s_1 \rangle \langle s_1 | (b_{Q_4}^\dagger + b_{-Q_4}) e^{-iE_{s'}t/\hbar} | s' \rangle, \end{aligned} \quad (54)$$

where all exponential factors containing electron energies have been placed in front of the phonon average. Employing $\langle s | e^{iE_s t/\hbar} = \langle s | e^{iH_{ph}^0 t/\hbar}$ and introducing $v_Q = b_Q + b_{-Q}^\dagger$, the above expression becomes

$$\begin{aligned} \mathcal{R}^{10}(q', q) = & -\frac{2\pi}{\hbar} \sum_{q_1} \sum_{Q_1, Q_2, Q_3, Q_4} \frac{1}{2\pi} \int_{-\infty}^{\infty} dt / \hbar e^{i(\omega_q - \omega_{q'})t} i \int_{-\infty}^0 d\tau / \hbar e^{i(\omega_q - \omega_{q_1} - i\epsilon)\tau} G_{q', q}^{(2)}(Q_1, Q_2) [G_{q', q_1}^{(1)}(Q_3) G_{q_1, q}^{(1)}(Q_4)]^* \\ & \times \langle \langle v_{Q_3}^\dagger(t + \tau) v_{Q_4}^\dagger(t) v_{Q_1} v_{Q_2} \rangle \rangle, \end{aligned} \quad (55)$$

where $\langle \langle \dots \rangle \rangle = \sum_s e^{-\beta E_s} \langle s | \dots | s \rangle / \sum_{s''} e^{-\beta E_{s''}}$ is the average over phonon states. The operator $v_Q(t)$ evolves in time according to H_{ph}^0 . Hence, the four-point phonon correlation function appearing in Eq. (55) may be rewritten as

$$\begin{aligned} \langle \langle v_{Q_3}^\dagger(t + \tau) v_{Q_4}^\dagger(t) v_{Q_1} v_{Q_2} \rangle \rangle = & e^{i\omega_{Q_3}(t+\tau)} e^{i\omega_{Q_4}t} \langle \langle b_{Q_3}^\dagger b_{Q_4}^\dagger b_{Q_1} b_{Q_2} \rangle \rangle + e^{i\omega_{Q_3}(t+\tau)} e^{-i\omega_{Q_4}t} \langle \langle b_{Q_3}^\dagger b_{-Q_4} b_{Q_1} b_{-Q_2}^\dagger \rangle \rangle \\ & + e^{i\omega_{Q_3}(t+\tau)} e^{-i\omega_{Q_4}t} \langle \langle b_{Q_3}^\dagger b_{-Q_4} b_{-Q_1}^\dagger b_{Q_2} \rangle \rangle + e^{-i\omega_{Q_3}(t+\tau)} e^{i\omega_{Q_4}t} \langle \langle b_{-Q_3} b_{Q_4}^\dagger b_{Q_1} b_{-Q_2}^\dagger \rangle \rangle \\ & + e^{-i\omega_{Q_3}(t+\tau)} e^{i\omega_{Q_4}t} \langle \langle b_{-Q_3} b_{Q_4}^\dagger b_{-Q_1}^\dagger b_{Q_2} \rangle \rangle + e^{-i\omega_{Q_3}(t+\tau)} e^{-i\omega_{Q_4}t} \langle \langle b_{-Q_3} b_{-Q_4} b_{-Q_1}^\dagger b_{-Q_2}^\dagger \rangle \rangle \end{aligned} \quad (56)$$

and further evaluated by forming all possible contractions. Using

$$\langle \langle b_{Q_1}^\dagger b_{Q_2} \rangle \rangle = \delta_{Q_1, Q_2} n_B(\hbar\omega_{Q_1}) \quad \text{and} \quad \langle \langle b_{Q_1} b_{Q_2}^\dagger \rangle \rangle = \delta_{Q_1, Q_2} [1 + n_B(\hbar\omega_{Q_1})] \quad (57)$$

and integrating over the times t and τ finally yields

$$\begin{aligned} \mathcal{R}^{10}(q', q) = & -\frac{2\pi}{\hbar} \sum_{q_1} \sum_{Q_1, Q_2} G_{q', q}^2(Q_1, Q_1) [G_{q_1, q}^1(Q_2) G_{q', q_1}^1(Q_2)]^* \left(2n_B(\hbar\omega_{Q_1}) n_B(\hbar\omega_{Q_2}) \frac{\delta(E_q - E_{q'} + \hbar\omega_{Q_1} + \hbar\omega_{Q_2})}{E_q - E_{q_1} + \hbar\omega_{Q_1} - i\epsilon} \right. \\ & + [2n_B(\hbar\omega_{Q_1}) n_B(\hbar\omega_{Q_2}) + n_B(\hbar\omega_{Q_1})] \frac{\delta(E_q - E_{q'})}{E_q - E_{q_1} + \hbar\omega_{Q_1} - i\epsilon} + 2n_B(\hbar\omega_{Q_1}) [1 + n_B(\hbar\omega_{Q_2})] \frac{\delta(E_q - E_{q'} + \hbar\omega_{Q_1} - \hbar\omega_{Q_2})}{E_q - E_{q_1} + \hbar\omega_{Q_1} - i\epsilon} \\ & + [2n_B(\hbar\omega_{Q_1}) n_B(\hbar\omega_{Q_2}) + 2n_B(\hbar\omega_{Q_2}) + n_B(\hbar\omega_{Q_1}) + 1] \frac{\delta(E_q - E_{q'})}{E_q - E_{q_1} - \hbar\omega_{Q_1} - i\epsilon} \\ & + 2[1 + n_B(\hbar\omega_{Q_2})] n_B(\hbar\omega_{Q_1}) \frac{\delta(E_q - E_{q'} + \hbar\omega_{Q_1} - \hbar\omega_{Q_2})}{E_q - E_{q_1} - \hbar\omega_{Q_2} - i\epsilon} \\ & \left. + 2[1 + n_B(\hbar\omega_{Q_1})] [1 + n_B(\hbar\omega_{Q_2})] \frac{\delta(E_q - E_{q'} - \hbar\omega_{Q_1} - \hbar\omega_{Q_2})}{E_q - E_{q_1} - \hbar\omega_{Q_1} - i\epsilon} \right). \end{aligned} \quad (58)$$

Similar expressions can be obtained for the other transition probabilities.⁶⁶ The formulas are all quite long. To gain more insight, we classify two-phonon processes by the energy difference they can bridge. As can be seen in the above example, this is controlled by delta functions which, quite generally, appear in two-phonon transition probabilities with four different arguments: $\delta(E_q - E_{q'})$, $\delta(E_q - E_{q'} \pm \hbar\omega_Q)$, $\delta[E_q - E_{q'} \pm (\hbar\omega_{Q_1} - \hbar\omega_{Q_2})]$, and $\delta[E_q - E_{q'} \pm (\hbar\omega_{Q_1} + \hbar\omega_{Q_2})]$. For the calculation of the transition probabilities, we can drop all contributions proportional to $\delta(E_q - E_{q'})$ because in the one-dimensional model we are considering it implies no transition.

In the Debye model, the maximum phonon energy is the Debye energy $\hbar\omega_D$. Hence for terms in the transition probabilities that are proportional to $\delta(E_q - E_{q'} \pm \hbar\omega_Q)$, the maximal energy difference between the initial and final states of the electron cannot exceed one Debye energy. The two-phonon transition probabilities \mathcal{R}^3 , \mathcal{R}^5 , \mathcal{R}^6 , \mathcal{R}^7 , \mathcal{R}^{11} , \mathcal{R}^{15} , \mathcal{R}^{16} , and \mathcal{R}^{17} have only contributions of this type. They are thus only corrections to the one-phonon transition probability \mathcal{R}^1 .

Next, we consider terms proportional to $\delta[E_q - E_{q'} \pm (\hbar\omega_{Q_1} - \hbar\omega_{Q_2})]$. The energies of the two phonons $\hbar\omega_{Q_1}$ and $\hbar\omega_{Q_2}$ are both between zero and the Debye energy $\hbar\omega_D$. As they appear with different signs in the delta function, the energy difference between the initial and final states of the electron can range from $-\hbar\omega_D$ to $\hbar\omega_D$. Thus these contributions do not allow to bridge levels that are farther apart than one Debye energy and are thus again merely corrections to the one-phonon transition probability \mathcal{R}^1 .

Finally, we look at the contributions to the transition probabilities proportional to $\delta[E_q - E_{q'} \pm (\hbar\omega_{Q_1} + \hbar\omega_{Q_2})]$. The energy difference that can be bridged by this type of process is between zero and two Debye energies. Up to an energy difference of one Debye energy, these processes are again corrections to the one-phonon transition probability. But for energy differences between one and two Debye energies, these are the only processes that contribute to the transition probability.

This analysis leads us to divide the two-phonon processes into two groups, one-Debye-energy transitions and two-Debye-energy transitions. One-Debye-energy transitions enable transitions between states that are at most one Debye energy apart, i.e., $-1 < \Delta_{q,q'} < 1$. Two-Debye-energy transitions enable transitions between states that are between one and two Debye energies apart, i.e., $-2 < \Delta_{q,q'} < -1$ and $1 < \Delta_{q,q'} < 2$.

All the transition probabilities in the two-phonon approximation contribute to one-Debye-energy transitions, but only the transition probabilities \mathcal{R}^9 , \mathcal{R}^{10} , \mathcal{R}^{13} , and \mathcal{R}^{14} contribute to two-Debye-energy transitions. Among the contributions to the one Debye energy transitions, the golden rule transition probability is the only “true” one-phonon process.

In the following, we assume that for one-Debye-energy transitions, the one-phonon transition probability (49) dominates the corrections from the two-phonon transition probabilities. Only when the one-phonon transition probability is zero, which is the case for two-Debye-energy transitions, we will take two-phonon processes into account. Hence, in our

numerical calculation, we use for one-Debye-energy transitions the one-phonon transition probability,

$$W_{q',q} = \mathcal{R}^1(q',q), \quad (59)$$

and for two-Debye-energy transitions the two-phonon transition probability

$$W_{q',q} = \tilde{\mathcal{R}}^9(q',q) + 2 \operatorname{Re} \tilde{\mathcal{R}}^{10}(q',q) + \tilde{\mathcal{R}}^{14}(q',q), \quad (60)$$

where the transition probabilities $\tilde{\mathcal{R}}^9$, $\tilde{\mathcal{R}}^{10}$, and $\tilde{\mathcal{R}}^{14}$ denote those parts of \mathcal{R}^9 , \mathcal{R}^{10} , and \mathcal{R}^{14} which give rise to two-Debye-energy transitions. They are given by Eqs. (C9)–(C11). The transition probability $\tilde{\mathcal{R}}^{13}$ does not appear explicitly. It is the complex conjugate to $\tilde{\mathcal{R}}^{10}$ and thus subsumed in the second term on the right-hand side of Eq. (60).

C. Regularization

The transition probabilities for the two-phonon processes contain, in the present form, divergences. Specifically within the two-Debye-energy approximation, which takes two-phonon processes into account only for transitions connecting (bound and unbound) surface states which are between one and two Debye energies apart, the transition probabilities $\tilde{\mathcal{R}}^{10}$ and $\tilde{\mathcal{R}}^{14}$ make trouble.

The divergences are artifacts of our one-dimensional model. They arise from the quantization of the electron motion perpendicular to the surface in conjunction with the harmonic approximation for the lattice. The former gives rise to arbitrarily sharp electronic energy levels for the bound states while the latter leads to infinite phonon lifetimes. Some divergent terms, for instance, $I_{(2)}^3(2,1;2)$ and $I_{(2)}^6(2,1;2,2)$ appearing, respectively, in the transition probabilities $\tilde{\mathcal{R}}^{10}(2,1)$ and $\tilde{\mathcal{R}}^{14}(2,1)$ (see Appendix C), can be traced back to the diagonal matrix element of the linear electron-phonon interaction (21) and could thus be eliminated with a dressing transformation of the type used by Gortel and co-workers.³⁶ But other divergences, for instance, the one in the integral $I_{(2)}^6(k',q;q_1,q_1)$ which appears in the rate $\tilde{\mathcal{R}}^{14}(k',q)$, cannot be removed in that manner. We decided therefore to regularize the divergences of the transition probabilities by taking a finite phonon lifetime into account which works in all cases. The drawback of this procedure is that it turns divergences only into resonances, whose width is set by the phonon lifetime, which thus becomes an important additional material parameter.

In order to see how a finite phonon lifetime regularizes the transition probabilities, we recall bringing the transition probabilities into a numerically feasible form required to evaluate time integrals over products of time-dependent phonon two-point functions. For the transition probability $\tilde{\mathcal{R}}^{10}$, we showed this explicitly [cf. Eq. (54) and the text which followed] but the same manipulations are necessary for the other transition probabilities.⁶⁶ Throughout, we assumed that the time evolution of the phonons is governed by the free phonon Hamiltonian H_{ph}^0 . As a result, the two-point functions acquired an undamped time dependence. In general, however, phonons interact because of the anharmonicities in the

lattice potential. A more realistic model would thus lead to phonon two-point functions whose time dependences are damped. Ultimately, the damping leads to divergence-free transition probabilities.

To account for the damping of phonons, we imagine the retarded and advanced phonon Green's functions to be given by

$$G^{R,A}(Q, \omega) = \frac{1}{\omega - \omega_Q \pm i\gamma_Q}, \quad (61)$$

where γ_Q is a decay constant arising from the phonon-phonon interaction and the upper (lower) sign corresponds to the retarded (advanced) Green's function. Since the phonon four-point functions appearing in the two-phonon transition probabilities can be linked to these two functions, γ_Q can be incorporated into the expressions for the transition probabilities. Unfortunately, for the surfaces we are interested in, little is known about the microphysics of phonons. We suggest therefore to use a phenomenological estimate for γ_Q which utilizes material parameters which, at least in principle, could be measured⁶⁷

$$\gamma_Q = \frac{1}{\tau} = \frac{v}{l} = \frac{2\gamma_G^2 \omega_Q^2 k_B T}{\mu V \omega_D}, \quad (62)$$

with γ_G the Grüneisen parameter, V the volume per atom, and μ the shear modulus.

In order to demonstrate how our regularization procedure works, we consider, again as an example, a four-point function of the type appearing in Eq. (55),

$$\begin{aligned} & \langle \langle v_{Q_1}^\dagger(t_1) v_{Q_2}^\dagger(t_2) v_{Q_3}(t_3) v_{Q_4}(t_4) \rangle \rangle \\ &= \langle \langle b_{Q_1}^\dagger(t_1) b_{Q_2}^\dagger(t_2) b_{Q_3}(t_3) b_{Q_4}(t_4) \rangle \rangle \\ &+ \langle \langle b_{Q_1}^\dagger(t_1) b_{-Q_2}(t_2) b_{Q_3}(t_3) b_{-Q_4}^\dagger(t_4) \rangle \rangle \\ &+ \langle \langle b_{Q_1}^\dagger(t_1) b_{-Q_2}(t_2) b_{-Q_3}^\dagger(t_3) b_{Q_4}(t_4) \rangle \rangle \\ &+ \langle \langle b_{-Q_1}(t_1) b_{Q_2}^\dagger(t_2) b_{Q_3}(t_3) b_{-Q_4}^\dagger(t_4) \rangle \rangle \\ &+ \langle \langle b_{-Q_1}(t_1) b_{Q_2}^\dagger(t_2) b_{-Q_3}^\dagger(t_3) b_{Q_4}(t_4) \rangle \rangle \\ &+ \langle \langle b_{-Q_1}(t_1) b_{-Q_2}(t_2) b_{-Q_3}^\dagger(t_3) b_{-Q_4}^\dagger(t_4) \rangle \rangle. \end{aligned} \quad (63)$$

First, the four-point functions have to be broken up into two point functions. For the first term, e.g., this means

$$\frac{1}{\pi} \frac{(\gamma_{Q_1} + \gamma_{Q_2})}{(\gamma_{Q_1} + \gamma_{Q_2})^2 + [\omega_q - \omega_{q'} \pm (\omega_{Q_1} + \omega_{Q_2})]^2} \frac{\omega_q - \omega_{q_1} \pm \omega_{Q_1}}{(\omega_q - \omega_{q_1} \pm \omega_{Q_1})^2 + \gamma_{Q_1}^2} \quad (71)$$

and, for small decay constants γ_Q , approximated by

$$\begin{aligned} & \langle \langle b_{Q_1}^\dagger(t_1) b_{Q_2}^\dagger(t_2) b_{Q_3}(t_3) b_{Q_4}(t_4) \rangle \rangle \\ &= \langle \langle b_{Q_1}^\dagger(t_1) b_{Q_3}(t_3) \rangle \rangle \langle \langle b_{Q_2}^\dagger(t_2) b_{Q_4}(t_4) \rangle \rangle \\ &+ \langle \langle b_{Q_1}^\dagger(t_1) b_{Q_4}(t_4) \rangle \rangle \langle \langle b_{Q_2}^\dagger(t_2) b_{Q_3}(t_3) \rangle \rangle. \end{aligned} \quad (64)$$

Because of translational invariance, the two-point functions are proportional to δ_{Q_1, Q_2} even in the interacting case. The diagonal elements of the expectation values in Eq. (64) can be evaluated using the spectral theorem

$$\langle \langle b_{Q_1}^\dagger(t') b_{Q_1}(t) \rangle \rangle = \frac{1}{2\pi} \int_{-\infty}^{\infty} J_{b^\dagger b}(\omega) e^{-i\omega(t-t')} d\omega \quad (65)$$

and

$$\langle \langle b_{Q_1}(t) b_{Q_1}^\dagger(t') \rangle \rangle = \frac{1}{2\pi} \int_{-\infty}^{\infty} J_{b^\dagger b}(\omega) e^{\beta\omega} e^{-i\omega(t-t')} d\omega, \quad (66)$$

with the spectral function

$$J_{b^\dagger b}(\omega) = \frac{i[G^R(\omega) - G^A(\omega)]}{e^{\beta\omega} - 1}, \quad (67)$$

which contains the damping factor γ_Q via the retarded and advanced phonon Green's functions. Note that we neglect in the spectral function the contribution proportional to $\delta(\omega)$. Since the formulas as they stand reproduce in the limit $\gamma_Q \rightarrow 0$ the correct expressions for infinite phonon lifetime, we conclude that the neglect of the $\delta(\omega)$ term is in this case justified. After integration, Eqs. (65) and (66) reduce, respectively, to

$$\langle \langle b_{Q_1}^\dagger(t') b_{Q_1}(t) \rangle \rangle = n_B(\omega_Q) e^{-i\omega_Q(t-t') - \gamma_Q|t-t'|} \quad (68)$$

and

$$\langle \langle b_{Q_1}(t) b_{Q_1}^\dagger(t') \rangle \rangle = [1 + n_B(\omega_Q)] e^{-i\omega_Q(t-t') - \gamma_Q|t-t'|}. \quad (69)$$

Because of the damping factors, the phonon four-point function in Eq. (55) becomes

$$\begin{aligned} & \langle \langle v_{Q_1}^\dagger(t + \tau_2) v_{Q_2}^\dagger(t) v_{Q_3} v_{Q_4} \rangle \rangle \\ &= 2n_B(\omega_{Q_1}) n_B(\omega_{Q_2}) e^{i\omega_{Q_1}(t+\tau_2) - \gamma_{Q_1}|t+\tau_2|} e^{i\omega_{Q_2}(t) - \gamma_{Q_2}|t|} \\ &+ 2[1 + n_B(\omega_{Q_1})][1 + n_B(\omega_{Q_2})] \\ &\times e^{-i\omega_{Q_1}(t+\tau_2) - \gamma_{Q_1}|t+\tau_2|} e^{-i\omega_{Q_2}t - \gamma_{Q_2}|t|} + \dots, \end{aligned} \quad (70)$$

where the ellipsis stands for terms that do not allow for two-Debye-energy transitions. Performing finally in Eq. (55) the integral over t and τ , with the phonon four-point function replaced by Eq. (70), the dominant contribution, that is, the term giving rise to two-Debye-energy transitions only, can be identified as

$$\begin{aligned} & \delta[\omega_q - \omega_{q'} \pm (\omega_{Q_1} + \omega_{Q_2})] \\ & \times \frac{\omega_{q'} - \omega_{q_1} \mp \omega_{Q_2}}{(\omega_{q'} - \omega_{q_1} \mp \omega_{Q_2})^2 + (2\gamma_{Q_1} + \gamma_{Q_2})^2}. \end{aligned} \quad (72)$$

$$\begin{aligned} & \times \delta(E_q - E_{q'} - \hbar\omega_{Q_1} - \hbar\omega_{Q_2}) \\ & \times g(E_{q'} - E_{q_1} + \hbar\omega_{Q_2}, 2\hbar\gamma_{Q_1} + \hbar\gamma_{Q_2}), \end{aligned} \quad (73)$$

Putting finally everything together, the corrected, divergence-free transition probability $\tilde{\mathcal{R}}^{10}$ becomes

$$\begin{aligned} & \tilde{\mathcal{R}}^{10}(q', q) \\ & = -\frac{2\pi}{\hbar} \sum_{q_1} \sum_{Q_1, Q_2} G_{q', q}^{(2)}(Q_1, Q_2) [G_{q_1, q'}^{(1)}(Q_2) G_{q', q_1}^{(1)}(Q_2)]^* \\ & \times \{2n_B(\hbar\omega_{Q_1}) n_B(\hbar\omega_{Q_2}) \delta(E_q - E_{q'} + \hbar\omega_{Q_1} + \hbar\omega_{Q_2}) \\ & \times g(E_{q'} - E_{q_1} - \hbar\omega_{Q_2}, 2\hbar\gamma_{Q_1} + \hbar\gamma_{Q_2}) \\ & + 2[1 + n_B(\hbar\omega_{Q_1})][1 + n_B(\hbar\omega_{Q_2})]\} \end{aligned}$$

where we have used the abbreviation

$$g(a, \gamma_a) = \frac{a}{a^2 + \gamma_a^2}. \quad (74)$$

A similar analysis can be performed for the transition probability $\tilde{\mathcal{R}}^{14}$. Introducing the function

$$f(a, b, \gamma_a, \gamma_b) = \frac{ab + \gamma_a \gamma_b}{(a^2 + \gamma_a^2)(b^2 + \gamma_b^2)}, \quad (75)$$

the corrected, divergence-free transition probability $\tilde{\mathcal{R}}^{14}$ is then given by

$$\begin{aligned} \tilde{\mathcal{R}}^{14} & = \frac{2\pi}{\hbar} \sum_{q_1, q_2} \sum_{Q_1, Q_2} G_{q, q_1}^{(1)}(Q_1) G_{q_1, q'}^{(1)}(Q_1) [G_{q, q_2}^{(1)}(Q_2) G_{q_2, q'}^{(1)}(Q_2)]^* \{n_B(\hbar\omega_{Q_1}) n_B(\hbar\omega_{Q_2}) \delta(E_q - E_{q'} + \hbar\omega_{Q_1} + \hbar\omega_{Q_2}) \\ & \times f(E_{q_2} - E_{q'} + \hbar\omega_{Q_2}, E_{q_1} - E_{q'} + \hbar\omega_{Q_1}, 2\hbar\gamma_{Q_1} + \hbar\gamma_{Q_2}, \hbar\gamma_{Q_1} + 2\hbar\gamma_{Q_2}) + n_B(\hbar\omega_{Q_1}) n_B(\hbar\omega_{Q_2}) \delta(E_q - E_{q'} + \hbar\omega_{Q_1} + \hbar\omega_{Q_2}) \\ & \times f(E_{q_2} - E_{q'} + \hbar\omega_{Q_2}, E_{q_1} - E_{q'} + \hbar\omega_{Q_2}, 2\hbar\gamma_{Q_1} + \hbar\gamma_{Q_2}, 2\hbar\gamma_{Q_1} + \hbar\gamma_{Q_2}) + [1 + n_B(\hbar\omega_{Q_1})][1 + n_B(\hbar\omega_{Q_2})] \\ & \times \delta(E_q - E_{q'} - \hbar\omega_{Q_1} - \hbar\omega_{Q_2}) f(E_{q_2} - E_{q'} - \hbar\omega_{Q_2}, E_{q_1} - E_{q'} - \hbar\omega_{Q_1}, 2\hbar\gamma_{Q_1} + \hbar\gamma_{Q_2}, \hbar\gamma_{Q_1} + 2\hbar\gamma_{Q_2}) \\ & + [1 + n_B(\hbar\omega_{Q_1})][1 + n_B(\hbar\omega_{Q_2})] \delta(E_q - E_{q'} - \hbar\omega_{Q_1} - \hbar\omega_{Q_2}) \\ & \times f(E_{q_2} - E_{q'} - \hbar\omega_{Q_2}, E_{q_1} - E_{q'} - \hbar\omega_{Q_2}, 2\hbar\gamma_{Q_1} + \hbar\gamma_{Q_2}, 2\hbar\gamma_{Q_1} + \hbar\gamma_{Q_2})\}. \end{aligned} \quad (76)$$

The transition probability $\tilde{\mathcal{R}}^9$ has no divergence and hence requires no regularization. Equations (C20) and (C21) give the final expressions for the corrected, divergence-free two-phonon transition probabilities as used in the numerical calculation.

V. RESULTS

We now insert the one- and (regularized) two-phonon transition probabilities into the rate Eq. (1) to investigate phonon-induced desorption for an electron image bound to a dielectric surface. The two-phonon approximation is of course only applicable to dielectrics which have a two-phonon deep potential, for instance, graphite (see discussion in Sec. I). For graphite, the material parameters required for a calculation of the desorption time are summarized in Table I. Apart from the Debye temperature, which we varied to study the dependence of the desorption time on the potential depth, all numerical results were obtained for these parameters.

A. One-phonon transition probability

To set the stage, we start with presenting results for the desorption time τ_e calculated with one-phonon processes

only, although these times do not apply to any of the dielectric materials we mentioned. First, we discuss the dependence of the desorption time on the surface temperature. If τ_e is much larger than the time, the electron needs to thermally equilibrate with the surface, prior to desorption, and electron surface states are populated according to $n_q \sim \exp[-E_q/kT_s]$. Since for $q \geq 2$, $-E_q/kT_s \ll -E_1/kT_s$, this means that the electron basically desorbs from the lowest surface bound state. Desorption requires therefore transitions from the lowest bound state to the upper bound states and finally to the continuum. They entail the absorption of a phonon. The likelihood of which is, according to Eq. (49), proportional to the Bose distribution n_B and thus increases strongly with temperature. This is reflected in Fig. 1 showing that an increase of the surface temperature leads to an increase of τ_e^{-1} over several orders of magnitude. Variations of the Debye temperature in contrast do not change the strong-temperature dependence significantly.

We now move on to study the effects of the potential depth on desorption. In Sec. II, we explained how the potential depth can be classified by the maximum phonon energy, the Debye energy $\hbar\omega_D$. The relative depth of the potential can be changed easily by tuning the Debye energy while keeping the absolute potential depth constant. This is advan-

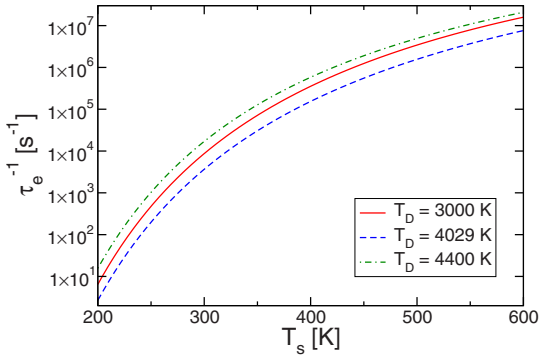


FIG. 1. (Color online) Inverse desorption time τ_e^{-1} in the one-phonon approximation as a function of the surface temperature T_s for a one-phonon deep potential ($T_D=3000$ K, $T_D=4029$ K) and a shallow potential ($T_D=4400$ K).

tageous from the technical perspective since the cumbersome calculation of the electronic matrix elements $Z_{qq'}^n$ does not have to be repeated. In order to keep the level of phonon excitation constant while the Debye temperature is varied, we set the inverse surface temperature constant

$$\delta = \frac{\hbar \omega_D}{k_B T_s}. \quad (77)$$

Figure 2 shows τ_e^{-1} depending on the Debye temperature T_D . The lower the T_D , the larger the effective potential depth. For a one-phonon-deep potential, $T_D > 2707$ K, the lowest level is coupled to at least one other bound state by a one-phonon process. In this region, the calculation of τ_e^{-1} using one-phonon processes only is applicable and leads to an increase of τ_e^{-1} with increasing T_D , that is, with decreasing effective potential depth. This is what one would expect as it should be easier to get the energy required to bridge a smaller energy difference than a larger one. For a shallow potential, $T_D > 4029$ K, the lowest bound state can be emptied directly to the continuum. This leads to a substantial increase of τ_e^{-1} signaled by the kink. The main conclusion at this point is that

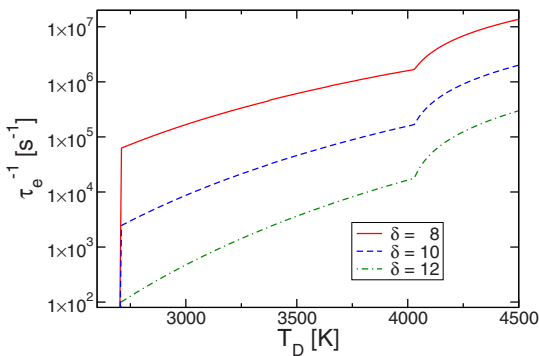


FIG. 2. (Color online) Inverse desorption time τ_e^{-1} in the one-phonon approximation as a function of the Debye temperature T_D for different inverse temperatures δ . Tuning T_D the potential can be made shallow ($T_D > 4029$ K), one-phonon deep (2707 K $< T_D < 4029$ K), or two-phonon deep ($T_D < 2707$ K) for which desorption by one-phonon processes is impossible.

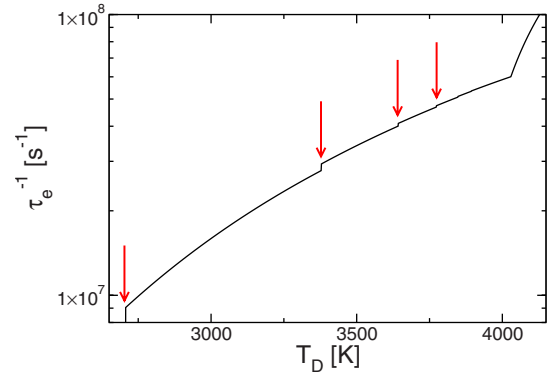


FIG. 3. (Color online) Inverse desorption time τ_e^{-1} in the one-phonon approximation as a function of the Debye temperature for a high surface temperature ($\delta=5$). The small steps under the red arrows coincide with the onset of transitions from the lowest to the second, third, fourth, fifth, etc. bound states.

direct transitions which are only possible for a shallow potential are more effective than a cascade of transitions which are the only means of emptying a deep potential.

To gain further insight, we identify the most relevant cascade. The one-phonon-deep potential, for which the transition between the lowest two bound states is a one-phonon process, can be subdivided further, depending on the accessibility of the higher bound states. For the one-phonon-deep potential, the lowest level does not couple to the continuum directly, but it is coupled to at least the second bound state. Transitions between the lowest bound state and the third, fourth, fifth, etc. bound states may or may not be possible. For example, for $\Delta_{1,2} > -1 > \Delta_{1,3}$ only the second bound state, for $\Delta_{1,3} > -1 > \Delta_{1,4}$ the second and third bound states, and hence for $\Delta_{1,n} > -1 > \Delta_{1,n+1}$ the second to n th bound state can be reached from the lowest state.

These accessibility thresholds mark the opening of new desorption channels when the potential depth is reduced. Figure 3 shows that when the second, third, or fourth level becomes available from the lowest level, τ_e^{-1} increases suddenly, although these steps are small. We deduce that the first leg of the cascade to the continuum is predominantly the transition to the second level.

The question arises as to how important the higher bound states $n=3, 4, 5, \dots$ are as intermediate steps for the second leg of a desorption cascade. To investigate this, we calculated τ_e^{-1} with different numbers of bound states. The image potential has an infinite sequence of bound states, yet for practical reasons we can take only a finite number of bound states into account. Figure 4 confirms that adding higher bound states to the calculation τ_e^{-1} saturates quickly. Neglecting all but a few bound states, say seven, is therefore justified. With two bound states, the value of τ_e^{-1} amounts already to about two thirds of the value obtained with 16 bound states. Hence, the second leg of the dominant desorption channel is a direct transition from the second bound state into the continuum. The reason for the importance of the second level lies in the matrix element $Z_{q,q'}^2$, which is large for low bound states for which more probability density is concentrated near the surface where the dynamic perturbation inducing desorption is strongest.

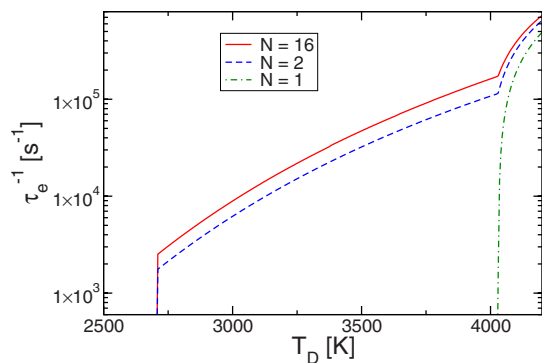


FIG. 4. (Color online) Inverse desorption time τ_e^{-1} in the one-phonon approximation as a function of the Debye temperature for $\delta=10$ calculated with different numbers of bound states N . For $N=1$, desorption occurs only due to direct transition to the continuum which dominates the rate for a shallow potential ($T_D > 4029$ K). For $N > 1$, cascade transitions allow for desorption from a one-phonon-deep potential (2707 K $< T_D < 4029$ K). In this case, the second bound state gives the most important contribution.

B. Two-phonon transition probability

Under the assumption that the true one-phonon transition probability (49) dominates for one-Debye-energy transitions the corrections coming from the two-phonon transition probabilities, the latter need only be considered for two-Debye-energy transitions, for which the transition probabilities would be zero otherwise. All the data presented in this section were obtained within this approximation.

For $T_D=2500$ K, the numerical results apply to an electron image bound to graphite, which has, in our notation, a two-phonon-deep surface potential. Indeed, using the dynamically corrected image potential, we find for the lowest two image states of graphite $E_1=-0.347$ eV and $E_2=-0.114$ eV. Hence, $\Delta_{12}=-1.06$ implying $-1 > \Delta_{12} > -2$ and thus a two-phonon-deep surface potential. Within our main assumption that the transition probability corresponding to the minimum number of phonons needed to open for the first time a particular transition is the dominant one, the two-phonon approximation is sufficient for graphite; n -phonon processes with $n \geq 3$ should yield only small corrections.

Figure 5 concerns once more the dependence of τ_e^{-1} on the Debye temperature, but this time also for Debye temperatures leading to two-phonon-deep potentials ($T_D < 2707$ K). Using one-phonon transition probabilities only, τ_e^{-1} would drop from a finite value to zero when the one-phonon-deep potential ($\Delta_{12} > -1$) becomes two-phonon deep ($\Delta_{12} < -1$). This happens at $T_D=2707$ K. Including two-phonon transition probabilities leads to a finite τ_e^{-1} even for two-phonon-deep potentials. The data in Fig. 5 for $T_D=2500$ K apply to graphite (thin vertical line). For instance, for $\delta=7$, that is, $T_s \approx 360$ K, we find $\tau_e^{-1} \approx 5 \times 10^4$ s $^{-1}$ and hence a desorption time $\tau_e \approx 2 \times 10^{-5}$ s.

If a two-phonon deep potential is made shallower so that it becomes one-phonon deep at $\Delta_{12}=-1$, the stronger one-phonon transitions set in and τ_e^{-1} increases considerably. For high surface temperatures, for instance for $\delta=5$, τ_e^{-1} increases about fivefold. Hence, for high surface temperatures,

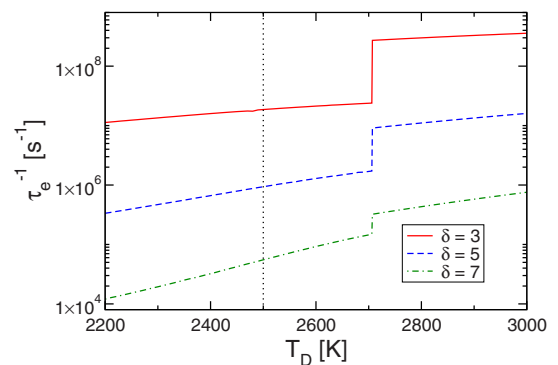


FIG. 5. (Color online) Inverse desorption time τ_e^{-1} in the two-phonon approximation as a function of the Debye temperature T_D for a two-phonon ($T_D < 2707$ K) and a one-phonon-deep potential ($T_D > 2707$ K) for different surface temperatures δ . At $T_D=2707$ K, the onset of one-phonon transitions between the lowest two states, τ_e^{-1} , increases considerably. Data for $T_D=2500$ K apply to graphite (thin vertical line).

the one-phonon transition probabilities dominate their two-phonon corrections as expected. For lower surface temperatures, however, the increase in τ_e^{-1} at the onset of one-phonon transitions becomes smaller. For instance, for $\delta=7$, it amounts only to a factor of 2. For very low surface temperatures, τ_e^{-1} even drops at the threshold, e.g., for $\delta=20$, by about 40% (not shown in Fig. 5). In this case, our assumption that the one-phonon transition probability dominates its two-phonon corrections is clearly not justified. An accurate calculation of τ_e^{-1} for a one-phonon-deep potential near $\Delta_{12}=-1$ requires therefore a calculation with all two-phonon transition probabilities included.

Within our model for the polarization-induced surface potential, graphite is very close to the $\Delta_{12}=-1$ threshold. The neglected two-phonon corrections to the one-phonon transition probabilities, however, would be only critical if Δ_{12} were slightly larger than -1 , not smaller, as it is in fact the case. Despite the approximations, we expect our numerical results to be reasonable for graphite, especially at higher temperatures, where the resonances of the regularized two-phonon transition probabilities, which are the reminiscences of the divergences of the original transition probabilities, are washed out making the transition probabilities rather robust against small changes in model parameters.

Figure 6 compares the dependence of τ_e^{-1} on the surface temperature for the potential depths shallow, one-phonon deep, and two-phonon deep, as realized by different values for the Debye temperature. For all potential depths, τ_e^{-1} increases with surface temperature. The increase of τ_e^{-1} for shallow and one-phonon-deep potentials is about the same and significantly steeper than for two-phonon deep potentials. For high temperatures, therefore, desorption from two-phonon-deep potentials lags behind desorption from one-phonon-deep potentials.

For the calculation with one-phonon transitions included only, we identified the second bound state as the most important intermediate state for the desorption cascade. We now study the role of intermediate bound states when two-phonon processes are taken into account. The goal is again to

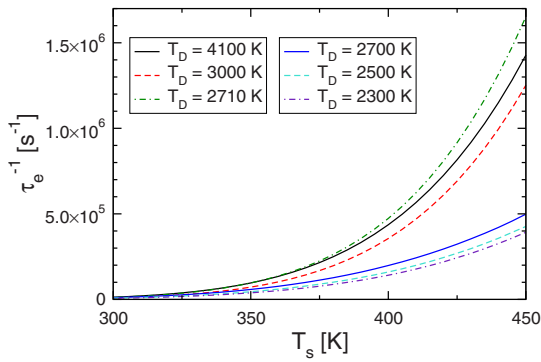


FIG. 6. (Color online) Inverse desorption time τ_e^{-1} in the two-phonon approximation as a function of the surface temperature for different potential depths. For high surface temperatures, desorption from a two-phonon-deep potential ($T_D=2700, 2500, 2300$ K) is significantly slower than desorption from a one-phonon-deep potential ($T_D=2710, 3000$ K) or a shallow potential ($T_D=4100$ K).

reveal the relative importance of direct desorption vs. desorption via cascades. Figure 7 shows that τ_e^{-1} saturates quickly with the number of bound states considered. Calculating τ_e^{-1} with only the two lowest bound states included gives essentially the correct result. In the case of the one-phonon calculation, we inferred from the fact that we need only two bound states, that the transition from the first to the second state is the most important one. Within the two-phonon calculation, however, the interpretation is not that simple because an additional bound state besides the lowest one has two influences: first, it makes cascade transitions with an intermediate bound state possible and second, it alters the transition probability for direct transitions from the lowest bound state to the continuum because it also acts as a virtual intermediate state in the contributions to the transition probabilities that stem from the iteration of the T matrix. Although the direct two-phonon transition probability from

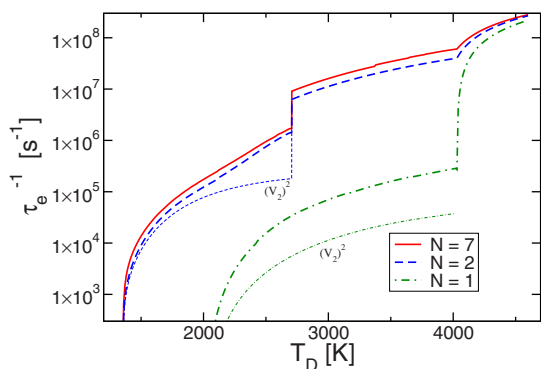


FIG. 7. (Color online) Inverse desorption time τ_e^{-1} in the two-phonon approximation for $\delta=5$ as a function of the Debye temperature T_D calculated with different numbers of bound states N . Above $T_D=2010$ K, the continuum is accessible from the lowest bound state by two-phonon processes; above $T_D=4029$ K by one-phonon processes. For $T_D < 2707$ K, the potential is two-phonon deep, for $2707 \text{ K} < T_D < 4029$ K it is one-phonon deep, and above $T_D = 4029$ K it is shallow. For the thin lines labeled with $(V_2)^2$, the two-phonon process has been calculated using $\tilde{\mathcal{R}}^9$ only.

the lowest bound state to the continuum is modified, it does not increase significantly with additional virtual intermediate bound states. Hence, the cascade transitions are by far more important than the modified direct transitions and make up almost the whole transition probability on their own.

In addition to the identification of the most efficient desorption channel, Fig. 7 enables us to compare our results to the ones obtained by Gortel *et al.*³⁶ Their Figs. 1–3, 5, and 6 show τ_e^{-1} for a single bound state as a function of the bound-state energy, whereas our Fig. 7 shows τ_e^{-1} as a function of the Debye temperature, which is proportional to the inverse of the potential depth. Hence, apart from scaling, Fig. 7 is mirror-inverted compared to their figures. For $N=1$, our approach applies to desorption from a single bound state, the situation studied by Gortel and co-workers. Despite the differences in the surface potential, arising from the fact that we are concerned with physisorption of an electron and Gortel *et al.* with physisorption of an atom, we also find that for potentials with depths allowing one-phonon transitions to the continuum desorption is much faster than for potentials whose depths require a two-phonon process for the transition from the bound state to the continuum. This results in a steep drop of τ_e^{-1} at $T_D < 2707$ K, when the one-phonon-deep potential becomes two-phonon deep. In contrast to Gortel *et al.*, however, we can include in the two-phonon calculation the other bound states. Then, for deep potentials, the stronger cascades set in and lead to a substantial increase of τ_e^{-1} .

Lastly, we look at the relative importance of the two-phonon processes arising, respectively, from the expansion of the perturbation (19) and the iteration of the T matrix (30). A two-phonon process can be simultaneous, as encoded in V_2 , or successive, as described by $V_1 G_0 V_1$. Hence, the total two-phonon transition probability (60) contains a contribution without virtual intermediate states, symbolically denoted by $(V_2)^2$ [see Eq. (41)] and two contributions with virtual intermediate states, symbolically denoted by $(V_1)^2 V_2$ and $(V_1)^4$ [see Eqs. (42), (44), and (45)].

The inverse desorption time obtained from a calculation where only two-phonon transitions due to $\tilde{\mathcal{R}}^9$, that is, due to the process $(V_2)^2$ have been included is shown by the thin green and blue lines in Fig. 7. For the direct transition from the lowest bound state ($N=1$, thin green line) to the continuum the process, $(V_2)^2$ is always dominated by the processes $(V_1)^2 V_2$ and $(V_1)^4$, as can be deduced by comparing the thick and thin green lines. For the more important cascade ($N=2$, thin blue line), however, the situation is more subtle. The processes $(V_1)^4$ and $(V_1)^2 V_2$, exhibiting resonances at $\Delta_{12}=-1$ [recall Eqs. (73) and (76) for the regularized two-phonon transition probabilities $\tilde{\mathcal{R}}^{10}$ and $\tilde{\mathcal{R}}^{14}$, respectively] are important only near $\Delta_{12}=-1$, that is, in the vicinity of $T_D=2707$ K. Far away from $T_D=2707$ K, it is in fact the process $(V_2)^2$ which gives the main contribution, as can be seen from the thin and thick blue lines in Fig. 7. Hence, depending on the type of the desorption process (direct vs. indirect via cascades), the energy difference between initial and final states, and the energy of the virtual intermediate states either of the two-phonon processes, $(V_2)^2$, $(V_1)^2 V_2$, and $(V_1)^4$, may be the most important one and neither can thus be neglected.

The role of simultaneous multiphonon vs. successive one-phonon processes has been also studied by Gumhalter and Šiber^{61–65} in the context of inelastic atom-surface scattering. In accordance with our observation of the dominance, in direct transitions, of $(V_1)^4$ and $(V_1)^2V_2$ over $(V_2)^2$, Šiber and Gumhalter⁶³ found that the main contribution to the inelastic multiphonon scattering probability stems from successive one-phonon processes and not from simultaneous multiphonon processes. Inelastic atom-surface scattering may also feature phonon-mediated resonances because in successive scattering events, bound states in the atom-surface potential act as virtual intermediate states in continuum-continuum transitions.^{64,65} In Gumhalter's cumulant formalism,⁶² this is encoded in the energy denominators of the operators he used to construct the scattering matrix for atom-surface scattering [see, for instance, Eq. (241) in Ref. 62 which represents, in our notation, the sequence $V_1G_0V_1$].

VI. CONCLUSIONS

We investigated phonon-mediated desorption of an image-bound electron from dielectric surfaces using a quantum-kinetic rate equation for the occupancies of the bound surface states for the electron. To avoid the unphysical divergence of the classical image potential, we included the recoil experienced by the electron when it couples to the dipole-active modes responsible for the polarization-induced interaction between the electron and the surface. Due to the coupling to bulk acoustic phonons, an electron initially occupying bound surface states may desorb when it gains enough energy to either directly reach an extended state or to successively climb up the ladder of bound states. To allow for an efficient calculation of the electronic matrix elements entering the transition probabilities in the quantum-kinetic rate equation, we derived asymptotic approximations for the electron wave functions and matrix elements.

For the dielectric materials relevant for bounded gas discharges (graphite, silicon oxide, aluminum oxide) or electron emitting devices (Cs-doped glass and GaAs heterostructures), the energy spacing of at least the two lowest image states is larger than the Debye energy. Hence, provided the surface temperatures are low enough for the electron to basically desorb from the lowest bound state, phonon-induced desorption has to occur for these materials via multiphonon processes, as they arise from the expansion of the electron-surface interaction potential with respect to the displacement field (originating from acoustic phonons) and the iteration of the T -matrix encoding the successive scattering of the external electron on the displacement field. Desorption channels involving internal electronic degrees of freedom are closed because the typical surface temperatures are too low for exciting these high-energy modes.

We presented results for a two-phonon-deep surface potential, where the energy difference between the lowest two bound states is between one and two Debye energies. Classifying two-phonon processes by the energy difference they allow to bridge in one- and two-Debye-energy transitions, we included two-phonon transition probabilities only for two-Debye-energy transitions, that is, for transitions where

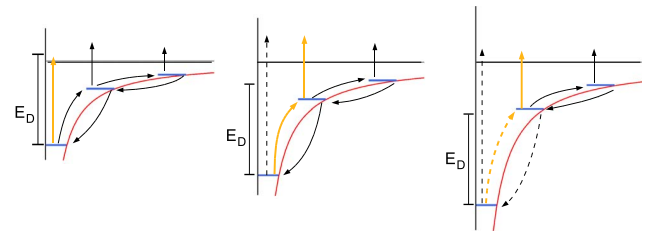


FIG. 8. (Color online) Desorption channels depending on the potential depth. Left panel shows a shallow potential, middle panel shows a one-phonon-deep potential, and right panel shows a two-phonon-deep potential. For the shallow potential, the predominant desorption channel (bold orange) is a direct transition to the continuum; for a deep potential the cascade via the second level is the most important channel. Full lines are one-phonon processes, dashed lines two-phonon processes, and $E_D = \hbar\omega_D = k_B T_D$.

the one-phonon transition probability vanishes. We regularized moreover spurious singularities in the two-phonon transition probabilities by taking a finite phonon lifetime into account.

The material parameters used for the numerical calculation apply to graphite, where the two-phonon approximation is applicable. For a surface temperature of 360 K, we find an electron desorption time of 2×10^{-5} s. Besides producing an estimate for the time τ_e with which an image-bound electron desorbs from a graphite surface, we also investigated, as a function of the surface temperature and the potential depth, the relative importance of direct vs. cascading desorption channels. For that purpose, we used the Debye energy as an adjustable parameter.

As expected, the inverse desorption time, τ_e^{-1} , depends strongly on the surface temperature, varying several orders of magnitude when the surface temperature changes. Depending on the depth of the surface potential, we identified various desorption scenarios. They are summarized in Fig. 8. For a shallow potential, all transitions between the bound states and the continuum are one-phonon processes. The lowest bound state can be emptied directly to the continuum. This is more efficient than the detour via higher bound states. For a one-phonon-deep potential, the transition from the lowest bound state to the continuum is a two-phonon process, whereas the transition to the second bound state and from there to the continuum is a one-phonon process. In this case, the cascade with two one-phonon processes is more efficient than the direct two-phonon process. For a two-phonon-deep potential, both the direct transition from the lowest bound state to the continuum and the transition from the lowest bound state to the second bound state are two-phonon processes. The direct transition to the continuum is much slower, so that the detour via the second state is the faster channel.

For most dielectrics of practical interest, more than two phonons are required implying that for these materials the desorption time for an image-bound electron may be in fact rather long. Indeed, in an ingenious experiment, using a field-effect transistor setup with the gate replaced by an externally provided electron surface charge, Biasini and co-workers^{25,26} determined the desorption time for an elec-

tron on a GaAs surface. They obtained 0.48 s which is rather long indeed but not unexpected, from our point of view, because the energy difference between the lowest two image states of GaAs, obtained from the dynamically corrected image potential, is $\Delta E_{12} = -0.152$ eV implying more than five phonons to be necessary for that transition ($\hbar\omega_D = 0.03$ eV for GaAs), which makes it accordingly unlikely.

In principle, the device of Biasini and co-workers^{25,26} would also allow to determine the electron sticking coefficient, making it a promising tool for a quantitative experimental investigation of physisorption of electrons specifically at GaAs surfaces. The empirical data about τ_e and s_e are however sparse in general. In view of the importance these two parameters have for the complete kinetic modeling of bounded plasmas, it is unacceptable to use them as adjustable parameters, as it is currently the case. We encourage therefore experimental groups to also design devices for the investigation of electron physisorption at surfaces which are used or naturally appear as boundaries of low-temperature gas discharges.

ACKNOWLEDGMENTS

This work was supported by the Deutsche Forschungsgemeinschaft (DFG) through the Transregional Collaborative Research Center SFB/TRR24. We acknowledge discussions with Hans Deutsch and Ralf Schneider.

APPENDIX A: SCHRÖDINGER EQUATION FOR SURFACE STATES

To obtain bound and unbound surface states, the Schrödinger equation (12) has to be solved with the proper boundary conditions. First, we consider bound states for which the wave functions have to vanish at $x=x_c$ and for $x \rightarrow \infty$. Substituting $y=2\Lambda_0 x/\kappa$, with $\kappa=\sqrt{-\Lambda_0^2/\eta}$, Eq. (12) takes the form

$$\phi''(y) + \left[\frac{\kappa}{y} - \frac{1}{4} \right] \phi(y) = 0, \quad (\text{A1})$$

whose solutions are Whittaker functions.⁶⁸ Hence, the wave functions which vanish at $x=x_c$ and for $x \rightarrow \infty$ are

$$\phi_q(x) = \frac{1}{\sqrt{a_B} \mathcal{N}_q} W_{\kappa, 1/2} \left(\frac{2\Lambda_0 x}{\kappa} \right), \quad (\text{A2})$$

where \mathcal{N}_q is a normalization constant defined by

$$\mathcal{N}_q^2 = \int_{x_c}^{\infty} dx W_{\kappa, 1/2}^2 \left(\frac{2\Lambda_0 x}{\kappa} \right). \quad (\text{A3})$$

The quantum number κ is determined by satisfying the boundary condition at the surface, $W_{\kappa, 1/2}(2\Lambda_0 x_c/\kappa) = 0$. This gives an infinite sequence of real numbers κ whose differences are however roughly one so that we can map them one-to-one onto integers q , that is, $q \leftrightarrow \kappa$. The energy of the bound state labeled with q is thus given by

$$E_q = - \frac{me^4 \Lambda_0^2}{2\hbar^2} \frac{1}{\kappa^2}. \quad (\text{A4})$$

Continuum states vanish only at $x=x_c$. Since for them the energy is positive, κ is imaginary. It is thus more convenient to label them with the real number $k=1/(i\kappa)$. The wave function for continuum states is given by a linear combination of Whittaker functions

$$\phi_k(x) = \frac{1}{\mathcal{N}_k} [W_{-ik, 1/2}(2i\Lambda_0 kx) + c W_{ik, 1/2}(-2i\Lambda_0 kx)], \quad (\text{A5})$$

where the constant,

$$c = -W_{-ik, 1/2}(2i\Lambda_0 kx_c)/W_{ik, 1/2}(-2i\Lambda_0 kx_c), \quad (\text{A6})$$

is chosen to enforce the boundary condition $\phi(x_c)=0$. Normalizing the wave function in a box of length L leads to the normalization constant $\mathcal{N}_k = \sqrt{2L} e^{\pi/k}$. The energy of the continuum states, finally, is given by

$$E_k = \frac{me^4 \Lambda_0^2}{2\hbar^2} k^2. \quad (\text{A7})$$

In the limit $L \rightarrow \infty$, sums over continuum states can thus be transformed into integrals according to⁶⁶

$$\sum_{k>0} \dots = \frac{\Lambda_0 L}{a_B \pi} \int dk \dots, \quad (\text{A8})$$

where the L factor in front of the integral cancels with the \sqrt{L} factor contained in the normalization constant \mathcal{N}_k .

APPENDIX B: EVALUATION OF THE MATRIX ELEMENTS

The electronic matrix element $Z_{q,q'}^n$ for two bound states labeled, respectively, by q and q' reads

$$Z_{q,q'}^n = \frac{1}{a_B^n \mathcal{N}_q \mathcal{N}_{q'}} \int_{x_c}^{\infty} dx W_{\kappa, 1/2} \left(\frac{2\Lambda_0 x}{\kappa} \right) \frac{1}{x^n} W_{\kappa', 1/2} \left(\frac{2\Lambda_0 x}{\kappa'} \right). \quad (\text{B1})$$

For the efficient numerical evaluation of \mathcal{N}_q and $Z_{q,q'}^n$, we use an expansion of Whittaker functions for $\kappa > 0$ in terms of Laguerre polynomials⁶⁶

$$W_{\kappa, 1/2}(x) = \sum_{n=0}^{\infty} \frac{\kappa(\kappa-1)e^{-1/2x} L_n(x)}{(\kappa-n)(\kappa-n-1)\Gamma(2-\kappa)}. \quad (\text{B2})$$

To calculate the bound-state matrix element $Z_{q,q'}^n$, we can compute one matrix element after another. First, we choose two states q and q' which fix the quantum numbers κ and κ' in the bound-state wave functions. Then, we integrate over x and obtain plain numbers for the matrix element which can be directly inserted into the calculation of the transition probabilities.

The evaluation of the electronic matrix element is more demanding if either one or both states are continuum states.

A wave function in the continuum is labeled by a real number k . If we were only interested in the value of the matrix element for some k , we could follow the same strategy as for bound states. Some transition probabilities however contain sums over all electronic states, e.g., the sum over q_1 in \mathcal{R}^{10} [see Eq. (58)], which for continuum states implies an integral over k . Hence, k is not merely a parameter that we can specify in advance. It is rather a variable in a matrix element which thus becomes a function of k ,

$$Z_{q,k}^n \rightarrow Z_q^n(k) = \int_{x_c}^{\infty} dx \phi_q(x) \frac{1}{a_B^{n-1} x^n} \phi_k(x). \quad (\text{B3})$$

For the two-phonon calculation, we specifically need the bound-continuum matrix element $Z_{q,k}^n$ for a given q and $0 < k < \infty$ and the continuum-continuum matrix element $Z_{k,k'}^2$ for $0 < k < \infty$ and k' small. Because of the complicated structure of the Whittaker function, the matrix elements cannot be obtained straightforwardly. To make their calculation feasible, we constructed approximate expressions for the continuum wave function $\phi_k(x)$ for small and large k , respectively, calculated the matrix elements in these two limits, and then interpolated between them with a Padé approximation.⁶⁶

We begin with the limit $k \rightarrow 0$. In this limit, the Schrödinger equation for the continuum states is

$$\phi''(x) + \frac{2\Lambda_0}{x} \phi(x) = 0, \quad (\text{B4})$$

which after the substitutions $t = 2\sqrt{2\Lambda_0}x$ and $\phi = t\psi$ takes the form of the Bessel differential equation,⁶⁹

$$\psi'' + \frac{1}{t} \psi' + \left(1 - \frac{1}{t^2}\right) \psi = 0. \quad (\text{B5})$$

Hence, in the limit $k \rightarrow 0$, the continuum wave function satisfying the boundary condition $\phi_k(x_c) = 0$ can be written as a linear combination of Bessel and Neumann functions.

There is however one technical caveat. Bessel and Neumann functions grow beyond limit for large x [see formula (9.2.1) in Ref. 70] and cannot be normalized. Within the matrix element, this is not dangerous because the decreasing factors $1/x^n$ compensate the divergence at large x . The only problem left is to find the prefactor by which we have to multiply the linear combination so that it has for small x the amplitude of the correct $\phi_{k \rightarrow 0}(x)$. Once we have this factor, the linear combination is normalized in the sense that its envelope coincides for small x with the envelope of the correct $\phi_{k \rightarrow 0}(x)$.

The most direct way to obtain the required multiplication factor is to perform the limit $k \rightarrow 0$ in the continuum wave function (A5). Due to the complicated structure of the Whittaker function, this is however not feasible. Instead, it is better to determine the factor from the solution of Eq. (B5),

$$\phi(x)_{k \rightarrow 0} = 2\sqrt{2\Lambda_0}x J_1(2\sqrt{2\Lambda_0}x), \quad (\text{B6})$$

which satisfies the boundary condition $\phi(0) = 0$. The solution of Eq. (12) satisfying the same boundary condition is given by

$$\phi_k(x) = \tilde{\mathcal{N}}_k^{-1} M_{-i/k, 1/2}(2i\Lambda_0 kx), \quad (\text{B7})$$

with the normalization constant

$$\tilde{\mathcal{N}}_k^{-1} = \sqrt{\frac{\pi}{Lk(1 - e^{-2\pi/k})}}. \quad (\text{B8})$$

In the limit $k \rightarrow 0$, Eq. (B7) merges into Eq. (B6) because

$$M_{-i/k, 1/2}(2i\Lambda_0 kx) \xrightarrow{k \rightarrow 0} ik\sqrt{2\Lambda_0}x J_1(\sqrt{8\Lambda_0}x). \quad (\text{B9})$$

For the normalization constant, we thus obtain $\tilde{\mathcal{N}}_k^{-1} \rightarrow \sqrt{\pi/(Lk)}$ for $k \rightarrow 0$. The fact that k and x are tied together in the argument of $M_{-i/k, 1/2}(2i\Lambda_0 kx)$ suggests that an approximation for small k is at the same time an approximation for small x . Since we need the wave function only for small x and small k , we expect the replacement (B9) to provide good results for the desired normalization factor.

Since the amplitudes of Bessel and Neumann functions are the same for large x , we can use the normalization obtained for the Bessel function for the Neumann function as well. A normalized approximation satisfying the correct boundary condition, $\phi_k(x_c) = 0$, is then given by

$$\begin{aligned} \phi(x)_{k \rightarrow 0} = \frac{1}{\sqrt{L}} \sqrt{\frac{\pi}{1 + \tilde{c}^2}} \sqrt{k2\Lambda_0}x [J_1(2\sqrt{2\Lambda_0}x) \\ - \tilde{c}N_1(2\sqrt{2\Lambda_0}x)], \end{aligned} \quad (\text{B10})$$

with

$$\tilde{c} = -J_1(2\sqrt{2\Lambda_0}x_c)/N_1(2\sqrt{2\Lambda_0}x_c). \quad (\text{B11})$$

Using Eq. (B10), the matrix element $Z_{q,k}^n$ can be evaluated in the limit $k \rightarrow 0$. We find

$$Z_{q,k \rightarrow 0}^n = \int_{x_c}^{\infty} dx \frac{\phi_q(x) \phi_{k \rightarrow 0}(x)}{a_B^{n-1} x^n} = \frac{\alpha_q^n \sqrt{k}}{a_B^{n-1/2} \sqrt{L} \mathcal{N}_q}, \quad (\text{B12})$$

where the k dependency is separated so that the remaining integral gives a k -independent quantity, α_q^n , which has to be obtained numerically. Similarly,

$$Z_{k \rightarrow 0, k' \rightarrow 0} = \int_{x_c}^{\infty} dx \frac{\phi_{k' \rightarrow 0}(x) \phi_{k \rightarrow 0}(x)}{a_B x^2} = \frac{\alpha_c^2 \sqrt{kk'}}{La_B}, \quad (\text{B13})$$

with α_c^2 again a constant to be determined numerically.

We now proceed to the approximation of the continuum wave functions for large k . The higher the energy of the continuum states, the lesser the potential at the surface changes the plane-wave behavior far from the surface. Therefore, in the limit $k \rightarrow \infty$, we can accurately describe the wave function by a plane wave. Using the asymptotic form for the Whittaker function (Ref. 69),

$$W_{-i/k,1/2}(2i\Lambda_0 kx) \approx e^{-i\Lambda_0 kx} e^{\pi/2k}, \quad (\text{B14})$$

the continuum wave function in the limit $k \rightarrow \infty$ satisfying the correct boundary condition, $\phi_k(x_c)=0$, can be approximated by

$$\phi_k(x) = \sqrt{2/L} \sin[\Lambda_0 k(x - x_c)]. \quad (\text{B15})$$

Employing, finally, the Fourier integral,⁷¹ the matrix elements for large k can be shown to be⁶⁶

$$\begin{aligned} Z_{q,k \rightarrow \infty}^n &= \frac{1}{a_B^{n-1/2} \sqrt{L} \mathcal{N}_q} \frac{2\sqrt{2}n}{(\Lambda_0 k)^3 x_c^{n+1}} W'_{\kappa,1/2} \left(\frac{2\Lambda_0}{\kappa} x_c \right) \\ &= \frac{1}{a_B^{n-1/2} \sqrt{L} \mathcal{N}_q} b_q^n \frac{1}{k^3} \end{aligned} \quad (\text{B16})$$

and

$$\begin{aligned} Z_{k' \rightarrow 0, k \rightarrow \infty}^2 &= \frac{1}{La_B} \sqrt{\frac{\pi}{1 + \tilde{c}^2}} \frac{32}{\Lambda_0^{3/2} x_c^3} \\ &\quad \times [J_0(\sqrt{8\Lambda_0 x_c}) - \tilde{c} N_0(\sqrt{8\Lambda_0 x_c})] \frac{\sqrt{k'}}{k^3} \\ &= \frac{1}{La_B} b_c^2 \frac{\sqrt{k'}}{k^3}, \end{aligned} \quad (\text{B17})$$

where the k -independent coefficients b_q^n and b_c^2 have to be worked out again numerically.

Having calculated the leading terms for the matrix elements for small and large k , we can combine these two limits via a Padé approximation in terms of \sqrt{k} . The coefficients are chosen in such a way that the Padé approximation matches the leading term of both limits: $k \rightarrow 0$ and $k \rightarrow \infty$. Then, the matrix elements read

$$Z_{q,k}^n = \frac{1}{\sqrt{La_B^{n-1/2} \mathcal{N}_q}} \frac{\alpha_q^n k^{1/2}}{1 + \beta_q^n k^{7/2}}, \quad (\text{B18})$$

where $\beta_q^n = \alpha_q^n / b_q^n$ and

$$Z_{k,k'}^2 = \frac{1}{La_B} \frac{\alpha_c^2 k'^{1/2} k^{1/2}}{1 + \beta_c^2 k'^{7/2}}, \quad (\text{B19})$$

where $\beta_c^2 = \alpha_c^2 / b_c^2$.

APPENDIX C: TRANSITION PROBABILITIES IN A COMPACT FORM

In this appendix, we list the one- and two-phonon transition probabilities as used in the numerical calculation of the desorption time. We implicitly assume that q labels both bound and unbound states. For a bound state, q is simply an integer [to be mapped onto $\kappa(q)$] whereas for a continuum state, q stands for a real number k . To obtain a compact form for the transition probabilities, it is moreover convenient to introduce dimensionless variables

$$x = \frac{\omega}{\omega_D}, \quad (\text{C1})$$

$$\epsilon_q = \frac{E_q}{\hbar\omega_D}, \quad (\text{C2})$$

$$\Delta_{q,q'} = \frac{E_q - E_{q'}}{\hbar\omega_D}, \quad (\text{C3})$$

$$\delta = \frac{\hbar\omega_D}{k_B T}, \quad (\text{C4})$$

$$\nu(x) = \frac{\gamma\omega}{\omega_D}. \quad (\text{C5})$$

The transition probability of $\mathcal{O}(u^2)$, that is, the one-phonon transition probability employed in a golden rule approximation, is given by

$$\begin{aligned} \mathcal{R}^1(q', q) &= \frac{2\pi}{\hbar} \sum_Q G_{q,q'}^1(Q) [G_{q,q'}^1(Q)]^* \{n_B(\hbar\omega_Q) \delta(E_q - E_{q'} \\ &\quad + \hbar\omega_Q) + [1 + n_B(\hbar\omega_Q)] \delta(E_q - E_{q'} - \hbar\omega_Q)\} \\ &= \frac{3\pi e^4 \Lambda_0^2}{\hbar \mu \omega_D^2} Z_{q,q'}^2 Z_{q,q'}^2 [I_{(1)}^1(q', q) + I_{(1)}^2(q', q)], \end{aligned} \quad (\text{C6})$$

where

$$I_{(1)}^1(q', q) = \frac{-\Delta_{q,q'}}{e^{-\delta\Delta_{q,q'}} - 1} \text{ for } 0 \leq -\Delta_{q,q'} \leq 1 \quad (\text{C7})$$

and

$$I_{(1)}^2(q', q) = \Delta_{q,q'} \left[1 + \frac{1}{e^{\delta\Delta_{q,q'}} - 1} \right] \text{ for } 0 \leq \Delta_{q,q'} \leq 1. \quad (\text{C8})$$

Otherwise, $I_{(1)}^1$ and $I_{(1)}^2$ are zero. Depending on whether q and q' denote bound or continuum states, the electronic matrix element $Z_{q,q'}^2$ is either given by Eq. (B1), (B18), or (B19).

As explained in Sec. IV B, we keep only those parts of the transition probabilities of $\mathcal{O}(u^4)$ which give rise to what we call two-Debye-energy transitions, which are transitions between states that are between one and two Debye energies apart. In the unregularized form, that is, in the form which diverges in particular situations (see Sec. IV C for a discussion), the two-phonon transition probabilities included in our calculation are given by

$$\begin{aligned} \tilde{\mathcal{R}}^9(q', q) &= \frac{2\pi}{\hbar} \sum_{Q_1, Q_2} G_{q', q}^2(Q_1, Q_1) [G_{q', q}^2(Q_2, Q_2)]^* \{2n_B(\hbar\omega_{Q_1})n_B(\hbar\omega_{Q_2})\delta(E_q - E_{q'} + \hbar\omega_{Q_1} + \hbar\omega_{Q_2}) \\ &+ 2[1 + n_B(\hbar\omega_{Q_1})][1 + n_B(\hbar\omega_{Q_2})]\delta(E_q - E_{q'} - \hbar\omega_{Q_1} - \hbar\omega_{Q_2})\} = \frac{9\pi e^4 \Lambda_0^2}{\mu^2 \omega_D^3} Z_{q, q'}^3 Z_{q, q'}^3 [I_{(2)}^1(q', q) + I_{(2)}^2(q', q)], \end{aligned} \quad (C9)$$

$$\begin{aligned} \tilde{\mathcal{R}}^{10}(q', q) &= -\frac{2\pi}{\hbar} \sum_{Q_1, Q_2} G_{q', q}^2(Q_1, Q_1) [G_{q_1, q}^1(Q_2) G_{q', q_1}^1(Q_2)]^* \left\{ 2n_B(\hbar\omega_{Q_1})n_B(\hbar\omega_{Q_2}) \frac{\delta(E_q - E_{q'} + \hbar\omega_{Q_1} + \hbar\omega_{Q_2})}{E_q - E_{q_1} + \hbar\omega_{Q_1} - i\epsilon} \right. \\ &+ \left. 2[1 + n_B(\hbar\omega_{Q_1})][1 + n_B(\hbar\omega_{Q_2})] \frac{\delta(E_q - E_{q'} - \hbar\omega_{Q_1} - \hbar\omega_{Q_2})}{E_q - E_{q_1} - \hbar\omega_{Q_1} - i\epsilon} \right\} \\ &= -\frac{9\pi e^6 \Lambda_0^3}{\hbar \mu^2 \omega_D^4} \sum_{q_1} Z_{q', q}^3 Z_{q, q_1}^2 Z_{q_1, q'}^2 [I_{(2)}^3(q', q; q_1) + I_{(2)}^4(q', q; q_1)], \end{aligned} \quad (C10)$$

$$\begin{aligned} \tilde{\mathcal{R}}^{14}(q', q) &= \frac{2\pi}{\hbar} \sum_{q_1, q_2} \sum_{Q_1, Q_2} G_{q', q_1}^1(Q_1) G_{q_1, q}^1(Q_1) [G_{q', q_2}^1(Q_2) G_{q_2, q}^1(Q_2)]^* \\ &\times \left\{ n_B(\hbar\omega_{Q_1})n_B(\hbar\omega_{Q_2}) \frac{\delta(E_q - E_{q'} + \hbar\omega_{Q_1} + \hbar\omega_{Q_2})}{(E_q - E_{q_1} + \hbar\omega_{Q_2} + i\epsilon)(E_q - E_{q_2} + \hbar\omega_{Q_1} - i\epsilon)} \right. \\ &+ n_B(\hbar\omega_{Q_1})n_B(\hbar\omega_{Q_2}) \frac{\delta(E_q - E_{q'} + \hbar\omega_{Q_1} + \hbar\omega_{Q_2})}{(E_q - E_{q_1} + \hbar\omega_{Q_1} + i\epsilon)(E_q - E_{q_2} + \hbar\omega_{Q_1} - i\epsilon)} \\ &+ [1 + n_B(\hbar\omega_{Q_1})][1 + n_B(\hbar\omega_{Q_2})] \frac{\delta(E_q - E_{q'} - \hbar\omega_{Q_1} - \hbar\omega_{Q_2})}{(E_q - E_{q_1} - \hbar\omega_{Q_2} + i\epsilon)(E_q - E_{q_2} - \hbar\omega_{Q_1} - i\epsilon)} \\ &+ \left. [1 + n_B(\hbar\omega_{Q_1})][1 + n_B(\hbar\omega_{Q_2})] \frac{\delta(E_q - E_{q'} - \hbar\omega_{Q_1} - \hbar\omega_{Q_2})}{(E_q - E_{q_1} - \hbar\omega_{Q_2} + i\epsilon)(E_q - E_{q_2} - \hbar\omega_{Q_2} - i\epsilon)} \right\} \\ &= \frac{9\pi e^8 \Lambda_0^4}{2\hbar^2 \mu^2 \omega_D^5} \sum_{q_1, q_2} Z_{q', q_1}^2 Z_{q_1, q}^2 Z_{q, q_2}^2 Z_{q_2, q'}^2 [I_{(2)}^5(q', q; q_1, q_2) + I_{(2)}^6(q', q; q_1, q_2) + I_{(2)}^7(q', q; q_1, q_2) + I_{(2)}^8(q', q; q_1, q_2)], \end{aligned} \quad (C11)$$

where, in the limit $\epsilon \rightarrow 0$, the auxiliary integrals are defined by

$$I_{(2)}^1(q', q) = \int_{-\Delta_{q, q'}-1}^1 dx \frac{x}{e^{\delta x} - 1} \frac{-\Delta_{q, q'} - x}{e^{\delta(-\Delta_{q, q'} - x)} - 1}, \quad (C12)$$

$$I_{(2)}^2(q', q) = \int_{\Delta_{q, q'}-1}^1 dx x \left[1 + \frac{1}{e^{\delta x} - 1} \right] (\Delta_{q, q'} - x) \left[1 + \frac{1}{e^{\delta(\Delta_{q, q'} - x)} - 1} \right], \quad (C13)$$

$$I_{(2)}^3(q', q; q_1) = \int_{-\Delta_{q, q'}-1}^1 dx \frac{x}{e^{\delta x} - 1} \frac{-\Delta_{q, q'} - x}{e^{\delta(-\Delta_{q, q'} - x)} - 1} \frac{1}{\Delta_{q, q_1} + x - i\epsilon}, \quad (C14)$$

$$I_{(2)}^4(q', q; q_1) = \int_{\Delta_{q, q'}-1}^1 dx x \left[1 + \frac{1}{e^{\delta x} - 1} \right] (\Delta_{q, q'} - x) \left[1 + \frac{1}{e^{\delta(\Delta_{q, q'} - x)} - 1} \right] \frac{1}{\Delta_{q, q_1} - x - i\epsilon}, \quad (C15)$$

$$I_{(2)}^5(q', q; q_1, q_2) = \int_{-\Delta_{q, q'}-1}^1 dx \frac{x}{e^{\delta x} - 1} \frac{-\Delta_{q, q'} - x}{e^{\delta(-\Delta_{q, q'} - x)} - 1} \frac{1}{\Delta_{q', q_1} - x + i\epsilon} \frac{1}{\Delta_{q, q_2} + x - i\epsilon}, \quad (C16)$$

$$I_{(2)}^6(q', q; q_1, q_2) = \int_{-\Delta_{q,q'}-1}^1 dx \frac{x}{e^{\delta x} - 1} \frac{-\Delta_{q,q'} - x}{e^{\delta(-\Delta_{q,q'} - x)} - 1} \frac{1}{\Delta_{q,q_1} + x + i\epsilon} \frac{1}{\Delta_{q,q_2} + x - i\epsilon}, \quad (\text{C17})$$

$$I_{(2)}^7(q', q; q_1, q_2) = \int_{\Delta_{q,q'}-1}^1 dx \left[1 + \frac{1}{e^{\delta x} - 1} \right] (\Delta_{q,q'} - x) \left[1 + \frac{1}{e^{\delta(\Delta_{q,q'} - x)} - 1} \right] \frac{1}{\Delta_{q',q_1} + x + i\epsilon} \frac{1}{\Delta_{q,q_2} - x - i\epsilon}, \quad (\text{C18})$$

$$I_{(2)}^8(q', q; q_1, q_2) = \int_{\Delta_{q,q'}-1}^1 dx \left[1 + \frac{1}{e^{\delta x} - 1} \right] (\Delta_{q,q'} - x) \left[1 + \frac{1}{e^{\delta(\Delta_{q,q'} - x)} - 1} \right] \frac{1}{\Delta_{q,q_1} - x + i\epsilon} \frac{1}{\Delta_{q,q_2} - x - i\epsilon}. \quad (\text{C19})$$

The two-phonon transition probabilities $\tilde{\mathcal{R}}^{10}$ and $\tilde{\mathcal{R}}^{14}$ diverge for the situations studied in this paper. They have to be therefore regularized. The regularization procedure outlined in Sec. IV C leads then to the divergence-free, regularized transition probabilities

$$\tilde{\mathcal{R}}^{10}(q', q) = -\frac{9\pi e^6 \Lambda_0^3}{\hbar \mu^2 \omega_D^4} \sum_{q_1} Z_{q',q}^3 Z_{q',q_1}^2 Z_{q_1,q}^2 [I_{(2)}^{3'}(q', q; q_1) + I_{(2)}^{4'}(q', q; q_1)], \quad (\text{C20})$$

$$\tilde{\mathcal{R}}^{14}(q', q) = \frac{9\pi e^8 \Lambda_0^4}{2\hbar^2 \mu^2 \omega_D^5} \sum_{q_1, q_2} Z_{q',q_1}^2 Z_{q_1,q}^2 Z_{q,q_2}^2 Z_{q_2,q'}^2 [I_{(2)}^{5'}(q', q; q_1, q_2) + I_{(2)}^{7'}(q', q; q_1, q_2)], \quad (\text{C21})$$

where the integrals are given by

$$I_{(2)}^{3'}(q', q; q_1) = \int_{-\Delta_{q,q'}-1}^1 dx \frac{x}{e^{\delta x} - 1} \frac{-\Delta_{q,q'} - x}{e^{\delta(-\Delta_{q,q'} - x)} - 1} g[\Delta_{q,q_1} + x, \nu(-x - \Delta_{q,q'}) + 2\nu(x)], \quad (\text{C22})$$

$$I_{(2)}^{4'}(q', q; q_1) = \int_{\Delta_{q,q'}-1}^1 dx \left(1 + \frac{1}{e^{\delta x} - 1} \right) (\Delta_{q,q'} - x) \left[1 + \frac{1}{e^{\delta(\Delta_{q,q'} - x)} - 1} \right] g[\Delta_{q,q_1} - x, \nu(\Delta_{q,q'} - x) + 2\nu(x)], \quad (\text{C23})$$

$$I_{(2)}^{5'}(q', q; q_1, q_2) = \int_{-\Delta_{q,q'}-1}^1 dx \frac{x}{e^{\delta x} - 1} \frac{-\Delta_{q,q'} - x}{e^{\delta(-\Delta_{q,q'} - x)} - 1} \{f[\Delta_{q',q_1} - x, \Delta_{q,q_2} + x, \nu(x) + 2\nu(-x - \Delta_{q,q'}), 2\nu(x) + \nu(-x - \Delta_{q,q'})] \\ + f[\Delta_{q,q_1} + x, \Delta_{q,q_2} + x, 2\nu(x) + \nu(-x - \Delta_{q,q'}), 2\nu(x) + \nu(-x - \Delta_{q,q'})]\}, \quad (\text{C24})$$

$$I_{(2)}^{7'}(q', q; q_1, q_2) = \int_{\Delta_{q,q'}-1}^1 dx \left(1 + \frac{1}{e^{\delta x} - 1} \right) (\Delta_{q,q'} - x) \left[1 + \frac{1}{e^{\delta(\Delta_{q,q'} - x)} - 1} \right] \{f[\Delta_{q',q_1} + x, \Delta_{q,q_2} - x, \nu(x) + 2\nu(\Delta_{q,q'} - x), 2\nu(x) \\ + \nu(\Delta_{q,q'} - x)] + f[\Delta_{q,q_1} - x, \Delta_{q,q_2} - x, 2\nu(x) + \nu(\Delta_{q,q'} - x), 2\nu(x) + \nu(\Delta_{q,q'} - x)]\}. \quad (\text{C25})$$

¹C. J. F. Boettcher, *Theory of Electric Polarization* (Elsevier Publishing Company, Amsterdam, 1952).

²M. W. Cole and M. H. Cohen, *Phys. Rev. Lett.* **23**, 1238 (1969).

³V. Dose, W. Altmann, A. Goldmann, U. Kolac, and J. Rogozik, *Phys. Rev. Lett.* **52**, 1919 (1984).

⁴D. Straub and F. J. Himpsel, *Phys. Rev. Lett.* **52**, 1922 (1984).

⁵D. P. Woodruff, S. L. Hulbert, P. D. Johnson, and N. V. Smith, *Phys. Rev. B* **31**, 4046 (1985).

⁶W. Jacob, V. Dose, U. Kolac, and T. Fauster, *Z. Phys. B* **63**, 459 (1986).

⁷T. Fauster, *Appl. Phys. A: Mater. Sci. Process.* **59**, 479 (1994).

⁸U. Höfer, I. L. Shumay, C. Reuss, U. Thomann, W. Wallauer, and T. Fauster, *Science* **277**, 1480 (1997).

⁹U. Höfer, *Appl. Phys. B: Lasers Opt.* **68**, 383 (1999).

¹⁰T. Fauster and M. Weinelt, *Surf. Sci.* **593**, 1 (2005).

¹¹B. Gumhalter, A. Šiber, H. Buljan, and T. Fauster, *Phys. Rev. B* **78**, 155410 (2008).

¹²M. W. Cole, *Rev. Mod. Phys.* **46**, 451 (1974).

¹³J. Lehmann, M. Merschdorf, A. Thon, S. Voll, and W. Pfeiffer, *Phys. Rev. B* **60**, 17037 (1999).

¹⁴M. Kutschera, M. Weinelt, M. Rohlfing, and T. Fauster, *Appl. Phys. A: Mater. Sci. Process.* **88**, 519 (2007).

¹⁵F. J. Himpsel, J. A. Knapp, J. A. VanVechten, and D. E. Eastman, *Phys. Rev. B* **20**, 624 (1979).

¹⁶J. B. Cui, J. Ristein, and L. Ley, *Phys. Rev. Lett.* **81**, 429 (1998).

¹⁷H. Yamaguchi, T. Masuzawa, S. Nozue, Y. Kudo, I. Saito,

- J. Koe, M. Kudo, T. Yamada, Y. Takakuwa, and K. Okano, *Phys. Rev. B* **80**, 165321 (2009).
- ¹⁸K. P. Loh, I. Sakaguchi, M. N. Gamo, S. Tagawa, T. Sugino, and T. Ando, *Appl. Phys. Lett.* **74**, 28 (1999).
- ¹⁹M. Rohlfling, N.-P. Wang, P. Kruger, and J. Pollmann, *Phys. Rev. Lett.* **91**, 256802 (2003).
- ²⁰B. Baumeier, P. Kruger, and J. Pollmann, *Phys. Rev. B* **76**, 205404 (2007).
- ²¹K. P. McKenna and A. L. Shluger, *Nature Mater.* **7**, 859 (2008).
- ²²L. N. Dinh, W. McLean, M. A. Schildbach, and M. Balooch, *Phys. Rev. B* **59**, 15513 (1999).
- ²³M. W. Geis, S. Deneault, K. E. Krohn, M. Marchant, T. M. Lyszczarz, and D. L. Cooke, *Appl. Phys. Lett.* **87**, 192115 (2005).
- ²⁴A. Mayer, M. S. Chung, N. Kumar, B. L. Weiss, N. M. Miskovsky, and P. H. Cutler, *J. Vac. Sci. Technol. B* **24**, 629 (2006).
- ²⁵M. Biasini, R. D. Gann, J. A. Yarmoff, A. P. Mills, L. N. Pfeiffer, K. W. West, X. P. W. Gao, and B. C. D. Williams, *Appl. Phys. Lett.* **86**, 162111 (2005).
- ²⁶M. Biasini, R. D. Gann, L. N. Pfeiffer, K. W. West, X. P. W. Gao, B. C. D. Williams, J. A. Yarmoff, and A. P. M. Jr, *Eur. Phys. J. B* **47**, 305 (2005).
- ²⁷N. Yamamoto *et al.*, *J. Appl. Phys.* **102**, 024904 (2007).
- ²⁸M.-C. Desjonqueres and D. Spanjaard, *Concepts of Surface Physics* (Springer-Verlag, Berlin, 1996).
- ²⁹J. E. Lennard-Jones and C. Strachan, *Proc. R. Soc. London, Ser. A* **150**, 442 (1935).
- ³⁰C. Strachan, *Proc. R. Soc. London, Ser. A* **150**, 456 (1935).
- ³¹J. E. Lennard-Jones and A. F. Devonshire, *Proc. R. Soc. London, Ser. A* **156**, 6 (1936).
- ³²B. Bendow and S.-C. Ying, *Phys. Rev. B* **7**, 622 (1973).
- ³³W. Brenig, *Z. Phys. B* **48**, 127 (1982).
- ³⁴Z. W. Gortel, H. J. Kreuzer, and D. Spaner, *J. Chem. Phys.* **72**, 234 (1980).
- ³⁵Z. W. Gortel, H. J. Kreuzer, and R. Teshima, *Phys. Rev. B* **22**, 5655 (1980).
- ³⁶Z. W. Gortel, H. J. Kreuzer, and R. Teshima, *Phys. Rev. B* **22**, 512 (1980).
- ³⁷H. J. Kreuzer and Z. W. Gortel, *Physisorption Kinetics* (Springer-Verlag, Berlin, 1986).
- ³⁸W. Brenig, *Phys. Scr.* **35**, 329 (1987).
- ³⁹F. X. Bronold, H. Fehske, H. Kersten, and H. Deutsch, *Phys. Rev. Lett.* **101**, 175002 (2008).
- ⁴⁰F. X. Bronold, H. Deutsch, and H. Fehske, *Eur. Phys. J. D* **54**, 519 (2009).
- ⁴¹E. C. Whipple, *Rep. Prog. Phys.* **44**, 1197 (1981).
- ⁴²B. T. Draine and B. Sutin, *Astrophys. J.* **320**, 803 (1987).
- ⁴³I. Mann, *Adv. Space Res.* **41**, 160 (2008).
- ⁴⁴M. Rapp and F.-J. Luebken, *J. Atmos. Sol.-Terr. Phys.* **63**, 759 (2001).
- ⁴⁵V. E. Fortov, A. V. Ivlev, S. A. Khrapak, A. G. Khrapak, and G. E. Morfill, *Phys. Rep.* **421**, 1 (2005).
- ⁴⁶O. Ishihara, *J. Phys. D* **40**, R121 (2007).
- ⁴⁷Y. B. Golubovskii, V. A. Maiorov, J. Behnke, and J. F. Behnke, *J. Phys. D* **35**, 751 (2002).
- ⁴⁸U. Kogelschatz, *Plasma Chem. Plasma Process.* **23**, 1 (2003).
- ⁴⁹M. Li, C. Li, H. Zhan, and J. Xu, Proceedings of the XV International Conference on Gas Discharges and their Applications, 2004.
- ⁵⁰L. Stollenwerk, S. Amiranashvili, J.-P. Boeuf, and H.-G. Purwins, *Phys. Rev. Lett.* **96**, 255001 (2006).
- ⁵¹L. Stollenwerk, J. G. Laven, and H.-G. Purwins, *Phys. Rev. Lett.* **98**, 255001 (2007).
- ⁵²M. Li, C. Li, H. Zhan, and J. Xu, *Appl. Phys. Lett.* **92**, 031503 (2008).
- ⁵³I. Kusčer, in *Fundamental Problems In Statistical Physics IV*, edited by E. G. D. Cohen and W. Fiszdon (Ossolineum, Warsaw, 1978), p. 441.
- ⁵⁴G. Fan and J. R. Manson, *Phys. Rev. B* **79**, 045424 (2009).
- ⁵⁵G. Fan and J. R. Manson, *J. Chem. Phys.* **130**, 064703 (2009).
- ⁵⁶D. Neilson, R. M. Nieminen, and J. Szymański, *Phys. Rev. B* **33**, 1567 (1986).
- ⁵⁷A. B. Walker, K. O. Jensen, J. Szymański, and D. Neilson, *Phys. Rev. B* **46**, 1687 (1992).
- ⁵⁸R. Ray and G. D. Mahan, *Phys. Lett.* **42A**, 301 (1972).
- ⁵⁹E. Evans and D. L. Mills, *Phys. Rev. B* **8**, 4004 (1973).
- ⁶⁰J. A. Misewich, T. F. Heinz, and D. M. Newns, *Phys. Rev. Lett.* **68**, 3737 (1992).
- ⁶¹B. Gumhalter, *Surf. Sci.* **347**, 237 (1996).
- ⁶²B. Gumhalter, *Phys. Rep.* **351**, 1 (2001).
- ⁶³A. Šiber and B. Gumhalter, *Phys. Rev. Lett.* **90**, 126103 (2003).
- ⁶⁴A. Šiber and B. Gumhalter, *Phys. Rev. B* **71**, 081401(R) (2005).
- ⁶⁵A. Šiber and B. Gumhalter, *J. Phys.: Condens. Matter* **20**, 224002 (2008).
- ⁶⁶R. L. Heinisch, Diploma thesis, Universität Greifswald, 2009.
- ⁶⁷P. G. Klemens, *Int. J. Thermophys.* **22**, 265 (2001).
- ⁶⁸E. T. Whittaker and G. N. Watson, *A Course of Modern Analysis* (Cambridge University Press, London, 1927).
- ⁶⁹W. Magnus and F. Oberhettinger, *Formeln und Sätze fuer die Speziellen Funktionen der Mathematischen Physik* (Springer, New York, 1948).
- ⁷⁰*Handbook of Mathematical Functions*, edited by M. Abramowitz and I. A. Stegun (Dover Publications, Inc., New York, 1973).
- ⁷¹F. W. J. Olver, *Asymptotics and Special Functions* (Academic Press, New York, 1974).

Phonon-mediated sticking of electrons at dielectric surfaces

R. L. Heinisch, F. X. Bronold, and H. Fehske

Institut für Physik, Ernst-Moritz-Arndt-Universität Greifswald, 17489 Greifswald, Germany

(Received 9 June 2010; published 7 September 2010)

We study phonon-mediated temporary trapping of an electron in polarization-induced external surface states (image states) of a dielectric surface. Our approach is based on a quantum-kinetic equation for the occupancy of the image states. It allows us to distinguish between prompt and kinetic sticking. Because the depth of the image potential is much larger than the Debye energy multiphonon processes are important. Taking two-phonon processes into account in cases where one-phonon processes yield a vanishing transition probability, as it is applicable, for instance, to graphite, we analyze the adsorption scenario as a function of potential depth and surface temperature and calculate prompt and kinetic sticking coefficients. We find rather small sticking coefficients, at most on the order of 10^{-3} , and a significant suppression of the kinetic sticking coefficient due to a relaxation bottleneck inhibiting thermalization of the electron with the surface at short time scales.

DOI: [10.1103/PhysRevB.82.125408](https://doi.org/10.1103/PhysRevB.82.125408)

PACS number(s): 52.40.Hf, 73.20.-r, 68.43.Mn

I. INTRODUCTION

A complete kinetic modeling of atmospheric,¹ interstellar,²⁻⁴ or man-made bounded plasmas⁵⁻¹² requires boundary conditions for the distribution functions of the relevant plasma species (electrons, ions, neutrals), that is, a quantitative microscopic understanding of the elementary processes at the plasma boundary. Of particular importance is the buildup of a quasistationary negative surface charge, which not only depletes the electron density in front of the boundary (sheath formation) but also acts as an electron reservoir for surface-supported electron-ion recombination and secondary electron emission which in turn affect the charge balance in the bulk of the plasma.¹³ Despite its unquestioned importance, little is quantitatively known about the microphysics of electrons at plasma boundaries. It is only until recently that we proposed that the charging of plasma boundaries can be perhaps microscopically understood in terms of an electron physisorption process.^{14,15}

The physisorption scenario applies to a plasma electron approaching a metallic or a dielectric boundary provided its kinetic energy is large enough to overcome the Coulomb barrier due to the charges already residing on the boundary but small enough to make the surface appear as having a negative electron affinity. If the electron can convert its energy into internal energy of the boundary, via exciting elementary excitations of the solid, it may get stuck (adsorbed) at the boundary. Later it may desorb again if it gains enough energy from the boundary.

Like physisorption of neutral particles¹⁶⁻³¹ physisorption of electrons is the polarization-induced temporary binding to a surface. It can be characterized by a desorption time and a sticking coefficient. At first glance physisorption of electrons seems to be not much different from physisorption of neutral particles. There are however important qualitative differences which warrant a separate theoretical investigation.

First, albeit not in the focus of our investigation, the long-range $1/z$ tail of the image potential leads to a finite-electron sticking coefficient at vanishing electron energy and surface temperature.^{27,32} This is in contrast to the quantum reflection, that is, the vanishing sticking coefficient, one finds in this

limit for the short-ranged surface potentials typical for physisorption of neutral particles.^{24,31}

Second, the surface potential in which physisorption of electrons occurs, in particular, at plasma boundaries, consists of a polarization-induced attractive part and a repulsive Coulomb part due to electrons already adsorbed on the surface. The limit of vanishing coverage, very often adopted in the theoretical description of physisorption of neutral particles, is thus only applicable to the very first (last) electron approaching (leaving) the boundary.

Third, in contrast to physisorption of neutral particles, physisorption of electrons has to be always described quantum mechanically because the image potential varies on a scale comparable to the thermal de Broglie wavelength of the electron.¹⁴ This is also the case for physisorption of positronium.³³⁻³⁵

Finally, and this will be the theme of our investigation, the polarization-induced image potential supports deep states, in addition to shallow ones. Direct transitions from the continuum to deep bound states are very unlikely. Hence, a modeling in terms of a quantum-kinetic rate equation for the occupancy of the bound surface states,^{21,22} and Brenig's distinction between prompt and kinetic sticking,²¹ is vital for a correct description of electron physisorption. For phonon-controlled adsorption and desorption, as it occurs at dielectric surfaces, deep states also imply that multiphonon processes have to be taken into account in the calculation of state-to-state transition probabilities. This can be done either via an expansion of the energy-dependent T matrix,^{16,18,26} the method we are using,³⁶ or via a Magnus-type resummation of the time-dependent scattering operator.³⁷⁻⁴¹

In the following we investigate adsorption of an electron to a dielectric surface at finite temperature assuming an acoustic longitudinal bulk phonon controlling electron energy relaxation at the surface. To avoid complications due to finite coverage we focus on the first approaching electron. Using the quantum-kinetic rate equation for the occupancy of the image states of our previous work³⁶ (thereafter referred to as I), where we studied desorption of an image-bound electron from a dielectric surface, we calculate prompt and kinetic sticking coefficients. Compared to semiclassical estimates⁴² they turn out to be extremely small. Instead on

the order of 10^{-1} we find them to be at most on the order of 10^{-3} . We also analyze in detail the adsorption scenario as a function of surface temperature and potential depth. Most notable, our results reveal an energy relaxation bottleneck prohibiting, on a short time scale, thermalization of the electron with the surface, that is, the trickling through of the electron from upper to deep states. The reduced accessibility of deep states makes the kinetic sticking coefficient much smaller than the prompt sticking coefficient in contrast to what is usually found in physisorption of neutral particles.²⁹

The remaining paper is structured as follows. In Sec. II, we specify the quantum-kinetic approach of our previous work concerning desorption [paper I (Ref. 36)] to the situation of adsorption and introduce prompt and kinetic sticking coefficients. We then briefly recall in Sec. III the calculation of the state-to-state transition probabilities based on a microscopic model for the electron-surface interaction and an expansion of the T matrix for the dynamic part of that interaction. Mathematical details not given can be found in I. Finally, in Sec. IV, we present and discuss our results before we conclude in Sec. V.

II. ELECTRON KINETICS

The probability for an approaching electron in the continuum state k to make a transition to any of the bound states n of the polarization-induced image potential is given by the prompt energy-resolved sticking coefficient,²²

$$s_{e,k}^{\text{prompt}} = \tau_t \sum_n W_{nk}, \quad (1)$$

where $\tau_t = 2L/v_z$ is the traveling time through the surface potential of width L which, in the limit $L \rightarrow \infty$, can be absorbed into the transition probability per unit time from the continuum state k to the bound state n , W_{nk} . If the incident unit electron flux (we consider only a single electron impinging on the surface) is stationary and corresponds to an electron with Boltzmann distributed kinetic energies, the prompt energy-averaged sticking coefficient is given by²²

$$s_e^{\text{prompt}} = \frac{\sum_k s_{e,k}^{\text{prompt}} k e^{-\beta_e E_k}}{\sum_k k e^{-\beta_e E_k}}, \quad (2)$$

where $\beta_e^{-1} = k_B T_e$ is the mean electron energy.

Prompt sticking coefficients are properly weighted sums over state-to-state transition probabilities from continuum to bound surface states. They give the probability for initial trapping, which, according to Iche and Nozières¹⁷ and Brenig,²¹ is the first out of three stages of physisorption. The second stage encompasses relaxation of the bound-state occupancy and the third stage is the desorption of the temporarily bound particle.

The second stage, which also includes transitions back to the continuum, cannot be captured by simple state-to-state transition probabilities. Instead, a quantum-kinetic rate equation for the time-dependent occupancy of the bound surface states $n_n(t)$ has to be employed^{18,21} This equation describes

processes on a time scale much longer than the lifetime of the individual surface states but shorter than the desorption time.^{18,21,22} Following Gortel and co-workers,^{18,22}

$$\begin{aligned} \frac{d}{dt} n_n(t) = & \sum_{n'} [W_{nn'} n_{n'}(t) - W_{n'n} n_n(t)] \\ & - \sum_k W_{kn} n_n(t) + \sum_k \tau_t W_{nk} j_k(t), \end{aligned} \quad (3)$$

where $W_{n'n}$ is the probability per unit time for a transition from a bound state n to another bound state n' , W_{kn} and W_{nk} are the probabilities per unit time, respectively, for a transition from a bound state n to a continuum state k and vice versa, and

$$j_k(t) = n_k(t) \tau_t^{-1} \quad (4)$$

is the incident electron flux which, in principle, can be non-stationary.

The solution to Eq. (3) can be obtained from the solution of the corresponding homogeneous equation,

$$\begin{aligned} \frac{d}{dt} n_n(t) = & \sum_{n'} [W_{nn'} n_{n'}(t) - W_{n'n} n_n(t)] - \sum_k W_{kn} n_n(t) \\ = & \sum_{n'} T_{nn'} n_{n'}(t), \end{aligned} \quad (5)$$

where the matrix \mathbf{T} is defined implicitly by Eq. (5) and treating the electron flux $j_k(t)$ as an externally specified quantity.^{21,22} In the simplest case, which is also the basis of Eq. (2), $j_k(t)$ is the stationary flux corresponding to a single electron whose energy is Boltzmann distributed over the continuum states k with a mean electron energy $k_B T_e$, that is, $j_k(t) \equiv j_k \sim k e^{-\beta_e E_k}$.

To solve Eq. (5) amounts to solving the eigenvalue problem for the matrix \mathbf{T} .^{21,22} For the particular case of an electron physisorbing at a dielectric surface this has been already done in I. If the transitions between bound states are much faster than the transitions to the continuum, so that the adsorbed electron escapes very slowly, one eigenvalue, $-\lambda_0$, turns out to be considerably smaller than all the other eigenvalues $-\lambda_k$. The equilibrium occupation of the bound states, n_n^{eq} , is then to a very good approximation the right eigenvector to $-\lambda_0$, which can be thus identified with the negative of the inverse of the desorption time, that is, $\lambda_0 = \tau_e^{-1}$.

The kinetic sticking coefficient, which takes into account not only the initial capture but also the subsequent relaxation of the occupancy of the bound surface states, can be obtained as follows.²² The solution of Eq. (3) is split according to

$$n_n(t) = n_n^s(t) + n_n^f(t), \quad (6)$$

where

$$n_n^s(t) = e^{-\lambda_0 t} \int_{-\infty}^t dt' e^{\lambda_0 t'} e_n^{(0)} \sum_{k,l} \tilde{e}_l^{(0)} \tau_t W_{lk} j_k(t') \quad (7)$$

is the slowly and

$$n_n^f(t) = \sum_{\kappa \neq 0} e^{-\lambda_\kappa t} \int_{-\infty}^t dt' e^{\lambda_\kappa t'} e_n^{(\kappa)} \sum_{k,l} \tilde{e}_l^{(\kappa)} \tau_l W_{lk} j_k(t'), \quad (8)$$

the quickly varying part of $n_n(t)$. The quantities $e_n^{(\kappa)}$ and $\tilde{e}_n^{(\kappa)}$ are, respectively, the components of the right and left eigenvectors of the matrix \mathbf{T} to the eigenvalue $-\lambda_\kappa$. The probability of the electron remaining in the surface states for times on the order of the desorption time is given by the slowly varying part only, that is, $n^s(t) = \sum_n n_n^s(t)$. Differentiating $n^s(t)$ with respect to time,

$$\frac{d}{dt} n^s(t) = \sum_k s_{e,k}^{\text{kinetic}} j_k(t) - \lambda_0 n^s(t), \quad (9)$$

enables us, following Brenig,²¹ to identify the kinetic-energy-resolved sticking coefficient,

$$s_{e,k}^{\text{kinetic}} = \tau_l \sum_{n,l} e_n^{(0)} \tilde{e}_l^{(0)} W_{lk}, \quad (10)$$

which gives the probability for the electron being trapped even after the energy relaxation of the second stage of physisorption. In analogy to Eq. (2) the energy-averaged kinetic sticking coefficient reads for a stationary Boltzmannian electron flux,

$$s_e^{\text{kinetic}} = \frac{\sum_k s_{e,k}^{\text{kinetic}} k e^{-\beta_e E_k}}{\sum_k k e^{-\beta_e E_k}}. \quad (11)$$

III. TRANSITION PROBABILITIES

The transition probabilities per unit time $W_{qq'}$, where q and q' stand either for k or n , are the fundamental building blocks of the foregoing analysis. They have to be calculated from a microscopic model for the electron-surface interaction. The necessary steps have been described in I.

In short, for a dielectric surface, the main source, leaving interband electronic excitations aside, which primarily affect the dielectric constant, of the attractive static electron-surface potential is the coupling of the electron to a dipole-active surface phonon.^{43,44} Far from the surface the surface potential merges with the classical image potential and thus $\sim 1/z$. Close to the surface, however, it is strongly modified by the recoil energy resulting from the momentum transfer parallel to the surface when the electron absorbs or emits a surface phonon. Taking this effect into account leads to a recoil-corrected image potential $\sim 1/(z+z_c)$ with z_c a cut-off parameter defined in I.

Transitions between the eigenstates of the recoil-corrected image potential are due to dynamic perturbations of the surface potential. The surface potential is very steep near the surface. A particularly strong perturbation arises therefore from the longitudinal-acoustic phonon perpendicular to the surface which causes the surface plane to oscillate. Hence, this should be a stronger perturbation than, for instance, the residual dynamical interaction with the dipole-active surface phonon. In the following we consider therefore only the dy-

namical interaction with the longitudinal-acoustic phonon.

The Hamiltonian from which we calculated the transition probabilities was introduced in I where all quantities entering the Hamiltonian are explicitly defined. It is given by³⁶

$$H = H_e^{\text{static}} + H_{ph} + H_{e-ph}^{\text{dyn}}, \quad (12)$$

where

$$H_e^{\text{static}} = \sum_q E_q c_q^\dagger c_q \quad (13)$$

describes the electron in the recoil-corrected image potential, which thus accounts for the coupling of the electron to the dipole-active surface phonon,

$$H_{ph} = \sum_Q \hbar \omega_Q b_Q^\dagger b_Q, \quad (14)$$

describes the free dynamics of the acoustic bulk phonon responsible for transitions between surface states, and

$$H_{e-ph}^{\text{dyn}} = \sum_{q,q'} \langle q' | V_p(u,z) | q \rangle c_q^\dagger c_{q'} \quad (15)$$

denotes the dynamic coupling of the electron to the bulk phonon. Expanding $V_p(u,z)$ with respect to the displacement field,

$$u = \sum_Q \sqrt{\frac{\hbar}{2\mu\omega_Q N_s}} (b_Q + b_{-Q}^\dagger), \quad (16)$$

allows us to classify the dynamic interaction according to the number of exchanged bulk phonons.

As in I we use for calculational convenience a bulk Debye model for the longitudinal-acoustic phonon, although it is less justified for the high-energy part of the phonon spectrum which also enters our calculation. Sums over phonon momenta are thus replaced by

$$\sum_Q \dots = \frac{3N_s}{\omega_D^3} \int d\omega \omega^2 \dots \quad (17)$$

Measuring energies in units of the Debye energy $\hbar\omega_D = k_B T_D$, important dimensionless energy parameters characterizing Eq. (12) are

$$\epsilon_n = \frac{E_n}{\hbar\omega_D} \quad \text{and} \quad \Delta_{nm'} = \frac{E_n - E_{n'}}{\hbar\omega_D}, \quad (18)$$

where $E_n < 0$ is the energy of the n th bound state. We call the surface potential shallow if the lowest bound state is at most one Debye energy beneath the continuum, that is, $\epsilon_1 > -1$, one-phonon deep if the energy difference between the lowest two bound states does not exceed one Debye energy, that is, $\Delta_{12} > -1$, two-phonon deep if the energy difference between the lowest two bound states is between one and two Debye energies, that is, $-1 > \Delta_{12} > -2$, and so forth.

Because of the strong interaction between the electron and the dipole-active surface phonon, physisorption of an electron typically takes place in an at least two-phonon deep image potential (see Table I). Hence, physisorption of an electron controlled by a bulk acoustic phonon, as anticipated in Eq. (12) and in fact applicable to dielectric surfaces, where

TABLE I. Dielectric constant ϵ_s , Debye energy $\hbar\omega_D$, energy difference of the lowest two bound states of the recoil-corrected image potential ΔE_{12} , and the corresponding potential depth parameter Δ_{12} for graphite, silicon dioxide, and gallium arsenide.

	ϵ_s	$\hbar\omega_D$ (eV)	ΔE_{12} (eV)	Δ_{12}
Graphite	13.5	0.215	0.233	1.06
SiO ₂	3.8	0.041	0.105	2.59
GaAs	13	0.030	0.152	5.13

large energy gaps block electronic relaxation channels due to internal electron-hole pairs and/or plasmons, has to involve the exchange of many bulk phonons.

The transition probability per unit time from an electronic state q to an electronic state q' is given by¹⁶

$$\mathcal{R}(q', q) = \frac{2\pi}{\hbar} \sum_{s, s'} \frac{e^{-\beta_s E_s}}{\sum_{s''} e^{-\beta_s E_{s''}}} |\langle s', q' | T | s, q \rangle|^2 \times \delta(E_s - E_{s'} + E_q - E_{q'}), \quad (19)$$

where T is the on-shell T matrix corresponding to H_{e-ph}^{dyn} and $\beta_s = (k_B T_s)^{-1}$ with T_s the surface temperature; $|s\rangle$ and $|s'\rangle$ are initial and final phonon states, which are averaged over.

Multiphonon processes have two possible origins.^{16,39} They arise from the expansion of H_{e-ph}^{dyn} with respect to u ,

$$H_{e-ph}^{\text{dyn}} = V_1 + V_2 + V_3 + \mathcal{O}(u^4) \quad (20)$$

and from the multiple action of this perturbation. Defining the free electron-phonon resolvent,

$$G_0 = (E - H_e^{\text{static}} - H_{ph} + i\epsilon)^{-1}, \quad (21)$$

the latter is encoded in the T -matrix equation,

$$T = H_{e-ph}^{\text{dyn}} + H_{e-ph}^{\text{dyn}} G_0 T. \quad (22)$$

Using the short-hand notation introduced in I, the one-phonon process, proportional to u^2 , is accounted for by

$$\langle s', q' | V_1 | s, q \rangle \langle s, q | V_1^* | s', q' \rangle. \quad (23)$$

It leads to the standard golden rule approximation for the transition probability.

Two-phonon processes are proportional to u^4 and thus less likely than one-phonon processes. Most of them renormalize only the one-phonon transition probability and can thus be neglected in a first approximation. There are however two-phonon processes which induce transitions absent in the one-phonon approximation and hence have to be included in the calculation of the transition probabilities. In our short-hand notation the processes in question are

$$\langle s', q' | V_2 | s, q \rangle \langle s, q | V_2^* | s', q' \rangle, \quad (24)$$

$$\langle s', q' | V_2 | s, q \rangle \langle s, q | V_1^* G_0^* V_1^* | s', q' \rangle, \quad (25)$$

$$\langle s', q' | V_1 G_0 V_1 | s, q \rangle \langle s, q | V_2^* | s', q' \rangle, \quad (26)$$

TABLE II. Material parameters for the numerical results.

Debye temperature	T_D	2500 K
Dielectric constant	ϵ_s	13.5
TO phonon mode frequency	$\hbar\omega_T$	170 meV
Grüneisen parameter	γ_G	1.7
Shear modulus	μ	5 GPa

$$\langle s', q' | V_1 G_0 V_1 | s, q \rangle \langle s, q | V_1^* G_0^* V_1^* | s', q' \rangle. \quad (27)$$

It is shown in I how these processes can be included in the calculation of the transition probabilities $W_{qq'}$ entering the rate equation (3). Singularities appearing in some of the two-phonon transition probabilities have been regularized by taking a finite phonon lifetime into account (see I and Ref. 45 for details).

The electronic matrix elements entering the transition probabilities have been also calculated in I using bound and unbound wave functions of the recoil-corrected image potential. Hence, not only bound states but also continuum states belong to the static surface potential.³⁶ Our approach is thus on par with Armand and Manson's calculation of the sticking coefficient for light neutral particles.²⁶

IV. RESULTS

The material parameters chosen for the numerical calculations are, unless specified otherwise, given in Table II. They correspond to graphite. For some calculations we use however the Debye temperature as a tunable parameter to realize different potential depths which is the main focus of this investigation.

A. One-phonon deep potentials

First, we present results for shallow and one-phonon deep surface potentials. In leading order, only one-phonon processes are involved and the one-phonon approximation for the transition probabilities is sufficient. Because the electron thermalizes then very quickly with the surface the prompt and kinetic sticking coefficients are almost identical. In this section we show therefore only results for the prompt sticking coefficient.

Figure 1 compares s_e^{prompt} for a shallow and a one-phonon deep potential. The sketches in the upper part of the figure illustrate the main difference between the two potentials. For a shallow potential the lowest bound state is less than one Debye energy below the continuum so that a low-lying electron from the continuum can be directly trapped in the lowest bound state, $n=1$, by a one-phonon transition. In the case of a one-phonon deep potential, one-phonon processes can only lead to trapping in one of the upper bound states $n > 1$.

The middle panels of Fig. 1 show the prompt energy-resolved sticking coefficient as a function of the energy of the incident electron. Apart from discontinuities the sticking coefficient depends linearly on the electron energy. As explained in Sec. III the one-phonon transition probability is proportional to u^2 . From Eq. (16) we have $u^2 \sim 1/\omega$ so that

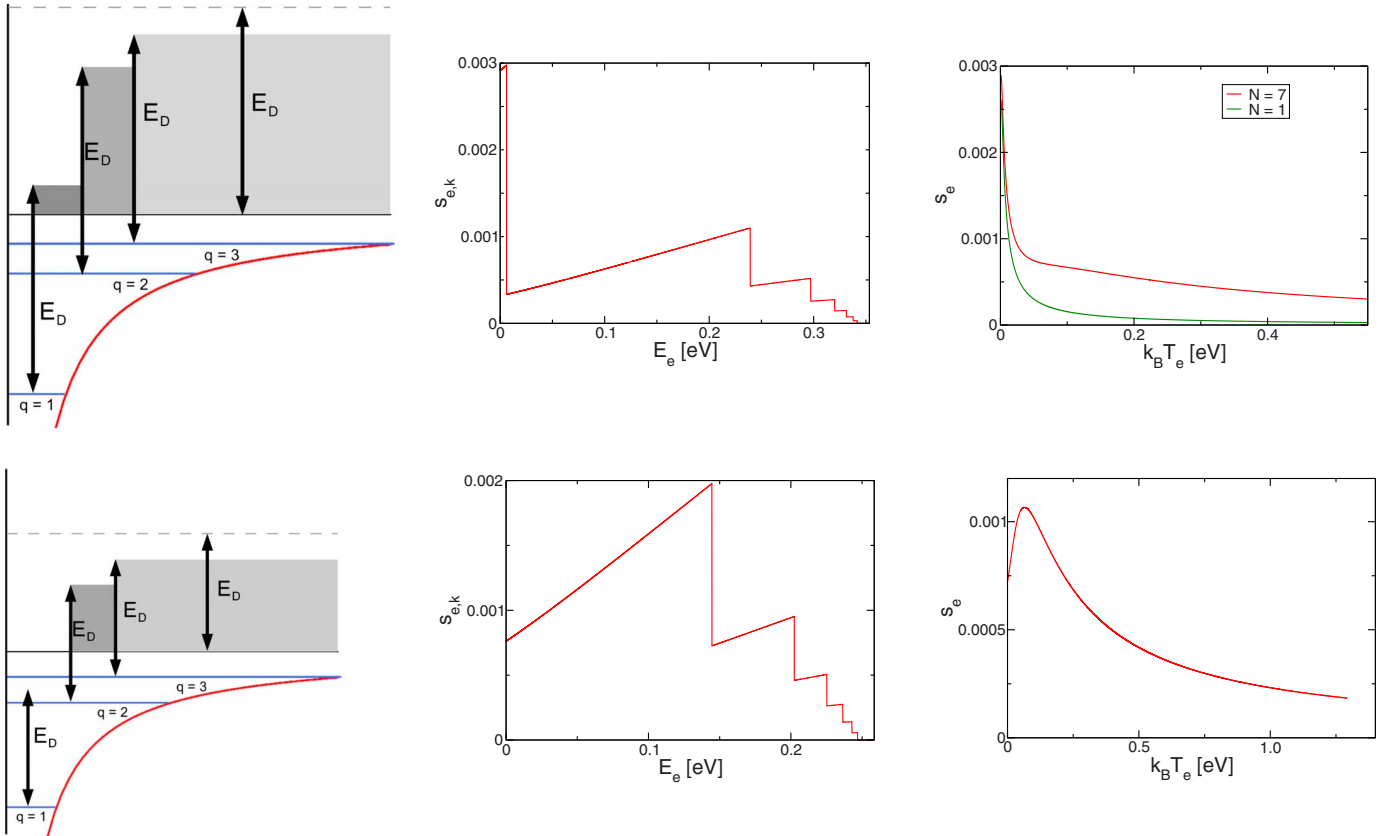


FIG. 1. (Color online) Left panel: Sketch of a shallow (top) and one-phonon deep (bottom) potential. The gray shaded areas show the energy range of sticking by one-phonon processes. Middle panel: Energy-resolved prompt sticking coefficient as a function of the electron energy for a shallow potential ($T_D=4100$ K) at $T_s=410$ K (top) and for a one-phonon deep potential ($T_D=3000$ K) at $T_s=300$ K (bottom). Right panel: Energy-averaged prompt sticking coefficient as a function of the mean electron energy for a shallow potential ($T_D=4100$ K) at $T_s=205$ K (top) and a one-phonon deep potential ($T_D=3000$ K) at $T_s=150$ K (bottom).

in conjunction with the Debye model, Eq. (17), the transition probability per unit time is proportional to ω which translates due to energy conservation to a proportionality to the electron energy. The phonon spectrum is thus reflected in the (one-phonon) energy-resolved sticking coefficient, as it is, for instance, also in the cross section for (one-phonon) inelastic particle-surface scattering.³⁸

Step jumps in the energy-resolved sticking coefficient reflect the level accessibility. When the energy difference between the electron and a bound state exceeds the Debye energy, one-phonon transitions are no longer possible and the electron can no longer directly reach that level. For a shallow potential, the first drop reflects therefore the accessibility of the first bound state, whereas for a one-phonon deep potential, where this bound state cannot be directly reached, the first drop reflects the accessibility of the second bound state. As energy differences between successive bound states of the image potential decrease toward the ionization threshold, that is, with increasing n (see upper panels of Fig. 1), more such steps are found near the maximum electron energy allowing for trapping, which is the Debye energy.

The contribution of the n th bound state to the sticking coefficient, reflected in the height of the corresponding accessibility threshold, decreases for higher bound states. The reason for this lies in the electronic matrix element appearing

in first-order perturbation theory, $\langle n|1/(z+z_c)^2|k\rangle$. This matrix element is smaller for higher bound states because higher bound states have less weight near the surface where the perturbation is strongest. Of considerable importance is hence the lowest bound state, which, if available, yields a particularly large contribution. The decreasing electronic matrix element also implies that neglecting all but a few, say, seven, of the infinitely many bound states suffices for the calculation of the sticking coefficient.

The prompt energy-averaged sticking coefficient is shown in the lower panels of Fig. 1 as function of the mean electron energy. Due to thermal averaging the sticking coefficient does no longer exhibit characteristics of the phonon spectrum and level accessibility, making it thus more robust against changes in the phonon model. It does however reflect the importance of the lowest bound state for shallow potentials. Note also, due to the long-range tail of the recoil-corrected image potential $\sim 1/(z+z_c)$ the energy-resolved and the energy-averaged electron sticking coefficients are finite for vanishing electron energy and electron temperature, irrespective of the surface temperature, as it should be.^{27,32}

B. Two-phonon deep potentials

We now turn our attention to two-phonon deep potentials. Under the assumption that the true one-phonon process

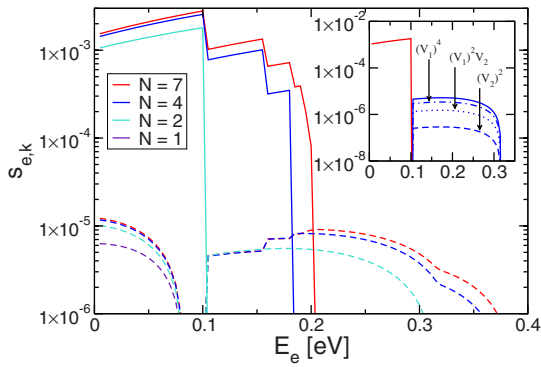


FIG. 2. (Color online) Energy-resolved prompt sticking coefficient for a two-phonon deep potential ($T_D=2500$ K and $T_s=500$ K) calculated with different numbers of bound states N . Full lines denote the one-phonon contribution, dashed lines the two-phonon contribution. Inset: contribution of the second bound state. One-phonon contribution (for $E_e < 0.1$ eV, red), two-phonon contribution (for $E_e > 0.1$ eV, blue) broken down into the processes $(V_2)^2 V_2$, $(V_1)^2 V_2$, and $(V_1)^4$.

dominates the corrections coming from two-phonon processes, the latter are only taken into account for transitions where one-phonon processes alone would yield no transition probability.

Two-phonon processes affect in a two-phonon deep potential sticking in two ways. They enable prompt trapping from higher-lying continuum states, outside the one-phonon trapping range, and they control the energy relaxation of the trapped electron and thus the formation of the quasistationary bound-state occupancy from which desorption occurs. There are thus two questions to be answered: how significant are two-phonon processes for prompt sticking and how does the relaxation thereafter depend on the type of phonon processes available.

To address the first question we show in Fig. 2 the contributions to the prompt energy-resolved sticking coefficient arising from, respectively, one- and two-phonon processes. If available, one-phonon processes provide for much larger sticking coefficients than two-phonon processes. Figure 2 also confirms that the sticking coefficient saturates quickly with the number of bound states included into the calculation. The vanishing of the two-phonon contributions to the sticking coefficient in a narrow energy range just below 0.1 eV is an artifact of our approximation, which neglects two-phonon corrections to transitions already enabled by a one-phonon process, and thus calculates two-phonon sticking coefficients only for levels which cannot be reached by a one-phonon process. Had we included two-phonon corrections to one-phonon transition rates the two-phonon contributions to the sticking coefficient would be also finite around 0.1 eV.

To investigate the relative importance of the various two-phonon processes arising, respectively, from the expansion of the dynamical perturbation and the T matrix we plot in the inset of Fig. 2 the partial contributions to the prompt sticking coefficient arising from the various two-phonon processes which trigger transition to the second bound state. A two-phonon process can be simultaneous, as encoded in V_2 , or successive, as described by $V_1 G_0 V_1$. Hence, the total two-

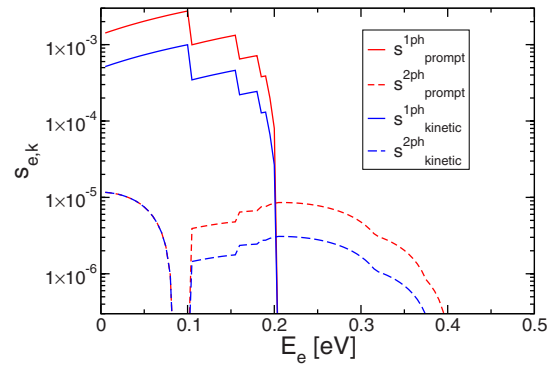


FIG. 3. (Color online) Prompt and kinetic energy-resolved sticking coefficient as a function of the electron energy for a two-phonon deep potential ($T_D=2500$ K and $T_s=357.14$ K). Full lines one-phonon contribution, dashed lines two-phonon contribution.

phonon transition probability contains a contribution without virtual intermediate states, symbolically denoted by V_2^2 [see Eq. (24)] and two contributions with virtual intermediate states, symbolically denoted by $(V_1)^2 V_2$ and $(V_1)^4$ [see Eqs. (25)–(27)]. The prompt energy-resolved sticking coefficient calculated with either V_2^2 , $(V_1)^2 V_2$, or V_1^4 only is shown in the inset of Fig. 2. In accordance to what we found in our calculation of the desorption time of an image-bound electron (paper I) and to what Gumhalter and Šiber found in their calculation of the cross section for inelastic particle-surface scattering,^{39–41} the direct two phonon process V_2^2 is dominated by the processes $V_1^2 V_2$ and $(V_1)^4$.

From the dominance of one-phonon processes over two-phonon processes we can also infer the validity of the truncation of the T matrix, which of course is only justified if the dynamic interaction is weak enough. The weakness of the dynamic interaction also guarantees that the unavoidable violation of the unitarity of the transition probabilities resulting from the truncation of the T matrix has no practical physical consequences. Indeed, a significant violation of unitarity would be indicated by a sticking coefficient > 1 .^{22,23} The sticking coefficients we obtain are on the order of 10^{-3} , ruling out a breach of unitarity and justifying the truncation of the T matrix.

Having clarified that two-phonon processes lead to a much smaller prompt sticking coefficient than one-phonon processes we now move on to study the effect of two-phonon transitions on the relaxation of the bound-state occupancy. For a two-phonon deep potential the energy difference between the lowest two bound states exceeds one Debye energy. Hence, the relaxation of an electron trapped in one of the upper bound states to the quasistationary occupancy can only occur via two-phonon processes. Since the kinetic sticking coefficient gives the probability for the incident electron making not only a transition to a bound state but also a subsequent relaxation to the quasistationary occupancy of these states, the importance of two-phonon processes should be signaled by the amount the kinetic sticking coefficient deviates from the prompt sticking coefficient.

Figure 3 shows that for a two-phonon deep potential the kinetic-energy-resolved sticking coefficient is for intermediate electron energies considerably smaller than the prompt

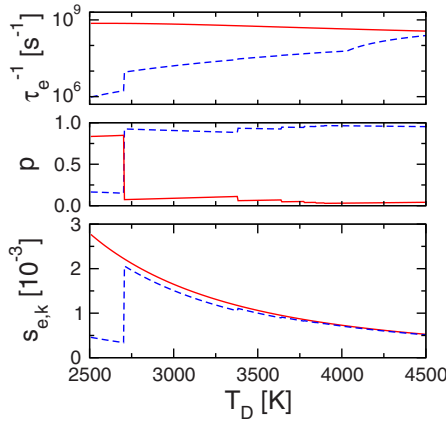


FIG. 4. (Color online) Upper panel: inverse desorption time from the lowest level (dashed blue line) and the upper levels (full red line). Middle panel: probability for an electron initially trapped in one of the upper levels of the surface potential ($n=2,3,4,\dots$) either to fall to the lowest bound state (dashed blue line) or to desorb without ever reaching the lowest bound state (full red line). Lower panel: prompt (full red line) and kinetic (dashed blue line) energy-resolved sticking coefficient. In all three panels, $E_e=0.1$ eV and $T_s/T_D=0.2$ [to keep the level of phonon excitation constant we set T_D/T_s constant (Ref. 36)]. For $T_D < 2707$ K the surface potential is two-phonon deep, for $2707 < T_D < 4029$ K it is one-phonon deep, and for $T_D > 4029$ K it is shallow.

energy-resolved sticking coefficient. This is due to the fact that the two-phonon transition to the lowest bound state, where the major part of the quasistationary occupancy resides, is very unlikely and thus very slow. Only for small energies, the first hump of the two-phonon contribution to the sticking coefficient, due to trapping in the lowest bound state, are prompt and kinetic sticking coefficients identical because no trickling through is needed. The artificial vanishing of the two-phonon contribution to the sticking coefficient around 0.1 eV is again a consequence of our approximation (see discussion of Fig. 2 above).

The weak coupling between the lowest two bound states in a two-phonon deep surface potential leads to a relaxation bottleneck for the electron if it is initially trapped in one of the upper states. In Figs. 4 and 5 we analyze the relaxation bottleneck in more detail as a function of the Debye temperature T_D (to realize different potential depths) and the surface temperature T_s . The upper panel shows the desorption time from the lowest bound state, that is, the desorption time for an electron capable to fall to the lowest bound state, and the desorption time from the upper bound states, that is, the desorption time for an electron not capable to fall to the lowest bound state. The probability for the electron initially trapped in the upper bound states to fall down to the lowest bound states and the probability to desorb to the continuum without ever passing through the lowest bound state are shown in the middle panel and the lower panel shows the prompt and the kinetic sticking coefficient.

Before we discuss Figs. 4 and 5, we say a few words about the way we calculated the quantities shown in the upper and middle panels. The desorption time from the lowest bound state is the desorption time for an electron equilibrated

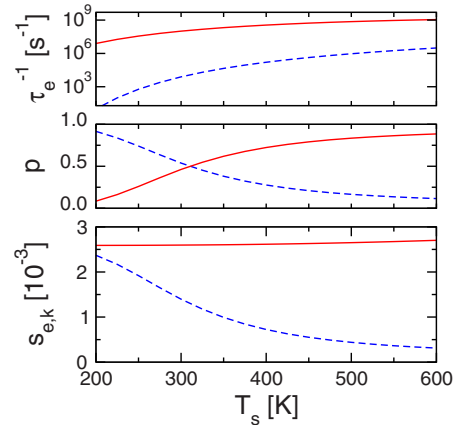


FIG. 5. (Color online) The three panels show, as a function of the surface temperature, the quantities of Fig. 4 for $T_D=2500$ K, that is, graphite, and $E_e=0.09$ eV.

with the surface, the quantity we calculated in I, because the quasistationary occupancy and the equilibrium occupancy coincide and both reside moreover, for the considered surface temperatures, mainly on the lowest level. The desorption time from the upper bound states we simply calculated from Eq. (5) with the lowest bound state excluded.

The probabilities shown in the middle panels we obtained from the following consideration. Whether an electron trapped in the upper bound states passes through to the lowest bound state or not depends on how large the transition probabilities from the upper bound states to the lowest bound state are in comparison to the transition probabilities to the continuum. Hence, the second stage of physisorption, that is, the time evolution of the occupancy after the initial trapping, can be captured by a rate equation for the occupancy of the upper bound states ($n=2,3,\dots$), similar to Eq. (5), but with a loss term to both the continuum and the lowest bound state,

$$\begin{aligned} \frac{d}{dt}n_n &= \sum_n [W_{nn'}n_{n'}(t) - W_{n'n}n_n(t)] - \sum_k W_{kn}n_n(t) - W_{1n}n_n(t) \\ &= \sum_{n'} D_{nn'}n_{n'}(t), \end{aligned} \quad (28)$$

where the matrix \mathbf{D} is defined implicitly by Eq. (28) and where n and n' run over the upper image states. Solving Eq. (28) with the initial condition,

$$n_l(0) = \frac{\sum_k W_{lk}j_k}{\sum_{l,k} W_{lk}j_k}, \quad (29)$$

which is the (conditional) probability that the electron is trapped in the l th image state under the condition that it is trapped in any of the bound states, we deduce for the probability for an electron trapped in one of the upper bound states to fall either to the lowest bound state ($f=1$) or to desorb without falling to the lowest bound state ($f=c$),

$$p_f = n_f(t \rightarrow \infty) = \sum_{n,\kappa} W_{fn} \frac{1}{\lambda_\kappa} d_n^{(\kappa)} \sum_l \tilde{d}_l^{(\kappa)} n_l(0), \quad (30)$$

where, $d_n^{(\kappa)}$ and $\tilde{d}_n^{(\kappa)}$ are the components of the right and left eigenvectors of the matrix \mathbf{D} .

We now turn our attention to Fig. 4. It shows the effect of different potential depths realized by tuning the Debye temperature. For a shallow potential ($T_D > 4029$ K) desorption from the lowest level is mainly due to direct one-phonon transitions to the continuum; the same type of transition emptying the upper bound states. Hence, the desorption time from the lowest bound state and the upper bound states, respectively, differ not too much for shallow potentials. For one-phonon deep potentials ($2707 < T_D < 4029$ K), however, the cascade of two one-phonon processes via the second level yields much larger desorption times from the lowest level compared to the desorption time from the upper levels. For a two-phonon deep potential ($T_D < 2707$ K), finally, the first leg of the cascade, the transition to the second bound state, is a two-phonon transition, which increases the desorption time compared to a one-phonon deep potential.

The second level is the link between the upper bound states and the lowest bound state. The ratio of the transition probabilities from the second bound state to the lowest bound state, W_{12} , and from the second bound state to the continuum, W_{c2} , determines if the electron trickles through after initial trapping or not, that is, whether it thermalizes with the surface or not. For a one-phonon deep potential both W_{12} and W_{c2} are due to one-phonon processes, in this case $W_{12} > W_{c2}$. For a two-phonon deep potential, however, the transition from the second to the lowest bound state is enabled by a two-phonon process only. In this case, and for moderate surface temperatures, $W_{12} < W_{c2}$ so that the electron is more likely to desorb before relaxing to the lowest bound state. As the kinetic sticking coefficient gives the probability of the trapped electron to relax to the quasistationary occupancy, the drop in the probability for reaching the lowest level at $T_D = 2707$ K, which is the one-phonon/two-phonon threshold, translates into the abrupt reduction in the kinetic sticking coefficient at $T_D = 2707$ K (see middle and lower panels of Fig. 4).

Figure 5 shows the quantities of Fig. 4 as a function of the surface temperature. The Debye temperature is fixed to the value for graphite. At low surface temperatures the kinetic sticking coefficient is only slightly smaller than the prompt sticking coefficient, yet for high surface temperatures their difference increases significantly as a consequence of the inhibited thermalization. This can be understood as follows: the transition from the second to the first bound state entails the emission of two phonons and the transition from the second bound state to the continuum requires only the absorption of a single phonon. However, at low enough surface temperatures it is nevertheless possible that the electron drops to the lowest bound state because the likelihood of phonon emission is proportional to $1+n_B$ while the likelihood of phonon absorption is proportional to n_B . Hence, for sufficiently low surface temperatures, $W_{12} > W_{c2}$, even when W_{12} entails a two-phonon and W_{c2} a one-phonon process, so

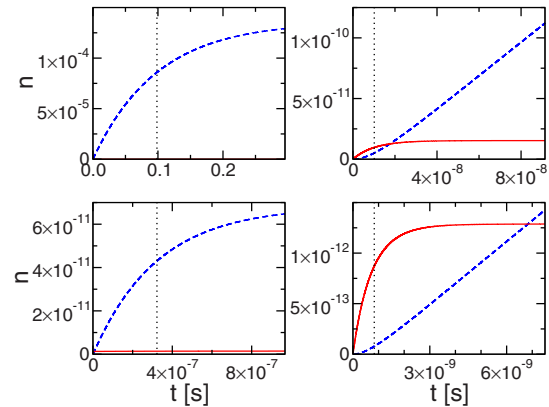


FIG. 6. (Color online) Bound-state occupancy of the lowest bound state (dashed blue line) and the upper bound states (solid red line) as a function of time for an unit flux of a Boltzmannian electron with $k_B T_e = 0.1$ eV. The left and right panels show the two occupancies on two time scales. The left panel on the scale of the desorption time $\lambda_0^{-1} = \tau_e$ (vertical dashed line in the left panels) and the right panel on the scale set by λ_1^{-1} (vertical dashed line in the right panels). The upper two panels are for $T_s = 200$ K and $T_D = 2500$ K whereas the lower two panels show results for $T_s = 600$ K and $T_D = 2500$ K.

that the electron has a good chance to trickle through. Increasing the surface temperature benefits however W_{c2} more than W_{12} so that $W_{12} < W_{c2}$, prohibiting the trickling through and leading to a considerable reduction in the kinetic sticking coefficient at high surface temperatures.

From the discussion of Figs. 4 and 5 we conclude that a pronounced relaxation bottleneck inhibiting thermalization can only occur for at least two-phonon deep potentials and sufficiently high surface temperatures. The question arises then on what time scale does the relaxation bottleneck affect physisorption. To answer this question we analyze, respectively, the time evolution of the occupancy of the lowest level and the occupancy of the upper levels of the surface potential under the assumption that initially all bound states were empty and that for $t > 0$ a stationary unit flux of a Boltzmannian electron fills the levels. Accordingly, the occupancy of the lowest state ($n=1$) and the upper states ($n \geq 2$) can be determined from Eq. (6) setting $j_k(t) = 0$ for $t < 0$ and $j_k(t) = j_k \sim k e^{-\beta_e E_k}$ for $t \geq 0$ with $\sum_k j_k = 1$.

The results of this calculation are shown in Fig. 6 for low (upper two panels) and high (lower two panels) surface temperature. Clearly, for times on the order of the desorption time, $\tau_e = \lambda_0^{-1}$, indicated by the vertical dashed line in the left panels, the upper levels are basically empty indicating that a thermalized electron desorbs; for $T_D = 2500$ K and $T_s = 500$ K the quasistationary occupancy deviates from the equilibrium occupancy less than 3%. The upper levels are more populated than the lower one only for very short time scales, set by λ_1^{-1} , indicated by the vertical dashed line in the right panels. Since $\lambda_1^{-1} \ll \lambda_0^{-1}$, the relaxation bottleneck does not affect desorption, which still occurs from the equilibrium occupancy. It does thus only affect the kinetic sticking coefficient which is significantly smaller than the prompt one and actually the one to be used to characterize polarization-induced trapping of an electron at a dielectric surface. The

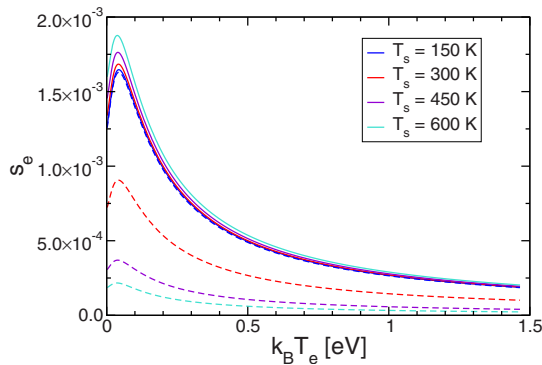


FIG. 7. (Color online) Prompt (full line) and kinetic (dashed line) energy-averaged sticking coefficient for graphite ($T_D = 2500$ K) as a function of the mean energy of the electron and the surface temperature.

relaxation bottleneck is absent in neutral physisorption systems because the level spacing is small compared to the Debye energy. Prompt and kinetic sticking coefficients are thus almost identical as has been indeed found for neon atoms physisorbing on a copper substrate.²⁹

Figure 7 finally shows for graphite the energy-averaged prompt and kinetic sticking coefficients as a function of the mean energy of the incident electron and the surface temperature. As two-phonon processes contribute little to the initial trapping of the electron, their most important role is to control relaxation to the lowest bound state. In agreement with the foregoing discussion, the kinetic sticking coefficient diminishes therefore for higher surface temperatures whereas the prompt sticking coefficient is less sensitive to the surface temperature. From Fig. 7 it can be also seen that even the prompt sticking coefficient for graphite is only at most on the order of 10^{-3} , the order we also found in our investigation of electron sticking at metallic surfaces.¹⁵ It is two orders of magnitude smaller than the value obtained from a semiclassical estimate⁴² whose range of applicability is however hard to grasp. We expect it, at best, to be applicable to very low mean electron energies, below 0.0026 eV, and rather high electron binding energies, larger than 1 eV.¹⁵

V. CONCLUSIONS

As a preparatory step toward a microscopic understanding of the buildup of surface charges at dielectric plasma boundaries, we investigated phonon-mediated temporary trapping of an electron on a dielectric surface. In our simple model for the polarization-induced interaction of the electron and the dielectric surface, the adsorbed electron occupies the bound states of a recoil-corrected image potential. Electron-energy relaxation responsible for transitions between the image states leading to adsorption and eventually to desorption is due to the coupling to an acoustic bulk phonon.

Dielectrics typically used as plasma boundaries are graphite, silicon oxide, aluminum oxide, and bismuth silicon oxide. They all have large energy gaps blocking internal elec-

tronic degrees of freedom and small Debye energies compared to the energy difference of at least the lowest two bound surface states. Electron physisorption at these boundaries is thus driven by multiphonon processes. As in I we presented results for a two-phonon deep surface potential, as it is applicable to graphite, where the energy difference between the lowest two bound states is between one and two Debye energies. Classifying two-phonon processes by the energy difference they allow to bridge, we included two-phonon transition probabilities only for transitions not already triggered by one-phonon processes. Besides the Debye temperature, which we varied to realize different potential depths, the material parameters used in the numerical calculations are the ones for graphite.

Similar to physisorption of a neutral particle, sticking and desorption of an electron can be subdivided into three characteristic stages. At first, the electron is trapped in one of the upper bound states of the surface potential. Then the bound-state occupancy relaxes to a quasistationary occupancy. Finally, over the time scale set by the desorption time, the electron desorbs. In order to account for both initial trapping and subsequent relaxation we employed a quantum-kinetic rate equation for the occupancy of the image states. Apart from calculating the energy-resolved and energy-averaged prompt and kinetic electron sticking coefficients, which typically turn out to be on the order of 10^{-3} , we also investigated the relative importance of one- and two-phonon processes for the two stages of the sticking process.

The initial trapping is almost entirely due to one-phonon transitions from the continuum, two-phonon processes from higher-lying continuum states contribute very little. The relaxation of the bound-state occupancy after the initial trapping depends strongly on the ratio of the probabilities for downward transitions to the lowest state and upward transitions to the continuum. For graphite, with its two-phonon deep surface potential, the upper bound states are linked to the lowest bound state only by a two-phonon process. The trapped electron has thus only a slim chance to drop to the lowest bound state, particularly at high surface temperatures, which favor transitions back to the continuum. The decreased accessibility of the lowest surface state leads to a significant reduction in the kinetic sticking coefficient compared to the prompt sticking coefficient. For the other dielectrics typically used as plasma boundaries, silicon dioxide, aluminum oxide, and bismuth silicon oxide, the surface potentials are much deeper because the Debye energy for these materials is very small. Hence, more than two phonons are required to link the upper image states to the lowest one, the accessibility of the lowest image state is thus even more suppressed, and the kinetic sticking coefficient should be accordingly small.

ACKNOWLEDGMENTS

This work was supported by the Deutsche Forschungsgemeinschaft through the transregional collaborative research center TRR 24. F.X.B. and H.F. acknowledge discussions with H. Deutsch in the early stages of this investigation.

- ¹M. Rapp and F.-J. Lübken, *J. Atmos. Sol.-Terr. Phys.* **63**, 759 (2001).
- ²E. C. Whipple, *Rep. Prog. Phys.* **44**, 1197 (1981).
- ³B. T. Draine and B. Sutin, *Astrophys. J.* **320**, 803 (1987).
- ⁴I. Mann, *Adv. Space Res.* **41**, 160 (2008).
- ⁵V. E. Fortov, A. V. Ivlev, S. A. Khrapak, A. G. Khrapak, and G. E. Morfill, *Phys. Rep.* **421**, 1 (2005).
- ⁶O. Ishihara, *J. Phys. D: Appl. Phys.* **40**, R121 (2007).
- ⁷Y. B. Golubovskii, V. A. Maiorov, J. Behnke, and J. F. Behnke, *J. Phys. D: Appl. Phys.* **35**, 751 (2002).
- ⁸U. Kogelschatz, *Plasma Chem. Plasma Process.* **23**, 1 (2003).
- ⁹M. Li, C. Li, H. Zhan, and J. Xu, Proceedings of the XV International Conference on Gas Discharges and their Applications, 2004 (unpublished).
- ¹⁰L. Stollenwerk, S. Amiranashvili, J.-P. Boeuf, and H.-G. Purwins, *Phys. Rev. Lett.* **96**, 255001 (2006).
- ¹¹L. Stollenwerk, J. G. Laven, and H.-G. Purwins, *Phys. Rev. Lett.* **98**, 255001 (2007).
- ¹²M. Li, C. Li, H. Zhan, and J. Xu, *Appl. Phys. Lett.* **92**, 031503 (2008).
- ¹³M. A. Lieberman and A. J. Lichtenberg, *Principles of Plasma Discharges and Materials Processing* (Wiley-Interscience, New York, 2005).
- ¹⁴F. X. Bronold, H. Fehske, H. Kersten, and H. Deutsch, *Phys. Rev. Lett.* **101**, 175002 (2008).
- ¹⁵F. X. Bronold, H. Deutsch, and H. Fehske, *Eur. Phys. J. D* **54**, 519 (2009).
- ¹⁶B. Bindow and S.-C. Ying, *Phys. Rev. B* **7**, 622 (1973).
- ¹⁷G. Iche and P. Nozières, *J. Phys. (Paris)* **37**, 1313 (1976).
- ¹⁸Z. W. Gortel, H. J. Kreuzer, and R. Teshima, *Phys. Rev. B* **22**, 5655 (1980).
- ¹⁹Z. W. Gortel, H. J. Kreuzer, and R. Teshima, *Phys. Rev. B* **22**, 512 (1980).
- ²⁰U. Leuthäusser, *Z. Phys. B: Condens. Matter* **44**, 101 (1981).
- ²¹W. Brenig, *Z. Phys. B: Condens. Matter* **48**, 127 (1982).
- ²²H. J. Kreuzer and Z. W. Gortel, *Physisorption Kinetics* (Springer-Verlag, Berlin, 1986).
- ²³W. Brenig, *Phys. Scr.* **35**, 329 (1987).
- ²⁴S. G. Chung and T. F. George, *Surf. Sci.* **194**, 347 (1988).
- ²⁵Z. W. Gortel and J. Szymanski, *Phys. Rev. B* **43**, 1919 (1991).
- ²⁶G. Armand and J. R. Manson, *Phys. Rev. B* **43**, 14371 (1991).
- ²⁷D. P. Clougherty and W. Kohn, *Phys. Rev. B* **46**, 4921 (1992).
- ²⁸G. P. Brivio and T. B. Grimley, *Surf. Sci. Rep.* **17**, 1 (1993).
- ²⁹G. P. Brivio, T. B. Grimley, V. Bortolani, and G. Santoro, *Chem. Phys. Lett.* **208**, 93 (1993).
- ³⁰W. Brenig, A. Gross, and R. Russ, *Z. Phys. B: Condens. Matter* **96**, 231 (1994).
- ³¹C. Carraro and M. W. Cole, *Prog. Surf. Sci.* **57**, 61 (1998).
- ³²W. Brenig and R. Russ, *Surf. Sci.* **278**, 397 (1992).
- ³³D. Neilson, R. M. Nieminen, and J. Szymański, *Phys. Rev. B* **33**, 1567 (1986).
- ³⁴A. P. Mills, E. D. Shaw, M. Leventhal, P. M. Platzman, R. J. Chichester, D. M. Zuckerman, T. Martin, R. Bruinsma, and R. R. Lee, *Phys. Rev. Lett.* **66**, 735 (1991).
- ³⁵A. B. Walker, K. O. Jensen, J. Szymański, and D. Neilson, *Phys. Rev. B* **46**, 1687 (1992).
- ³⁶R. L. Heinish, F. X. Bronold, and H. Fehske, *Phys. Rev. B* **81**, 155420 (2010).
- ³⁷B. Gumhalter, *Surf. Sci.* **347**, 237 (1996).
- ³⁸B. Gumhalter, *Phys. Rep.* **351**, 1 (2001).
- ³⁹A. Šiber and B. Gumhalter, *Phys. Rev. Lett.* **90**, 126103 (2003).
- ⁴⁰A. Šiber and B. Gumhalter, *Phys. Rev. B* **71**, 081401(R) (2005).
- ⁴¹A. Šiber and B. Gumhalter, *J. Phys.: Condens. Matter* **20**, 224002 (2008).
- ⁴²T. Umabayashi and T. Nakano, *Publ. Astron. Soc. Jpn.* **32**, 405 (1980).
- ⁴³R. Ray and G. D. Mahan, *Phys. Lett.* **42A**, 301 (1972).
- ⁴⁴E. Evans and D. L. Mills, *Phys. Rev. B* **8**, 4004 (1973).
- ⁴⁵R. L. Heinish, Diploma thesis, Universität Greifswald, 2009.

Physisorption of an electron in deep surface potentials off a dielectric surface

R. L. Heinisch, F. X. Bronold, and H. Fehske

Institut für Physik, Ernst-Moritz-Arndt-Universität Greifswald, DE-17489 Greifswald, Germany

(Received 3 February 2011; published 4 May 2011)

We study phonon-mediated adsorption and desorption of an electron at dielectric surfaces with deep polarization-induced surface potentials where multiphonon transitions are responsible for electron energy relaxation. Focusing on multiphonon processes due to the nonlinearity of the coupling between the external electron and the acoustic bulk phonon triggering the transitions between surface states, we calculate electron desorption times for graphite, MgO, CaO, Al₂O₃, and SiO₂ and electron sticking coefficients for Al₂O₃, CaO, and SiO₂. To reveal the kinetic stages of electron physisorption, we moreover study the time evolution of the image-state occupancy and the energy-resolved desorption flux. Depending on the potential depth and the surface temperature, we identify two generic scenarios: (i) adsorption via trapping in shallow image states followed by relaxation to the lowest image state and desorption from that state via a cascade through the second strongly bound image state in not too deep potentials, and (ii) adsorption via trapping in shallow image states but followed by a relaxation bottleneck retarding the transition to the lowest image state and desorption from that state via a one-step process to the continuum in deep potentials.

DOI: [10.1103/PhysRevB.83.195407](https://doi.org/10.1103/PhysRevB.83.195407)

PACS number(s): 52.40.Hf, 73.20.-r, 68.43.Mn, 68.43.Nr

I. INTRODUCTION

Image states, arising from the polarization-induced interaction between an electron and a surface, offer the possibility for electron trapping at a surface. Since their original prediction¹ for the surface of liquid and solid He, they have been extensively studied for metallic surfaces.²⁻⁶ However, image states also exist for dielectric surfaces provided the electron affinity of the dielectric is negative, that is, the vacuum level falls inside the gap between the valence and the conduction band. Image states are then the lowest unoccupied states and should, hence, allow for temporary trapping of external electrons. So far, image states at a dielectric surface have been only observed for graphite,⁷ but they are expected for other dielectrics with negative electron affinity as well, for instance, boron nitride⁸ and the alkaline earth oxides.⁹

Based on the idea of a two-dimensional electron surface plasma,¹⁰⁻¹³ electron trapping in image states has been suspected for a long time to be responsible for the buildup of surface charges at plasma walls. We have recently proposed, therefore, to consider the charging of a plasma wall as an electron physisorption process.^{14,15} Indeed, for plasma walls with negative electron affinity, image states should contribute to the very beginning of the charging process when the wall carries no charges yet and the image states thus fall inside the energy gap of the wall. Only with increasing surface charge are image states expected to play a less important role because the Coulomb barrier due to the electrons already residing on the wall shifts image states to an energy range where they are destabilized by unoccupied bulk states. The later stages of charge collection most probably occur via surface resonances or empty volume states.¹⁶

Regardless of its importance for charge collection at dielectric plasma walls, the electron kinetics in the image states of a dielectric surface is an interesting phenomenon in its own right. In addition, it is relevant in other physical contexts as well. For instance, (i) in electron emitters, such as cesium-doped silicon oxide films with negative electron affinity, electron emission via image states reduces the operational voltage

considerably;¹⁷ (ii) in gallium-arsenide-based heterostructures, surface charging can be used for the contactless gating of field devices;¹⁸ and (iii) for the alkaline earth oxides, studied in the field of heterogeneous catalysis,¹⁹⁻²² the electronic surface states provide the environment for catalytic reactions. Some situations encompass electronic transitions from bulk to surface states, as it is the case for electron emitters, while for others, the electron does not penetrate into the bulk and the electron kinetics takes place only in surface states. Interesting questions in this case are the probability for temporary trapping in these states, the mechanism of electron energy relaxation at the surface, and the time after which a trapped electron is released.

This is the concluding paper out of a series of three on the phonon-mediated physisorption of an electron in the image states of a dielectric surface. As in our previous work, Refs. 23 and 24 (hereafter referred to as I and II), we investigate adsorption and desorption of an electron at finite temperatures assuming an acoustic-longitudinal bulk phonon to control energy relaxation at the surface. For the dielectric material we are considering, the level spacing of the lowest two bound states typically exceeds the Debye energy, implying that multiphonon processes have to be taken into account. In I and II, we have studied desorption and sticking using an expansion of the energy-dependent T matrix,²⁵⁻²⁷ allowing us to calculate one- and two-phonon transition probabilities. This approach is, however, limited to very few materials, for instance, graphite and MgO. In the following, we will adopt a different strategy, calculating multiphonon transition probabilities due to the nonlinear electron-phonon coupling nonperturbatively. This allows us to calculate the desorption time and the sticking coefficient for the deeper surface potentials of CaO, Al₂O₃, and SiO₂.

The remainder of this paper is structured as follows. In Sec. II, we briefly recall the quantum-kinetic approach to physisorption. In Sec. III, we calculate the multiphonon state-to-state transition probabilities. In Sec. IV, we present our results for the desorption time and the prompt and kinetic

energy-resolved and energy-averaged sticking coefficients. In this section, we also discuss the time evolution of the bound-state occupancy and the energy-resolved desorption flux. Section V is devoted to the analytic treatment of a simplified two-state model used to identify two generic physisorption scenarios into which we can classify the results of this paper as well as our previous results, before we conclude in Sec. VI.

II. ELECTRON KINETICS

As in I (Ref. 23) and II (Ref. 24), we describe the time evolution of the occupancy of the bound surface states with a quantum-kinetic rate equation.^{28,29} It captures all three characteristic stages of physisorption^{30,31}: initial trapping, subsequent relaxation, and desorption.

The time dependence of the occupancies of the bound states is given by^{28,29}

$$\frac{d}{dt}n_n(t) = \sum_{n'} [W_{nn'}n_{n'}(t) - W_{n'n}n_n(t)] - \sum_k W_{kn}n_n(t) + \sum_k \tau_t W_{nk}j_k(t) \quad (1)$$

$$= \sum_{n'} T_{nn'}n_{n'}(t) + \sum_k \tau_t W_{nk}j_k(t), \quad (2)$$

where $W_{n'n}$ is the probability per unit time for a transition from a bound state n to another bound state n' , W_{kn} and W_{nk} are the probabilities per unit time for a transition from the bound state n to the continuum state k and vice versa, and $\tau_t = 2L/v_z$ is the transit time through the surface potential of width L , which, in the limit $L \rightarrow \infty$, can be absorbed into the transition probability. The matrix T_{nm} is defined implicitly by the above equation. The last term in Eqs. (1) and (2), respectively, gives the increase in the bound-state occupancy due to trapping of an electron in bound surface states.

The probability for an approaching electron in the continuum state k to make a transition to any of the bound states is given by the prompt energy-resolved sticking coefficient

$$s_{e,k}^{\text{prompt}} = \tau_t \sum_n W_{nk}. \quad (3)$$

By treating the incident electron flux as an externally specified parameter, the solution of Eq. (1) describes the subsequent relaxation and desorption. It is given by

$$n_n(t) = \sum_k e^{-\lambda_\kappa t} \int_{-\infty}^t dt' e^{\lambda_\kappa t'} e_n^{(\kappa)} \sum_{kl} \tilde{e}_l^{(\kappa)} \tau_t W_{lk} j_k(t'), \quad (4)$$

where $e_n^{(\kappa)}$ and $\tilde{e}_n^{(\kappa)}$ are the right and left eigenvectors to the eigenvalue $-\lambda_\kappa$ of the matrix T_{nm} .

If the modulus of one eigenvalue λ_0 is considerably smaller than the moduli of the other eigenvalues λ_κ , a unique desorption time and a unique sticking coefficient can be identified.²⁹ In this case, λ_0 governs the long time behavior of the equilibrium occupation of the bound states $n_n^{\text{eq}} \sim e^{-E_n/k_B T_s}$ and its inverse can be identified with the desorption time $\lambda_0^{-1} = \tau_e$. In this case, the bound-state occupancy $n_n(t)$ splits into a slowly varying part $n_n^0(t)$ given by the $\kappa = 0$ summand

in Eq. (4) and a quickly varying part $n_n^f(t)$ given by the sum over $\kappa \neq 0$ in Eq. (4).

The adsorbate, i.e., the fraction of the trapped electron remaining in the surface states for times on the order of the desorption time, is given by the slowly varying part only $n^0(t) = \sum_n n_n^0(t)$. By differentiating $n^0(t)$ with respect to the time

$$\frac{d}{dt}n^0(t) = \sum_k s_{e,k}^{\text{kinetic}} j_k(t) - \lambda_0 n^0(t), \quad (5)$$

we can, following Brenig,³¹ identify the kinetic energy-resolved sticking coefficient

$$s_{e,k}^{\text{kinetic}} = \tau_t \sum_{n,n'} e_n^{(0)} \tilde{e}_n^{(0)} W_{nk}, \quad (6)$$

giving the probability for both initial trapping and subsequent relaxation.

If the incident unit electron flux corresponds to an electron with Boltzmann distributed kinetic energies, the prompt or kinetic energy-averaged sticking coefficient is given by

$$s_e^{\text{kin}} = \frac{\sum_k s_{e,k}^{\text{kinetic}} k e^{-\beta_e E_k}}{\sum_k k e^{-\beta_e E_k}}, \quad (7)$$

where $\beta_e^{-1} = k_B T_e$ is the mean electron energy.

The desorption flux, that is, the flux due to an electron that is not instantly reflected at the boundary but sticks to the surface for a finite time, can also be calculated from the occupancy of the bound surface states. From Eq. (1), we infer that the losses of the bound-state occupancy increase the continuum state occupancy by

$$\frac{dn_k}{dt} = \sum_n W_{kn} n_n(t). \quad (8)$$

As the electron remains in the surface potential for the time it needs to travel through the surface potential, the occupancy of the continuum state k is given by $n_k = \tau_t j_k$. To obtain the energy-resolved desorption flux, we multiply the occupancy of the continuum state k with the flux j_k^{box} associated with the box-normalized state $|\phi_k\rangle$.²³ Thus, the energy-resolved desorption flux is given by

$$j_k(t) = \tau_t j_k^{\text{box}} \sum_n W_{kn} n_n(t), \quad (9)$$

which is well defined in the limit $L \rightarrow \infty$.

III. TRANSITION PROBABILITIES

The kinetic equations presented in the last section rely on the knowledge of the transition probabilities. They have to be calculated from a microscopic model for the electron-surface interaction.

For a dielectric surface, the transitions are driven by phonons, the maximum energy of which is, within the Debye model, the Debye energy $\hbar\omega_D$. By measuring energies in units of the Debye energy, important dimensionless parameters characterizing the potential depth are

$$\epsilon_n = \frac{E_n}{\hbar\omega_D} \quad \text{and} \quad \Delta_{nn'} = \frac{E_n - E_{n'}}{\hbar\omega_D}, \quad (10)$$

where $E_n < 0$ is the energy of the n th bound state.

In I, we introduced the following classification for the potential depth. If $-n + 1 > \Delta_{12} > -n$, we call the potential n -phonon deep. For the calculations in I and II, we considered only one- or two-phonon deep potentials, for which one- and two-phonon transition probabilities are sufficient. Dielectrics with two-phonon deep potentials such as graphite or MgO are, however, an exception. Many dielectrics, for instance, Al_2O_3 , CaO , GaAs , or SiO_2 , have more than two-phonon deep potentials. Hence, the more relevant situation is physisorption in deep surface potentials for which multiphonon transition probabilities are required.

To calculate multiphonon transition probabilities for the one-dimensional microscopic model used in I and II, we briefly recall its main features. In short, for a dielectric surface, the main source of the attractive static electron-surface potential is the coupling of the electron to a dipole-active surface phonon.³² Far from the surface, the surface potential arising from this coupling merges with the classical image potential and thus $\sim 1/z$. Close to the surface, however, the surface potential is strongly modified by the recoil energy resulting from the momentum transfer parallel to the surface when the electron absorbs or emits a surface phonon. Taking this effect into account leads to a recoil-corrected image potential $\sim 1/(z + z_c)$ with z_c a cutoff parameter defined in I.

Transitions between the eigenstates of the recoil-corrected image potential are due to dynamic perturbations of the surface potential. The surface potential is very steep near the surface. A particularly strong perturbation arises, therefore, from the longitudinal-acoustic bulk phonon perpendicular to the surface, which causes the surface plane to oscillate.

The Hamiltonian from which we calculate the transition probabilities was introduced in I, where all quantities entering the Hamiltonian are explicitly defined. It is given by

$$H = H_e^{\text{static}} + H_{ph} + H_{e-ph}^{\text{dyn}}, \quad (11)$$

where

$$H_e^{\text{static}} = \sum_q E_q c_q^\dagger c_q \quad (12)$$

describes the electron in the recoil-corrected image potential,

$$H_{ph} = \sum_Q \hbar\omega_Q b_Q^\dagger b_Q \quad (13)$$

describes the free dynamics of the bulk longitudinal-acoustic phonon responsible for transitions between surface states, and

$$H_{e-ph}^{\text{dyn}} = \sum_{q,q'} \langle q' | V_p(u, z) | q \rangle c_q^\dagger c_{q'} \quad (14)$$

denotes the dynamic coupling of the electron to the bulk phonon.

The perturbation $V_p(u, z)$ can be identified as the difference between the displaced surface potential and the static surface potential. It reads, after the transformation $z \rightarrow z - z_c$, as

$$V_p(u, z) = -\frac{e^2 \Lambda_0}{z + u} + \frac{e^2 \Lambda_0}{z}, \quad (15)$$

where $\Lambda_0 = (\epsilon_s - 1)/4(\epsilon_s + 1)$ with ϵ_s the static dielectric constant. In general, multiphonon processes can arise both

from the nonlinearity of the electron-phonon coupling H_{e-ph}^{dyn} as well as from the successive actions of H_{e-ph}^{dyn} encoded in the T-matrix equation

$$T = H_{e-ph}^{\text{dyn}} + H_{e-ph}^{\text{dyn}} G_0 T, \quad (16)$$

where G_0 is given by

$$G_0 = (E - H_e^{\text{static}} - H_{ph} + i\epsilon)^{-1}. \quad (17)$$

The transition probability per unit time from an electronic state q to an electronic state q' encompassing both types of processes is given by²⁵

$$W_{q'q} = \frac{2\pi}{\hbar} \sum_{s,s'} \frac{e^{-\beta_s E_s}}{\sum_{s',s''} e^{-\beta_s E_{s''}}} |\langle s', q' | T | s, q \rangle|^2 \times \delta(E_s - E_{s'} + E_q - E_{q'}), \quad (18)$$

where $\beta_s = (k_B T_s)^{-1}$, with T_s the surface temperature and $|s\rangle$ and $|s'\rangle$ the initial and final phonon states. We are only interested in the transitions between electronic states. It is thus natural to average in Eq. (18) over all phonon states. The delta function guarantees energy conservation.

In our previous work, we have used an expansion of the T matrix to calculate multiphonon transition rates. In principle, this ensures that both linear and nonlinear terms in the interaction as well as successive actions of the perturbation are taken into account up to a certain order of the phonon process. However, even for a two-phonon deep potential, taking all two-phonon processes into account is nearly impossible. The calculation becomes feasible if two-phonon processes are only taken into account for transitions not already enabled by a one-phonon process. This amounts to computing only the lowest required phonon order for a given transition, neglecting higher-order corrections to it. For higher-order phonon processes, even this simplified strategy becomes unfeasible. A different approach is thus needed.

From I and II, we qualitatively know the relevance of the different types of multiphonon processes for particular electronic transitions. For transitions between bound and continuum states, for instance, one-phonon processes are sufficient at low electron energies. We will therefore compute the transition probability between bound and continuum states in the one-phonon approximation. For transitions between bound states, we found that multiphonon processes due to the nonlinearity of the electron-phonon coupling tend to be more important than the multiphonon processes due to the iteration of the T matrix, unlike what we found for the two-phonon bound-state and continuum transitions (see I) or to what Šiber and Gumhalter^{33,34} found in the context of atom-surface scattering. Indeed, multiphonon processes from the iteration of the T matrix give a minor contribution, unless resonances arising from the T matrix become relevant. This happens whenever the energy difference between two bound states is a multiple of the Debye energy. Resonances then smoothen the abrupt steps in the transition probability at the depth thresholds. Since the electronic matrix element between the first and the second bound states is the largest one, this effect is most pronounced for $|\Delta_{12}| = n$. Incidentally, bound-state resonances can also lead to significant corrections in atom-surface scattering as discussed by Brenig³⁵ and Šiber and Gumhalter.³⁶

In view of the above discussion, we expect an approximation that takes only the nonlinearity of the electron-phonon interaction nonperturbatively into account to give an acceptable first estimate for the multiphonon transition rates. We denote this approximation as the nonlinear multiphonon approximation. In particular, it should be sufficient for the identification of the generic behavior of multiphonon-mediated adsorption and desorption.

Calculating multiphonon processes due to nonlinear terms in the interaction potential³⁷ amounts to a distorted-wave Born approximation with the full interaction potential. Thus, the transition probability per unit time is given by

$$W_{q'q} = \frac{2\pi}{\hbar} \sum_{s,s'} \frac{e^{-\beta_s E_s}}{\sum_{s''} e^{-\beta_s E_{s''}}} |\langle q, s | H_{e-ph}^{\text{dyn}} | s', q' \rangle|^2 \times \delta(E_s + E_q - E_{q'} - E_{s'}). \quad (19)$$

To evaluate the multiphonon transition probability, we use H_{e-ph}^{dyn} in the form of Eq. (15). The transition matrix element in Eq. (19) is then given by

$$\langle q, s | H_{e-ph}^{\text{dyn.}} | q', s' \rangle = \langle s | \int_{z_c}^{\infty} dz \phi_q^*(z) \times [v(z+u) - v(z)] \phi_{q'}(z) | s' \rangle, \quad (20)$$

where $v(z) = -(e^2 \Lambda_0)/z$. By introducing dimensionless variables $x = z/a_B$, the Fourier transform of the static potential

$$v(p) = \int_{x_c}^{\infty} dx e^{ipx} v(x) \quad (21)$$

and the state-to-state matrix element

$$f_{qq'}(p) = \int_{x_c}^{\infty} dx \phi_q^*(x) e^{-ipx} \phi_{q'}(x), \quad (22)$$

the transition probability can be rewritten as

$$W_{q'q} = \frac{2\pi}{\hbar} \sum_{s,s'} \frac{e^{-\beta_s E_s}}{\sum_{s''} e^{-\beta_s E_{s''}}} \int_{-\infty}^{\infty} \frac{dp}{2\pi} \int_{-\infty}^{\infty} \frac{d\tilde{p}}{2\pi} v(p) v^*(\tilde{p}) \times f_{qq'}(p) f_{qq'}^*(\tilde{p}) \langle s | [e^{-i\frac{p}{a_B}u} - 1] | s' \rangle \times \langle s' | [e^{i\frac{\tilde{p}}{a_B}u} - 1] | s \rangle \delta(E_s + E_q - E_{s'} - E_{q'}). \quad (23)$$

By using the identity $\delta(x) = 1/(2\pi) \int_{-\infty}^{\infty} dt e^{ixt}$ and employing $\langle s | e^{iE_s t/\hbar} = \langle s | e^{iH_{ph} t/\hbar}$, the above expression becomes

$$W_{q'q} = \frac{1}{\hbar^2} \int_{-\infty}^{\infty} \frac{dp}{2\pi} \int_{-\infty}^{\infty} \frac{d\tilde{p}}{2\pi} v(p) v^*(\tilde{p}) f_{qq'}(p) f_{qq'}^*(\tilde{p}) \times \int_{-\infty}^{\infty} dt e^{i(E_q - E_{q'})t/\hbar} \langle [e^{-i\frac{p}{a_B}u(0)} - 1] [e^{i\frac{\tilde{p}}{a_B}u(t)} - 1] \rangle \quad (24)$$

with $\langle \dots \rangle = \sum_s e^{-\beta_s E_s} \langle s | \dots | s \rangle / \sum_{s''} e^{-\beta_s E_{s''}}$ the average over phonon states. This average can be evaluated for $q \neq q'$ employing Glauber's theorem,³⁸ which yields

$$\langle [e^{-i\frac{p}{a_B}u(0)} - 1] [e^{i\frac{\tilde{p}}{a_B}u(t)} - 1] \rangle = e^{-\frac{1}{2a_B^2} p^2 \langle (u(0))^2 \rangle} e^{-\frac{1}{2a_B^2} \tilde{p}^2 \langle (u(t))^2 \rangle} e^{\frac{1}{a_B} p \tilde{p} \langle (u(0)u(t)) \rangle} \quad (25)$$

with

$$\langle (u(0)u(t)) \rangle = \sum_Q \frac{\hbar}{2\mu N_s \omega_Q} \{ [1 + n_B(\hbar\omega_Q)] e^{-i\omega_Q t} + n_B(\hbar\omega_Q) e^{i\omega_Q t} \} \quad (26)$$

the correlation function of the displacement field

$$u = \sum_Q \sqrt{\frac{\hbar}{2\mu\omega_Q N_s}} (b_Q + b_{-Q}^\dagger), \quad (27)$$

where μ is the mass of the unit cell of the lattice and N_s is the number of unit cells.

As in I and II, we use for calculational convenience a bulk Debye model for the longitudinal-acoustic phonon, although it is less justified for the high-energy part of the spectrum, which also enters our calculation. Sums over phonon momenta are thus replaced by

$$\sum_Q \dots = \frac{3N_s}{\omega_D^3} \int_0^{\omega_D} d\omega \omega^2 \dots \quad (28)$$

In terms of the dimensionless variables

$$x = \frac{\omega}{\omega_D}, \quad \delta = \frac{\hbar\omega_D}{k_B T_s}, \quad \text{and} \quad \tau = \omega_D t, \quad (29)$$

the phonon correlation function becomes

$$\langle (u(0)u(\tau)) \rangle = \frac{3\hbar}{2\mu\omega_D} \int_0^1 dx x \left[\frac{e^{-ix\tau}}{1 - e^{-\delta x}} + \frac{e^{ix\tau}}{e^{\delta x} - 1} \right]. \quad (30)$$

Hence, for the transition probability per unit time we obtain

$$W_{q'q} = \frac{e^4 \Lambda_0^2}{\hbar^2 \omega_D a_B^2} \int_{-\infty}^{\infty} \frac{dp}{2\pi} \int_{-\infty}^{\infty} \frac{d\tilde{p}}{2\pi} v(p) v(\tilde{p}) f_{qq'}(p) f_{qq'}^*(\tilde{p}) \times e^{-\frac{1}{2}\gamma p^2 q(0)} e^{-\frac{1}{2}\gamma \tilde{p}^2 q(0)} \int_{-\infty}^{\infty} d\tau e^{i\Delta_{qq'}\tau + \gamma p \tilde{p} q(\tau)}, \quad (31)$$

where

$$q(\tau) = \int_0^1 dx x \left[\frac{e^{-ix\tau}}{1 - e^{-\delta x}} + \frac{e^{ix\tau}}{e^{\delta x} - 1} \right] \quad \text{and} \quad \gamma = \frac{3\hbar}{2\mu a_B^2 \omega_D}. \quad (32)$$

The transition probability (31) contains two Debye-Waller factors $\exp[-\gamma p^2 q(0)/2]$ and $\exp[-\gamma \tilde{p}^2 q(0)/2]$ governing the reduction of the transition probability as a function of the surface temperature. It also contains phonon processes of all orders as can be most easily seen from the Taylor expansion

$$e^{\gamma p \tilde{p} q(\tau)} = 1 + \gamma p \tilde{p} q(\tau) + \frac{1}{2} [\gamma p \tilde{p} q(\tau)]^2 + \dots \quad (33)$$

Clearly, the second term on the right-hand side represents the one-phonon and the third term the two-phonon process. From I, we know that two-phonon processes are much weaker than one-phonon processes. We expect, therefore, lower-order phonon processes to dominate their higher-order corrections, so that the expansion (33) converges quickly.

As higher-order phonon processes are small compared to lower-order processes, we take, for a given $\Delta_{qq'}$, only

the leading term of $\exp[\gamma p \tilde{p} q(\tau)]$ into account, that is, the lowest-order phonon process that enables a transition between the states q and q' . The Fourier transformation of powers of $q(\tau)$, however, required when (33) is used in (31), can not be evaluated in closed form, making it necessary to construct an approximation for $q(\tau)$.

To derive an approximation for $q(\tau)$ subject to the constraint

$$\int_{-\infty}^{\infty} d\tau e^{i\Delta_{qq'}\tau} q^n(\tau) = 0 \quad \text{for } |\Delta_{qq'}| > n, \quad (34)$$

which states that an n -phonon process yields a nonvanishing transition probability only for $-n < \Delta < n$ and vanishes otherwise, we split $q(\tau) = q^s(\tau) + q^i(\tau)$ into a contribution arising from spontaneous phonon emission $q^s(\tau)$ and a contribution from induced phonon emission or absorption $q^i(\tau)$. They are, respectively, given by

$$q^s(\tau) = \int_0^1 dx x e^{-ix\tau} \quad \text{and} \quad q^i(\tau) = 2 \int_0^1 dx x \frac{\cos(x\tau)}{e^{\delta x} - 1}. \quad (35)$$

The former can be evaluated giving

$$q^s(\tau) = \frac{\cos \tau - 1}{\tau^2} + i \frac{\tau \cos \tau - \sin \tau}{\tau^2} + \frac{\sin \tau}{\tau}. \quad (36)$$

For $q^i(\tau)$, we need to find an approximation. For this purpose, we look at the Fourier transform of q^i :

$$\int_{-\infty}^{\infty} d\tau e^{i\Delta\tau} q^i(\tau) = \begin{cases} 2\pi \frac{|\Delta|}{e^{|\Delta|} - 1} & \text{for } -1 < \Delta < 1 \\ 0 & \text{else} \end{cases}. \quad (37)$$

Expanding the Fourier transform in terms of $|\Delta|$,

$$2\pi \frac{|\Delta|}{e^{|\Delta|} - 1} \approx 2\pi \left[\frac{1}{\delta} - \frac{1}{2}|\Delta| + \frac{1}{12}\delta|\Delta|^2 + \mathcal{O}(\delta^2) \right] \quad (38)$$

yields a high-temperature approximation, which converges quickly for the temperatures we are interested in and guarantees at the same time that the one-phonon contribution can only bridge energy differences up to $|\Delta_{qq'}| = 1$. Applying the inverse transformation gives

$$q^i(\tau) = \left(\frac{2}{\delta} - 1 + \frac{\delta}{6} \right) \frac{\sin(\tau)}{\tau} + \frac{1}{\tau^2} + \left(-1 + \frac{\delta}{3} \right) \frac{\cos(\tau)}{\tau^2} - \frac{\delta \sin(\tau)}{3\tau^3} + \mathcal{O}(\delta^2), \quad (39)$$

which satisfies Eq. (34). By using this approximation, the Fourier transform of powers of $q(\tau)$ can be done analytically.

As the n -phonon process gives a vanishing transition probability at $|\Delta| = n$, we take the maximum of the n -phonon and the $n + 1$ -phonon process to obtain a better approximation in the vicinity of $|\Delta| = n$. Then, the Fourier transformation of $\exp[\gamma p \tilde{p} q(\tau)]$ in leading nonvanishing order is given by

$$\int_{-\infty}^{\infty} d\tau e^{i\Delta\tau + \gamma p \tilde{p} q(\tau, \delta)} \approx \begin{cases} \max(A_n, A_{n+1}) & \text{for } n - 1 < \Delta < n, \\ \max(B_n, B_{n+1}) & \text{for } -n < \Delta < -n + 1 \end{cases}, \quad (40)$$

where

$$A_n = -2\pi \frac{(\gamma p \tilde{p})^n}{n!} \sum_{k=0}^n \binom{n}{k} \sum_{j=0}^k \binom{k}{j} (-1)^{n+j} \left(\frac{1}{\delta} + \frac{1}{2} + \frac{\delta}{12} \right)^{n-k} \left(\frac{1}{2} + \frac{\delta}{6} \right)^{k-j} \left(-\frac{\delta}{6} \right)^j \frac{(\Delta - n)^{n+k+j-1}}{(n+k+j-1)!} + \mathcal{O}(\delta^2) \quad (41)$$

and

$$B_n = 2\pi \frac{(\gamma p \tilde{p})^n}{n!} \sum_{k=0}^n \binom{n}{k} \sum_{j=0}^k \binom{k}{j} (-1)^{n+j} \left(-\frac{1}{\delta} + \frac{1}{2} - \frac{\delta}{12} \right)^{n-k} \left(-\frac{1}{2} + \frac{\delta}{6} \right)^{k-j} \left(\frac{\delta}{6} \right)^j \frac{(\Delta + n)^{n+k+j-1}}{(n+k+j-1)!} + \mathcal{O}(\delta^2). \quad (42)$$

Using the approximation given by Eq. (40) allows an efficient numerical evaluation of the transition probabilities (31). Equations (39)–(42) are first order in δ . For the materials and temperatures we are interested in, this is sufficient. Note, however, that the expansion can be continued to higher orders in δ . The Fourier transformation of $\exp[\gamma p \tilde{p} q(\tau)]$ is then still a polynomial in Δ and, thus, amenable for numerical calculations.

IV. Results

We now use the multiphonon transition probability to study the electron kinetics in front of a CaO, Al₂O₃, and SiO₂ surface. They all have three-phonon deep surface potentials, that is, the energy difference of the two lowest image states is between two

and three Debye energies. The material parameters required for the numerical computation are summarized in Table I. All numerical results were obtained for these parameters. Where indicated, we varied the Debye temperature to simulate different potential depths. Furthermore, the multiphonon calculation for CaO, Al₂O₃, and SiO₂ is compared to the one- and two-phonon calculations from I and II, which are applicable to graphite and MgO.

A. Desorption

To judge the quality of the nonlinear multiphonon approximation derived in the previous section, we first compare in Fig. 1 the inverse desorption time obtained from it with the inverse desorption time obtained from our previous one- and

TABLE I. Material parameters for the numerical results.

	CaO	Al ₂ O ₃	SiO ₂
Debye temperature T_D	648 K	980 K	470 K
Dielectric constant ϵ_s	12.01	9.9	3.78
TO-phonon frequency $\hbar\omega_T$	41 meV	79 meV	133 meV

two-phonon approximations. Shown is the dependence of τ_e^{-1} on the Debye temperature T_D , which is tuned to vary the potential depth. The dimensionless inverse temperature δ , as defined in Eq. (29), is kept constant to keep the level of phonon excitation the same while the Debye temperature is varied.

The nonlinear multiphonon approximation can be, of course, only compared with the two-phonon approximation in the range of Debye temperatures for which the potential is two-phonon deep. Calculated in the multiphonon approximation, τ_e^{-1} changes very little over the range of two-phonon depth, but shows steep jumps at the threshold to one- and three-phonon depth. For τ_e^{-1} calculated in the two-phonon approximation, which is based on an iteration of the T matrix with the nonlinear electron-phonon coupling, these thresholds are washed out by the resonances. Nevertheless, τ_e^{-1} is on the same order of magnitude in both approximations. The main effect of the neglected resonances is the rounding off of the drops at the thresholds. As the steps, an artifact of taking only nonlinear multiphonon processes into account, are less steep for deeper potentials, the nonlinear multiphonon approximation might be even more appropriate for deeper potentials. The thin dotted vertical line in Fig. 1 corresponds to Al₂O₃. Unfortunately, the potential depth is just below the two-phonon three-phonon threshold, so the value for τ_e^{-1} is most likely underestimated.

Figure 1 suggests that the nonlinear multiphonon approximation, that is, the Born approximation with the full nonlinear

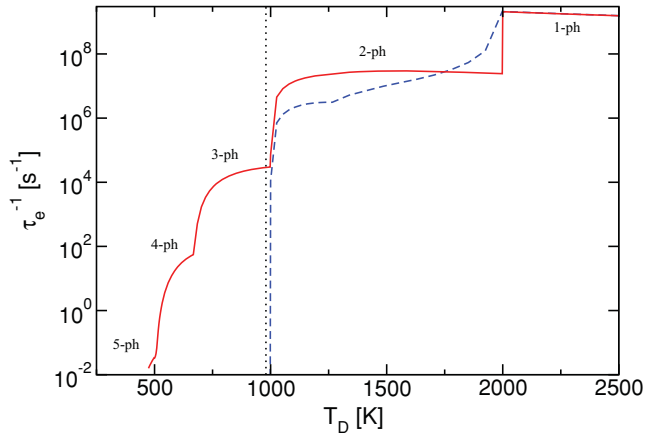


FIG. 1. (Color online) Inverse desorption time τ_e^{-1} as a function of the Debye temperature T_D for $\delta = 1$ (surface temperature $T_s = T_D/\delta$) calculated in the nonlinear multiphonon approximation (solid red line) and the two-phonon approximation from I for two-phonon depth (dashed blue line). The surface potential is one-phonon deep for $T_D > 2000$ K, two-phonon deep for $2000 \text{ K} > T_D > 1000$ K, three-phonon deep for $1000 \text{ K} > T_D > 666$ K, and four-phonon deep for $666 \text{ K} > T_D > 500$ K. Data for $T_D = 980$ K apply to Al₂O₃ (thin vertical line).

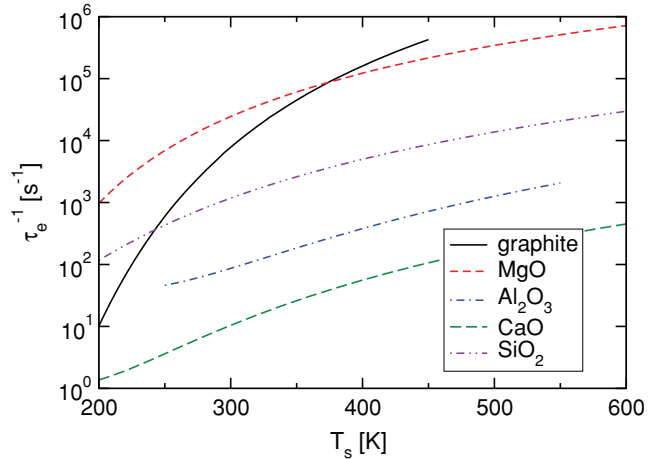


FIG. 2. (Color online) Inverse desorption time τ_e^{-1} as a function of the surface temperature T_s for graphite, MgO, CaO, Al₂O₃, and SiO₂.

electron-phonon coupling, should be adequate for identifying different scenarios of phonon-driven electron physisorption in deep potentials. Nevertheless, we can not rigorously assess its range of validity compared, for instance, to an approximation based on an iteration of the T matrix with only linear electron-phonon coupling. For transitions between deep bound states, higher orders in the nonlinear electron-phonon coupling tend to benefit from the large electronic matrix elements, while, in particular for low temperatures, bound-state resonances enhance the relevance of iterations of lower orders of the nonlinear electron-phonon coupling. For a better understanding, an expansion of the T matrix with the full nonlinear electron-phonon coupling would be necessary. Taking virtual processes involving the Rydberg series of image states into account would make this an interesting yet strenuous continuation of this work.

We now move on to the study of the dependence of τ_e^{-1} on the surface temperature. Figure 2 shows the inverse desorption time τ_e^{-1} as a function of the surface temperature for graphite, MgO, Al₂O₃, CaO, and SiO₂. For graphite and MgO, both two-phonon deep, τ_e^{-1} was calculated in the two-phonon approximation; for Al₂O₃, CaO, and SiO₂, all of them three-phonon deep, the nonlinear multiphonon approximation has been used. For all materials, τ_e^{-1} increases significantly with the surface temperature.

By comparing, in Fig. 2, τ_e^{-1} for Al₂O₃, CaO, and SiO₂, we notice that τ_e^{-1} increases with decreasing ϵ_s (see Table I) in accordance with the fact that a smaller ϵ_s implies a less deep surface potential and thus a faster desorption. From Fig. 2, we also see that, for high surface temperatures, desorption from the two-phonon deep potentials of graphite and MgO is quicker than from the three-phonon deep potentials of Al₂O₃, CaO, and SiO₂ as expected. For low surface temperature, however, τ_e^{-1} for graphite decreases much steeper than for the other materials. This might be due to the high Debye temperature of graphite, so for room temperature, the dimensionless inverse temperature $\delta = T_D/T_s$, which controls phonon excitation, is already in the low-temperature regime where downward transitions due to spontaneous phonon

emission remain constant, while upward transitions are extremely temperature dependent, causing the desorption time to be equally temperature dependent. This peculiarity leads to the surprising fact that, at low temperatures, desorption from two-phonon deep potentials can be in some cases slower than desorption from three-phonon deep potentials.

Figure 2 also gives insight into the validity of the high-temperature expansion (39). Up to first order in δ , it is valid for $\delta < 3$. This corresponds to a surface temperature of 300 K for Al_2O_3 and 225 K for CaO . The small upward bends at these temperatures indicate that, for lower surface temperatures, the expansion given by Eq. (39) should be continued to higher orders in δ .

B. Sticking

In II, we found that one-phonon processes give much higher contributions to the sticking coefficient than two-phonon processes. For this reason, we calculate the transition probabilities for continuum and bound-state transitions only in the one-phonon approximation. The effect of multiphonon processes with regard to sticking lies in the relaxation from the state in which the electron is initially trapped to the lowest bound state. This is captured by the kinetic sticking coefficient. Before we address this question in more detail, we take a look at the prompt sticking coefficient.

The prompt sticking coefficient for Al_2O_3 , CaO , and SiO_2 is presented in Fig. 3. First, we consider the prompt energy-resolved sticking coefficient shown in the inset. Note that the quadratic phonon dispersion of the Debye model translates into an energy-resolved sticking coefficient which, apart from the discontinuities, is proportional to the electron energy. The step jumps in the energy-resolved sticking coefficient reflect level accessibility. When the energy difference between the approaching electron and a bound state exceeds the Debye energy, one-phonon processes no longer enable sticking to this level. Since the lowest two bound states of the image potential of Al_2O_3 and SiO_2 have energies $\epsilon_n < -1$, they can

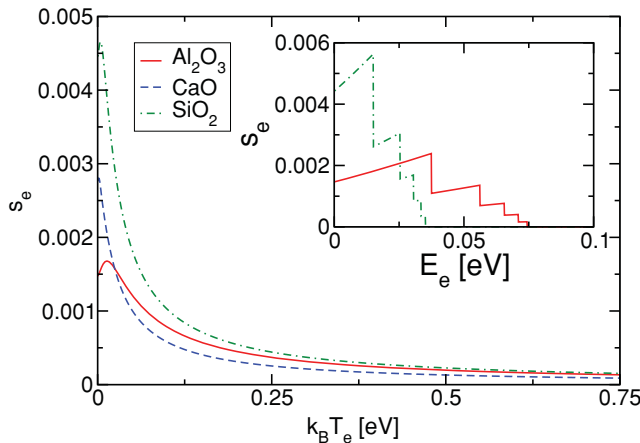


FIG. 3. (Color online) Prompt energy-averaged sticking coefficient for CaO , Al_2O_3 , and SiO_2 as a function of the mean energy of the electron at a surface temperature of $T_s = 300$ K. Inset: Prompt energy-resolved sticking coefficient for Al_2O_3 and SiO_2 as a function of the electron energy for $T_s = 300$ K.

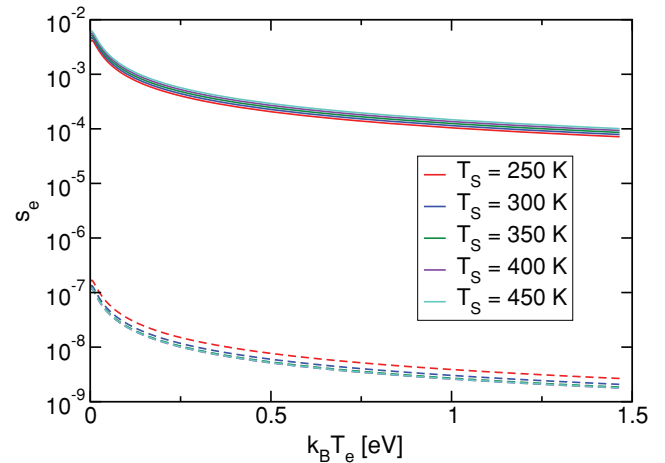


FIG. 4. (Color online) Prompt (full line) and kinetic (dashed line) energy-averaged sticking coefficient for SiO_2 as a function of the mean energy of the electron and the surface temperature T_s .

not be reached by one-phonon processes from the continuum. Thus, the lowest bound state contributing to prompt sticking is the third bound state. Due to the differences in the Debye energy, the energy-resolved sticking coefficient for SiO_2 is larger and increases faster for low electron energies than the sticking coefficients for Al_2O_3 and CaO (not explicitly shown). Compared to Al_2O_3 and CaO , the energy-resolved sticking coefficient for SiO_2 is thus strongly peaked at low electron energies. As a result, the energy-averaged sticking coefficient shown in the main panel of Fig. 3 is much larger for SiO_2 than for Al_2O_3 and CaO .

Figure 4 shows the prompt and kinetic energy-averaged sticking coefficient for SiO_2 as a function of the mean electron energy and the surface temperature. The prompt sticking coefficient increases slightly with temperature due to the increased contribution of induced phonon emission responsible for continuum and bound-state transitions. The kinetic sticking coefficient is smaller than the prompt sticking coefficient by four to five orders of magnitude and decreases with temperature as a higher surface temperature favors quick transitions back into the continuum after initial trapping.

Depending on whether transitions from the upper bound states to the lowest state or to the continuum are more likely, the electron trickles through after initial trapping or desorbs before relaxing to the lowest bound state. For the three-phonon deep surface potentials of Al_2O_3 , CaO , and SiO_2 , trickling through is suppressed, leading to a considerable reduction of the kinetic compared to the prompt sticking coefficient.

C. Electron kinetics

So far, we have calculated from the kinetic rate equation (2) the prompt and kinetic sticking coefficients and the desorption time. The rate equation contains, however, more information. For a specified electron influx or initial condition, the time evolution of the bound-state occupancy and the energy resolution of the desorption flux can be calculated as well.

To address the first question, we plot in Fig. 5 the time evolution of the bound-state occupancy. Our aim is to identify the stages of physisorption and to relate them to the eigenvalues

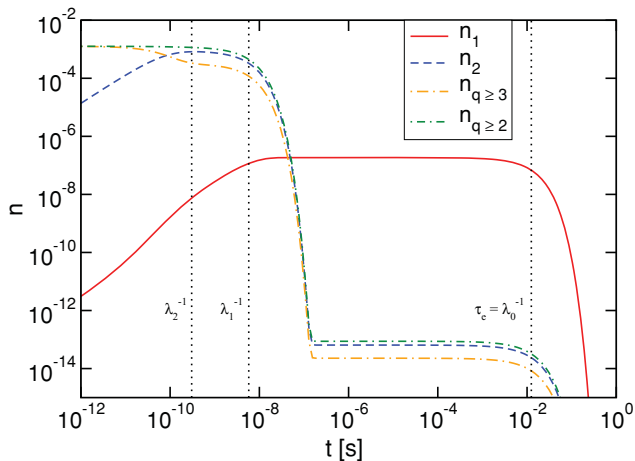


FIG. 5. (Color online) Time evolution of the bound-state occupancy of a single electron trapped at $t = 0$ in the upper bound states of Al_2O_3 at $T_s = 300$ K. The thin vertical lines correspond to λ_0^{-1} , λ_1^{-1} , and λ_2^{-1} , respectively, where $-\lambda_i$ are the three lowest eigenvalues of the matrix T_{nm} .

of the matrix T_{nm} . The situation we are considering is a three-phonon deep potential, that is, $-3 < \Delta_{12} < -2$, with the second bound state lying more than one Debye energy below the continuum, that is, $\epsilon_2 < -1$, so that electron trapping, due to one-phonon processes, can occur only in the third and higher bound states. The bound states $i \geq 2$, which we call upper bound states, are linked by one-phonon transitions.

To obtain the time evolution of the bound-state occupancy after trapping of an electron at $t = 0$, we solve the rate equation with the initial condition for the bound-state occupancy $n_i(0) = \tau_i W_{ik}$ for a specified k , which is the probability that the electron is trapped in state i . In Fig. 5, k corresponds to an electron energy of $E = 0.05$ eV. Due to the high electron energy, the third state can not be reached by a one-phonon process. Thus, trapping occurs in the fourth and higher bound states.

In a first stage after trapping of the electron, the fast one-phonon transitions between the upper bound states dominate the electron kinetics. Due to trapping of the electron in the fourth and higher bound states, the occupancy of the upper bound states is out of equilibrium. Over the time scale set by λ_2^{-1} , the inverse of the third eigenvalue of T_{nm} , the occupancy in the upper bound states relaxes toward its equilibrium value. The electron trickles through from the fourth and higher bound states to the second bound state, as can be seen from the increase in the occupancy of the second bound state n_2 and the reduction of the occupancy of the third and higher bound states $n_{q \geq 3}$.

Then, the strong one-phonon transitions between the upper bound states and the continuum, occurring over the time scale set by λ_1^{-1} , empty the upper bound states. The weak multiphonon transitions from the upper states to the lowest bound state are only a small perturbation to the electron kinetics in the upper bound states so that λ_1^{-1} corresponds to the desorption time for the system of the upper bound states without the lowest bound state.

Until the upper bound states are emptied, a small fraction of the occupancy reaches the lowest bound state as can be seen

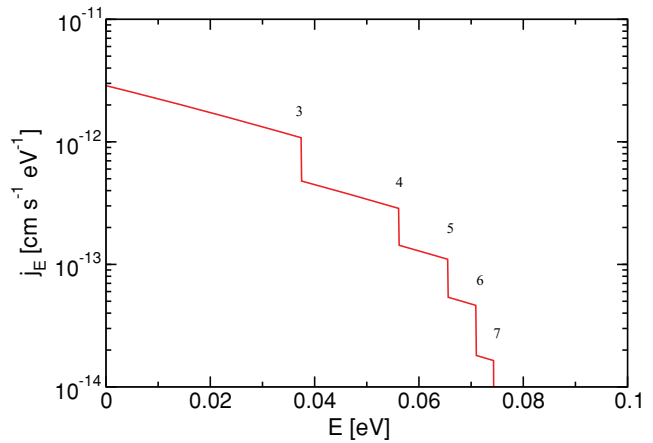


FIG. 6. (Color online) Energy-resolved desorption flux at $t = 10^{-4}$ s for an electron trapped at $t = 0$ in the upper bound states under the same conditions as in Fig. 5. For Al_2O_3 , one-phonon transitions between bound and continuum states are only possible from the third and higher bound states. The small numbers give the bound state from which transitions to the continuum are no longer possible at the respective energy.

from the discrepancy of the initial occupancy of the upper bound states $n_{q \geq 2}$ and the maximum occupancy of n_1 . This difference corresponds to the reduction of the kinetic with respect to the prompt sticking coefficient in Fig. 4. The lowest bound state remains occupied for a much longer time, until desorption takes place at times on the order of $\tau_e = \lambda_0^{-1}$.

Figure 6 finally shows the energy-resolved desorption flux at $t = 10^{-4}$ s [given by Eq. (9)] after trapping of the electron under the same conditions as in Fig. 5. The final transition that sets the electron free is a one-phonon transition from one of the upper bound states to the continuum. From each bound state i , one-phonon transitions are only possible to continuum states with an energy $E \leq E_i + \hbar\omega_D$. Hence, the energy-resolved desorption flux exhibits the same discontinuities as the energy-resolved sticking coefficient shown in Fig. 3, located at electron energies for which one-phonon transitions between bound states and the continuum cease to be operational.

V. TWO-STATE SYSTEM: DISCUSSION

To clarify the generic behavior of electron physisorption at dielectric surfaces, and to put the results presented in the previous section and in I and II into perspective, we study a simple model of two bound states coupled to a continuum of states. Electron physisorption occurs in the image potential that supports a deep lowest bound state, well separated from a group of relatively closely packed upper bound states. Since the upper bound states are strongly coupled by one-phonon processes, they can be subsumed under an effective upper bound state. The effective state is then weakly coupled to the lowest bound state via multiphonon processes and strongly coupled to the continuum via one-phonon processes.

The left panel of Fig. 7 schematically shows the system of the two surface states. Gearing toward deep potentials, we include only transitions between the two bound states and

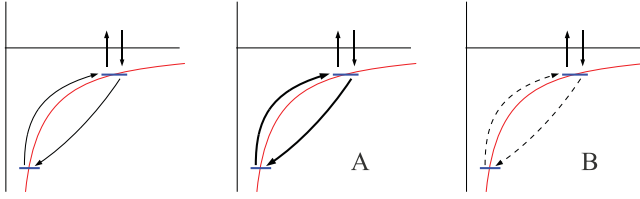


FIG. 7. (Color online) Left panel: Schematic drawing of the two-state model discussed in the main text. Middle panel: Physisorption scenario of type A. A trapped electron has a high chance to drop to the bottom, then it revolves between the two bound states, until it desorbs. Right panel: Physisorption scenario of type B. Due to a relaxation bottleneck, the electron is unlikely to drop to the lowest state. Transitions that the electron makes once per temporary trapping event are represented by a thin line; a bold line represents transitions made more than once; and dashed lines represent transitions that are made with a very low probability.

between the upper state and the continuum. The matrix T_{nm} defined by Eq. (1) reads, for this system, as

$$\mathbf{T} = \begin{pmatrix} -W_{21} & W_{12} \\ W_{21} & -W_{12} - W_{c2} \end{pmatrix}, \quad (43)$$

where W_{12} and W_{21} are the transition probabilities from the second to the first bound state and vice versa, and W_{c2} is the transition probability from the second bound state to the continuum. For the two-state model, the eigenvalues $-\lambda_k$ and the right and left eigenvectors $\mathbf{e}^{(k)}$ and $\tilde{\mathbf{e}}^{(k)}$ can be calculated analytically. The eigenvalues are given by

$$-\lambda_{0,1} = -\frac{1}{2}(W_{21} + W_{12} + W_{c2}) \pm \frac{1}{2}\sqrt{(W_{21} + W_{12} + W_{c2})^2 - 4W_{21}W_{c2}}. \quad (44)$$

Parameters of physical interest can be also obtained analytically. The desorption time, for instance, is the negative inverse of the lowest eigenvalue $\tau_e = \lambda_0^{-1}$. Since only the upper bound state can be reached from the continuum, prompt sticking arises solely from trapping in the upper bound state. The prompt sticking coefficient is thus given by $s_{e,k}^{\text{prompt}} = \tau_e W_{2k}$. In the two-state model, the kinetic sticking coefficient is moreover related to the prompt sticking coefficient by $s_e^{\text{kin}} = \tilde{e}_2^{(0)} s_e^{\text{prompt}}$. Hence, the probability for the electron to trickle through from the upper to the lower bound state is $\tilde{e}_2^{(0)}$.

For many dielectrics, the weakest transitions are from the lowest bound state to the upper bound states. They are typically triggered by more than two phonons. To mimic this situation within the two-state model, we set $W_{21} \ll W_{12}, W_{c2}$. The inverse of the desorption time becomes, in this limit,

$$\tau_e^{-1} = \frac{W_{c2}}{W_{12} + W_{c2}} W_{21}, \quad (45)$$

and the ratio between kinetic and prompt sticking coefficient becomes

$$\frac{s_e^{\text{kin}}}{s_e^{\text{prompt}}} = \frac{W_{12}}{W_{12} + W_{c2}}. \quad (46)$$

The physical behavior of the two-state model depends, therefore, on the ratio between W_{12} and W_{c2} and, thus, on the potential depth and the surface temperature. Two extreme

cases are possible and represent different physisorption scenarios. For $W_{c2} \ll W_{12}$, $\tau_e^{-1} \cong (W_{21}/W_{12})W_{c2}$, which, using detailed balance, can be brought into the Arrhenius form $\tau_e^{-1} = e^{-\beta(E_2-E_1)}W_{c2}$. Kinetic and prompt sticking coefficients coincide moreover in this parameter range. Hence, an electron trapped in the upper state drops to the lowest state before desorption. Desorption from the lowest state occurs then via a cascade, that is, a series of fast transitions $1 \rightarrow 2 \rightarrow 1 \rightarrow 2 \rightarrow 1 \dots$ until eventually the transition $2 \rightarrow$ removes the electron from the bound states. The just-described physisorption scenario, which we call type-A scenario, is illustrated in the middle panel of Fig. 7. Recalling that the upper level stands for a manifold of strongly coupled bound states, it resembles the physisorption of neutral particles via cascades originally proposed and investigated by Gortel and co-workers.²⁸

In the other limit, $W_{12} \ll W_{c2}$. The inverse of the desorption time and the ratio between prompt and kinetic sticking coefficient are then given by $\tau_e^{-1} \cong W_{21}$ and $s_e^{\text{kin}}/s_e^{\text{prompt}} \cong W_{12}/W_{c2}$, respectively. The physisorption scenario is now dramatically different from the one discussed before because the desorption time is solely determined by the transition probability from the lower to the upper bound state. As a result, desorption does not occur via a cascade, but as a one-way process $1 \rightarrow 2 \rightarrow$ continuum, where the second transition is so fast that it basically does not affect the desorption time. Hence, in this scenario, which we call type B, the upper bound state can be considered as *de facto* belonging to the continuum and desorption as basically equivalent to desorption from a single deep state. For sticking, the type-B scenario exhibits moreover a relaxation bottleneck. An electron trapped in the upper state is very unlikely to drop to the lowest bound state, as schematically shown in the right panel of Fig. 7.

Within the limits set by the model for the electron-surface interaction introduced in I and briefly recalled in Sec. III, the two-state model contains the essential physics of electron physisorption. For potentials with $\epsilon_2 > -1$, where a direct one-phonon transition from the second bound state to the continuum is possible, the two-state model can be applied directly. Calculating the desorption time within the two-state model shows very good agreement with the results for graphite obtained in I. For the ratio between kinetic and prompt sticking coefficient $s_e^{\text{kin}}/s_e^{\text{prompt}}$, which is given in the two-state model by $\tilde{e}_2^{(0)}$, the agreement is less good but qualitatively correct, reproducing, for instance, the temperature-dependent transition between types A and B. For potentials with $\epsilon_2 < -1$, no one-phonon process from the second bound state to the continuum is possible and the two-state model can not be applied directly. For physisorption of type B, however, the electron kinetics in the upper bound states is only marginally perturbed by transitions to and from the lowest bound state. The time it takes an electron to get from the second bound state into the continuum is then the desorption time of the system of the upper bound states alone, that is, the negative inverse of the smallest eigenvalue $-\lambda_0^{\text{up}}$ of the matrix T_{nm}^{up} , which is the matrix T_{nm} defined in Eq. (2) with $n, m > 1$. In the two-state model, λ_0^{up} can be regarded as an effective transition rate between the second state and the continuum. Hence, to apply the two-state model with potentials where the second bound state does not

couple by one-phonon processes to the continuum, we simply replace in Eqs. (45) and (46) W_{c2} by λ_0^{up} .

Let us finally look at the results obtained in the previous section and in I and II from the perspective of the two-state model. In a one-phonon deep potential, the transitions from the upper bound states to the lowest bound state and from the upper bound states to the continuum are enabled by one-phonon processes. In this case, the downward transitions are always more likely than the upward transitions so that one-phonon deep potentials always give rise to physisorption of type A. Hence, they show no relaxation bottleneck and prompt and kinetic sticking coefficient coincide. Two- or more-phonon deep potentials can either lead to physisorption of type A or B, depending on the surface temperature. In this case, one-phonon transitions from the upper bound states to the continuum compete with multiphonon transitions from the upper bound states to the lowest bound state. As a transition from the upper states to the continuum requires phonon absorption, proportional to n_B , while a transition from the upper states to the lowest requires phonon emission, proportional to $1 + n_B$, we expect that, for sufficiently low temperature, physisorption is always of type A, even for multiphonon deep potentials. For sufficiently high temperatures, all two- or more-phonon deep potentials are, however, of type B. In this case, a relaxation bottleneck results in the discrepancy between prompt and kinetic sticking coefficient (see Fig. 4). The electron kinetics is primarily determined by the one-phonon transitions among the upper states (see Fig. 5). The temperature at which type A merges into type B depends on the potential depth and the Debye temperature. For room temperature, the three-phonon deep potentials of Al_2O_3 , CaO , and SiO_2 and the two-phonon deep potential of MgO are all of type B. The crossover between types A and B occurs for the two-phonon deep potential of graphite at room temperature (see Fig. 5 of our previous work II).

VI. CONCLUSIONS

Within a simplified one-dimensional model for the polarization-induced interaction between an external electron and a dielectric surface with a sufficiently large energy gap and a sufficiently negative electron affinity, we investigated phonon-induced adsorption and desorption of an electron at a dielectric surface. The required electron energy relaxation, inducing transitions between the eigenstates of the surface potential, which we approximated by a recoil-corrected image potential, is due to the coupling to an acoustic bulk phonon.

The majority of dielectrics of interest have a surface potential that is three- or more-phonon deep, that is, the energy difference between the two lowest bound states is more than two Debye energies of the bulk phonon. In our previous

work,^{23,24} we took multiphonon processes into account using a T matrix approach, which is, however, only feasible for one- and two-phonon deep potentials, as it is, for instance, in the case for graphite. To overcome this limitation, we derived in this paper a nonperturbative expression for the multiphonon transition probability arising solely from the nonlinearity of the electron-phonon interaction. In view of our previous results for one- and two-phonon deep potentials, we expect this approximation to give an acceptable correct order-of-magnitude estimate for the multiphonon transition probability involving more than two phonons, despite the neglect of resonant processes stemming from the iteration of the T matrix.

We presented numerical results for the electron desorption time for graphite, MgO , CaO , Al_2O_3 , and SiO_2 and the prompt and kinetic energy-resolved and energy-averaged electron sticking coefficient for CaO , Al_2O_3 , and SiO_2 . In addition, we calculated the energy-resolved desorption flux and investigated the time evolution of the bound-state occupancy after initial trapping of an electron, revealing the characteristic stages of electron physisorption: initial trapping, relaxation in the upper bound states, trickling through to the lowest bound state, and desorption. Ultrafast electron spectroscopy at surfaces with stable image states⁴⁻⁶ should be able to resolve these different stages experimentally.

Using a simple two-state model, we finally identified two vastly different scenarios of electron physisorption, depending on potential depth and surface temperature, and put our results, including the ones of our previous work,^{23,24} into perspective. For almost all dielectrics of practical interest, the trapped electron has, only for very low temperatures well below room temperature, a significant chance to trickle through to the lowest bound state. The desorption process in this case would then proceed via a cascade between the first and second bound state until it eventually makes a transition from there to the continuum. The shallow bound states, albeit important for adsorption, play a minor role for desorption. The second bound state is the most important one. It is a relay state. At room temperature, however, a relaxation bottleneck prevents the trapped electron from falling to the lowest bound state. The electron physisorption kinetics is thus dominated by fast one-phonon transitions in the upper bound states. Only a small fraction of the electron trickles through to the lowest bound state and resides there for a very long time until it makes a one-step desorbing transition to the continuum.

ACKNOWLEDGMENT

This work was supported by the Deutsche Forschungsgemeinschaft (DFG) through the transregional collaborative research center SFB/TRR 24.

¹M. W. Cole and M. H. Cohen, *Phys. Rev. Lett.* **23**, 1238 (1969).

²V. Dose, W. Altmann, A. Goldmann, U. Kolac, and J. Rogozik, *Phys. Rev. Lett.* **52**, 1919 (1984).

³D. Straub and F. J. Himpsel, *Phys. Rev. Lett.* **52**, 1922 (1984).

⁴T. Fauster, *Appl. Phys. A: Mater. Sci. Process.* **59**, 479 (1994).

⁵U. Höfer, I. L. Shumay, C. Reuss, U. Thomann, W. Wallauer, and T. Fauster, *Science* **277**, 1480 (1997).

⁶U. Höfer, *Appl. Phys. B: Lasers Opt.* **68**, 383 (1999).

- ⁷J. Lehmann, M. Merschdorf, A. Thon, S. Voll, and W. Pfeiffer, *Phys. Rev. B* **60**, 17037 (1999).
- ⁸K. P. Loh, I. Sakaguchi, M. N. Gamo, S. Tagawa, T. Sugino, and T. Ando, *Appl. Phys. Lett.* **74**, 28 (1999).
- ⁹B. Baumeier, P. Kruger, and J. Pollmann, *Phys. Rev. B* **76**, 205404 (2007).
- ¹⁰K. G. Emeleus and J. R. M. Coulter, *Int. J. Electron.* **62**, 225 (1987).
- ¹¹K. G. Emeleus and J. R. M. Coulter, *IEE Proceedings A Science Measurement and Technology* **135**, 76 (1988).
- ¹²J. F. Behnke, T. Bindemann, H. Deutsch, and K. Becker, *Contrib. Plasma Phys.* **37**, 345 (1997).
- ¹³Y. B. Golubovskii, V. A. Maiorov, J. Behnke, and J. F. Behnke, *J. Phys. D: Appl. Phys.* **35**, 751 (2002).
- ¹⁴F. X. Bronold, H. Fehske, H. Kersten, and H. Deutsch, *Phys. Rev. Lett.* **101**, 175002 (2008).
- ¹⁵F. X. Bronold, H. Deutsch, and H. Fehske, *Eur. Phys. J. D* **54**, 519 (2009).
- ¹⁶F. X. Bronold, R. L. Heinisch, J. Marbach, and H. Fehske, *IEEE Trans. Plasma Sci.* **39**, 644 (2011).
- ¹⁷M. W. Geis, S. Deneault, K. E. Krohn, M. Marchant, T. M. Lyszczarz, and D. L. Cooke, *Appl. Phys. Lett.* **87**, 192115 (2005).
- ¹⁸M. Biasini, R. D. Gann, J. A. Yarmoff, A. P. Mills, L. N. Pfeiffer, K. W. West, X. P. W. Gao, and B. C. D. Williams, *Appl. Phys. Lett.* **86**, 162111 (2005).
- ¹⁹H. Hattori, *Chem. Rev. (Washington, DC, U. S.)* **95**, 537 (1995).
- ²⁰H. Hattori, *J. Jpn. Petrol. Inst.* **47**, 67 (2003).
- ²¹M. Wolf and G. Ertl, *Science* **288**, 1352 (2000).
- ²²H.-J. Freund, *Surf. Sci.* **601**, 1438 (2007).
- ²³R. L. Heinisch, F. X. Bronold, and H. Fehske, *Phys. Rev. B* **81**, 155420 (2010).
- ²⁴R. L. Heinisch, F. X. Bronold, and H. Fehske, *Phys. Rev. B* **82**, 125408 (2010).
- ²⁵B. Bendow and S.-C. Ying, *Phys. Rev. B* **7**, 622 (1973).
- ²⁶Z. W. Gortel, H. J. Kreuzer, and R. Teshima, *Phys. Rev. B* **22**, 512 (1980).
- ²⁷G. Armand and J. R. Manson, *Phys. Rev. B* **43**, 14371 (1991).
- ²⁸Z. W. Gortel, H. J. Kreuzer, and R. Teshima, *Phys. Rev. B* **22**, 5655 (1980).
- ²⁹H. J. Kreuzer and Z. W. Gortel, *Physisorption Kinetics* (Springer-Verlag, Berlin, 1986).
- ³⁰G. Iche and P. Nozières, *Journal de Physique (Paris)* **37**, 1313 (1976).
- ³¹W. Brenig, *Z. Phys. B: Condens. Matter* **48**, 127 (1982).
- ³²E. Evans and D. L. Mills, *Phys. Rev. B* **8**, 4004 (1973).
- ³³A. Šiber and B. Gumhalter, *Phys. Rev. Lett.* **90**, 126103 (2003).
- ³⁴A. Šiber and B. Gumhalter, *Phys. Rev. B* **71**, 081401 (2005).
- ³⁵W. Brenig, *Phys. Rev. Lett.* **92**, 056102 (2004).
- ³⁶A. Šiber and B. Gumhalter, *J. Phys. Condens. Matter* **20**, 224002 (2008).
- ³⁷J. R. Manson, *Phys. Rev. B* **43**, 6924 (1991).
- ³⁸R. J. Glauber, *Phys. Rev.* **98**, 1692 (1955).

Mie Scattering by a Charged Dielectric Particle

R. L. Heinisch, F. X. Bronold, and H. Fehske

Institut für Physik, Ernst-Moritz-Arndt-Universität Greifswald, 17489 Greifswald, Germany

(Received 30 May 2012; published 10 December 2012)

We study for a dielectric particle the effect of surplus electrons on the anomalous scattering of light arising from the transverse optical phonon resonance in the particle's dielectric function. Excess electrons affect the polarizability of the particle by their phonon-limited conductivity, either in a surface layer (negative electron affinity) or the conduction band (positive electron affinity). We show that surplus electrons shift an extinction resonance in the infrared. This offers an optical way to measure the charge of the particle and to use it in a plasma as a minimally invasive electric probe.

DOI: [10.1103/PhysRevLett.109.243903](https://doi.org/10.1103/PhysRevLett.109.243903)

PACS numbers: 42.25.Bs, 42.25.Fx, 73.20.-r, 73.25.+i

The scattering of light by a spherical particle is a fundamental problem of electromagnetic theory. Solved by Mie in 1908 [1], it encompasses a wealth of scattering phenomena owing to the complicated mathematical form of the scattering coefficients and the variety of the underlying material-specific dielectric constants [2,3]. While Mie scattering is routinely used as a particle size diagnostic [2], the particle charge has not yet been determined from the Mie signal. Most particles of interest in astronomy, astrophysics, atmospheric sciences, and laboratory experiments are however charged [4–8]. The particle charge is a rather important parameter. It determines the coupling of the particles among each other and to external electromagnetic fields. An optical measurement of it would be extremely useful. In principle, light scattering contains information about excess electrons as their electrical conductivity modifies either the boundary condition for electromagnetic fields or the polarizability of the material [2,9–11]. But how strong and in what spectral range the particle charge reveals itself by distorting the Mie signal of the neutral particle is an unsettled issue.

In this Letter, we revisit Mie scattering by a negatively charged dielectric particle. Where electrons are trapped on the particle depends on the electron affinity χ of the dielectric, that is, the offset of the conduction band minimum to the potential in front of the surface. For $\chi < 0$, as it is the case for MgO, CaO, or LiF [12,13], the conduction band lies above the potential outside the grain and electrons are trapped in the image potential induced by a surface mode associated with the transverse optical (TO) phonon [14,15]. The conductivity σ_s of this two-dimensional electron gas is limited by the residual scattering with the surface mode and modifies the boundary condition for the electromagnetic fields at the surface of the grain. For $\chi > 0$, as it is the case for Al₂O₃ or SiO₂, electrons accumulate in the conduction band forming a space charge [15]. Its width, limited by the screening in the dielectric, is typically larger than a micron. For micron-sized particles we can thus assume a homogeneous distribution of the excess electrons in the bulk. The effect on

light scattering is now encoded in the bulk conductivity of the excess electrons σ_b , which is limited by scattering with a longitudinal optical (LO) bulk phonon and gives rise to an additional polarizability per volume $\alpha = 4\pi i\sigma_b/\omega$, where ω is the frequency of the light. We focus on the scattering of light in the vicinity of anomalous optical resonances that have been identified for metal particles by Tribelsky *et al.* [16,17]. These resonances occur at frequencies ω where the complex dielectric function $\epsilon(\omega) = \epsilon'(\omega) + i\epsilon''(\omega)$ has $\epsilon' < 0$ and $\epsilon'' \ll 1$. For a dielectric they are induced by the TO phonon and lie in the infrared. Using Mie theory, we show that for submicron-sized particles the extinction resonance shifts with the particle charge and can thus be used to determine the particle charge.

In the framework of Mie theory, the scattering and transmission coefficients connecting incident (*i*), reflected (*r*), and transmitted (*t*) partial waves are determined by the boundary conditions for the electric and magnetic fields at the surface of the particle [2,18]. For a charged particle with $\chi < 0$ the surface charges may sustain a surface current \mathbf{K} which enters the boundary condition for the magnetic field. Thus, $\hat{\mathbf{e}}_r \times (\mathbf{H}_i + \mathbf{H}_r - \mathbf{H}_t) = \frac{4\pi}{c}\mathbf{K}$, where c is the speed of light [11]. The surface current $\mathbf{K} = \sigma_s \mathbf{E}_{\parallel}$ is induced by the component of the electric field parallel to the surface and is proportional to the surface conductivity σ_s . For $\chi > 0$ the bulk surplus charge enters the refractive index $N = \sqrt{\epsilon + \alpha}$ through its polarizability. Matching the fields at the boundary of a dielectric sphere with radius a gives, following Bohren and Hunt [11], the scattering coefficients

$$\begin{aligned} a_n^r &= \frac{\psi_n(N\rho)\psi_n'(\rho) - [N\psi_n'(N\rho) - i\tau\psi_n(N\rho)]\psi_n(\rho)}{[N\psi_n'(N\rho) - i\tau\psi_n(N\rho)]\xi_n(\rho) - \psi_n(N\rho)\xi_n'(\rho)}, \\ b_n^r &= \frac{\psi_n'(N\rho)\psi_n(\rho) - [N\psi_n(N\rho) + i\tau\psi_n'(N\rho)]\psi_n'(\rho)}{[N\psi_n(N\rho) + i\tau\psi_n'(N\rho)]\xi_n(\rho) - \psi_n'(N\rho)\xi_n(\rho)}, \end{aligned} \quad (1)$$

where for $\chi < 0$ ($\chi > 0$) the dimensionless surface conductivity $\tau(\omega) = 4\pi\sigma_s(\omega)/c$ ($\tau = 0$) and the refractive

index $N = \sqrt{\epsilon}$ ($N = \sqrt{\epsilon + \alpha}$), the size parameter $\rho = ka = 2\pi a/\lambda$, where k is the wave number, $\psi_n(\rho) = \sqrt{\pi\rho/2}J_{n+1/2}(\rho)$, $\xi_n(\rho) = \sqrt{\pi\rho/2}H_{n+1/2}^{(1)}(\rho)$ with $J_n(\rho)$ the Bessel and $H_n^{(1)}(\rho)$ the Hankel function of the first kind. As for uncharged particles the extinction efficiency becomes $Q_t = -(2/\rho^2)\sum_{n=1}^{\infty}(2n+1)\text{Re}(a_n' + b_n')$. Any effect of the surplus electrons on the scattering of light, encoded in a_n' and b_n' , is due to the surface conductivity ($\chi < 0$) or the bulk conductivity ($\chi > 0$).

For $\chi < 0$ we describe the surface electron film in a planar model to be justified below. For the dielectrics which we consider, the low-frequency dielectric function is dominated by an optically active TO phonon with frequency ω_{TO} . For the modeling of the surface electrons it suffices to approximate it by $\epsilon(\omega) = 1 + \omega_{\text{TO}}^2(\epsilon_0 - 1)/(\omega_{\text{TO}}^2 - \omega^2)$, where ϵ_0 is the static dielectric constant. This allows for a TO surface mode whose frequency is given by $\epsilon(\omega_s) = -1$ leading to $\omega_s = \omega_{\text{TO}}\sqrt{(1 + \epsilon_0)/2}$ [19]. The coupling of the electron to this surface mode consists of a static and a dynamic part [20]. The former leads to the image potential $V = -\Lambda_0 e^2/z$ with $\Lambda_0 = (\epsilon_0 - 1)/[4(\epsilon_0 + 1)]$ supporting a series of bound Rydberg states whose wave functions read $\phi_{n\mathbf{k}}(\mathbf{x}, z) = \sqrt{\Lambda_0/Aa_B n n!^2} e^{i\mathbf{k}\cdot\mathbf{x}} W_{n,1/2}(2\Lambda_0 z/na_B)$ with a_B the Bohr radius, $\mathbf{k} = (k_x, k_y)$, $\mathbf{x} = (x, y)$, and A the surface area. Since trapped electrons are thermalized with the surface and the spacing between Rydberg states is large compared to $k_B T$, they occupy only the lowest image band $n = 1$. Assuming a planar surface is justified provided the de Broglie wavelength λ_{dB} of the electron on the surface is smaller than the radius a of the sphere. For a surface electron with energy $E_{\text{kin}}/k_B = 300$ K one finds $\lambda_{dB} \approx 10^{-6}$ cm. Thus, for particle radii $a > 10$ nm the plane-surface approximation is justified. The dynamic interaction enables momentum relaxation parallel to the surface and limits the surface conductivity. Introducing annihilation operators $c_{\mathbf{k}}$ and $a_{\mathbf{Q}}$ for electrons and phonons, the Hamiltonian describing the dynamic electron-phonon coupling in the lowest image band reads $H = \sum_{\mathbf{k}} \epsilon_{\mathbf{k}} c_{\mathbf{k}}^\dagger c_{\mathbf{k}} + \hbar\omega_s \sum_{\mathbf{Q}} a_{\mathbf{Q}}^\dagger a_{\mathbf{Q}} + H_{\text{int}}$ [21] with $H_{\text{int}} = \sum_{\mathbf{k}, \mathbf{Q}} (M_{\mathbf{k}, \mathbf{Q}}/\sqrt{A}) c_{\mathbf{k}+\mathbf{Q}}^\dagger (a_{\mathbf{Q}} - a_{-\mathbf{Q}}^\dagger) c_{\mathbf{k}}$, where the matrix element is given by (m is the electron mass)

$$M_{\mathbf{k}\mathbf{Q}} = \frac{2e\sqrt{\pi\Lambda_0\hbar^3}}{m\sqrt{\omega_s Q}} \left(\frac{2\Lambda_0}{Qa_B + 2\Lambda_0} \right)^3 \left[\mathbf{Q}\mathbf{k} + \frac{Q^2}{2} \right]. \quad (2)$$

Within the memory function approach [22] the surface conductivity can be written as

$$\sigma_s(\omega) = \frac{e^2 n_s}{m} \frac{i}{\omega + M(\omega)} \quad (3)$$

with n_s the surface electron density. Up to second order in the electron-phonon coupling the memory function

$$M(\omega) = \frac{\sqrt{m\omega_s} \delta e^2 \Lambda_0}{\sqrt{2\pi\hbar^3}} \int_{-\infty}^{\infty} d\bar{\nu} \frac{j(-\bar{\nu}) - j(\bar{\nu})}{\bar{\nu}(\bar{\nu} - \nu - i0^+)}, \quad (4)$$

$$j(\nu) = \frac{e^\delta}{e^\delta - 1} |\nu + 1|^3 e^{-\delta(\nu+1)/2} I_{(\gamma/\sqrt{|\nu+1|})} \left(\frac{\delta|\nu+1|}{4} \right) + \frac{1}{e^\delta - 1} |\nu - 1|^3 e^{-\delta(\nu-1)/2} I_{(\gamma/\sqrt{|\nu-1|})} \left(\frac{\delta|\nu-1|}{4} \right), \quad (5)$$

where $\nu = \omega/\omega_s$, $\delta = \beta\hbar\omega_s$, $\gamma = \sqrt{2\Lambda_0^2\hbar/a_B^2 m\omega_s}$, and $I_a(x) = \int_0^\infty dt e^{-x(1/t+t)} a^6/(a + \sqrt{t})^6$ which for low temperature, that is $x \rightarrow \infty$, has the asymptotic form $I_a(x) \sim \sqrt{\pi/x} e^{-2x} a^6/(1+a)^6$. Since $M(\omega)$ is independent of n_s , the surface conductivity is proportional to n_s .

For $\chi > 0$ the bulk conductivity is limited by a LO phonon with frequency ω_{LO} . The coupling of the electron to this mode is described by $H_{\text{int}} = \sum_{\mathbf{k}, \mathbf{q}} M c_{\mathbf{k}+\mathbf{q}}^\dagger c_{\mathbf{k}} (a_{\mathbf{q}} + a_{-\mathbf{q}}^\dagger)/\sqrt{V} q$ [23], where $M = \sqrt{2\pi e^2 \hbar \omega_{\text{LO}} (\epsilon_\infty^{-1} - \epsilon_0^{-1})}$. Employing the memory function approach, the bulk conductivity is given by Eq. (3) where n_s is replaced by the bulk electron density n_b and m by the conduction band effective mass m^* , the prefactor of the memory function [Eq. (4)] is then $4e^2 \sqrt{m^* \omega_{\text{LO}} \delta} (\epsilon_\infty^{-1} - \epsilon_0^{-1}) / (3\sqrt{(2\pi\hbar)^3})$, and

$$j(\nu) = \frac{e^\delta}{e^\delta - 1} |\nu + 1| e^{-\delta(\nu+1)/2} K_1(\delta|\nu + 1|/2) + \frac{1}{e^\delta - 1} |\nu - 1| e^{-\delta(\nu-1)/2} K_1(\delta|\nu - 1|/2), \quad (6)$$

where $\nu = \omega/\omega_{\text{LO}}$, $\delta = \beta\hbar\omega_{\text{LO}}$, and $K_1(x)$ is a modified Bessel function. For low temperature, i.e., $\delta \rightarrow \infty$ $j(\nu) \sim \sqrt{\pi/\delta} \sqrt{|\nu + 1|} \theta(-\nu - 1)$.

To exemplify light scattering by a charged dielectric particle we consider a MgO ($\chi < 0$) and an Al₂O₃ ($\chi > 0$) particle [24]. The charge effect on scattering is controlled by the dimensionless surface conductivity $\tau = \tau' + i\tau''$ (for $\chi < 0$) or the excess electron polarizability $\alpha = \alpha' + i\alpha''$ (for $\chi > 0$), both shown in Fig. 1, which are small even for a highly charged particle with $n_s = 10^{13}$ cm⁻² (corresponding to $n_b = 3 \times 10^{17}$ cm⁻³ for $\chi > 0$ and $a = 1$ μm). The electron-phonon coupling reduces τ'' and α' compared to a free electron gas where $M(\omega) = 0$, implying $\tau' = 0$ and $\alpha'' = 0$. For $T = 0$ K, $\tau' = 0$ ($\alpha'' = 0$) for $\lambda^{-1} < \lambda_s^{-1} = 909$ cm⁻¹, the inverse wavelength of the surface phonon ($\lambda^{-1} < \lambda_{\text{LO}}^{-1} = 807$ cm⁻¹, the inverse wavelength of the bulk LO phonon) since light absorption is only possible above the surface (bulk LO) phonon frequency. At room temperature τ'' and α' still outweigh τ' and α'' . The temperature effect on τ'' is less apparent for $\lambda^{-1} > 300$ cm⁻¹ than for α' but for $\lambda^{-1} < 300$ cm⁻¹ a higher temperature lowers τ'' considerably. The upper panel of Fig. 2 shows the complex dielectric constant ϵ and the refractive index N . For MgO we use a two-oscillator fit for

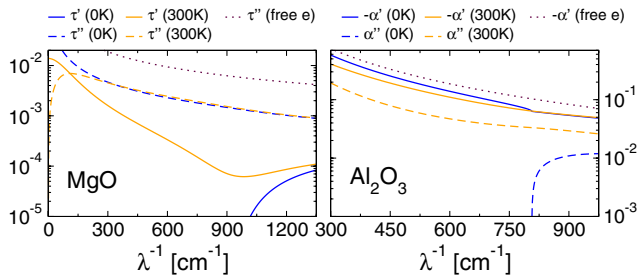


FIG. 1 (color online). Dimensionless surface conductivity $\tau = \tau' + i\tau''$ for MgO for $n_s = 10^{13} \text{ cm}^{-2}$ (left) and polarizability of excess electrons $\alpha = \alpha' + i\alpha''$ for Al₂O₃ for $n_b = 3 \times 10^{17} \text{ cm}^{-3}$ (right) as a function of the inverse wavelength λ^{-1} .

ϵ [26,31]. In the infrared, ϵ is dominated by a TO phonon at 401 cm^{-1} . The second phonon at 640 cm^{-1} is much weaker, justifying our model for the image potential based on one dominant phonon. Far above the highest TO phonon, that is, for $\lambda^{-1} > 800 \text{ cm}^{-1}$ ($\lambda^{-1} > 900 \text{ cm}^{-1}$) for MgO (Al₂O₃) $\epsilon' > 0$ and $\epsilon'' \ll 1$. For these wave numbers a micron-sized grain would give rise to a typical Mie plot exhibiting interference and ripples due to the functional form of a_n^r and b_n^r and not due to the dielectric constant. Surplus electrons would not alter the extinction in this region because $|\epsilon| \gg |\tau|$ and $|\epsilon| \gg |\alpha|$.

To observe a stronger dependence of extinction on the parameters ϵ and τ or α , we turn to $400 \text{ cm}^{-1} < \lambda^{-1} < 700 \text{ cm}^{-1}$ for MgO ($700 \text{ cm}^{-1} < \lambda^{-1} < 900 \text{ cm}^{-1}$ for Al₂O₃) where $\epsilon' < 0$ and $\epsilon'' \ll 1$ allowing for optical resonances, sensitive to even small changes in ϵ . They correspond to resonant excitation of transverse surface modes of the sphere [32]. For a metal particle the resonances are due to plasmons and lie in the ultraviolet [16,17]. For a dielectric the TO phonon induces them. As the polarizability of excess electrons, encoded in τ or α , is

larger at low frequency, the resonances of a dielectric particle, lying in the infrared, should be more susceptible to surface charges. The lower panel of Fig. 2 shows a clearly distinguishable series of resonances in the extinction efficiency. The effect of negative excess charges is shown by the crosses in Fig. 3. The extinction maxima are shifted to higher λ^{-1} for both surface and bulk excess electrons. For comparison the circles show the shift for a free electron gas. The effect is strongest for the first resonance, where a surface electron density 10^{13} cm^{-2} (or an equivalent bulk charge), realized for instance in dusty plasmas [33], yields a shift of a few wave numbers.

The shift can be more clearly seen in Fig. 4 where the tail of the first resonance is plotted for MgO on an enlarged scale. The main panel shows the extinction efficiency for $n_s = 10^{13} \text{ cm}^{-2}$ with its maxima indicated by blue dots. Without surface charge the resonance is at $\lambda^{-1} = 606 \text{ cm}^{-1}$ for $a < 0.25 \mu\text{m}$. For a charged particle it moves to higher λ^{-1} and this effect becomes stronger the smaller the particle is. The line shape of the extinction resonance for fixed particle size is shown in the top and bottom panels for $a = 0.2 \mu\text{m}$ and $a = 0.05 \mu\text{m}$, respectively. For comparison, data for other surface charge densities are also shown. Figure 4 also suggests that the resonance shift is even more significant for particles with radius $a < 0.01 \mu\text{m}$ where the planar model for the image states is inapplicable. An extension of our model, guided by the study of multielectron bubbles in helium [34], requires surface phonons, image potential, and electron-phonon coupling for a sphere. Because of its insensitivity to the location of the excess electrons, we expect qualitatively the same resonance shift for very small grains.

As we are considering particles small compared to λ we expand the scattering coefficients for small ρ . To ensure that in the limit of an uncharged grain, that is, for $\tau \rightarrow 0$, a_n^r and b_n^r converge to their small ρ expansions [18], we

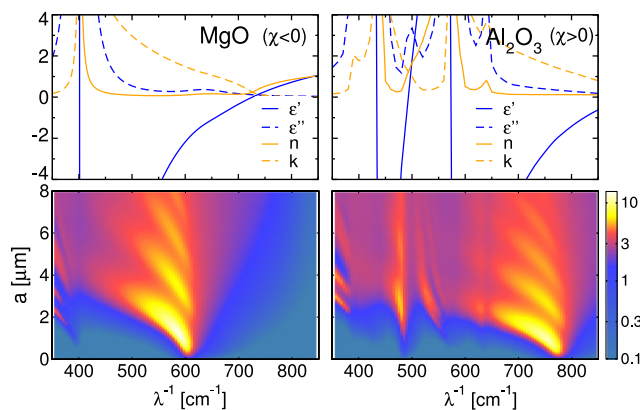


FIG. 2 (color online). Dielectric constant $\epsilon = \epsilon' + i\epsilon''$, refractive index $N = n + ik$ (top), and extinction efficiency Q_t (bottom) depending on the particle radius a for MgO and Al₂O₃ as a function of the inverse wavelength λ^{-1} .

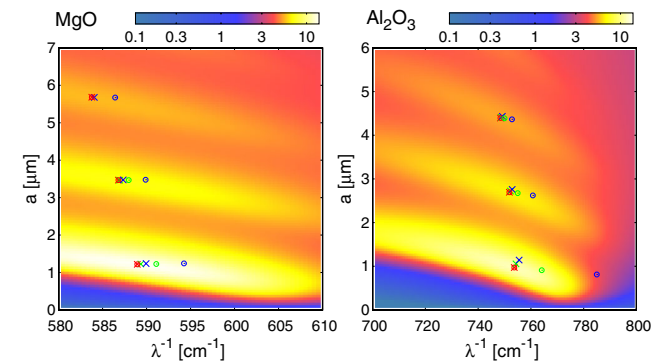


FIG. 3 (color online). Magnification of the extinction resonances depending on λ^{-1} and a . Crosses indicate their maxima (from left to right) for $n_s = 0$ (red), 2×10^{13} (green), and $5 \times 10^{13} \text{ cm}^{-2}$ (blue) at $T = 300 \text{ K}$ for MgO (left panel) and for $n_b = 3n_s/a$ for Al₂O₃ (right panel). Open circles indicate the maxima for free electrons.

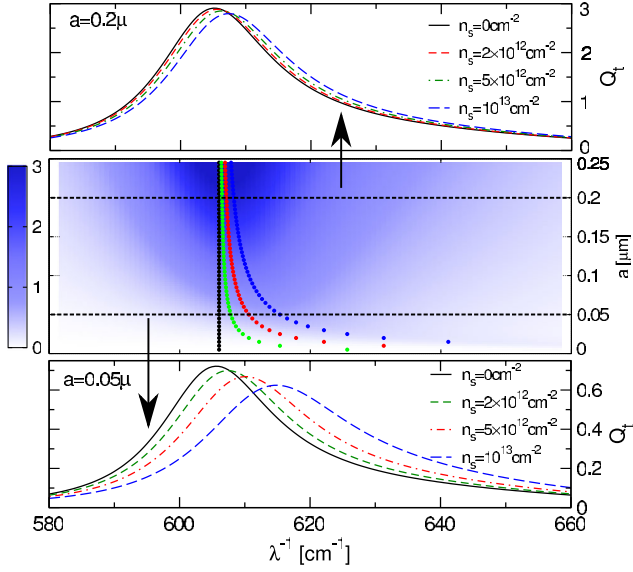


FIG. 4 (color online). Middle: Extinction efficiency Q_t as a function of the inverse wavelength λ^{-1} and the radius a for a MgO particle with $n_s = 10^{13} \text{ cm}^{-2}$ and $T = 300 \text{ K}$. The dotted lines indicate the extinction maximum for $n_s = 0$ (black), 2×10^{12} (green), 5×10^{12} (red), and 10^{13} cm^{-2} (blue) obtained from (8). Top and bottom: Extinction efficiency Q_t as a function of λ^{-1} for $a = 0.2 \mu\text{m}$ (top) and $a = 0.05 \mu\text{m}$ (bottom) for different surface electron densities.

substitute $t = \tau/\rho$ before expanding the coefficients. Up to $\mathcal{O}(\rho^3)$ this yields $a_1^t = a_2^t = b_2^t = 0$ and only $b_1^t \sim \mathcal{O}(\rho^3)$ contributes. Then the extinction efficiency reads

$$Q_t = \frac{12\rho(\epsilon'' + \alpha'' + 2\tau'/\rho)}{(\epsilon' + \alpha' + 2 - 2\tau''/\rho)^2 + (\epsilon'' + \alpha'' + 2\tau'/\rho)^2}, \quad (7)$$

where the excess charges enter either through τ with $\alpha = 0$ for $\chi < 0$ or through α with $\tau = 0$ for $\chi > 0$. For $\tau, \alpha \rightarrow 0$ this gives the limit of Rayleigh scattering. The resonance is located at the wave number where

$$\epsilon' + \alpha' + 2 - 2\tau''/\rho = 0 \quad (8)$$

and has a Lorentzian shape, already apparent from Fig. 4, provided ϵ'' and τ' (or α'') vary only negligibly near the resonance wavelength. For an uncharged surface the resonance is at λ_0^{-1} for which $\epsilon' = -2$. For $\chi < 0$ the shift of the resonance is proportional to τ'' and thus to n_s , provided ϵ' is well approximated linearly in λ^{-1} and τ'' does not vary significantly near λ_0^{-1} . In this case, we substitute in (8) the expansions $\epsilon' = -2 + c_\epsilon(\lambda^{-1} - \lambda_0^{-1})$ and $\tau'' = c_\tau n_s$ where $c_\epsilon = \frac{\partial \epsilon'}{\partial \lambda^{-1}}|_{\lambda_0^{-1}}$ and $c_\tau = \frac{\tau''}{n_s}|_{\lambda_0^{-1}}$. Then the resonance is located at $\lambda^{-1} = \lambda_0^{-1} + c_\tau n_s / (c_\epsilon a \lambda_0^{-1})$. For $\chi > 0$ the resonance is located at $\lambda^{-1} = \lambda_0^{-1} - c_\alpha n_b / c_\epsilon$ where $c_\alpha = \frac{\alpha'}{n_b}|_{\lambda_0^{-1}}$. The dotted lines in Fig. 4 give the location of the resonance obtained from Eq. (8) for MgO,

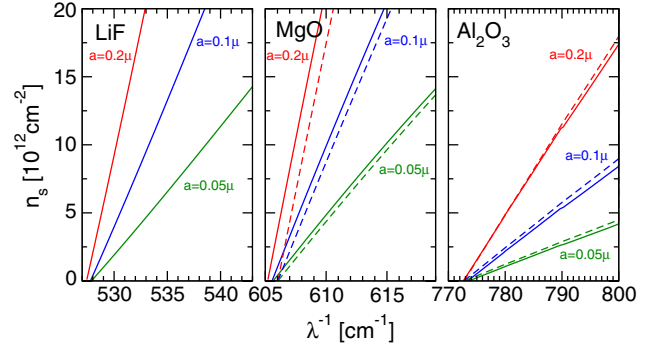


FIG. 5 (color online). Position of the extinction resonance depending on the surface charge n_s for LiF, MgO, and Al_2O_3 (for equivalent bulk charge $n_b = 3n_s/a$) particles with different radii a . Solid (dashed) lines are obtained from the Mie contour [Eq. (8)].

where $\lambda_0^{-1} = 606 \text{ cm}^{-1}$ for several surface electron densities. They agree well with the underlying contour calculated from the exact Mie solution, as exemplified for $n_s = 10^{13} \text{ cm}^{-2}$. The proportionality of the resonance shift to n_s (n_b) can also be seen in Fig. 5 where we plot on the abscissa the shift of the extinction resonance arising from the surface electron density given on the ordinate for LiF [24], MgO ($\chi < 0$), and Al_2O_3 ($\chi > 0$). Both bulk and surface electrons lead to a resonance shift. To illustrate the similarity of the shift we consider (8) for free electrons, which then becomes $\epsilon' - 2N_e e^2 / (m a^3 \omega^2) = -2$ for $\chi < 0$ and $\epsilon' - 3N_e e^2 / (m^* a^3 \omega^2) = -2$ for $\chi > 0$; N_e is the number of excess electrons. The effect of surface electrons is weaker by a factor $2m^*/3m$ where the $2/3$ arises from geometry as only the parallel component of the electric field acts on the spherically confined electrons. Most important, however, τ/ρ and α enter the resonance condition on the same footing showing that the shift is essentially an electron density effect on the polarizability of the grain. We therefore expect the shift to prevail also for electron distributions between the two limiting cases of a surface and a homogeneous bulk charge.

To conclude, our results suggest that for dielectric particles showing anomalous optical resonances the extinction maximum in the infrared can be used to determine the particle charge (see Fig. 5). For dusty plasmas this can be rather attractive because established methods for measuring the particle charge [35–37] require plasma parameters that are not precisely known whereas the charge measurement by Mie scattering does not. Particles with surface (negative electron affinity χ , e.g., MgO, LiF) as well as bulk excess electrons ($\chi > 0$ e.g., Al_2O_3) show the effect and could serve as model systems for submicron-sized dust in space, the laboratory, and the atmosphere. These particles could be used also as minimally invasive electric probes in a plasma, which collect electrons depending on the local plasma environment. Determining their charge from Mie scattering and the forces acting on them by

conventional means [35–37] would provide a way to extract plasma parameters locally.

We acknowledge support by the Deutsche Forschungsgemeinschaft through SFB-TRR 24, Project B10.

-
- [1] G. Mie, *Ann. Phys. (Berlin)* **330**, 377 (1908).
- [2] C.F. Bohren and D.R. Huffman, *Absorption and Scattering of Light by Small Particles* (Wiley, New York, 1983).
- [3] M. Born and E. Wolf, *Principles of Optics* (Cambridge University Press, Cambridge, England, 1999).
- [4] A. Heifetz, H. T. Chien, S. Liao, N. Gopalsami, and A. C. Raptis, *J. Quant. Spectrosc. Radiat. Transfer* **111**, 2550 (2010).
- [5] M. Friedrich and M. Rapp, *Surv. Geophys.* **30**, 525 (2009).
- [6] I. Mann, *Adv. Space Res.* **41**, 160 (2008).
- [7] O. Ishihara, *J. Phys. D* **40**, R121 (2007).
- [8] D. A. Mendis, *Plasma Sources Sci. Technol.* **11**, A219 (2002).
- [9] J. Klačka and M. Kocifaj, *Prog. Electromagn. Res.* **109**, 17 (2010).
- [10] J. Klačka and M. Kocifaj, *J. Quant. Spectrosc. Radiat. Transfer* **106**, 170 (2007).
- [11] C.F. Bohren and A.J. Hunt, *Can. J. Phys.* **55**, 1930 (1977).
- [12] M. Rohlfing, N.-P. Wang, P. Kruger, and J. Pollmann, *Phys. Rev. Lett.* **91**, 256802 (2003).
- [13] B. Baumeier, P. Kruger, and J. Pollmann, *Phys. Rev. B* **76**, 205404 (2007).
- [14] R. L. Heinisch, F. X. Bronold, and H. Fehske, *Phys. Rev. B* **83**, 195407 (2011).
- [15] R. L. Heinisch, F. X. Bronold, and H. Fehske, *Phys. Rev. B* **85**, 075323 (2012).
- [16] M. I. Tribelsky and B. S. Lykanchuk, *Phys. Rev. Lett.* **97**, 263902 (2006).
- [17] M. I. Tribelsky, *Europhys. Lett.* **94**, 14004 (2011).
- [18] J. A. Stratton, *Electromagnetic Theory* (McGraw-Hill, New York, 1941).
- [19] E. Evans and D. L. Mills, *Phys. Rev. B* **8**, 4004 (1973).
- [20] G. Barton, *J. Phys. C* **14**, 3975 (1981).
- [21] M. Kato and A. Ishii, *Appl. Surf. Sci.* **85**, 69 (1995).
- [22] W. Götzke and P. Wölfle, *Phys. Rev. B* **6**, 1226 (1972).
- [23] G. D. Mahan, *Many-Particle Physics* (Plenum, New York, 1990), pp. 703–708.
- [24] We use for MgO $\epsilon_0 = 9.8$ [25], $f_{\text{TO}} = \omega_{\text{TO}}/2\pi = 11.7$ THz and $\epsilon(\omega)$ from Ref. [26], for LiF $\epsilon_s = 8.8$ [27], $f_{\text{TO}} = 9.2$ THz [27] and $\epsilon(\omega)$ from Ref. [28], and for Al_2O_3 $f_0 = 24.2$ THz, $\epsilon_0 = 9$, $\epsilon_\infty = 3$ [29], $m^* = 0.4m_e$ [30], and $\epsilon(\omega)$ from Ref. [31].
- [25] M. Wintersgill, J. Fontanella, C. Andeen, and D. Schuele, *J. Appl. Phys.* **50**, 8259 (1979).
- [26] J. R. Jasperse, A. Kahan, J. N. Plendl, and S. S. Mitra, *Phys. Rev.* **146**, 526 (1966).
- [27] G. Dolling, H. G. Smith, R. M. Nicklow, P. R. Vijayaraghavan, and M. K. Wilkinson, *Phys. Rev.* **168**, 970 (1968).
- [28] A. M. Hofmeister, E. Keppel, and A. K. Speck, *Mon. Not. R. Astron. Soc.* **345**, 16 (2003).
- [29] M. Schubert, T. E. Tiwald, and C. M. Herzinger, *Phys. Rev. B* **61**, 8187 (2000).
- [30] T. V. Perevalov, A. V. Shaposhnikov, V. A. Gritsenko, H. Wong, J. H. Han, and C. W. Kim, *JETP Lett.* **85**, 165 (2007).
- [31] E. D. Palik, *Handbook of Optical Constants of Solids* (Academic, New York, 1985).
- [32] R. Fuchs and K. L. Kliewer, *J. Opt. Soc. Am.* **58**, 319 (1968).
- [33] V. E. Fortov, A. V. Gavrikov, O. F. Petrov, V. S. Sidorov, M. N. Vasiliev, and N. A. Vorona, *Europhys. Lett.* **94**, 55001 (2011).
- [34] J. Tempere, I. Silvera, and J. Devreese, *Surf. Sci. Rep.* **62**, 159 (2007).
- [35] J. Carstensen, H. Jung, F. Greiner, and A. Piel, *Phys. Plasmas* **18**, 033701 (2011).
- [36] S. A. Khrapak, S. V. Ratynskaia, A. V. Zobnin, A. D. Usachev, V. V. Yaroshenko, M. H. Thoma, M. Kretschmer, H. Hoefner, G. E. Morfill, O. F. Petrov *et al.*, *Phys. Rev. E* **72**, 016406 (2005).
- [37] E. B. Tomme, D. A. Law, B. M. Annaratone, and J. E. Allen, *Phys. Rev. Lett.* **85**, 2518 (2000).

Optical signatures of the Charge of a Dielectric Particle in a Plasma

R. L. Heinisch, F. X. Bronold, and H. Fehske

Institut für Physik, Ernst-Moritz-Arndt-Universität Greifswald, 17487 Greifswald, Germany

(Dated: August 7, 2013)

With an eye on dust particles immersed into an ionized gas, we study the effect of a negative charge on the scattering of light by a dielectric particle with a strong transverse optical phonon resonance in the dielectric constant. Surplus electrons alter the scattering behavior of the particle by their phonon limited conductivity in the surface layer (negative electron affinity) or in the bulk of the particle (positive electron affinity). We identify a charge-dependent increase of the extinction efficiency for low frequencies, a shift of the extinction resonance above the transverse optical phonon frequency, and a rapid variation of the polarization angles over this resonance. These effects could be used for non-invasive optical measurements of the charge of the particle.

PACS numbers: 42.25.Bs, 42.25.Fx, 52.27.Lw

I. INTRODUCTION

Charged dust particles embedded in a plasma environment are an ubiquitous phenomenon in nature.^{1,2} They are found in the interstellar medium,^{3,4} planetary magnetospheres,⁵ the upper atmosphere,⁶ and in industrial plasmas.⁷ Dusty laboratory plasmas,⁸ containing self-organized dust clouds, serve moreover as model systems for studying the dynamic behavior of strongly Coulomb-correlated systems of finite extent.

From the plasma physics point of view, the most important property of a dust particle is the charge it accumulates from the plasma. It controls the coupling to other dust particles and to external electromagnetic fields as well as the overall charge balance of the plasma. As a consequence various methods have been devised to measure the particle charge. They range from force balance methods for particles drifting in the plasma⁹ or trapped in the plasma sheath^{10,11} to methods based on wave dispersion,¹² normal mode analysis,¹³ and dust cluster rotation.¹⁴ Yet, the precise determination of the particle charge in a plasma environment remains a challenge. Methods independent of the plasma parameters,^{12–14} which are usually not precisely known, require specific experimental configurations, long measurement times or cannot yield the charge of individual dust particles. The phase-resolved resonance method,¹¹ for instance, allows only a precise relative charge measurement. For an absolute charge measurement the potential profile in the vicinity of the particle has to be additionally obtained by Langmuir probe measurements which however are only about 20% accurate. Thus an optical measurement of the particle charge, independent of the plasma parameters, would be extremely useful.

The scattering of light by a small particle (Mie scattering¹⁵) encodes—at least in principle—the particle charge.^{16–21} It enters the scattering coefficients through the electrical conductivity of the surplus electrons which modifies either the boundary conditions for the electromagnetic fields or the polarizability of the particle. To assess how and at which frequencies charges are revealed by the Mie signal requires however not only a microscopic

calculation of the surface and bulk conductivities but also a detailed analysis of the conductivities' impact on the different scattering regimes the particle's dielectric constant gives rise to.

So far, the dependence of the Mie signal on the particle charge has not been investigated systematically. In our previous work²¹ we made a first step to clarify this issue which has also been raised by Rosenberg.²² We identified the extinction at anomalous optical resonances of dielectric particles with a strong transverse optical (TO) phonon resonance in the dielectric constant to be sensitive to surplus electrons. In the present work we give a more comprehensive survey of Mie scattering by small negatively charged dielectric particles. Our aim is to identify over the whole frequency range, not only in the vicinity of anomalous resonances, features in the Mie signal which respond to surplus electrons. From these features the surplus electron density of the particle could be determined optically via light scattering.

After a brief outline of the Mie theory of light scattering by small charged particles in the next section, we present in Section III results for the four generic scattering features which occur for a charged dielectric particle with a strong resonance in the dielectric constant at the TO phonon frequency ω_{TO} : low-frequency scattering, ordinary resonances below ω_{TO} , anomalous resonances above ω_{TO} , and high-frequency scattering. We investigate the intensity of the Mie signal and its polarization. Thereby we include ellipsometric techniques into our considerations. Section IV finally summarizes the results and points out possibilities for an optical measurement of the particle charge.

II. THEORY

The scattering behavior of an uncharged dielectric particle is determined by its radius a and frequency-dependent dielectric constant $\epsilon(\omega)$. For a negatively charged dielectric particle light scattering is also influenced by the electric conductivity of the surplus electrons. Whether surplus electrons are trapped inside the

particle or in a surface layer around it depends on the electron affinity χ of the particle.²¹

For $\chi < 0$, as it is the case for instance for MgO and LiF,²³ the conduction band inside the dielectric is above the potential outside the particle. Electrons do not penetrate into the dielectric. Instead they are trapped in the image potential in front of the surface.^{24,25} The image potential is due to a surface mode associated with the TO phonon. The interaction of an electron with the surface mode comprises a static part, which induces the image potential,^{26,27} and a dynamic part, which enables momentum relaxation parallel to the surface limiting the surface conductivity.²⁸ The phonon-limited surface conductivity σ_s , calculated in our previous work²¹ using the memory function approach,²⁹ modifies the boundary condition for the magnetic field at the surface of the grain.¹⁶

For $\chi > 0$, as it is the case for instance for Al₂O₃, Cu₂O and PbS, the conduction band inside the dielectric lies below the potential outside the particle. Electrons thus accumulate in the conduction band where they form an extended space charge.²⁴ Its width, limited by the screening in the dielectric, is typically larger than a micron. For micron-sized particles we can thus assume a homogeneous electron distribution in the bulk. The bulk conductivity is limited by scattering with a longitudinal optical (LO) phonon³⁰ and can be also calculated²¹ within the memory function approach. The bulk conductivity of the surplus electrons σ_b leads to an additional polarizability per volume $\alpha = 4\pi i\sigma_b/\omega$ which alters the refractive index.

The scattering behavior of the particle is controlled by the scattering coefficients. They are determined by expanding the incident (*i*) plane wave into spherical vector harmonics and matching the reflected (*r*) and transmitted (*t*) waves at the boundary of the sphere.^{17,31} In the case of $\chi > 0$ the boundary conditions at the surface are given by $\hat{\mathbf{e}}_r \times (\mathbf{C}_i + \mathbf{C}_r - \mathbf{C}_t) = 0$ for $\mathbf{C} = \mathbf{E}, \mathbf{H}$. For $\chi < 0$ the surface charges may sustain a surface current $\mathbf{K} = \sigma_s \mathbf{E}_\parallel$ which is induced by the parallel component of the electric field and proportional to the surface conductivity. This changes the boundary condition for the

magnetic field to $\hat{\mathbf{e}}_r \times (\mathbf{H}_i + \mathbf{H}_r - \mathbf{H}_t) = 4\pi\mathbf{K}/c$, where c is the velocity of light. The boundary condition for the electric field is still $\hat{\mathbf{e}}_r \times (\mathbf{E}_i + \mathbf{E}_r - \mathbf{E}_t) = 0$. The refractive index of the particle $N = \sqrt{\epsilon}$ ($\chi < 0$) or $N = \sqrt{\epsilon + \alpha}$ ($\chi > 0$). Matching the fields at the particle surface gives the scattering coefficients¹⁶

$$a_n^r = -\frac{F_n^a}{F_n^a + iG_n^a}, \quad b_n^r = -\frac{F_n^b}{F_n^b + iG_n^b}, \quad (1)$$

where

$$F_n^a = \psi_n(N\rho)\psi_n'(\rho) - [N\psi_n'(N\rho) - i\tau\psi_n(N\rho)]\psi_n(\rho), \quad (2)$$

$$G_n^a = \psi_n(N\rho)\chi_n'(\rho) - [N\psi_n'(N\rho) - i\tau\psi_n(N\rho)]\chi_n(\rho), \quad (3)$$

$$F_n^b = \psi_n'(N\rho)\psi_n(\rho) - [N\psi_n(N\rho) + i\tau\psi_n'(N\rho)]\psi_n'(\rho), \quad (4)$$

$$G_n^b = \psi_n'(N\rho)\chi_n(\rho) - [N\psi_n(N\rho) + i\tau\psi_n'(N\rho)]\chi_n'(\rho) \quad (5)$$

with the dimensionless surface conductivity $\tau(\omega) = 4\pi\sigma_s(\omega)/c$ ($\chi < 0$) or $\tau = 0$ ($\chi > 0$). The size parameter $\rho = ka = 2\pi a/\lambda$ where λ is the wavelength and $\psi_n(\rho) = \sqrt{\pi\rho/2}J_{n+1/2}(\rho)$, $\chi_n(\rho) = \sqrt{\pi\rho/2}Y_{n+1/2}(\rho)$ with J_n the Bessel and Y_n the Neumann function. The efficiencies for extinction (*t*) and scattering (*s*) are

$$Q_t = -\frac{2}{\rho^2} \sum_{n=1}^{\infty} (2n+1) \text{Re}(a_n^r + b_n^r) \quad (6)$$

$$Q_s = \frac{2}{\rho^2} \sum_{n=1}^{\infty} (2n+1) (|a_n^r|^2 + |b_n^r|^2) \quad (7)$$

from which the absorption efficiency $Q_a = Q_t - Q_s$ can be also obtained.

An important special case is the scattering by small particles, for which $\rho \ll 1$. Inspired by the expressions used in Ref. 32 we write in this case $F_n^a = N^{n+1}f_n^a/(2n+1)$ and $G_n^a = N^{n+1}g_n^a/(2n+1)$ with

$$f_n^a = \frac{2^{2n}(n+1)n!}{(2n+1)!(2n)!} \rho^{2n+1} \left(\frac{i\tau}{n+1} \rho + \frac{N^2-1}{(n+1)(2n+3)} \rho^2 + \mathcal{O}(\rho^3) \right), \quad (8)$$

$$g_n^a = 2n+1 - i\tau\rho + \frac{1-N^2}{2} \rho^2 + \mathcal{O}(\rho^3), \quad (9)$$

and similarly $F_n^b = N^n f_n^b/(2n+1)$ and $G_n^b = N^n g_n^b/(2n+1)$ with

$$f_n^b = \frac{2^{2n}n!(n+1)!}{(2n)!(2n+1)!} \rho^{2n+1} \left(1 - N^2 - i(n+1)\frac{\tau}{\rho} + \mathcal{O}(\rho) \right), \quad (10)$$

$$g_n^b = -(n+1) - nN^2 - in(n+1)\frac{\tau}{\rho} + \left[\frac{(n+3)N^2 + nN^4}{2(2n+3)} - \frac{(n+1) + (n-2)N^2}{2(2n-1)} \right] \rho^2 + \left[-i\frac{(n+1)(n-2)}{2(2n-1)} + i\frac{n(n+3)}{2(2n+3)} \right] N^2 \tau\rho + \mathcal{O}(\rho^3). \quad (11)$$

The leading scattering coefficients for small uncharged particles are $b_1 \sim \mathcal{O}(\rho^3)$ and $a_1, b_2 \sim \mathcal{O}(\rho^5)$. For them

$$f_1^a = i\frac{\tau}{3}\rho^4 + \frac{N^2 - 1}{15}\rho^5, \quad g_1^a = 3 - i\tau\rho + \frac{1 - N^2}{2}\rho^2, \quad (12)$$

$$f_1^b = -i\frac{4\tau}{3}\rho^2 + \frac{2(1 - N^2)}{3}\rho^3, \quad g_1^b = -2 - N^2 - i2\frac{\tau}{\rho}, \quad (13)$$

$$f_2^b = -i\frac{\tau}{5}\rho^4 + \frac{1 - N^2}{15}\rho^5, \quad g_2^b = -3 - 2N^2 - i6\frac{\tau}{\rho}. \quad (14)$$

Keeping only the coefficient b_1 the extinction efficiency $Q_t = -6 \text{Re}(b_1^r)/\rho^2$. Approximating $b_1^r = f/ig$ (we have neglected $f \sim \rho^3$ compared to $g \sim \rho^0$ in the denominator) we obtain for the extinction efficiency

$$Q_t = \frac{12\rho(\epsilon'' + \alpha'' + 2\tau'/\rho)}{(\epsilon' + \alpha' + 2 - 2\tau''/\rho)^2 + (\epsilon'' + \alpha'' + 2\tau'/\rho)^2} \quad (15)$$

which is valid for small particles, that is, for $\rho \ll 1$.

III. RESULTS

In the following we will discuss light scattering for a MgO ($\chi < 0$) and an Al₂O₃ ($\chi > 0$) particle (for material parameters see Ref. 33). The particle charge affects light scattering through the dimensionless surface conductivity $\tau = \tau' + i\tau''$ (MgO) or the surplus electron polarizability $\alpha = \alpha' + i\alpha''$ (Al₂O₃). Both τ and α are shown as a function of the inverse wavelength λ^{-1} in the first row of Fig. 1. They are small even for a highly charged particle with $n_s = 10^{13} \text{ cm}^{-2}$ which corresponds to $n_b = 3 \times 10^{17} \text{ cm}^{-3}$ for $a = 1 \mu\text{m}$. For $T = 300 \text{ K}$ $\tau'' > \tau'$ and $-\alpha' > \alpha''$ except at very low frequencies. For $\lambda^{-1} \rightarrow 0$ the conductivities σ_s and σ_b tend to a real value so that $\tau' > \tau''$ and $\alpha'' > -\alpha'$ for very small λ^{-1} . Both τ and α decrease with increasing λ^{-1} and vary smoothly over the considered frequencies. Shown for comparison are also τ and α for $T = 0$ where $\tau' = 0$ for $\lambda^{-1} < \lambda_s^{-1} = 909 \text{ cm}^{-1}$, the inverse surface phonon wavelength ($\alpha'' = 0$ for $\lambda^{-1} < \lambda_{LO}^{-1} = 807 \text{ cm}^{-1}$, the inverse LO phonon wavelength), since light absorption is possible only above λ_s^{-1} (or λ_{LO}^{-1}).

The scattering behavior of the uncharged particles is primarily determined by the dielectric constants $\epsilon(\omega)$ (second row of Fig. 1). For MgO it is dominated by a TO phonon at $\lambda^{-1} = 401 \text{ cm}^{-1}$. For Al₂O₃ two TO phonon modes at $\lambda^{-1} = 434 \text{ cm}^{-1}$ and $\lambda^{-1} = 573 \text{ cm}^{-1}$ dominate $\epsilon(\omega)$. At frequencies well below the TO phonon resonance the dielectric constant tends towards its real static value ϵ_0 . In this regime (marker A in Fig. 1) $\epsilon'' \ll \epsilon'$. For constant radius a , the extinction efficiency $Q_t \rightarrow 0$ for $\lambda^{-1} \rightarrow 0$. Just below the TO phonon resonance (for

Al₂O₃ below the lower TO-phonon) ϵ' is large and positive and $\epsilon'' \ll \epsilon'$ (except in the immediate vicinity of the resonance). This gives rise to ordinary optical resonances (marker B in Fig. 1).³⁴ Above the TO phonon resonance (for Al₂O₃ above the higher TO-phonon) $\epsilon' < 0$ and $\epsilon'' \ll 1$. This entails anomalous optical resonances (marker C in Fig.1).³⁵⁻³⁷ Far above the TO phonon resonance ϵ' takes a small positive value and $\epsilon'' \ll 1$. This gives rise to an interference and ripple structure (marker D in Fig. 1).¹⁷

In the context of plasma physics dielectric particles with a strong TO phonon resonance have already been studied theoretically as wave-length selective infra-red absorbers.²² In the following we explore the modification of the features A–D by surplus electrons. We are particularly interested in identifying dependencies in the optical signal which can be used as a charge diagnostic.

A. Low-Frequency Scattering

In the low frequency limit of scattering (marker A in Fig. 1) the extinction efficiency Q_t is relatively small. For $\lambda^{-1} < 200 \text{ cm}^{-1}$ particles with a radius of a few microns are small compared to the wavelength. In this limit the dominant scattering coefficient is b_1^r and the extinction efficiency is given approximately by Eq. (15). Extinction is due to absorption which is controlled by ϵ'' . As ϵ'' is small in this frequency range energy dissipation on the grain and thus extinction is inhibited. For $\lambda^{-1} \rightarrow 0$, $\epsilon'' \rightarrow 0$ and hence $Q_t \rightarrow 0$.

For charged dielectric particles light absorption is controlled not only by ϵ'' but also by τ' for $\chi < 0$ and by α'' for $\chi > 0$ which stem from the real part of the surface or bulk conductivity of the surplus electrons, respectively. For low frequency τ' and α'' are larger than for higher frequencies and for $\lambda^{-1} \rightarrow 0$ even outweigh τ'' and $-\alpha'$ as the real parts of the surface and bulk conductivities tend to finite values whereas the imaginary parts vanish for $\lambda^{-1} = 0$. This allows increased energy dissipation on charged dust particles entailing increased light absorption. Figure 2 shows this saturation of the extinction efficiency for charged particles.

For comparison, we also show the results for free surface (MgO) or bulk electrons (Al₂O₃). In this case the conductivities are purely imaginary and the saturation of the extinction efficiency is not observed. Instead we find a plasmon resonance of the electron gas around or inside the particle. The resonance is located where $\text{Re}(g_1^b) = 0$ (with g_1^b given by Eq. (13)). This discrepancy with results from the phonon-limited conductivities shows that in the low-frequency limit the model of free surplus electrons cannot offer even a qualitative explanation.

The saturation of the extinction efficiency for low frequencies could be employed as a charge measurement. Performing an extinction measurement at fixed wavelength would give an approximately linear increase of Q_t with the surface density or bulk density of surplus elec-

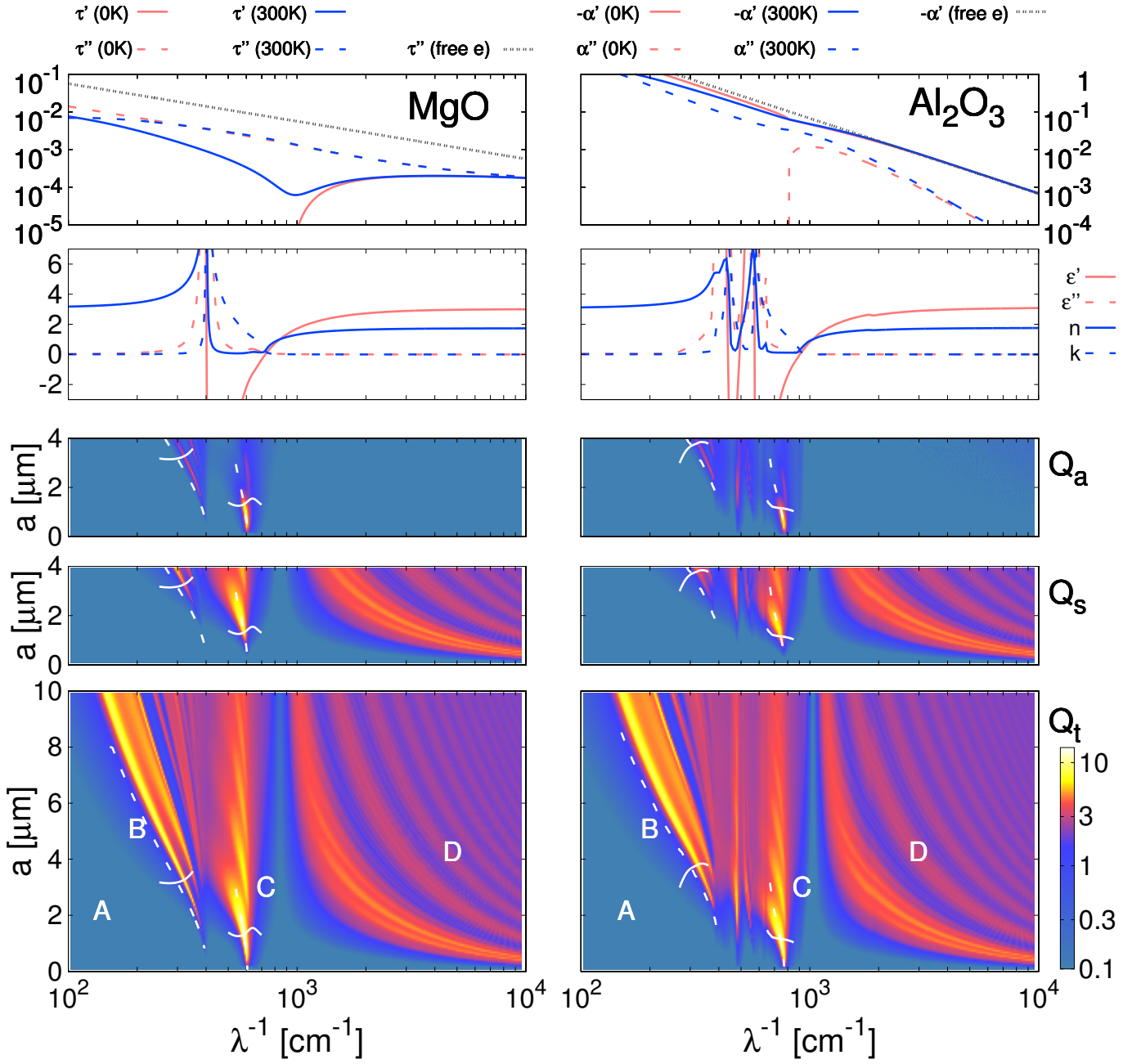


FIG. 1: (Color online) First row: Dimensionless surface conductivity $\tau = \tau' + i\tau''$ for MgO for $n_s = 10^{13}\text{cm}^{-2}$ (left) and polarizability of excess electrons $\alpha = \alpha' + i\alpha''$ for Al₂O₃ for $n_b = 3 \times 10^{17}\text{cm}^{-3}$ (right) as a function of the inverse wavelength λ^{-1} . Second row: Dielectric constant $\epsilon = \epsilon' + i\epsilon''$ and refractive index $N = n + ik$ as a function of λ^{-1} . Third to fifth row: Absorption efficiency Q_a (third row), scattering efficiency Q_s (fourth row), and extinction efficiency Q_t (fifth row) as a function of λ^{-1} and the particle radius a for an uncharged MgO and Al₂O₃ particle. The labels indicate the four characteristic scattering regimes: low frequencies (A), ordinary resonances (B), anomalous resonances (C), and interference and ripple structure (D). The dashed lines give the approximate position of the a_1^r (B) and b_1^r (C) resonance. The full lines give the approximate cross-over from absorption to scattering dominance of the resonances.

trons (see right panels of Fig. 2).

B. Ordinary Resonances

Below the TO phonon resonance at λ_{TO}^{-1} in the dielectric constant ϵ' is large while ϵ'' is still comparatively small (except at λ_{TO}^{-1}). The large positive ϵ' (which en-

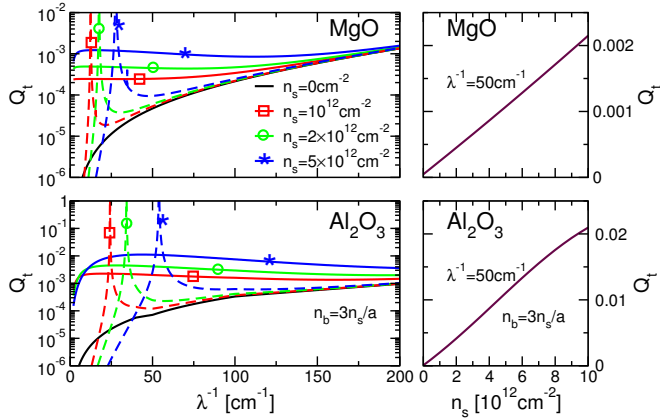


FIG. 2: (Color online) Left: Extinction efficiency Q_t as a function of the inverse wavelength λ^{-1} for a charged MgO particle (top) and a charged Al_2O_3 particle (bottom) with radius $a = 1\mu\text{m}$ at $T = 300\text{K}$. Full lines give the results for the phonon-limited surface or bulk conductivity, dashed lines show for comparison the results for free surface or bulk electrons. Right: Extinction efficiency as a function of the surface electron density for an MgO particle (or corresponding bulk electron density for Al_2O_3) for $\lambda^{-1} = 50\text{cm}^{-1}$.

tails a large positive real part of refractive index N) allows for ordinary optical resonances,³⁴ which are clearly seen in Fig. 1. The lowest resonance is due to the a_1 mode. The contribution of this mode to the extinction efficiency is $Q_{a_1}^t = -6\text{Re}(a_1^r)/\rho^2$. More generally, the extinction efficiency due to one mode only reads $Q_{a,b_n}^t = 2(2n+1)q_{a,b_n}^t/\rho^2$ where

$$q_{a,b_n}^t = \frac{f'(f' - g'')}{(f' - g'')^2 + g'^2} \quad (16)$$

with $f = f' + if''$ and $g = g' + ig''$ (given for $\rho \ll 1$ by Eqs. (8)-(11)). Note that we have neglected f'' as $\epsilon'' \ll 1$. The resonance is approximately located where $g' = 0$. This gives for $n = 1$ the condition

$$3 + \tau''\rho + (1 - \epsilon' - \alpha')\rho^2/2 = 0. \quad (17)$$

The approximate resonance location for an uncharged sphere, obtained from $3 + (1 - \epsilon')\rho^2/2 = 0$ is shown in Fig. 1 by the dashed line. It deviates somewhat from the true resonance location but captures its size dependence qualitatively. The contribution of one mode to absorption and scattering, respectively, is $Q_{a,b_n}^{a,s} = 2(2n+1)q_{a,b_n}^{a,s}/\rho^2$ with

$$q_{a,b_n}^a = \frac{-f'g''}{(f' - g'')^2 + g'^2}, \quad q_{a,b_n}^s = \frac{f'^2}{(f' - g'')^2 + g'^2}. \quad (18)$$

For $f' > -g''$ scattering outweighs absorption while absorption outweighs scattering for $-g'' > f'$. The boundary between the two regimes is given by $-g'' = f'$. For $n = 1$ this gives for an uncharged particle

$$\rho = \left(\frac{15}{2} \frac{\epsilon''}{\epsilon' - 1} \right)^{\frac{1}{3}}, \quad (19)$$

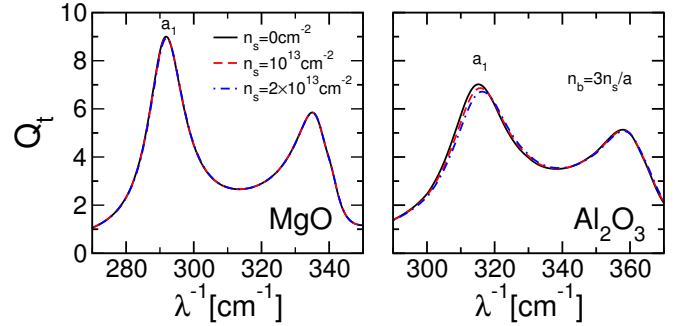


FIG. 3: (Color online) Extinction efficiency Q_t as a function of the inverse wavelength for MgO (left) and Al_2O_3 (right) particles with radius $a = 4\mu\text{m}$ for $n_s = 0, 10^{13}$, and $2 \times 10^{13}\text{cm}^{-2}$ (or corresponding bulk electron density $n_b = 3n_s/a$) at $T = 300\text{K}$.

which is shown in Fig. 1 by the solid line and agrees with the underlying contour.

Fig. 3 shows that the a_1 resonance is not shifted significantly by surplus charges. As the charge enters $\sim \tau\rho$ or $\sim \alpha\rho^2$ the shift cannot be increased by reducing the particle size. Ordinary resonances thus offer no possibility to measure the particle charge.

C. Ripple and Interference Structure

Far above the highest TO phonon frequency (that is, for MgO and Al_2O_3 for $\lambda^{-1} > 1000\text{cm}^{-1}$) the extinction efficiency shows the typical interference and ripple structure of Mie scattering (marker D in Fig. 1).¹⁷ It consists of a broad interference pattern superseded by fine ripples which are due to individual modes. They become sharper for larger frequencies. Figure 4 shows the overall interference and ripple structure (top) and exemplifies the charge sensitivity of the ripple due to the mode b_{10} (bottom). It is shifted only very slightly with increasing particle charge. This is due to the small values of the surface conductivity or the polarizability of the surplus electrons for $\lambda^{-1} > 1000\text{cm}^{-1}$. Thus the ripple structure is not a suitable candidate for a charge measurement either.

D. Anomalous Resonances

At the TO phonon resonance the real part of the dielectric constant changes sign. For $\lambda^{-1} > \lambda_{TO}^{-1}$ $\epsilon' < 0$ and $\epsilon'' \ll 1$. This gives rise to a series of anomalous optical resonances, which can be seen in Fig. 1 (marker C). They correspond to the resonant excitation of transverse surface modes of the sphere.³⁵ For a metal particle they are tied to the plasmon resonance^{36,37} whereas for a dielectric particle they are due to the TO-phonon. The resonances are associated with the scattering coefficients b_n . The lowest resonance is due to the mode b_1 . The resonance

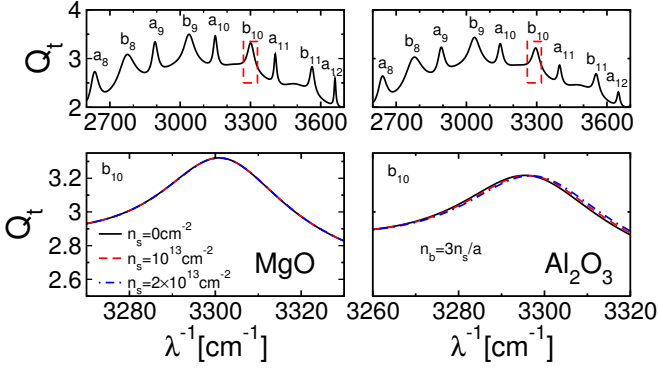


FIG. 4: (Color online) Top panel: Overview of the ripple and interference structure. Bottom panel: Extinction efficiency Q_t close to the b_{10} ripple as a function of the inverse wavelength for MgO (left) and Al_2O_3 (right) particles with radius $a = 4\mu\text{m}$ for $n_s = 0, 10^{13}$ and $2 \times 10^{13} \text{ cm}^{-2}$ (or corresponding bulk electron density $n_b = 3n_s/a$) at $T = 300 \text{ K}$.

location is approximately given by $\text{Re}(g_1^b) = 0$, which according to Eq. (11) gives for an uncharged sphere

$$-2 - \epsilon' + \left(-1 - \frac{\epsilon'}{10} + \frac{\epsilon'^2 - \epsilon''^2}{10} \right) \rho^2 = 0. \quad (20)$$

This approximation, shown by the dashed line near marker C in Fig. 1, agrees well with the underlying Mie contour.

The higher resonances are scattering dominated, while the lowest resonance shows a cross-over from absorption to scattering dominance (see Fig. 1). This cross-over can be understood from the contribution of the b_1 mode to the scattering and absorption efficiencies (given by Eq. (18)). Absorption dominates for $-g'' > f'$, while scattering dominates for $-g'' < f'$. The boundary between the two regimes lies where $-g'' = f'$. For $n = 1$ this gives

$$\rho = \left(\frac{3}{2} \frac{\epsilon''}{1 - \epsilon'} \right)^{\frac{1}{3}} \quad (21)$$

which agrees well with the Mie contour (see Fig 1).

The anomalous resonances are sensitive to small changes in ϵ and τ or α . Surplus electrons lead to a blue-shift of the resonances.²¹ This effect is strongest for small particles with radius $a < 1\mu\text{m}$. In the small particle limit the extinction efficiency is approximately given by Eq. (15). The resonance is located at

$$\epsilon' + \alpha' + 2 - 2\tau''/\rho = 0. \quad (22)$$

Compared to the resonance condition for ordinary resonances, Eq. (17), the charge sensitivity increases for small particles as surplus charges enter by $-2\tau''/\rho \sim n_s/a$ (for $\chi < 0$) or $\alpha' \sim n_b$ (for $\chi > 0$). This shows that the resonance shift by the surplus electrons is primarily an electron density effect on the polarizability of the dust particle.²¹

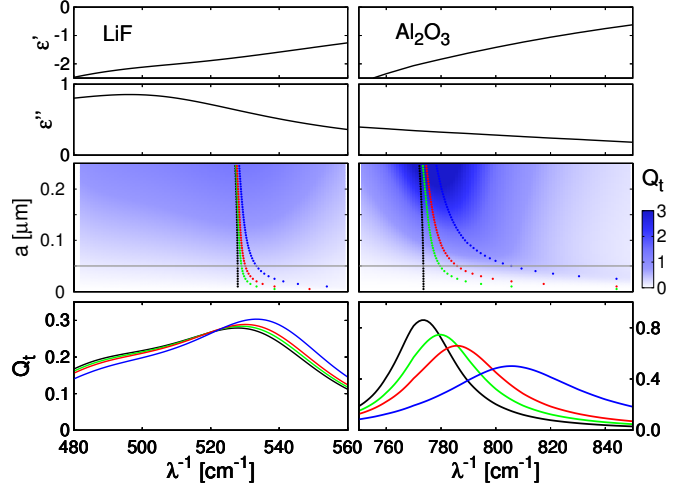


FIG. 5: (Color online) Top panels: Real part ϵ' and imaginary part ϵ'' of the dielectric constant as a function of the inverse wavelength λ^{-1} . The maximum of ϵ'' for LiF stems from a TO phonon mode at 503 cm^{-1} . Middle panel: Extinction efficiency Q_t as a function of λ^{-1} and the radius a for a LiF particle with $n_s = 5 \times 10^{12} \text{ cm}^{-2}$ (left) and an Al_2O_3 particle with $n_b = 3n_s/a$ (right) for $T = 300 \text{ K}$. The dotted lines indicate the extinction maximum for (from left to right) $n_s = 0$ (black), 10^{12} (green), 2×10^{12} (red), and $5 \times 10^{12} \text{ cm}^{-2}$ (blue). Bottom panel: Extinction efficiency Q_t as a function of λ^{-1} for different surface electron densities (corresponding to the middle panel) and fixed radius $a = 0.05\mu\text{m}$. The extinction maximum is shifted to higher frequencies with increasing electron density.

Figure 5 shows the resonance shift for charged sub-micron-sized LiF^{33} and Al_2O_3 particles. For Al_2O_3 the resonance shift is relatively large and the extinction resonance has a Lorentzian shape. As ϵ' is well approximated linearly close to -2 and ϵ'' varies only slightly this follows from Eq. (15). For LiF the shift is smaller and the lineshape is not Lorentzian. The reason is the minor TO phonon at $\lambda^{-1} = 503 \text{ cm}^{-1}$. This leads to a bump in ϵ'' disturbing the Lorentzian shape.

A comparison of the resonance shift for MgO and LiF ($\chi < 0$) as well as Al_2O_3 , PbS and Cu_2O^{33} ($\chi > 0$) is given by Fig. 6. The shift tends to be larger for bulk ($\chi > 0$) than for surface ($\chi < 0$) surplus electrons. Cu_2O is an example for a dielectric where ϵ'' is too large for a well-resolved series of extinction resonances to form. Nevertheless a tail of the lowest resonance for small particles is discernible which is blue-shifted by surplus electrons, albeit by a lesser extent than for Al_2O_3 or PbS. PbS has a particularly strong resonance shift. Compared to the other materials the TO phonon resonance of PbS is located at a significantly lower frequency where α is particularly large. Together with the small conduction band effective mass which benefits the electrons' mobility this leads to the larger charge-induced blue-shift.

The blue-shift of the extinction resonance could be used as a charge measurement for particles with $a < 1\mu\text{m}$. The resonance shift is found for particles with $\chi < 0$, e.g.

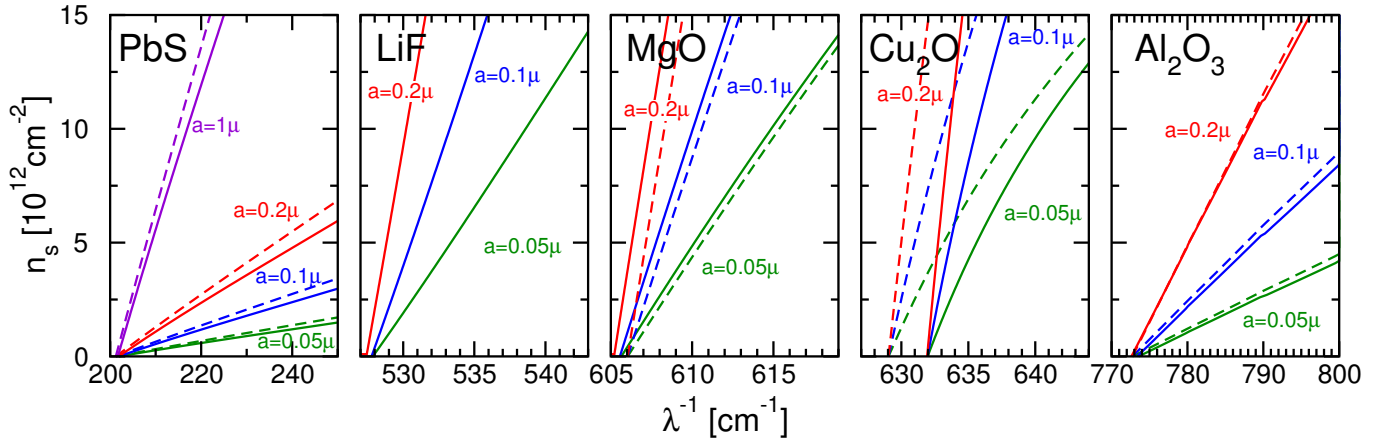


FIG. 6: (Color online) Position of the extinction resonance depending on the surface charge n_s (or the equivalent bulk charge $n_b = 3n_s/a$) for PbS, LiF, MgO, Cu₂O, and Al₂O₃ particles with different radii a . Solid (dashed) lines are obtained from the Mie contour [Eq. (22)].

MgO or LiF, and $\chi > 0$, e.g. PbS, Cu₂O or Al₂O₃. The most promising candidates are particles made from Al₂O₃ or PbS. The latter may even allow a measurement for micron-sized particles.

E. Polarization Angles

So far we have considered charge effects in the extinction efficiency. In the following we will turn to the charge signatures in the polarization of the scattered light. While the extinction (or scattering) efficiency gives only access to the magnitude of the scattering coefficients the polarization of scattered light also reveals the phase of the scattering coefficients. The phase information is particularly useful close to the ordinary and anomalous optical resonances. They occur for $\text{Re}(g_n^{a,b}) = 0$ where the sign change of $g_n^{a,b}$ leads to a rapid phase change around the resonances. For $\epsilon'' = 0$ the functions $f_n^{a,b}$ and $g_n^{a,b}$ are real in the small particle limit (cf. Eqs. (12)–(14)). In this limit $f_n^a \sim \rho^{2n+3}$ and $f_n^b \sim \rho^{2n+1}$ while $g_n^{a,b} \sim \rho^0$ (for uncharged particles), which entails $g_n^{a,b} > f_n^{a,b}$ except very close to the resonance. As a consequence the phase of the scattering coefficients varies over the resonances by about π .

For linearly polarized incident light ($\mathbf{E}_i \sim \hat{\mathbf{e}}_x$) the electric field of the reflected light,

$$\begin{aligned} \mathbf{E}_r \sim E_0 \frac{e^{-i\omega t + ikr}}{ikr} \sum_{n=1}^{\infty} \frac{2n+1}{n(n+1)} \\ \times \left[\left(a_n^r \frac{P_n^1(\cos\theta)}{\sin\theta} + b_n^r \frac{dP_n^1(\cos\theta)}{d\theta} \right) \cos\phi \hat{\mathbf{e}}_\theta \right. \\ \left. - \left(a_n^r \frac{dP_n^1(\cos\theta)}{d\theta} + b_n^r \frac{P_n^1(\cos\theta)}{\sin\theta} \right) \sin\phi \hat{\mathbf{e}}_\phi \right], \quad (23) \end{aligned}$$

is in general elliptically polarized ($P_n^1(\mu) = \sqrt{1-\mu^2} dP_n(\mu)/d\mu$ with $P_n(\mu)$ a Legendre polyno-

mial). Rewriting the reflected electric field as

$$\mathbf{E}_r \sim E_0 \frac{e^{-i\omega t + ikr}}{ikr} (A_2 e^{i\phi_2} \hat{\mathbf{e}}_\theta + A_3 e^{i\phi_3} \hat{\mathbf{e}}_\phi), \quad (24)$$

where the amplitudes A_2 , A_3 and the phases ϕ_2 , ϕ_3 are given implicitly by the above equation, the ellipsometric angles are defined by

$$\Delta\phi = \phi_2 - \phi_3 \quad \text{and} \quad \tan\psi = \frac{A_2}{A_3}. \quad (25)$$

The angle ψ gives the amplitude ratio and the phase difference $\Delta\phi$ characterizes the opening of the polarization ellipse. For $\Delta\phi = 0, \pm\pi$ the reflected light is linearly polarized while for $\Delta\phi = \pm\pi/2$ the opening of the polarization ellipse is maximal.

Note that forward scattered light ($\theta = 0$),

$$\mathbf{E}_r \sim E_0 \frac{e^{-i\omega t + ikr}}{ikr} \sum_{n=1}^{\infty} \frac{2n+1}{2} (a_n^r + b_n^r) \hat{\mathbf{e}}_x, \quad (26)$$

is linearly polarized. The same applies to backscattered light ($\theta = \pi$) or light that is scattered perpendicularly to the incident wave and in plane or perpendicularly to the direction of polarization of the incident light ($\theta = \pi/2$ and $\phi = 0$ or $\phi = \pi/2$).

An important scattering angle where the scattered light is elliptically polarized is perpendicular to the incident wave and at 45° to the plane of polarization of the incident wave ($\theta = \pi/2$ and $\phi = \pi/4$). This configuration is also used to determine from the Mie signal the particle size of nanodust.³⁸ Figure 7 shows the polarization angles $\Delta\phi$ and ψ for this scattering direction for MgO and Al₂O₃ particles with radius $a = 0.5\mu\text{m}$. Panels (i) (MgO) and (iv) (Al₂O₃) give an overview for an uncharged particle.

In the small particle limit only the scattering coefficients a_1^r , b_1^r , and b_2^r are relevant. The reflected electric

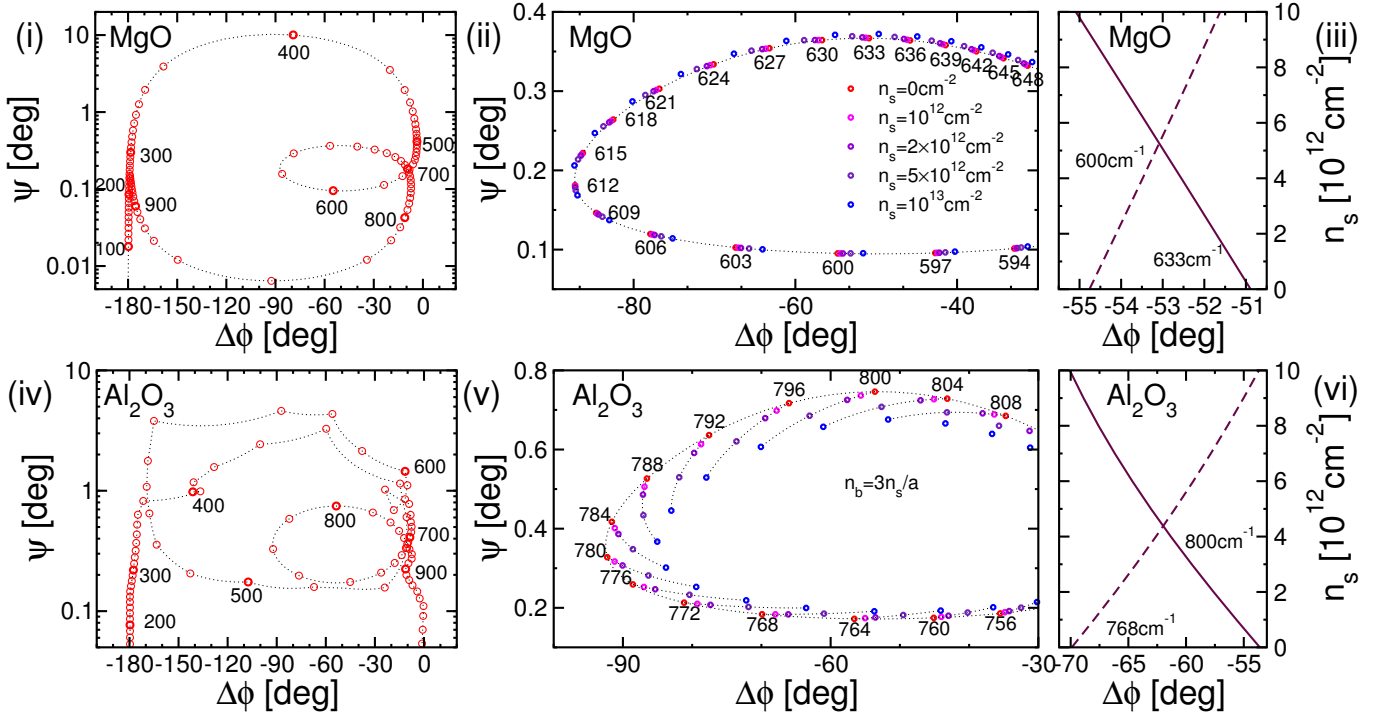


FIG. 7: (Color online) Ellipsometric angles Ψ and $\Delta\phi$ for scattering by an MgO and Al_2O_3 particle with radius $a = 0.5\mu\text{m}$ in the direction $\theta = \pi/2$ and $\phi = \pi/4$. (i) (MgO) and (iv) (Al_2O_3) show Ψ and $\Delta\phi$ for $0\text{ cm}^{-1} < \lambda^{-1} < 1000\text{ cm}^{-1}$ for an uncharged particle. (ii) (MgO) and (v) (Al_2O_3) magnify the vicinity of the extinction resonance. Ψ and $\Delta\phi$ are shifted with increasing surface electron density n_s (or corresponding bulk electron density $n_b = 3n_s/a$). The annotated value at the base point gives the wave-number. From there the electron density increases counter-clockwise along the branches. The shift in $\Delta\phi$ as a function of n_s or correspondingly n_b is shown for two representative λ^{-1} in (iii) (MgO) and (vi) (Al_2O_3).

field is given by

$$\mathbf{E}_r \sim E_0 \frac{e^{ikr-i\omega t}}{ikr} \left[\left(\frac{3}{2\sqrt{2}}a_1^r - \frac{5}{2\sqrt{2}}b_2^r \right) \hat{\mathbf{e}}_\theta - \frac{3}{2\sqrt{2}}b_1^r \hat{\mathbf{e}}_\phi \right]. \quad (27)$$

Figure 7 (i) shows a strong variation of $\Delta\phi$ for MgO as a function of λ^{-1} which can be related to the variation of the phase of the scattering coefficients. For low frequencies $\lambda^{-1} < 300\text{ cm}^{-1}$ the reflected light is linearly polarized. Close to 400 cm^{-1} the rapid phase variation by π of the coefficient a_1^r increases $\Delta\phi$ by about π . Above λ_{TO}^{-1} resonances appear in the coefficients b_1^r and b_2^r for $\epsilon' = -2$ and $\epsilon' = -3/2$ (for $\rho \ll 1$), respectively. As these resonances are located very close to each other, the phase shifts by π partly cancel and $\Delta\phi$ acquires and loses a phase of about $-\pi/2$ at around $\lambda^{-1} = 600\text{ cm}^{-1}$. For Al_2O_3 the variation of $\Delta\phi$ is more complicated because two TO phonon modes dominate ϵ . Nevertheless the interplay of the b_1 and the b_2 mode above the higher TO phonon resonance leads to the rapid variation of $\Delta\phi$ from close to 0 to $-\pi/2$ and back to close to 0 near 800 cm^{-1} .

Surplus charges alter the polarization angles very little except near the rapid opening and closing of the polarization ellipse at the anomalous resonances. Here surplus charges lead to a blue shift of the resonances in b_1^r and b_2^r . The shift is approximately given by Eq. (22) for

the mode b_1 and by $2\epsilon' + 2\alpha' + 3 - 6\tau''/\rho = 0$ for the mode b_2 (in both cases $\rho \ll 1$). The resonance blue-shift translates into a shift of $\Delta\phi$. For a charged particle $\Delta\phi$ acquires and loses $-\pi/2$ as for an uncharged particle but this takes place at higher λ^{-1} than for an uncharged particle. This is shown in panels (ii) and (v) of Fig. 7. Panels (iii) and (vi) exemplify it for fixed λ^{-1} where $\Delta\phi$ increases or decreases with the particle charge. This shift of $\Delta\phi$ by several degrees should also offer a possibility for a charge measurement.

IV. CONCLUSIONS

We studied the scattering behavior of a charged dielectric particle with an eye on identifying a strategy for an optical charge measurement. Our focus lay on the four characteristic regimes of scattering for particles with a strong TO phonon resonance: (i) low-frequency scattering, (ii) ordinary resonances, (iii) anomalous resonances, and (iv) interference and ripple structure. Surplus charges enter into the scattering coefficients through their phonon-limited surface (for negative electron affinity) or bulk (positive electron affinity) conductivities.

No significant charge effects are found for the ordinary resonances and the interference and ripple struc-

ture. Surplus charges affect however the low-frequency regime and the anomalous optical resonances.

We have identified three charge-dependent features of light scattering: (i) a charge-induced increase in extinction for low-frequencies, (ii) a blue-shift of the anomalous extinction resonance, and (iii) a rapid variation of one of the two polarization angles at the anomalous extinction resonance. At low frequencies energy relaxation is inhibited for uncharged particles as the imaginary part of the dielectric constant is very small. Surplus charges enable energy relaxation on the grain through their electrical conductivity which has a significant real part at low frequencies. This leads to increased absorption at low frequencies. Above the TO phonon frequency the real part of the dielectric constant is negative which leads to anomalous optical resonances. Surplus charges enter into the resonance condition through the imaginary part of their electrical conductivity. They lead to a resonance blue-shift which is most significant for sub-micron-sized particles. Moreover, at the anomalous resonances the phase of the resonant scattering coefficients varies rapidly. This causes the opening and closing—characterized by the angle $\Delta\phi$ —of the polarization ellipse of the reflected light. Surplus charges lead to the rapid variation in $\Delta\phi$ being shifted to higher frequency.

We suggest to use these charge signatures in the Mie signal to measure the particle charge. For plasmonic particles charge-induced resonance shifts have already been detected experimentally for metallic nanorods which were charged by an electrolytic solution^{39,40} and for an array

of nanodiscs exposed to an argon plasma.⁴¹

In order to detect the charge-sensitive effects of light scattering by dust particles in a dusty plasma would require to shine infra-red light through the plasma and to measure light attenuation or the polarization of reflected light. The low-frequency increase in extinction or the shift in the polarization angle $\Delta\phi$ could be observed with monochromatic light while the resonance shift would require a frequency dependent extinction measurement. This would not only allow a determination of the particle charge without knowing any plasma parameters but also of nanodust particles^{38,42,43} where traditional techniques cannot be applied at all.

Eventually suitable particles with a strong charge sensitivity (e.g. Al_2O_3 or PbS particles) could even be employed as minimally invasive electric plasma probes. The particles would accumulate a charge depending on the local plasma environment. Performing simultaneously an optical charge measurement and a traditional force measurement^{9–11} would then allow to infer the local electron density and temperature at the position of the probe particle.

Acknowledgement

This work was supported by the Deutsche Forschungsgemeinschaft through SFB-TR 24.

-
- ¹ D. A. Mendis, *Plasma Sources Sci. Technol.* **11**, A219 (2002).
- ² O. Ishihara, *J. Phys. D: Appl. Phys* **40**, R121 (2007).
- ³ L. Spitzer, *Processes in the Interstellar Medium* (Wiley, 1982).
- ⁴ I. Mann, *Adv. Space Res.* **41**, 160 (2008).
- ⁵ E. Grün, G. Morfill, and D. A. Mendis, in *Planetary Rings*, edited by R. Greenberg and A. Brahic (University of Arizona Press, Tuscon, 1984), p. 275.
- ⁶ M. Friedrich and M. Rapp, *Surv. Geophys.* **30**, 525 (2009).
- ⁷ C. Hollenstein, *Plasma Phys. Control. Fusion* **42**, R93 (2000).
- ⁸ A. Piel and A. Melzer, *Plasma Phys. Control. Fusion* **44**, R1 (2002).
- ⁹ S. A. Khrapak, S. V. Ratynskaia, A. V. Zobnin, A. D. Usachev, V. V. Yaroshenko, M. H. Thoma, M. Kretschmer, H. Hoefner, G. E. Morfill, O. F. Petrov, et al., *Phys. Rev. E* **72**, 016406 (2005).
- ¹⁰ E. B. Tomme, D. A. Law, B. M. Annaratone, and J. E. Allen, *Phys. Rev. Lett.* **85**, 2518 (2000).
- ¹¹ J. Carstensen, H. Jung, F. Greiner, and A. Piel, *Phys. Plasmas* **18**, 033701 (2011).
- ¹² A. Homann, A. Melzer, S. Peters, and A. Piel, *Phys. Rev. E* **56**, 7138 (1997).
- ¹³ A. Melzer, *Phys. Rev. E* **67**, 016411 (2003).
- ¹⁴ J. Carstensen, F. Greiner, and A. Piel, *Phys. Plasmas* **17**, 083703 (2010).
- ¹⁵ G. Mie, *Ann. Phys. (Berlin)* **330**, 377 (1908).
- ¹⁶ C. F. Bohren and A. J. Hunt, *Can. J. Phys.* **55**, 1930 (1977).
- ¹⁷ C. F. Bohren and D. R. Huffman, *Absorption and Scattering of Light by Small Particles* (Wiley, 1983).
- ¹⁸ J. Kláčka and M. Kocifaj, *J. Quant. Spectr. Rad. Transfer* **106**, 170 (2007).
- ¹⁹ J. Kláčka and M. Kocifaj, *Prog. Electromagn. Res.* **109**, 17 (2010).
- ²⁰ A. Heifetz, H. T. Chien, S. Liao, N. Gopalsami, and A. C. Raptis, *J. Quant. Spectr. Rad. Transfer* **111**, 2550 (2010).
- ²¹ R. L. Heinisch, F. X. Bronold, and H. Fehske, *Phys. Rev. Lett.* **109**, 243903 (2012).
- ²² M. Rosenberg, *IEEE Trans. Plasma Sci.* **40**, 1229 (2012).
- ²³ M. Rohlffing, N.-P. Wang, P. Kruger, and J. Pollmann, *Phys. Rev. Lett.* **91**, 256802 (2003).
- ²⁴ R. L. Heinisch, F. X. Bronold, and H. Fehske, *Phys. Rev. B* **85**, 075323 (2012).
- ²⁵ R. L. Heinisch, F. X. Bronold, and H. Fehske, *Phys. Rev. B* **83**, 195407 (2011).
- ²⁶ E. Evans and D. L. Mills, *Phys. Rev. B* **8**, 4004 (1973).
- ²⁷ G. Barton, *J. Phys. C* **14**, 3975 (1981).
- ²⁸ M. Kato and A. Ishii, *Appl. Surf. Sci.* **85**, 69 (1995).
- ²⁹ W. Götzke and P. Wölfle, *Phys. Rev. B* **6**, 1226 (1972).
- ³⁰ G. D. Mahan, *Many-Particle Physics* (Plenum, 1990), p. 703-708.
- ³¹ J. A. Stratton, *Electromagnetic Theory* (McGraw-Hill,

- 1941).
- ³² B. S. Lykyanchuk, M. I. Tribelsky, V. Ternovsky, Z. B. Wang, M. H. Hong, L. P. Shi, and T. C. Chong, *J. Opt. A* **9**, S294 (2007).
- ³³ We use for MgO $\epsilon_0 = 9.8$,⁴⁴ $f_{TO} = \omega_{TO}/2\pi = 11.7\text{THz}$ and $\epsilon(\omega)$ from Ref. 45, for LiF $\epsilon_s = 8.8$,⁴⁶ $f_{TO} = 9.2\text{THz}$,⁴⁶ and $\epsilon(\omega)$ from Ref. 47, for Al_2O_3 $f_0 = 24.2\text{THz}$, $\epsilon_0 = 9$, $\epsilon_\infty = 3$,⁴⁸ $m^* = 0.4m_e$,⁴⁹ and $\epsilon(\omega)$ from Ref. 50, for PbS $f_{LO} = 6.36\text{THz}$, $\epsilon_0 = 150$, $\epsilon_\infty = 16.8$,⁵¹ $m^* = 0.175m_e$,⁵² and $\epsilon(\omega)$ from Ref. 51, for Cu_2O $f_{LO} = 19.1\text{THz}$,⁵³ $\epsilon_0 = 7.11$, $\epsilon_\infty = 6.46$,⁵⁴ $m^* = 0.56m_e$,⁵⁵ and $\epsilon(\omega)$ from Ref. 54.
- ³⁴ H. C. van de Hulst, *Light Scattering by Small Particles* (Wiley, 1957).
- ³⁵ R. Fuchs and K. L. Kliewer, *J. Opt. Soc. Am.* **58**, 319 (1968).
- ³⁶ M. I. Tribelsky and B. S. Lykyanchuk, *Phys. Rev. Lett.* **97**, 263902 (2006).
- ³⁷ M. I. Tribelsky, *Europhys. Lett.* **94**, 14004 (2011).
- ³⁸ F. Greiner, J. Carstensen, N. Koehler, I. Pilch, H. Ketelsen, S. Knist, and A. Piel, *Plasma Sources Sci. Technol.* **21**, 065005 (2012).
- ³⁹ P. Mulvaney, J. Perez-Juste, M. Giersig, L. M. Liz-Marzan, and C. Pecharroman, *Plasmonics* **1**, 61 (2006).
- ⁴⁰ C. Novo and P. Mulvaney, *Nano Lett.* **7**, 520 (2007).
- ⁴¹ M. I. Lapsley, A. Shahravan, Q. Hao, B. K. Juluri, S. Giardinelli, M. Lu, Y. Zhao, I.-K. Chiang, T. Matsoukas, and T. J. Huang, *Apl. Phys. Lett.* **100**, 101903 (2012).
- ⁴² E. Kovascevic, I. Stefanovic, J. Berndt, Y. J. Pendleton, and J. Winter, *Astrophys. J.* **623**, 242 (2005).
- ⁴³ J. Berndt, E. Kovascevic, I. Stefanovic, O. Stefanovic, S. H. Hong, L. Boufendi, and J. Winter, *Contrib. Plasma Phys.* **49**, 107 (2009).
- ⁴⁴ M. Wintersgill, J. Fontanella, C. Andeen, and D. Schuele, *J. Appl. Phys.* **50**, 8259 (1979).
- ⁴⁵ J. R. Jasperse, A. Kahan, J. N. Plendl, and S. S. Mitra, *Phys. Rev.* **146**, 526 (1966).
- ⁴⁶ G. Dolling, H. G. Smith, R. M. Nicklow, P. R. Vijayaraghavan, and M. K. Wilkinson, *Phys. Rev.* **168**, 970 (1968).
- ⁴⁷ A. M. Hofmeister, E. Keppel, and A. K. Speck, *Mon. Not. R. Astron. Soc.* **345**, 16 (2003).
- ⁴⁸ M. Schubert, T. E. Tiwald, and C. M. Herzinger, *Phys. Rev. B* **61**, 8187 (2000).
- ⁴⁹ T. V. Perevalov, A. V. Shaposhnikov, V. A. Gritsenko, H. Wong, J. H. Han, and C. W. Kim, *JETP Letters* **85**, 165 (2007).
- ⁵⁰ E. D. Palik, *Handbook of Optical Constants of Solids* (Academic, 1985).
- ⁵¹ R. Geick, *Phys. Lett.* **10**, 51 (1964).
- ⁵² A. K. Walton, T. S. Moss, and B. Ellis, *Proc. Phys. Soc.* **79**, 1065 (1962).
- ⁵³ P. Dawson, M. M. Hargreave, and G. R. Wilson, *J. Phys. Chem. Solids* **34**, 2201 (1973).
- ⁵⁴ M. O’Keeffe, *J. Chem. Phys.* **39**, 1789 (1963).
- ⁵⁵ J. W. Hodby, T. E. Jenkins, C. Schwab, H. Tamura, and D. Trivich, *J. Phys. C* **9**, 1429 (1976).

Bibliography

- [1] R. N. Franklin, *Plasma phenomena in gas discharges* (Clarendon Press, Oxford, 1976).
- [2] F. X. Bronold, H. Deutsch, and H. Fehske, Physisorption kinetics of electrons at plasma boundaries. *Eur. Phys. J. D* **54**, 519 (2009).
- [3] H. Baumgartner, D. Block, and M. Bonitz, Structure and phase transitions of Yukawa balls. *Contrib. Plasma Phys.* **49**, 281 (2009).
- [4] A. Piel, O. Arp, D. Block, I. Pilch, T. Trottenberg, S. Käding, A. Melzer, H. Baumgartner, C. Henning, and M. Bonitz, Complex plasmas: forces and dynamical behaviour. *Plasma Phys. Control. Fusion* **50**, 124003 (2008).
- [5] V. E. Fortov, A. V. Ivlev, S. A. Khrapak, A. G. Khrapak, and G. E. Morfill, Complex (dusty) plasmas: Current status, open issues, perspectives. *Physics Reports* **421**, 1 (2005).
- [6] J. Berndt, E. Kovacevic, V. Selenin, I. Stefanovic, and J. Winter, Anomalous behaviour of the electron density in a pulsed complex plasma. *Plasma Sources Sci. Technol.* **15**, 18 (2006).
- [7] E. B. Tomme, D. A. Law, B. M. Annaratone, and J. E. Allen, Parabolic plasma sheath potentials and their implications for the charge on levitated dust particles. *Phys. Rev. Lett.* **85**, 2518 (2000).
- [8] J. Carstensen, H. Jung, F. Greiner, and A. Piel, Mass changes of microparticles in a plasma observed by a phase-resolved resonance method. *Phys. Plasmas* **18**, 033701 (2011).
- [9] A. Homann, A. Melzer, S. Peters, and A. Piel, Determination of the dust screening length by laser-excited lattice waves. *Phys. Rev. E* **56**, 7138 (1997).
- [10] A. Melzer, Mode spectra of thermally excited two-dimensional dust Coulomb clusters. *Phys. Rev. E* **67**, 016411 (2003).
- [11] J. Carstensen, F. Greiner, and A. Piel, Determination of dust grain charge and screening lengths in the plasma sheath by means of a controlled cluster rotation. *Phys. Plasmas* **17**, 083703 (2010).
- [12] U. Kogelschatz, Dielectric-barrier discharges: Their history, discharge physics, and industrial applications. *Plasma Chemistry and Plasma Processing* **23**, 1 (2003).
- [13] Y. B. Golubovskii, V. A. Maiorov, J. Behnke, and J. F. Behnke, Influence of interaction between charged particles and dielectric surface over a homogeneous barrier discharge in nitrogen. *J. Phys. D: Appl. Phys.* **35**, 751 (2002).

- [14] H.-E. Wagner, Y. V. Yurgelenas, and R. Brandenburg, The development of microdischarges of barrier discharges in N_2/O_2 mixtures—experimental investigations and modelling. *Plasma Phys. Control. Fusion* **47**, B641 (2005).
- [15] R. Brandenburg, V. A. Maiorov, Y. B. Golubovskii, H.-E. Wagner, J. Behnke, and J. F. Behnke, Diffuse barrier discharges in nitrogen with small admixtures of oxygen: discharge mechanism and transition to the filamentary regime. *J. Phys. D: Appl. Phys.* **38**, 2187 (2005).
- [16] L. Stollenwerk, S. Amiranashvili, J.-P. Boeuf, and H.-G. Purwins, Measurement and 3d simulation of self-organized filaments in a barrier discharge. *Phys. Rev. Lett.* **96**, 255001 (2006).
- [17] L. Stollenwerk, J. G. Laven, and H.-G. Purwins, Spatially resolved surface-charge measurement in a planar dielectric-barrier discharge system. *Phys. Rev. Lett.* **98**, 255001 (2007).
- [18] M. Bogaczyk, R. Wild, L. Stollenwerk, and H.-E. Wagner, Surface charge accumulation and discharge development in diffuse and filamentary barrier discharges operating in He, N_2 and mixtures. *J. Phys. D: Appl. Phys.* **46**, 465202 (2012).
- [19] M. Bogaczyk, S. Nemschokmichal, R. Wild, L. Stollenwerk, R. Brandenburg, J. Meichsner, and H.-E. Wagner, Development of barrier discharges: Operation modes and structure formation. *Contrib. Plasma Phys.* **52**, 847 (2012).
- [20] K. H. Becker, K. H. Schoenbach, and J. G. Eden, Microplasmas and applications. *J. Phys. D: Appl. Phys.* **39**, R55 (2006).
- [21] M. J. Kushner, Modelling of microdischarge devices: plasma and gas dynamics. *J. Phys. D: Appl. Phys.* **38**, 1633 (2005).
- [22] P. A. Tschertchian, C. J. Wagner, T. J. Houlahan, B. Li, D. J. Sievers, and J. G. Eden, Control of the interface between electron-hole and electron-ion plasmas: Hybrid semiconductor-gas phase devices as a gateway for plasma science. *Contrib. Plasma Phys.* **51**, 889 (2011).
- [23] R. Dussart, L. J. Overzet, P. Lefauchaux, T. Dufour, M. Kulsreshath, M. A. Mandra, T. Tillocher, O. Aubry, S. Dozias, P. Ranson, J. B. Lee, and M. Goeckner, Integrated micro-plasmas in silicon operating in helium. *Eur. Phys. J. D* **60**, 601 (2010).
- [24] C. J. Wagner, P. A. Tschertchian, and J. G. Eden, Coupling electron-hole and electron-ion plasmas: Realization of an npn plasma bipolar junction phototransistor. *Appl. Phys. Lett.* **97**, 134102 (2010).
- [25] B. Li, T. J. Houlahan, C. J. Wagner, and J. G. Eden, Modulating the secondary electron emission coefficient at the base-collector interface of the plasma bipolar junction transistor. *Appl. Phys. Lett.* **102**, 083502 (2013).
- [26] K. G. Emeleus and J. R. M. Coulter, Kinetic theory of the surface recombination of electrons and ions on glass surfaces. *Int. J. Electronics* **62**, 225 (1987).
- [27] K. G. Emeleus and J. R. M. Coulter, Surface recombination of ions and cratering by ion impact. *IEE Proceedings A Science Measurement and Technology* **135**, 76 (1988).

-
- [28] J. F. Behnke, T. Bindemann, H. Deutsch, and K. Becker, Wall recombination in glow discharges. *Contrib. Plasma Phys.* **37**, 345 (1997).
- [29] M. Lampe, V. Gavrishchaka, G. Ganguli, and G. Joyce, Effect of trapped ions on shielding of a charged spherical object in a plasma. *Phys. Rev. Lett.* **86**, 5278 (2001).
- [30] M. Lampe, R. Goswami, Z. Sternovsky, S. Robertson, V. Gavrishchaka, G. Ganguli, and G. Joyce, Trapped ion effect on shielding, current flow, and charging of a small object in a plasma. *Phys. Plasmas* **10**, 1500 (2003).
- [31] F. Stern, Image potential near a gradual interface between two dielectrics. *Phys. Rev. B* **17**, 5009 (1978).
- [32] E. E. Tkharev and A. L. Danilyuk, Electron density and potential distribution at a plasma-insulator interface. *Vacuum* **35**, 183 (1985).
- [33] M. A. Lieberman and A. J. Lichtenberg, *Principles of plasma discharges and materials processing* (Wiley, New York, 2005).
- [34] K.-U. Riemann, The Bohm criterion and sheath formation. *J. Phys. D: Appl. Phys.* **24**, 493 (1991).
- [35] J. D. Jackson, *Classical electrodynamics* (Wiley, New York, 1998).
- [36] J. B. Cui, J. Ristein, and L. Ley, Electron affinity of the bare and hydrogen covered single crystal diamond (111) surface. *Phys. Rev. Lett.* **81**, 429 (1998).
- [37] F. Maier, J. Ristein, and L. Ley, Electron affinity of plasma-hydrogenated and chemically oxidized diamond (100) surfaces. *Phys. Rev. B* **64**, 165411 (2001).
- [38] F. Stern and S. D. Sarma, Electron energy levels in GaAs-Ga_{1-x}Al_xAs heterojunctions. *Phys. Rev. B* **30**, 840 (1984).
- [39] H. Lüth, *Solid Surfaces, Interfaces and Thin Films* (Springer Verlag, Berlin, 1992).
- [40] W. Kohn and L. J. Sham, Self-consistent equations including exchange and correlation effects. *Phys. Rev.* **140A**, 1133 (1965).
- [41] N. D. Mermin, Thermal properties of the inhomogeneous electron gas. *Phys. Rev.* **137A**, 1441 (1965).
- [42] Z. W. Gortel, H. J. Kreuzer, and R. Teshima, Desorption by phonon cascades for gas-solid systems with many physisorbed surface bound states. *Phys. Rev. B* **22**, 5655 (1980).
- [43] H. J. Kreuzer and Z. W. Gortel, *Physisorption Kinetics* (Springer Verlag, Berlin, 1986).
- [44] G. Iche and P. Nozieres, A simple stochastic description of desorption rates. *J. Phys. (Paris)* **37**, 1313 (1976).
- [45] W. Brenig, Microscopic theory of gas-surface interaction. *Z. Phys. B* **48**, 127 (1982).
- [46] E. Evans and D. L. Mills, Interaction of slow electrons with the surface of a model dielectric: Theory of surface polarons. *Phys. Rev. B* **8**, 4004 (1973).

- [47] G. Barton, Image-induced surface states on electronically dense metals. *J. Phys. C* **14**, 3975 (1981).
- [48] B. Bendow and S.-C. Ying, Phonon-induced desorption of adatoms from crystal surfaces. I. Formal theory. *Phys. Rev. B* **7**, 622 (1973).
- [49] E. T. Whittaker and G. N. Watson, *A course of modern analysis* (Cambridge University Press, Cambridge, 1927).
- [50] C. F. Bohren and D. R. Huffman, *Absorption and Scattering of Light by small particles* (Wiley, New York, 1983).
- [51] G. Mie, Beiträge zu Optik trüber Medien, speziell kolloidaler Metallösungen. *Ann. Phys. (Leipzig)* **25**, 377 (1908).
- [52] C. F. Bohren and A. J. Hunt, Scattering of electromagnetic-waves by a charged sphere. *Can. J. Phys.* **55**, 1930 (1977).
- [53] J. Klačka and M. Kocifaj, Scattering of electromagnetic waves by charged spheres and some physical consequences. *J. Quant. Spectrosc. and Radiat. Transfer* **106**, 170 (2007).
- [54] J. Shan, F. Wang, E. Knoesel, M. Bonn, and T. F. Heinz, Measurement of the frequency-dependent conductivity in sapphire. *Phys. Rev. Lett.* **90**, 247401 (2003).
- [55] W. Götze and P. Wölfle, Homogeneous dynamical conductivity of simple metals. *Phys. Rev. B* **6**, 1226 (1972).
- [56] G. D. Mahan, *Many-particle physics* (Plenum, New York, 1990), p. 703-708.
- [57] R. Fuchs and K. L. Kliewer, Optical modes of vibration in an ionic crystal sphere. *J. Opt. Soc. Am.* **58**, 319 (1968).
- [58] M. I. Tribelsky and B. S. Luk'yanchuk, Anomalous light scattering by small particles. *Phys. Rev. Lett.* **97**, 263902 (2006).
- [59] M. I. Tribelsky, Anomalous light absorption by small particles. *Europhys. Lett.* **94**, 14004 (2011).
- [60] F. Greiner, J. Carstensen, N. Köhler, I. Pilch, H. Ketelsen, S. Knist, and A. Piel, Imaging Mie ellipsometry: dynamics of nanodust clouds in an argonacetylene plasma. *Plasma Sources Sci. Technol.* **21**, 065005 (2012).

Publications and Conferences

Publications

- [A] R. L. Heinisch, F. X. Bronold, and H. Fehske, Phonon-mediated desorption of image-bound electrons from dielectric surfaces, *Phys. Rev. B* **81**, 155420 (2010)
- [B] R. L. Heinisch, F. X. Bronold, and H. Fehske, Phonon-mediated sticking of electrons at dielectric surfaces, *Phys. Rev. B* **82**, 125408 (2010)
- [C] F. X. Bronold, R. L. Heinisch, J. Marbach, and H. Fehske, Plasma walls beyond the perfect absorber approximation for electrons, *IEEE Trans. Plasma Science* **39**, 644 (2011)
- [D] R. L. Heinisch, F. X. Bronold, and H. Fehske, Physisorption of an electron in deep surface potentials off a dielectric surface, *Phys. Rev. B* **83**, 195407 (2011)
- [E] R. L. Heinisch, F. X. Bronold, and H. Fehske, Electron surface layer at the interface of a plasma and a dielectric wall, *Phys. Rev. B* **85**, 075323 (2012)
- [F] F. X. Bronold, H. Fehske, R. L. Heinisch, J. Marbach, Wall charge and potential from a microscopic point of view, *Contrib. Plasma Phys.* **52**, 856 (2012)
- [G] R. L. Heinisch, F. X. Bronold, and H. Fehske, Mie scattering by a charged dielectric particle, *Phys. Rev. Lett.* **109**, 243903 (2012)
- [H] R. L. Heinisch, F. X. Bronold, and H. Fehske, Mie scattering analog in graphene: Lensing, particle confinement, and depletion of Klein tunnelling, *Phys. Rev. B* **87**, 155409 (2013)
- [I] R. L. Heinisch, F. X. Bronold, and H. Fehske, "Optical signatures of the charge of a dielectric particle in a plasma", accepted for publication in *Phys. Rev. E* (2013)
- [J] R. L. Heinisch, F. X. Bronold, and H. Fehske, Surface electrons at plasma walls, to appear in *Complex Plasmas: Scientific Challenges and Technological Opportunities*, Editors: M. Bonitz, K. Becker, J. Lopez and H. Thomsen, Springer, to be published 2013

Posters

1. R. L. Heinisch, F. X. Bronold, and H. Fehske, "Phonon-mediated adsorption and desorption of electrons at surfaces", DPG Spring Meeting, Hannover, 2010
2. F. X. Bronold, H. Fehske, R. L. Heinisch, and J. Marbach, "Quantum kinetics of electrons at plasma boundaries", DPG Spring Meeting, Regensburg, 2010
3. R. L. Heinisch, F. X. Bronold, and H. Fehske, "Phonon-mediated adsorption and desorption of electrons at surfaces", 2nd Graduate Summer Institute Complex Plasmas, Greifswald, 2010
4. R. L. Heinisch, F. X. Bronold, and H. Fehske, "Electronic physisorption at plasma walls", 30th International Conference on Phenomena in Ionized Gases (ICPIG), Belfast, 2011
5. R. L. Heinisch, F. X. Bronold, and H. Fehske, "Mie Scattering by a Charged Dielectric Particle Proposal of a Novel Plasma Probe", DPG Spring Meeting, Jena, 2013
6. R. L. Heinisch, F. X. Bronold, and H. Fehske, "Anomalous Light Scattering by a Charged Dielectric Particle", DPG Spring Meeting, Regensburg, 2013

Talks

1. "Phonon-mediated adsorption and desorption of an image-bound electron", DPG Spring Meeting, Dresden, 2011
2. "Electron surface layers at dielectric plasma walls", Physics of Complex Plasmas, International Workshop, TRR24, Potsdam, 2011
3. "Electron surface layer at the interface of a plasma and a dielectric wall" (topical talk), DPG Spring Meeting, Stuttgart, 2012
4. "Surface electrons at plasma walls", 3rd Graduate Summer Institute Complex Plasmas, South Orange, NJ, USA
5. "Mie scattering by a charged dielectric particle", 3rd International Workshop on Diagnostics and Simulation of Dusty Plasmas, Kiel, 2012
6. "Mie Scattering Analogue in Graphene: lensing, particle confinement, and depletion of Klein tunnelling", DPG Spring Meeting, Regensburg, 2013
7. "Mie Scattering Analogue in Graphene: lensing, particle confinement, and depletion of Klein tunnelling", 7th Graphene Week, Chemnitz, 2013
8. "Mie scattering by a charged dielectric particle: proposal for a novel plasma probe", 40th European Physical Society Conference on Plasma Physics, Helsinki, 2013

Erklärung

Hiermit erkläre ich, dass diese Arbeit bisher von mir weder an der Mathematisch-Naturwissenschaftlichen Fakultät der Ernst-Moritz-Arndt-Universität Greifswald noch einer anderen wissenschaftlichen Einrichtung zum Zwecke der Promotion eingereicht wurde.

Ferner erkläre ich, dass ich diese Arbeit selbständig verfasst und keine anderen als die darin angegebenen Hilfsmittel und Hilfen benutzt und keine Textabschnitte eines Dritten ohne Kennzeichnung übernommen habe.

(Rafael Heinisch)

Greifswald, 19 August 2013

Curriculum Vitae

Personal Data

Name: Rafael Leslie Heinisch
Date of Birth: 21 February 1985
Place of Birth: Tübingen
Family status: married, one daughter

School Education

Sept 1990 - Jul 1995 Grundschole Winkelwiese Tübingen
Sept 1995 - Jul 2004 Kepler-Gymnasium Tübingen

Training

Oct 2004 - Oct 2009 Study of physics at the University of Greifswald, Germany
Mar 2005 - Oct 2009 Scholarship: Studienstiftung des deutschen Volkes
Oct 2007 - Jul 2008 Study of physics at the University of St. Andrews, Scotland
Oct 2009 Diploma degree, University of Greifswald
Diploma thesis: ‘Trapping and detrapping of charged particles at surfaces’
since Nov 2009 PhD student in physics,
Chair of Prof. Dr. Holger Fehske,
University of Greifswald, Germany

Acknowledgement

I extend my deepest gratitude to

Franz Xaver Bronold,

Holger Fehske,

Bernd Zenker, and

Ida Heidecker-Heinisch

for their advice, inspiration, and support.